Imperial College London

*Doctoral Thesis*

# Understanding and modelling the thermal behaviour of incumbent and future lithium ion batteries

***Author:***

Xiao Hua

***Supervisors:***

Dr. Gregory J. Offer

Prof. Ricardo Martinez-Botas

Dr. Monica Marinescu

Dr. Yatish Patel

*A thesis submitted in fulfilment of the requirements for the degree of Doctor of Philosophy*

*in the*

Electrochemical Science & Engineering Group

Department of Mechanical Engineering

May 22, 2020

# ***Declaration of Originality***

I, Xiao Hua, declare that this thesis, "Understanding and modelling the thermal behaviour of incumbent and future lithium ion batteries" and the work presented in it are my own, except where appropriately referenced or acknowledged.

Xiao Hua (2020)

# ***Copyright Declaration***

*To my parents, Tianlai Hua & Aihong Xu,*
*for their patience, for their love, for everything.*

*"Shoot for the moon.*

*Even if you miss, you'll land among the stars."*

*-Les Brown*

*"If you want to go fast, go alone.*

*If you want to go far, go together."*

*-African Proverb*

Imperial College London

# *Abstract*

Electrochemical Science & Engineering Group

Department of Mechanical Engineering

Doctor of Philosophy

## Understanding and modelling the thermal behaviour of incumbent and future lithium ion batteries

by Xiao Hua

The thesis begins with a literature review on the thermal behaviours for an incumbent and a future lithium ion battery, which are Lithium iron phosphate (LFP) prismatic batteries and Lithium sulfur (Li-S) pouch batteries, respectively. Research gaps were identified for both types of batteries, requiring the development of novel experimental techniques and/or modelling approaches for each type.

Lithium sulfur batteries are an important next generation high energy density battery technology. However, the phenomenon known as the polysulfide shuttle was identified as one of the most important challenges needing to be overcome. It causes accelerated degradation, reduced Coulombic efficiency and increased heat generation, particularly towards the end of charge. Research was conducted on how to track, quantify and therefore prevent the shuttle effect, in order to improve the safety and increase cycle life of Li-S batteries in real applications. This required the real-time detection of the onset of shuttle during charge. The diagnostic technique Differential Thermal Voltammetry (DTV) was used to track the shuttle effect during charging for the first time, and quantitative interpretations of the experimental DTV curves were performed by thermally-coupling a zero-dimensional Li-S model. The DTV technique, together with the model, is a promising tool for real-time detection of shuttle

in applications, to inform control algorithms for deciding the end of charging, thus preventing excessive degradation and charge inefficiency.

Lithium iron phosphate prismatic batteries are widely used in both sustainable transportation and stationary energy storage. However, system level thermal management for large format prismatic cells is rarely considered in the literature. Equivalent circuit models (ECM) were shortlisted, due to their ease of implementation and low complexity. The accuracy of an ECM is critical to the functionality and usefulness of the battery management system (BMS). However, their accuracy is limited by how easy they are parameterised, and therefore different experimental techniques and model parameter identification methods (PIM) have been widely studied. Yet, how to account for significant changes in time constants between operation under load and during relaxation has not been resolved. In this work a novel PIM and a modified ECM is presented that increases accuracy by 77.4% during drive cycle validation and 87.6% during constant current load validation for a large format LFP prismatic cell. The modified ECM uses switching RC network values for each phase, which is significant for this cell and particularly at low state-of-charge for all lithium ion batteries. Different characterisation tests and the corresponding experimental data have been trained together across a complete State-of-Charge (SoC) and temperature range, which enables a smooth transition between identified parameters. Ultimately, the model created using parameters captured by the proposed PIM shows an improved model accuracy in comparison with conventional PIM techniques.

Large format prismatic cell's thermal management is challenging due to the large internal heat generation rate, longer distance for internal battery core away from the heat exchange cooling interface and therefore larger thermal gradient across the cell. The standardised surface Cell Cooling Coefficient (CCC) can be used to quantify the degree of difficulty of a target cell to be thermally managed. Here, in this thesis, the novel metric surface CCC is introduced and implemented onto a large format LFP prismatic cell, with aluminium alloy prismatic casing. Further, based on developed PIM, a parameterised and discretised 3-dimentional Electro-Thermal Equivalent Circuit Model is developed. The developed model is validated using the experimental data through embedding corresponding boundary conditions, including drive cycle noisy load and constant current CCC square wave load, electrically and thermally at the same time. The study offers a quantitative guide of the trade-off between cell energy density and surface CCC, and also a casing selection analysis is conducted. The CCC metric together with proposed model enable the cell manufacturer and Original Equipment

Makers (OEMs) to customise the cell design based on the casing material, single cell energy density, cell thickness and CCC/capability to be thermally managed. In the future cell design process, this study offers a cost-effective, time-efficient, convenient and quantitative way, in order to achieve a better and safe battery design (high capacity, power and longer lifetime) for wider application needs.

Finally, it is concluded that, for both incumbent and future lithium ion batteries, understanding the thermal behaviour is the key for a safer, lighter, longer lifetime, longer range application. By using engineering customised experimental techniques together with empirical and/or physical simulations, enhanced understanding with quantitative battery optimisation and thermal management are achieved in this thesis. The findings in thesis are beneficial for wide range of communities including research community, industry OEMs, application engineers, battery management system developers, control engineers and electric vehicle end users.

# Acknowledgement

I would like to express my gratefulness to my dear Dr. Gregory J. Offer, my primary supervisor, my mentor and my friend. Over the past 4 years, it was a fruitful and pleasant journey with Greg, where he guided me how to be a good PhD, a battery expert, a man. I love his style of coaching young researchers, where it is not possible for me to tackle many tough challenges without the freedom to learn, the inspiration, the support, the continuous engagement that he contributed to my PhD research. Thank you, Greg.

I also want to thank my associate supervisor, Prof. Ricardo Martinez-Botas, for his kind guidance and support. Particularly, thank the insights gained from Dr. Monica Marinescu on Lithium-sulfur modelling, Dr. Yatish Patel on experimental design and funding proposal. A particular thanks to Dr. Teng Zhang, for his kind inspiration on Lithium-sulfur modelling, constant support, where he acted as my unofficial associated supervisor.

I would like to thank my funders, Envision AESC and Envision Group for the project funding and kind technical supports during my PhD, especially to Lei Zhang, Weijun Zhao, Jie Sun, Dr. Liang Tao, Dr. Le Yu, Zhonghua Xu, Dr. Hongwu She, Dr. Jie Cheng, Qingqing Sun and Ye Yuan.

Also, I would like to thank Dassault Systèmes for the modelling collaboration project in the past 2 years. Particularly for Nils Modrow and Claas Heckel for their expertise on Modelica coding and Dymola modelling.

A big thank you, for all the past and present members of the research group. They acted as my family to support me. Special thanks to Dr. Yu Merla, for his kind help on Differential Thermal Voltammetry analysis, Dr. Cheng Zhang, for his professional ECM parameterisation skills, Dr. Alastair Hales, for his professional thermal management experimental skills, Dr. Yan Zhao and Dr. Shen Li, for their ECM modelling insights. Also, thanks to Ian C, Alex, Emma, Waseem, Laura, Ryan, Oisin, for their friendship and company.

Thanks to all my friends outside my research life, especially Dr. Jun Liu and his family, Dr. Zhaoheng Cai and his family, for their emotional support and company. Also, Yinjun Luo and his wife Lu Li, Linfei Wu and Bowen Gao, who pulled me through all these years while I am thousands of miles away from my hometown.

Finally, to my family, to my parents, for the support, for the love, for everything.

# ***Project Outputs***

## *Academic Journal Publications (5)*

- ***First and corresponding author:***

**Xiao Hua***, Teng Zhang, Gregory Offer, Monica Marinescu*. '***Towards online tracking of the shuttle effect in lithium sulfur batteries using differential thermal voltammetry***' *Journal of Energy Storage, 21 (2019), pp. 765-772.* https://doi.org/10.1016/j.est.2019.01.002

- ***First author:***

**Xiao Hua**, Cheng Zhang, Gregory Offer*. '***Finding a better fit for lithium ion batteries: a simple, novel, load dependent, modified equivalent circuit model and parameterization method'*** *under review in Journal of Power Sources.*

**Xiao Hua**, Claas Heckel, Nils Modrow, Cheng Zhang, Alastair Hales, Justin Holloway, Anmol Jnawali, Shen Li, Yifei Yu, Melanie Loveridge, Paul Shearing, Yatish Patel, Monica Marinescu, Liang Tao, Gregory Offer*. '***The Prismatic Surface cell cooling coefficient: a novel cell design optimisation tool & thermal parameterisation method for a 3D discretised Electro-Thermal Equivalent-Circuit Model'*** *under review in Journal of eTransportation.*

- ***Co-author:***

Shen Li, Niall Kirkaldy, Cheng Zhang, Krishnakumar Gopalakrishnan, Taz Amietszajew, Laura Bravo Diaz, Jorge Varela Barreras, Mosayeb Shams, Xiao Hua, Yatish Patel, Gregory Offer, Monica Marinescu*. ***'Cell tab design and cooling strategy of cylindrical lithium-ion batteries'*** under review in Journal of Power Sources.

Emma Vendola, Mei-Chin Pang, Ian Campbell, **Xiao Hua**, Laura Lander, Jacqueline Edge, Gregory Offer*. '***Strategies towards the next disruptive battery technology'*** *in preparation, target journals: Nature or Nature Energy.*

## *Software (1)*

- ***Dymola - Dassault Systèmes®***

Co-developed a major update package for the software package ***'battery library'***, detailed contribution by thesis author is attached to the Appendices.

https://www.3ds.com/fileadmin/PRODUCTS/CATIA/DYMOLA/PDF/3DS_2015_CATIA_BTY_Battery__Flyer_A4_WEB.pdf

## *Funding (1)*

- ***'Imperial College London Industry Studentship',*** London, UK, Full PhD Scholarship awarded, 2017.

## *Conference presentations (2)*

- ***United Kingdom:***

**Xiao Hua**, Teng Zhang, Monica Marinescu, Gregory Offer. '***Towards online tracking of the shuttle effect in lithium sulfur batteries using differential thermal voltammetry***' *UK Energy Storage (UKES)*, Newcastle, UK, 2018. https://www.meetnewcastlegateshead.com/case-studies/uk-energy-storage-ukes-conference-2018/

- ***United States of America:***

**Xiao Hua**, Teng Zhang, Monica Marinescu, Gregory Offer. '***Detecting Polysulfide Shuttle in Li-S Batteries with Differential Thermal Voltammetry***' *LI-SM$^3$ 2018 Conference: Lithium Sulfur Batteries: Mechanisms, Modelling and Materials*, Chicago, USA, 2018. http://www.lism3.org/ https://app.box.com/s/19il5fy39n4boxjhj9i5sq3lf1t16vjd

## *Conference poster (1)*

- ***Japan:***

**Xiao Hua**, Yan Zhao, Alastair Hales, Yatish Patel, Gregory Offer. '***How do we thermal manage the Li-ion battery? An inside out solution***' *3rd International advanced automotive battery conference (AABC)*, Tokyo, Japan, 2019. https://www.advancedautobat.com/asia

## *Training (1)*

- ***'Battery School 2019' by Faraday Institution,*** WMG, Warwick, UK, 2019.

# ***Table of Contents***

# List of Figures

# List of Tables

# List of Abbreviations

| *Abbreviation* | *Stands for* |
|---|---|
| ARC | Accelerating Rate Calorimeter |
| Al | Aluminium (Material) |
| ASSLSBs | All-solid-state lithium-sulfur batteries |
| BEV | Battery Electric Vehicle |
| BMS | Battery Management System |
| BTMS | Battery Thermal Management System |
| EPA | Environmental Protection Agency |
| CC | Constant Current |
| CCC | Cell Cooling Coefficient |
| CCCV | Constant Current Constant Voltage |
| Co | Cobalt (material) |
| Cu | Copper (Material) |
| CT | Computed Tomography |
| DTV | Differential Thermal Voltammetry |
| DoD | Depth of Discharge |
| ECM | Equivalent Circuit Modelling |
| EU | European Union |
| EIS | Electrochemical Impedance Spectroscopy |
| EV | Electric Vehicle |
| EoL | End of Life |
| FMU | Functional Mock-up Unit |
| FVM | Finite Volume Method |
| GA | Genetic Algorithm |
| GITT | Galvanostatic Intermittent Titration Technique |
| HEV | Hybrid Electric Vehicle |
| ICA | Incremental Capacity Analysis |
| ICE | Internal Combustion Engine |
| It | Coulomb Counting |
| LAM | Loss of Active Material |
| LCO | Lithium Cobalt Oxide |
| LFP | Lithium Iron Phosphate |

| | |
|---|---|
| Li-ion | Lithium-ion |
| LIB | Lithium-ion Battery |
| LiS | Lithium Sulfur |
| LLI | Loss of Lithium Inventory |
| LMO | Lithium Manganese Oxide |
| LTO | Lithium Titanate |
| Mn | Magnesium (Material) |
| MnO | Magnesium Oxide |
| Ni | Nickel (Material) |
| NCA | Nickel Cobalt Aluminium Oxide |
| NMC | Nickel Manganese Cobalt |
| NTGK | Newman, Tiedemann, Gu and Kwon |
| OEM | Original Equipment Manufacturer |
| OCV | Open Circuit Voltage |
| PD | Pulse Discharge |
| PE | Peltier Elements |
| PHEV | Plug-in Hybrid Electric Vehicle |
| PSO | Particle Swarm Optimization |
| RC | Resistor-capacitor |
| RMSE | Root Mean Square Error |
| ROM | Reduced Order Model |
| SEI | Solid-Electrolyte Interface |
| SEM | Scanning Electron Microscope |
| TC | Thermocouple |
| SoC | State of Charge |
| SoH | State of Health |
| SRCV | Slow-rate Cyclic Voltammetry |
| THT | Thermal Hazards Technology® |
| TMS | Thermal Management System |
| XRD | X-ray diffraction |
| UK | United Kingdom |
| USA | United States of America |
| 0D | Zero-dimensional |

# List of Symbols

| Symbols | Unit | Name |
|---|---|---|
| $A$ | - | the pre-exponent factor |
| $\alpha_a$ | - | Anodic charge transfer coefficient, dimensionless ($0 \leq \alpha_a \leq 1$) |
| $\alpha_c$ | - | Cathodic charge transfer coefficient, dimensionless ($0 \leq \alpha_c \leq 1$) |
| $\alpha_h$ | - | Cell heat-transfer coefficient |
| $E$ | V | Cell Potential (Electromotive Force, EMF) |
| $E^{0'}$ | V | Standard electrode potential |
| $E_{eq}$ | V | Electrode potential at equilibrium |
| $E_a$ | J | Activation energy for the reaction |
| $R_g$ | - | Universal gas constant |
| $R$ | Ω | Internal equivalent resistance of the cell |
| $R_{cell}$ | Ω | Cell resistance |
| $R_0$ | Ω | Ohmic resistance |
| $R_i$ | Ω | Resistance value for each indivudal component $i$ within the ECM networks |
| $R_{ECM}$ | Ω | Resistance value the ECM networks |
| $T$ | K | Temperature in kelvins |
| $F$ | - | Faraday constant, the number of coulombs per mole of electrons |
| $C_i^*$ | mol/m$^3$ | Bulk concentration of species $i$ |
| $C_i$ | F | Capacitance value for each indivudal component $i$ within the ECM networks |
| $C_{ECM}$ | F | Capacitance value the ECM networks |
| $C_n$ | Ah | Battery nominal capacity at 25°$C$ |
| $C$ | J/K | Heat capacity |
| $c_p$ | J/(kg.K) | Specific heat capacity of the element |
| $CCC_{surf}$ | W/K | Cell Cooling Coefficient of cell surface |
| $k_r$ | - | ate constant, which is the frequency of the collisions resulting in a reaction |
| $\dot{Q}$ | W | Battery heat generation rate |
| $\dot{Q}_{cond}$ | W | Heat transfer rate through conduction |
| $\dot{Q}_{\mathrm{irr}}$ | W | Irreversible heat generation rate |

| | | |
|---|---|---|
| $\dot{Q}_{\text{rev}}$ | W | Reversible heat generation |
| $\dot{Q}_{loss}$ | W | Total heat flow generated by each ECM |
| $\dot{Q}_{Surf}$ | W | Surface heat rejection rate |
| $\dot{Q}_{fn}$ | W | Heat transfer rates from one fin |
| $I$ | A | Applied current into the battery, charge/discharge |
| $i_{th}$ | A | Current threshold |
| $k$ | W/(m·K) | Thermal conductivity of the element |
| $S_H$ | mol/m$^3$ | High polysulfide amount (high plateau polysulfide concentration) |
| $S_H^0$ | mol/m$^3$ | Polysulfide concentration when $t$ equals 0 at high plateau |
| $t$ | s | Time |
| $T_s$ | s | Sampling interval |
| $\bar{T}_{Back}$ | °C | Average cell surface back temperature |
| $\bar{T}_{Front}$ | °C | Average cell surface front temperature |
| $\Delta T_{Cell}$ | K | Difference between $\bar{T}_{Back}$ and $\bar{T}_{Front}$ |
| $q_H$ | Ah | Specific capacity of sulfur to high voltage plateau |
| $k_S$ | - | shuttle constant or heterogeneous reaction constant. |
| $m$ | kg | Cell mass |
| $M_S$ | g | the molar mass of $S_8^0$ |
| $U_{RC}$ | V | Votlage loss at each R-C branch |
| $U_i$ | V | Votlage value for each indivudal component $i$ within the ECM networks |
| $V_H$ | V | Cell voltage at high plateau |
| $V_{terminal}$ | V | Cell terminal voltage |
| $V$ | m$^3$ | Volume of the element |
| $x$ | m | Distance of the heat conduction range of the element |
| $\eta$ | V | Overpotential |
| $n_{rc}$ | - | Number of R-C network |
| $n_{soc}$ | - | Number of SoC breakpoints |
| $\tau_{j,u}$ | s | Underload time constant |
| $\tau_{j,r}$ | s | Relaxation time constant |
| $\rho$ | kg/ m$^3$ | Density of the element |

# 1. Introduction

## 1.1. Backgrounds: the motivation of Electrification

The majority of the countries in the EU, China and USA have announced the plan to ban the sale of the internal combustion engine (ICE) vehicles in next few decades[1], to improve air quality and reduce greenhouse gas emissions [2]. The research and development of Electric Vehicles (EVs) (Hybrid Electric Vehicles (HEVs), Plug in Hybrid Electric Vehicles (PHEV) and Battery Electric Vehicles (BEVs)) are essential to this low-emission transformation.

The sales of EVs have increased dramatically, there were over 2 million electric vehicles sold in 2018, up from just a few thousand in 2010. Bloomberg NEF forecast the sales of annual passenger EVs to rise to 10 million in 2025, 28 million in 2030 and 56 million by 2040, illustrated in the figure below [3], and many now consider the electrification of transport to be inevitable.

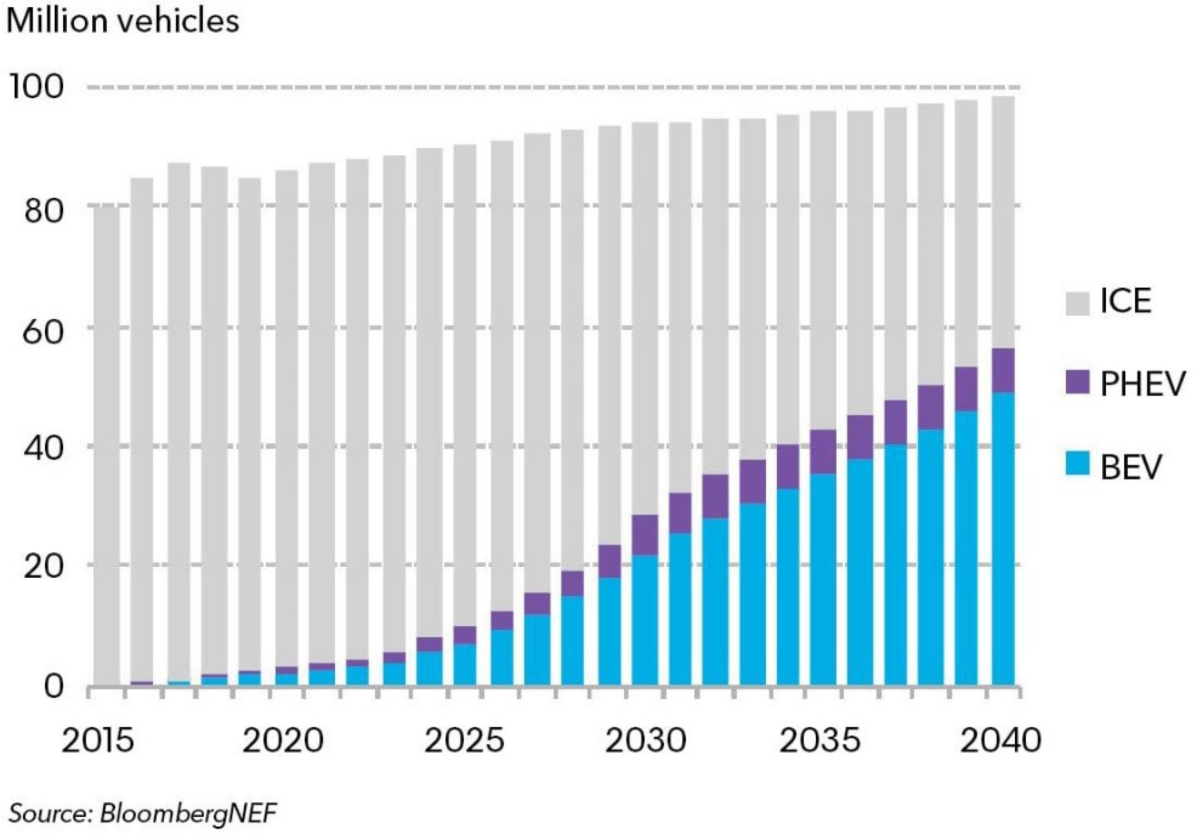

*Figure 1 Global long-term passenger vehicle sales by drivetrain: by 2040 57% of all passenger vehicle sales and over 30% of the global passenger vehicle fleet, will be electric [4]*

One noticeable point is that, the demand for batteries isn't entirely coming from passenger EVs, there is also significant demand from commercial EVs, stationary storage, consumer electronics and electric buses, etc. Unsurprisingly, the demand for lithium-ion batteries is currently growing rapidly. Forecasted demand is predicted to approach 2000 GWh annually by around 2030. [4]

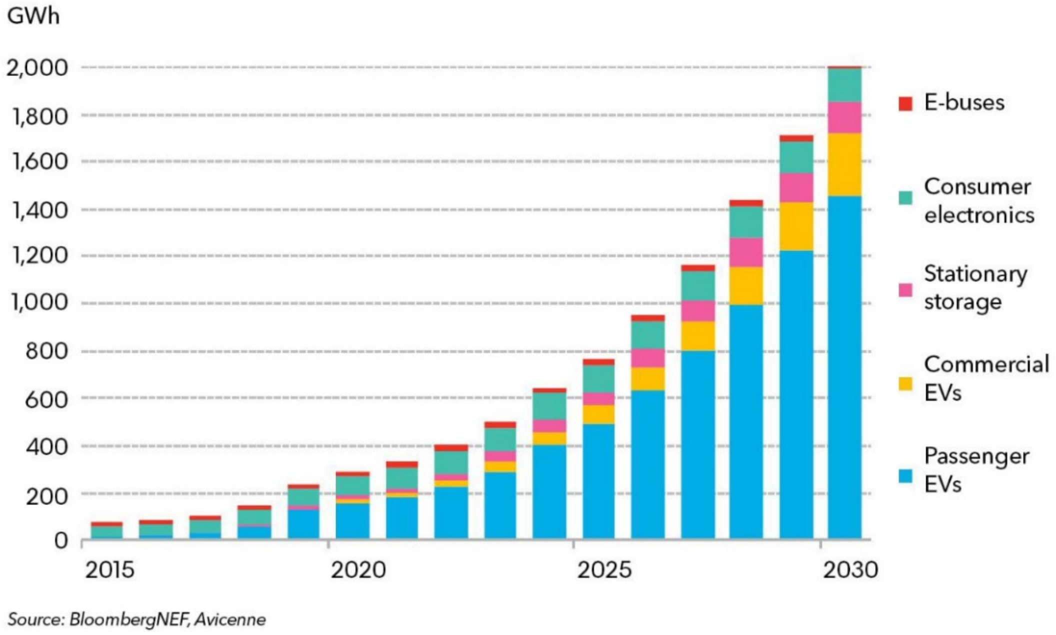

Source: BloombergNEF, Avicenne

*Figure 2 Annual lithium-ion battery demand.[4]*

Despite the rapid growth in sales today, there are over a billion vehicles on the road and EVs are still less than 0.5% of the global vehicle fleet. [5] One key factor is the battery pack unit price, as it affects the sales price directly. However, the volume weighted average lithium-ion pack price has also dropped significantly since 2010, reaching 176 $/kWh in 2018. [4]

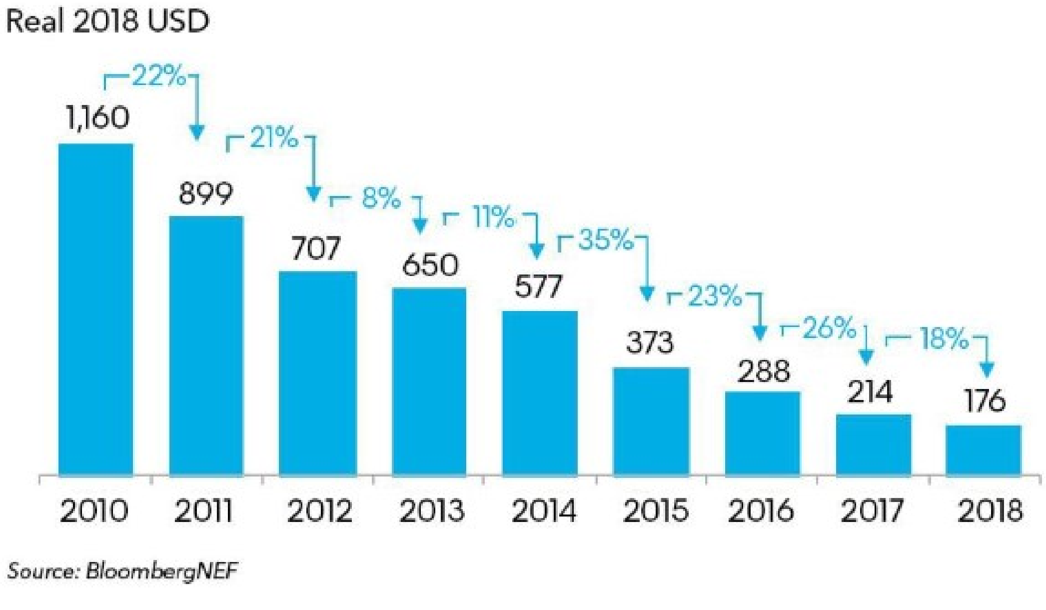

Source: BloombergNEF

*Figure 3 Average lithium-ion pack price: $/kWh[4]*

A good example of how to electrify transport rapidly is China, due to its aggressive policy-supported push and pull at both national and regional levels. [4] As a consequence China has become a global leader in both EV demand and production. [6] For example Elon Musk and his Tesla Inc collaborated with Shanghai government, and went from permits to a finished plant in just 168 working days. That Gigafactory is able to produce 35 GWh of batteries annually. [7] This is already helping improve air quality in China. The United Nations Environment Programme published a report for Air Pollution Control in Beijing, and the greenhouse emission of Beijing and its surround areas have decreased significantly from 2013 to 2017, due in part to the rise in transportation structure optimisation: electric vehicles in public fleets. [8] A visualised evidence is demonstrated in the figure below.

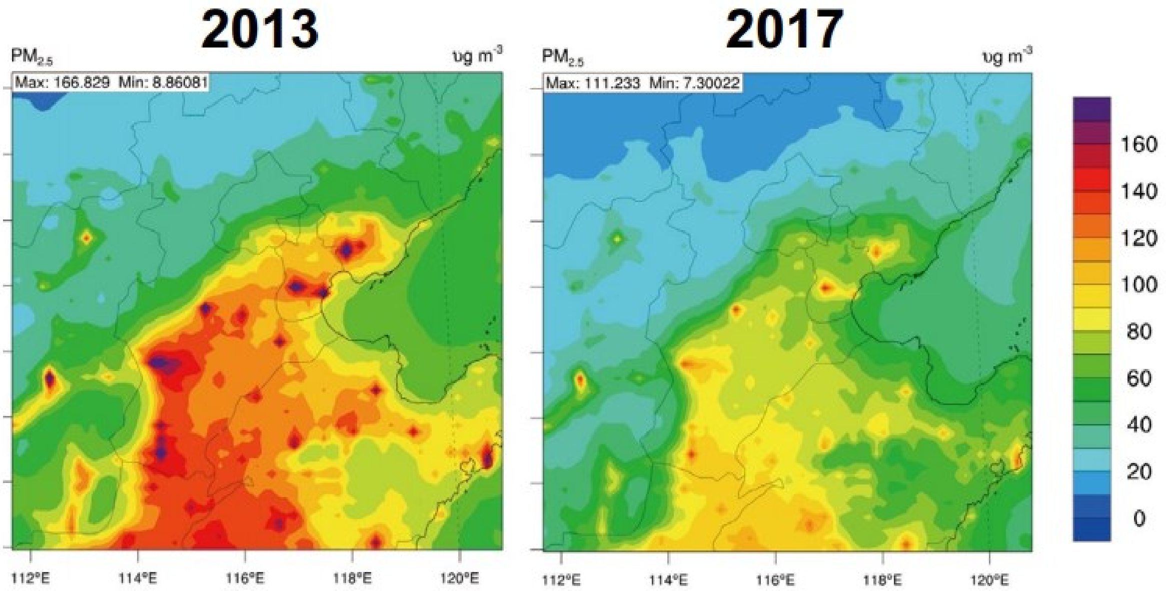

*Figure 4 Spatial distributions of annual average PM2.5 concentrations in Beijing and its surrounding areas. (2013, 2017)[8]*

However, to continue widespread electrification at an acceptable cost, there are still many technical barriers. One of the key challenges is the immature Lithium-ion technology. With the inevitable trend for electrification and dramatic increase in battery demand, the research community and industrial OEMs are aligned, to make Li-ion battery cheaper, safer and extended range and longer lifetime. The goal of this thesis is to contribute a small part towards this wider international effort.

## 1.2. Thesis Aim and research objectives

In order to progress battery technology, there are 2 ways to approach the problem.

The first is to use engineering to maximise the performance of existing Li-ion battery technologies which are already commercialised widespread e.g. Lithium iron phosphate (LFP) or Nickel Manganese Cobalt (NMC) cells. For example, through better Battery Management Systems (BMS) and/or better pack design particularly Battery Thermal Management Systems (BTMS).

Lithium iron phosphate (LFP) was first described as a cathode material for batteries in 1997 by Padhi et al. [9] After a decade of development, Nishimura et al. in 2008 demonstrated the high charge-discharge rate capability of LFP through combined high-temperature powder neutron diffraction and the maximum entropy method. [10] At a similar time LFP based lithium-ion batteries were being scaled up for mass production for PHEVs and/or EVs. Since then, LFP is projected to capture significant part of the EV industry because its essential benefits: intrinsic safety, low cost, high cycle-lifetime, high power capability, reliability, widespread availability of materials, low toxicity and flat voltage profile. On the other hand, the key drawbacks of the LFP are its lower nominal voltage which leads to lower volumetric energy density and specific energy. [11–13]

The second approach is improving the cell performance internally through new material development, such as new cathode/anode material or solid-state batteries, which exceed the limits on volumetric energy density and specific energy of LFP or NMC cells. A representative of this approach is the Li-metal cell, which includes Lithium-sulfur (LiS) cells.

LiS cells stand out among other technologies because of their promising energy density compared to conventional lithium-ion batteries: a theoretical specific energy (Gravimetric Energy Density) of 2,567 Wh kg$^{-1}$ and theoretical energy density (Volumetric Energy Density) of 2,199 Wh l$^{-1}$, which almost 7 times greater(Gravimetric) and 2 times greater (Volumetric) compared with today's Li-ion batteries (Li-ion has 387 Wh kg$^{-1}$ and 1,015 Wh l$^{-1}$).[14,15] The disadvantages of LiS cells, such as self-discharge, rapid capacity fade, low charging efficiency and difficulties of estimating State-of-Charge (SOC), [16] mean it is not yet ready for mass production.

Both approaches require detailed thermal characterisation as temperature is one of the key limiting factors for all batteries' performance and lifetime. For most material combinations, the suitable operating temperature range is between 20 °C – 40 °C, coinciding with most environmental temperature conditions around the world. Large temperature deviations, especially during fast charging, can lead to accelerated degradation and, in extreme cases, thermal runaway. [17–22] Therefore, BTMSs are a key limiting factor for EV development, and the majority of EVs on the market nowadays are equipped with BTMSs.[23] Yet, there are still significant limitations in how most BTMSs are designed, and the compromises they have to make are mostly caused by the way the cells are designed. [24]

As a battery researcher, understanding every single type, chemistry, and format is my ultimate dream. However, due to limited timescale for the PhD as well as priorities influenced by my funder (a cell manufacturer), this thesis has focussed on studying two cells in detail. For the future battery candidate selection, Li-S cells were selected, over all-solid-states or Li-Air cells because our group had a project funded, the ‘Revolutionary Electric Vehicle Battery’ REVB project involving a UK based Li-S cell manufacturer, OXIS Energy. The cells that have been studied are all provided by OXIS Energy. Although of interest the Li-Air cells and All-Solid-State Li-ion cells were difficult to obtain from a sustainable and reliable vender, therefore were not selected. To represent the incumbent technology, the LFP prismatic cell was selected, as the PhD personal funding started in the middle of the second year, provided by Envision AESC. The cells that were studied were of particular interest to Envision AESC and were provided by them. The theme of the thesis linking the research done on both the incumbent and future battery technology is thermal management.

LiS has a significant temperature dependency on its usable capacity and its lifetime. Degradation is strongly linked with operating conditions, cycling rates as well as operating ambient temperature due to the accumulation of precipitated $Li_2S$ and the effect of shuttle. [25–27] However, the thermal behaviour of LiS cells was poorly understood, therefore, and as the major heat source the thermal behaviour of the shuttle reaction needed to be quantified and modelled.

In contrast, the understanding of heat generation in LFP cells is well studied and understood by the research community, therefore the major task identified was to develop a model to study different cell designs and how they interact with cell cooling methods. The BTMS for large format prismatic cell is challenging to design and optimise and requires advanced simulation tools for design. Prismatic cells typically have a very low surface area to capacity ratio making it harder to exchange heat with a cooling system compared to smaller capacity cells. [28] Although a single cell in an open space may easily radiate the heat generated from charge and discharge it is not easy to do so inside a large battery pack. [29]

In summary, studying the thermal behaviour of lithium ion batteries is essential for EV development. This is true for both LFP cells and LiS cells. However, their very different maturity level required an individual approach. In order to address the objectives above and within the PhD timeframe,

This thesis had the following objectives for the ***LFP cells***:

- Develop a client facing (user-interface friendly), thermally coupled, Equivalent-Circuits-Model (ECM). Do this for one of the most common battery chemistries with a conventional form factor, which is mass produced, but not fully thermally optimised. The cell chosen was a large-format prismatic LFP.
- As part of the Electrochemical Science & Engineering (ESE) group at Imperial College London be part of the team developing the newest understanding in how to evaluate how easy or hard it is to thermally manage a battery. Therefore, use the Cell Cooling Coefficient (CCC) which quantifies the rate of heat rejection in the above study. Demonstrate this metric on prismatic cells for the first time and use the ECM model developed to study the internal thermal gradient distribution.
- With the information gained from the CCC together with the model to conduct a cell design optimisation study (Cell thickness, cell casing material) for better thermal management performance and less difficulty to be thermal managed.

And for the ***LiS cells***:

- Develop a new diagnosis technique using Differential Thermal Voltammetry (DTV) that can monitor the LiS cells internal states and quantify the amount of shuttle in real time. Use such quantification to study the relationship between shuttle and heat generation of LiS cells. Also, the technique should minimise the cost of hardware to be cost-feasible for mass production.
- Develop a thermally coupled zero-dimensional model for LiS cells, that can be used to interpret the data in real time. Such model should be able to form the basis of a DTV based LiS control algorithm to prevent degradation and improve charge efficiency.

These objectives then led to the following research questions:

***For LiS cells:***

1. Could one in-situ experimental diagnostic tool (e.g. DTV) quantify, track Li-S shuttle effect?
2. Could this diagnostic tool, DTV, be used as a charging cut-off tool to minimise shuttle?
3. Could thermally-coupled 0-Dimentinal LiS model provide optimal charging algorithms?

***For LFP cells:***

4. Could the CCC metric be capable of providing better thermal gradient understanding for large format LFP prismatic cells?
5. Could the CCC be used as a novel method for thermal parameterisation of an ECM?
6. Could the discretised Electro-thermal ECM model have developed together with embedded CCC boundary conditions be used for cell optimisation?
7. Are existing ECM electrical parameterisation methods suitable for large form factor LFP cells, and if not, what improvements are needed?
8. Could changes in cell configuration affect the large format LFP prismatic cells thermal behaviours? And decrease the difficulties of thermal management for such large format cells?

To efficiently use the time and resource allocated, the scope of the PhD and this thesis is limited as follows:

- Although it would have been a natural follow on, this work did not include developing a degradation model for LiS due to multiple reasons: low Li-S battery stock, end of the research project. *[1]
- The thermal management system development and modelling will only be researched at the cell level. The pack level study was beyond the scope of this thesis.
- Each lithium-ion cell variants and chemistries will be used to develop their own model and assess the relevant applications. The ECM model and CCC focussed on the LFP prismatic cells*[2] and the 0-D model and DTV focussed on LiS pouch cells. Assessing alternative cell formats and chemistries was beyond the scope of this thesis.
- The Hydrogen Fuel Cell, which is one possible alternative power sources, was beyond the scope of this thesis.

*[1] The project involving OXIS energy ended during the second year of PhD, and the supply of Li-S pouch cells stopped.

*[2] The PhD was funded since the second year of the study, by Envision AESC, who provided the prismatic cell. The ECM model developed was in collaboration with Dassault Systèmes, under paid software *Dymola*. Detailed collaboration information and proof of contribution is attached in the Appendices.

## 1.3. Thesis Outline

The thesis starts with a detailed literature review, in order to establish the research gaps. Then the following chapters answer the research questions stated above.

This section summarises each chapter of this thesis:

- Chapter 1: Introduction
  - ✓ This chapter introduces the reasons behind the battery research, which stated from authoritative organisations. The research aim, research questions and outline of this thesis are presented into details.
- Chapter 2: Literature review
  - ✓ This chapter introduces working principles, format, chemistry of lithium-ion cell, specifically on Li-S cell and LFP cell. Identifying gap in the research.
- Chapter 3: DTV technique on LiS cell and corresponding 0D modelling
  - ✓ This chapter demonstrates the experimental implementation of the novel diagnosis technique DTV on single LiS pouch cell.
  - ✓ Presents the details of how DTV quantify and track the polysulfide shuttle effect.
  - ✓ Shows the 0D thermally coupled model can capture DTV patterns and used to interpret DTV experimental data.
  - ✓ Describes the charge control algorithms based on qualitatively analysis of DTV.
  - ✓ Presents optimal charge cut-off points to prevent degradation & charge inefficiency
- Chapter 4: Novel Equivalent circuit model parameterisation method for Li-ion batteries
  - ✓ This chapter demonstrates a novel method to parameterise the LFP prismatic cell for ECM modelling.
  - ✓ Discussed the difference and the achieved enhancement on the new parameter identification method, compares with conventional methods.
- Chapter 5: CCC Surface technique on LFP cell and corresponding Discretised ECM modelling
  - ✓ This chapter demonstrates experimental technique CCC is implemented on the LFP prismatic cell.
  - ✓ Discussed this cutting-edge metric, which has the capability of evaluating cell's ability of heat rejection.

- ✓ Describes the development of the 3-dimensional thermo-electric ECM model.
- ✓ The model is used to demonstrate the internal heat distribution of the thermal gradient under different cooling strategies. Proposing any cell configuration optimisation that maximise the performance of thermal management.
- ✓ Discusses the optimal cell configuration change concluded, using the cell design quantitative study to compare, revise and update the cell optimisation.
- ✓ Shows that CCC as a new thermal parameterisation method for lithium-ion Electro-thermal ECM modelling.

## 1.4. Publication explanation:

This thesis has the work both from previous published academic journal papers and the academic journal papers that are submitted and under review. The first author of the journal papers published/submitted is also the author of this thesis, Xiao Hua. This section explains the permission of the usage of the materials and also the contribution of co-authors.

Chapter 3 is based on the journal publication by Xiao Hua, Teng Zhang, Gregory Offer and Monica Marinescu. '*Towards online tracking of the shuttle effect in lithium sulfur batteries using differential thermal voltammetry*' *Journal of Energy Storage, 21 (2019), pp. 765-772.* The article is published with ELSEVIER, which grants the author to retain the right to include it in a thesis or dissertation using the full article, where permission is not required. The thesis author has led this work in all areas, acted as first & corresponding author. Dr Teng Zhang, Dr Gregory Offer and Dr Monica Marinescu have contributed to the article in providing supervision and edited the manuscript. Additionally, Dr Monica Marinescu assisted on the 0D model development and the implementation of the mathematical equations into the model. The contents of this chapter include (in part/full) material copied verbatim from the journal publication. All authors were notified of the use of the material for this thesis and no objection was raised.

Chapter 4 is based on the journal publication by Xiao Hua, Cheng Zhang, Gregory Offer. '*Finding a better fit for lithium ion batteries: a simple novel, load dependent, modified equivalent circuit model and parameterization method 'under review in Journal of Power Sources.* The article is publishing with ELSEVIER, which grants the author to retain the right to include it in a thesis or dissertation using the full article, where permission is not required.

The thesis author has led this work in all areas, acted as first & leading author. Dr Cheng Zhang, Dr Gregory Offer have contributed to the article in providing supervision and edited the manuscript. Additionally, Dr Cheng Zhang has contributed towards the data analysis prior the parameter identification process, also the mathematical implementation of the parameterisation procedure. The contents in this chapter includes (in part/full) material copied verbatim from the journal publication. All authors were notified of the use of the material for this thesis and no objection was raised.

Chapter 5 is based on the journal publication by Xiao Hua, Claas Heckel, Nils Modrow, Cheng Zhang, Alastair Hales, Justin Holloway, Anmol Jnawali, Shen Li, Yifei Yu, Melanie Loveridge, Paul Shearing, Yatish Patel, Monica Marinescu, Liang Tao, Gregory Offer. '*The Prismatic Surface cell cooling coefficient: a novel cell design optimisation tool & thermal parameterisation method for a 3D discretised Electro-Thermal Equivalent-Circuit Model 'under review in Journal of eTransportation.* The article is publishing with ELSEVIER, which grants the author to retain the right to include it in a thesis or dissertation using the full article, where permission is not required. The thesis author has led this work in all areas, acted as first & leading author. Dr Cheng Zhang, Dr Gregory Offer have contributed to the article in providing supervision and edited the manuscript. Additionally, Dr Cheng Zhang & Dr Shen Li has contributed towards the equivalent circuit model parameterisation procedure. Dr Alastair Hales contributed towards the construction of the Surface Cell Cooling Coefficient experimental apparatus, Dr Liang Tao contributed to providing the testing cells and providing cell datasheet, Justin Holloway, Dr Yifei Yu and Prof. Melanie Loveridge contributed the cell dismantling experiments. Prof Paul Shearing and Anmol Jnawali contributed into the CT scanning/imaging experiments. Claas Heckel and Nils Modrow contributed to the coding of the electrical and thermal model development. The model is developed within software '*Dymola*' from Dassault Systèmes, where the detailed contribution of the model is attached to the appendices. The contents in this chapter includes (in part/full) material copied verbatim from the journal publication. All authors were notified of the use of the material for this thesis and no objection was raised.

# 2. Literature Review

## 2.1. Introduction

This chapter introduces a detailed literature review of the lithium-ion and lithium sulfur cell. The working principle of the cells, electrode materials, degradation modes and various type of cell configurations are presented. Also, in order to identify the gap between the latest research literature and the current work, a few specific battery related topics are discussed, such as modelling techniques, diagnosis techniques, cell evaluation techniques, where those topics are relevant to the research aims.

### 2.1.1. Why we research, produce and use Lithium-ion battery

As briefly discussed in the introduction, the significant rise in the EV market is driving the battery industry into a fast-growing stage. The annual demand of Lithium-ion battery/battery packs today is over 200 GWh (2019) and is predicted grow exponentially in the next decade. [4] Under such welcoming circumstances, the battery related activities are well-funded and well-focused, among both industry and research communities. However, one of the key barriers of the EV R&D nowadays is the range limit, which is limited by the energy density of the battery system. Optimising the existing battery technology through engineering is needed, in order to maximise its performance. Meanwhile, scientists and engineers are also working on other battery chemistries with higher theoretical limits.

### 2.1.2. Why we move to Lithium-sulfur

Today’s lithium-ion batteries have limits of 387 Wh kg$^{-1}$ theoretical specific energy (Gravimetric Energy Density) and 1015 Wh l$^{-1}$ theoretical energy density (Volumetric Energy Density). By contrast, the Li-S cell has a theoretical specific energy of 2,567 Wh kg$^{-1}$ and theoretical energy density of 2,199 Wh l$^{-1}$, which almost 7 times greater (Gravimetric) and 2 times greater (Volumetric) compared with today’s Li-ion batteries. [14,15] (Please note, these comparisons are fair only within theoretical limits and didn’t take into account the extra material needed to make a functional cell, e.g. current collectors, tab, casing material) The figure below, although being slightly outdated from 2011, shows how increased energy density translates directly into increased driving range. [14] State-of-the-art commercially available EVs now can already achieve ranges of 600 km (EPA), i.e. Tesla Model S Long range with 100 kWh Lithium-ion battery pack. [30,31] With the same volume & ratio of the battery-pack, an EV with Li-S battery pack could have an even longer driving range or a lighter battery pack. (Battery pack prices now are approaching $150/kWh, and Li-ion is achieving 300 Wh/kg)

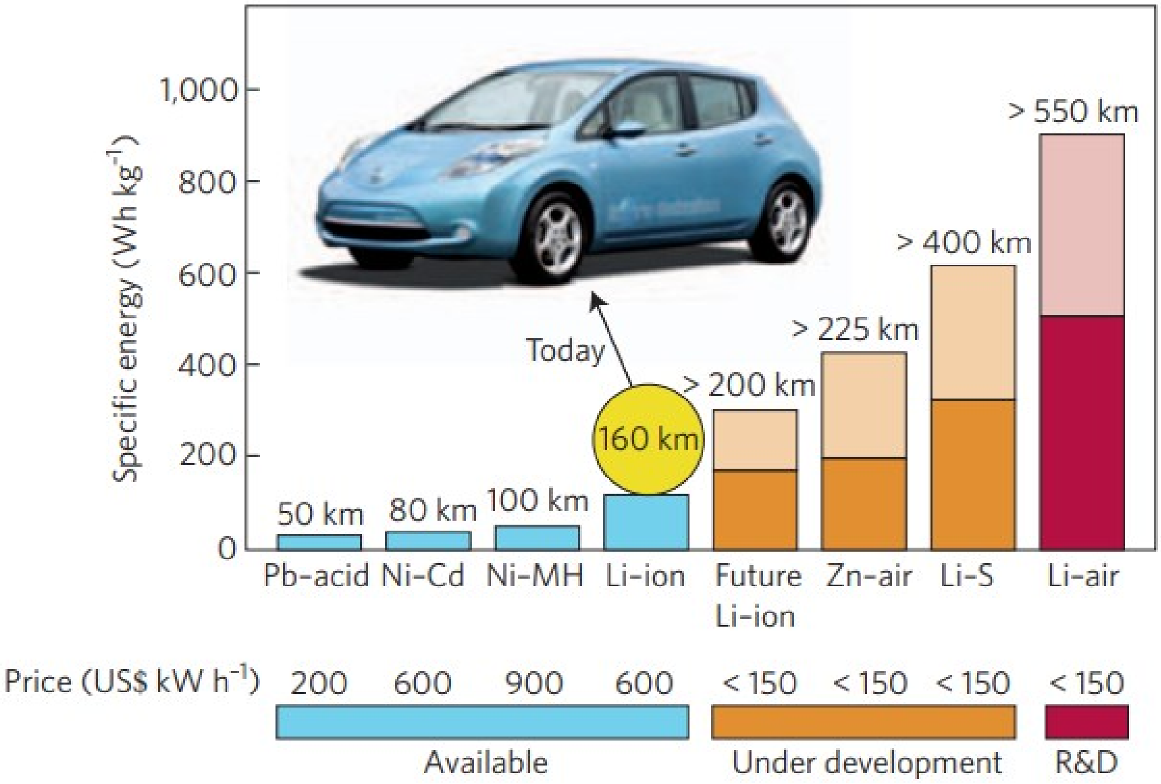

*Figure 5 Practical specific energies for some rechargeable batteries, along with estimated driving distances and pack prices (Data captured in 2011) [14]*

The figure below demonstrates a few common types of cathode/anode materials and their experimental and theoretical specific capacity, showing that sulfur is a promising candidate for cathode material because of its higher theoretical limits. [32]

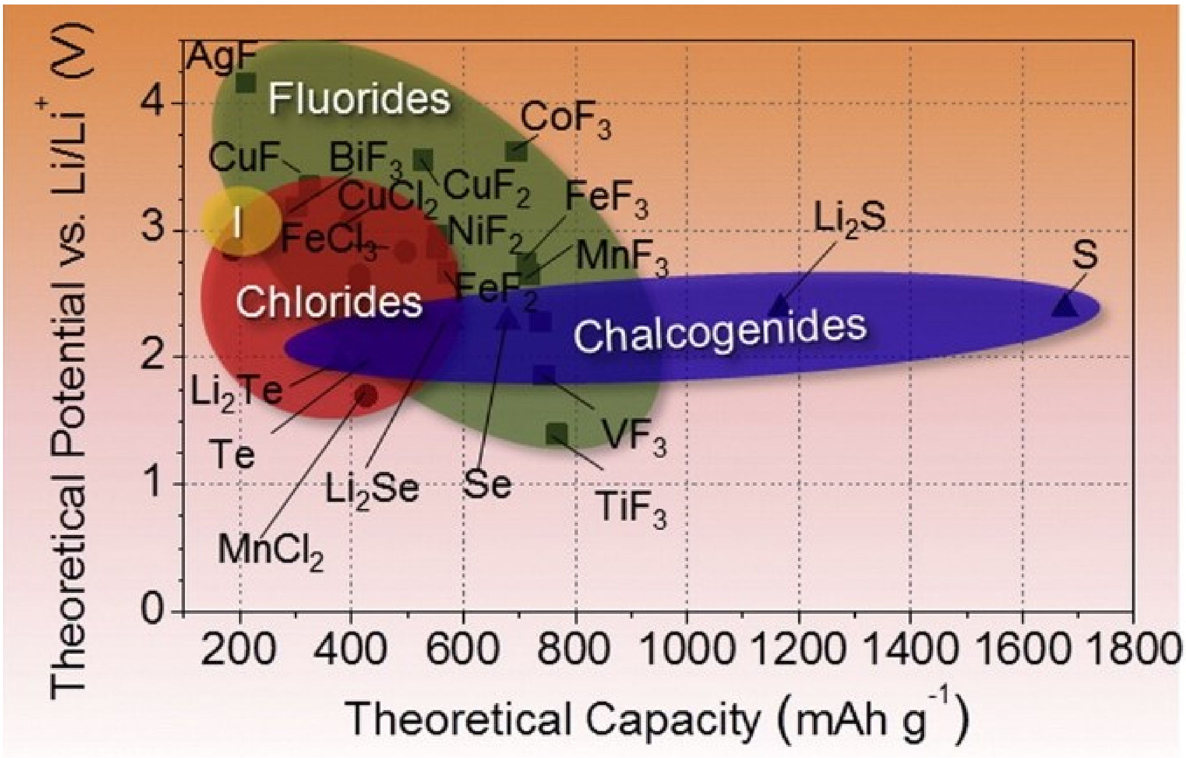

*Figure 6 Approximate range of average discharge potentials and specific capacity of some of the most common conversion-type cathodes (theoretical)*[32]

## 2.2. What is Lithium-ion battery: working principle

Rechargeable Li-ion battery have a few essential components: positive electrode, negative electrode, ion-conducting electrolyte, electrically insulating separator, metallic foil current collectors, tabs, and an outer casing of some kind. In the figure below, it shows the particle and cell scale structures of a cylindrical cell. [33] The outer layers of positive and negative electrodes are coated on current collectors, which sandwich the separator which is permeated with the electrolyte, as shown in the figure below. [34]

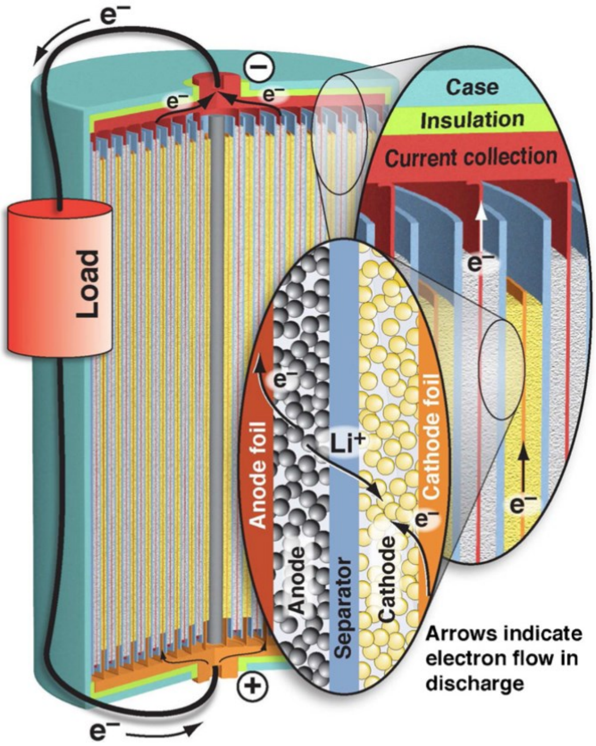

*Figure 7 Structure of a Li-ion battery, showing cell-scale and particle-scale structures.*[33]

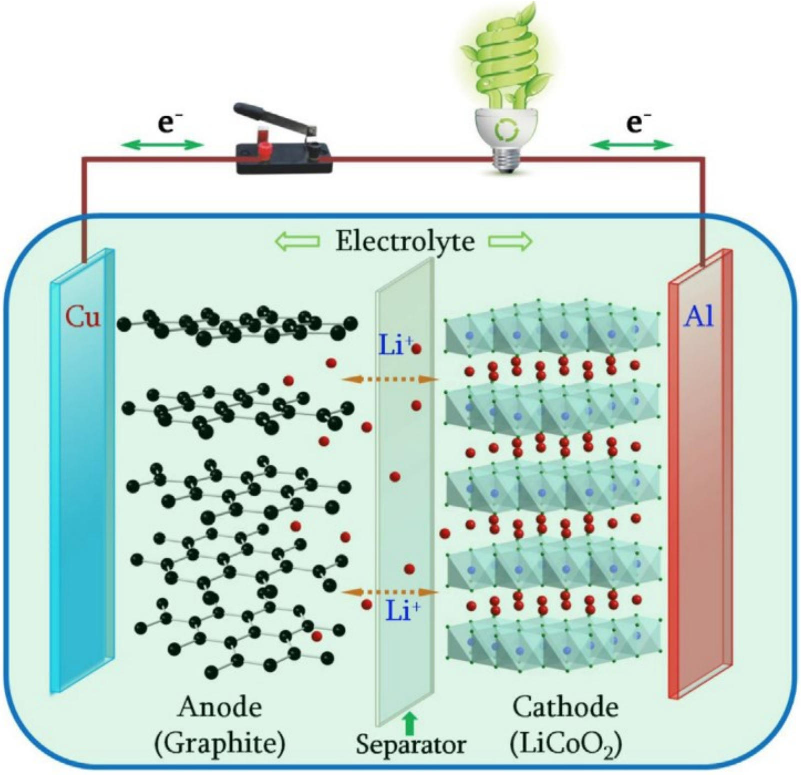

*Figure 8 Schematic of the configuration of rechargeable Li-ion batteries.* [34]

Lithium has only one electron in its outer shell and is therefore highly reactive with water and air. However, when lithium is part of a metal oxide, it is stable and makes a good positive electrode material. By definition, the anode is the electrode where oxidation occurs, and the cathode is the electrode where reduction occurs. However, the negative electrode and positive electrode are often called the anode and cathode respectively, even though this is only actually true under discharge.

As shown in figure 8, when the battery is fully charged the lithium is stored in the anode, which is often made from porous materials such as carbon graphite. During discharge an oxidation reaction occurs, and lithium ions and electrons are produced. The lithium ions transport into the electrolyte and travel through the electrically insulating separator, while the cathode accepts the lithium-ion where it is reduced. At the same time, the electrons are released through current collectors and move from the anode via the external load to the cathode. The equations 1 & 2 demonstrate the discharge reaction at anode and cathode respectively.

$$Discharge: Li_xC_6 \rightarrow nLi^+ + ne^- + Li_{x-n}C_6 \tag{1}$$

$$Discharge: Li_yMO_2 \ + nLi^+ + ne^- \rightarrow Li_{y+n}MO_2 \tag{2}$$

Similarly, in the charging process, the entire reaction reverses. The lithium ions diffuse back from positive electrode to negative electrode, while the electrons are accepted at the negative electrode. The equations 3 & 4 show the charge reaction at both ends.

$$Charge: Li_{y+n}MO_2 \rightarrow Li_yMO_2 \ + nLi^+ + ne^- \tag{3}$$

$$Charge: \ nLi^+ + ne^- + Li_{x-n}C_6 \rightarrow Li_xC_6 \tag{4}$$

During the charge and discharge reactions, both positive and negative electrodes have their own electrochemical potential values. The difference in the electrochemical potential values of the positive and negative electrodes is called the Open-Circuit Voltage (OCV).

### 2.2.1. How Lithium Sulfur works

Similar to some Li-ion batteries, lithium sulfur batteries use lithium as negative electrode material, but sulfur for the cathode material. Equation 5 describes the charge and discharge overall process of the lithium sulfur cell, where the sulfur is stored in the porous conducting carbon matrix in the cathode. During discharge, the reduction of elemental sulfur $S_8$ occurs via various polysulphides intermediates such as $Li_2S_8$, $Li_2S_4$ and $Li_2S_2$, and to ultimately produce $Li_2S$, where the element sulfur is offering a theoretically capacity of 1672mAh $g^{-1}$ [14,35]. Figure 9 shows the discharge process graphically.

$$2\mathrm{Li}^+ + 2e^- + S \leftrightarrow Li_2S \tag{5}$$

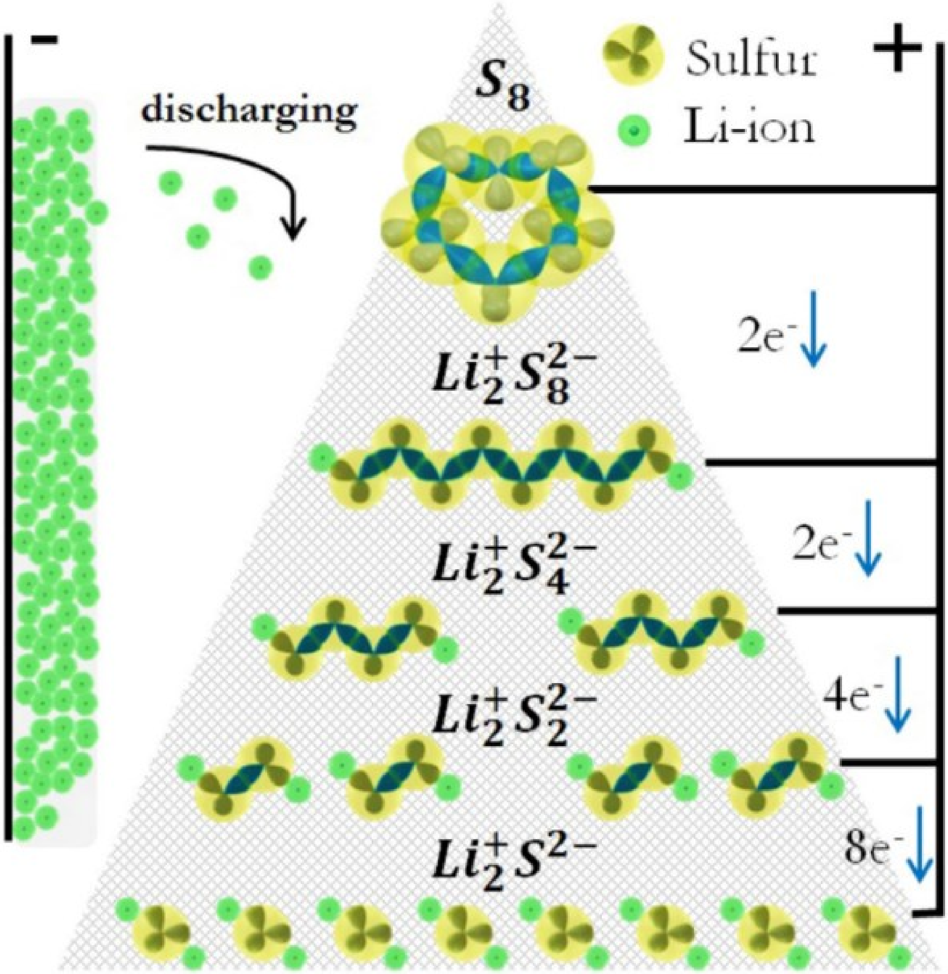

*Figure 9 Work principle of Li-S battery* [36]

Figure 10 and equation 6-12 summarise the equations that were used in the mathematical model by K. Kumaresan, Y. Mikhaylik, and R. E. White *et al*, to describe the discharge process of a Li-S battery in a schematic way. [37,38]

Elemental sulfur $S_8$ has low solubility (19 mol/$m^3$)[39], thus it is mostly in the solid phase $S_{8(s)}$ at the beginning of discharge. The dissolution reaction below in equation 6 is therefore the first step required. Thereafter, during the discharge process the liquid phase sulfur $S_{8(l)}$is reduced to sulphide ions with decreasing oxidation number as shown in equation 7-11 below.

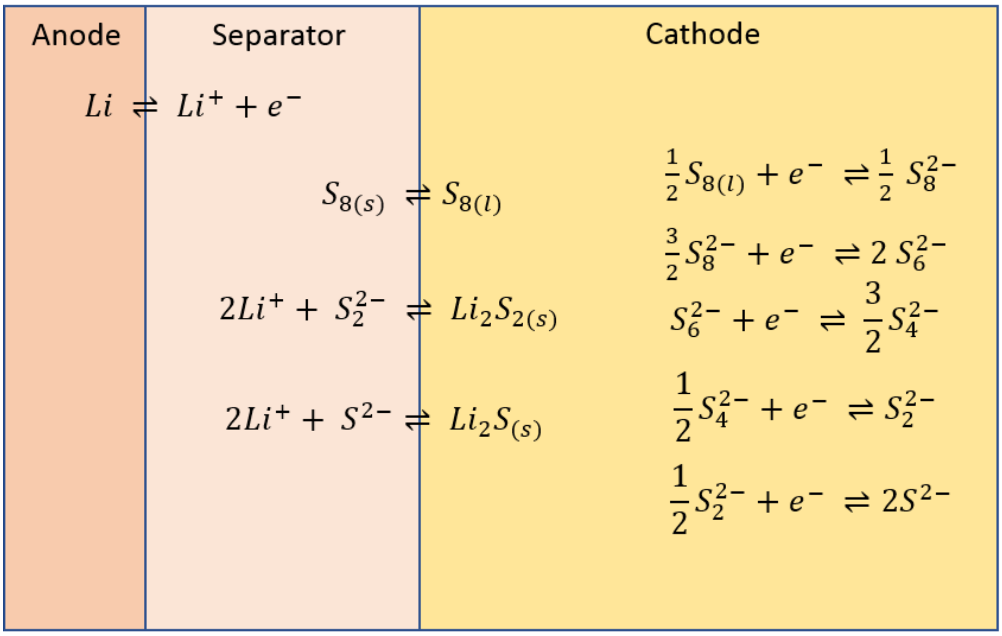

*Figure 10 Schematic of Lithium-Sulfur battery with electrochemical reaction equations.*

$$S_{8(s)} \rightleftharpoons S_{8(l)} \tag{6}$$

$$\frac{1}{2}S_{8(l)} + e^- \rightleftharpoons \frac{1}{2}\,S_8^{2-} \tag{7}$$

$$\frac{3}{2}S_8^{2-} + e^- \rightleftharpoons 2\,S_6^{2-} \tag{8}$$

$$S_6^{2-} + e^- \rightleftharpoons \frac{3}{2}S_4^{2-} \tag{9}$$

$$\frac{1}{2}S_4^{2-} + e^- \rightleftharpoons S_2^{2-} \tag{10}$$

$$\frac{1}{2}S_2^{2-} + e^- \rightleftharpoons 2S^{2-} \tag{11}$$

The Lithium metal at the anode surface is therefore oxidised when discharging, lithium ions are formed, as shown in equation 12.

$$Li \rightleftharpoons Li^+ + e^- \tag{12}$$

As the discharging process continues, the concentration of both lithium ions and sulphide ions increase.[39] However, some of the lower order polysulfides also have limited solubility and therefore, the following dissolution/ precipitation equations (13 & 14) describe the formation of $Li_2S_{2(s)}$ and $Li_2S_{(s)}$.

$$2Li^+ + S_2^{2-} \rightleftharpoons Li_2S_{2(s)} \tag{13}$$

$$2Li^+ + S^{2-} \rightleftharpoons Li_2S_{(s)} \tag{14}$$

Similar to discharge process, the charging reactions reverse the equations 5 – 14, the lithium is extracted from the positive electrode via electrochemical reactions at the solid-electrolyte interface and the Li-ions diffuse to negative electrode surface. During charging, the polysulfides produced during discharge reactions are oxidised from short chain polysulfides such as ($Li_2^+S_2^{2-}$ and $Li_2^+S^{2-}$) into long chain polysulfides such as ($Li_2^+S_8^{2-}$ & $Li_2^+S_6^{2-}$), and ultimately back into liquid & solid element phase sulfur $S_{8(l)}$ and $S_{8(s)}$.

## 2.3. Electrode Material

### 2.3.1. Cathode/Positive Electrode

The majority of the intercalation cathode of lithium-ion battery are made from metal chalcogenides, transition metal oxides and polyanion compounds. [32] As introduced in previous section, the intercalation cathode of a lithium battery is a solid host network to store lithium ions, where the lithium ions can be inserted into and be removed from the host network reversibly. A qualified cathode material would ideally be equipped with the following characteristics:

1. High coulombic efficiency and high free energy of reaction with lithium, which enables storing large quantities of lithium ions with high specific capacity.
2. Good electronic conductivity, high lithium-ion diffusivity, high potential, which enables good rate capability and high power.
3. Long cycle life, low cost of raw materials and production.
4. Good thermal satiability which enable higher safety.

There is no ‘perfect’ cathode material as there are inevitable trade-offs between the characteristics stated above. Therefore, choosing specific cathode material for different operating scenarios is a critical decision to be made in the battery powered applications such as electric vehicles, energy storage station or Unmanned aerial vehicles (UAVs).

As figure 11 shows, there are mainly 4 types of intercalation cathode crystal structures, which are (a) layered, (b) spinel, (c) olivine and (d) tavorite.

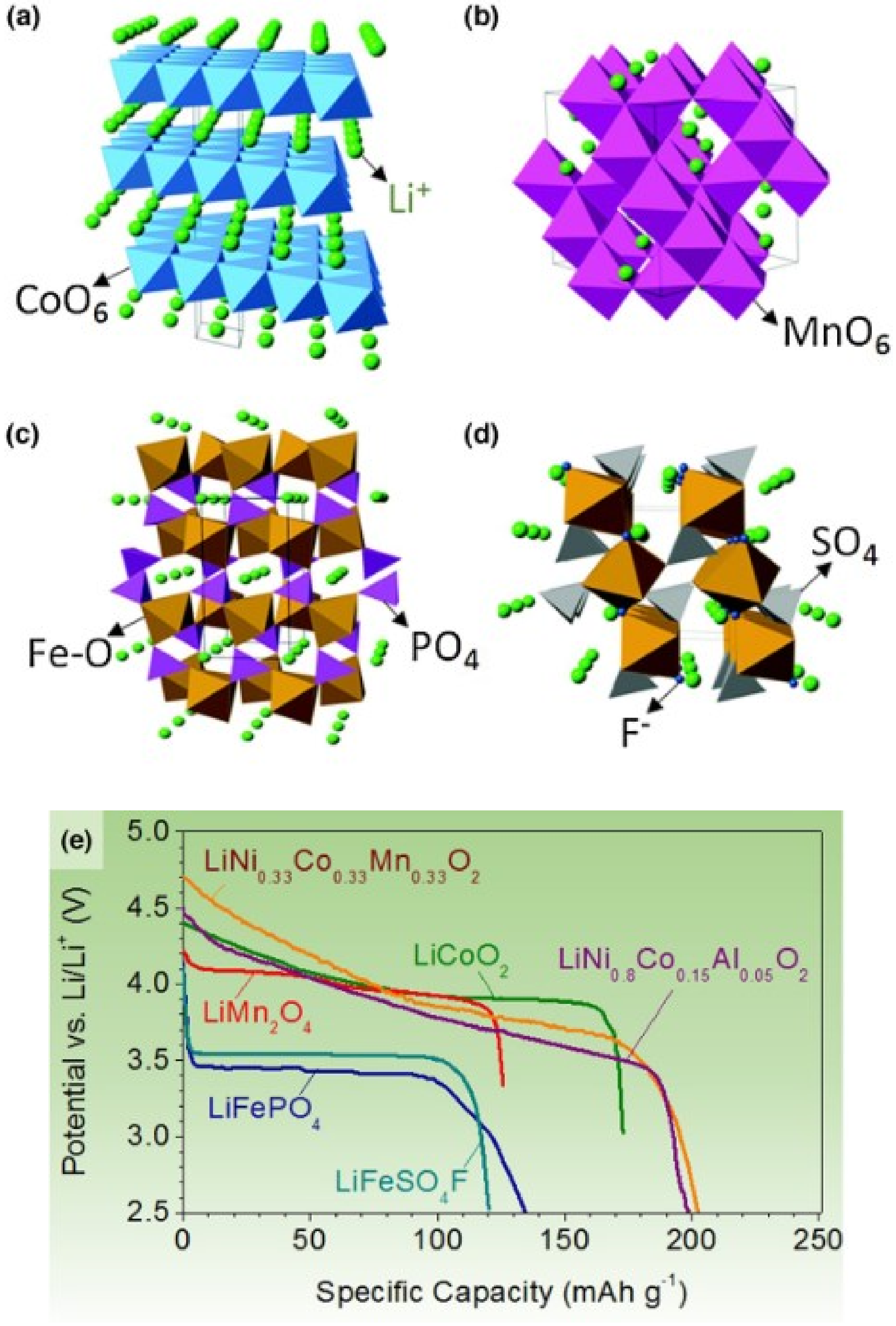

*Figure 11 Crystal structures and discharge profiles of representative intercalation cathodes: structure of (a) layered (LiCoO2), (b) spinel (LiMn2O4), (c) olivine(LiFePO4), and (d) tavorite (LiFeSO4F) (e) typical discharge profiles of intercalation cathodes.* [32]

$LiCoO_2$ (LCO) was introduced by Goodenough et al in 1980 [40] and was the first form of layered transition metal oxide cathode. It was originally commercialised by SONY, and this material is still used in the majority of commercial Li-ion battery in consumer electronics applications. [32] Among its benefits of relatively high theoretical specific capacity 274 mAh $g^{-1}$, high theoretical volumetric capacity 1363 mAh $cm^{-3}$, low self-discharge, high discharge voltage and good cycling performance [41], LCO has drawbacks such as the high cost of cobalt (Co), low thermal stability and fast capacity fade at high current rates.

To solve such challenges, partial substitution of Nickel (Ni) with Co was found to be an effective way to reduce cationic disorder [42] while reducing the cost of using Co and maintaining the same level of capacity. However, at higher range of SOC, the insertion of Ni will lead to insufficient thermal stability. Popular commercial solution to this issue it to dope aluminium into the cathode material, [43,44] As a result, the $LiNi_{0.8}Co_{0.15}Al_{0.05}O_2$ (NCA) cathode has been commercialised (used by Tesla).

As figure 11 (b) presents, $LiMn_2O_4$ (LMO) is a promising cathode material because of cheaper raw manganese (Mn) cost and also less toxic compare to Co or Ni. However, LMO has undesirable structural changes during cycling. The layered structure tends to change into the spinel structure during Li ion extraction. To solve such structural instability, Ni and Co can be inserted into the cathode material to form lithium nickel manganese cobalt oxide (NMC) cathode. The NMC cathode has similar or higher achievable specific capacity than LCO/LMO, and similar operating voltage while having a reduced cost. $LiNi_{0.33}Co_{0.33}Mn_{0.33}O_2$ is the common form of NMC on the market in the recent decade, while nickel-rich layered oxide $LiNi_{0.8}Co_{0.1}Mn_{0.1}O_2$ with a Ni, Co, Mn ratio of 8:1:1 and various intermediate ratios (i.e. 5:3:2, 6:2:2) are being pursued by most of the lithium battery manufacturers to achieve higher energy/power density, where high nickel ones have already been implemented in application of EV. (higher nickel content allows higher Li extraction without structure deterioration). [32]

$LiFePO_4$ (LFP) is considered as the representative polyanions cathode material, which occupy lattice positions and increase cathode redox potential while stabilising its structure. [45] In recent decades, LFP is widely used in EVs and E-bus due to its thermal stability under normal or low C rates (e.g. below 2C rate). However, LFP cathode has a few major disadvantages such as low operating voltage (as figure 10 (e) demonstrates) and low ionic and electrical conductivity. As a consequence, during fast charging (e.g. 2C or higher rates) the LFP cathode quite often generates large amounts of heat giving rise to large thermal gradients across the cell, which could lead to accelerated degradation. [46]

Figure 12 demonstrates the specific capacity and potential vs Li/Li$^+$ for the most common intercalation-type cathodes described above (LFP, LCO, LMO & NMC):

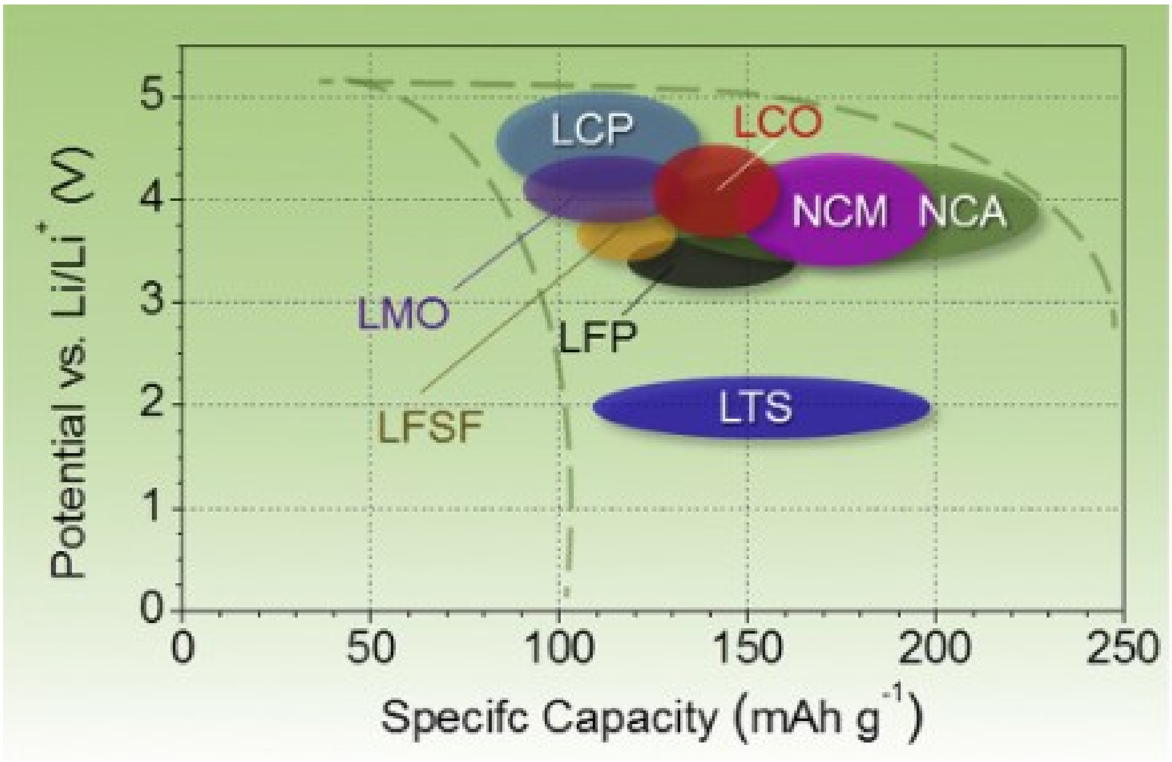

*Figure 12 Approximate range of average discharge potentials and specific capacity of some of the most common intercalation-type cathodes (experimental).* [32]

By contrast to intercalation-type cathodes, conversion electrodes undergo a redox reaction during lithiation/delithiation, in which there is a change in the crystalline structure, followed by the breaking and recombining of chemical bonds. Sulfur cathode stands out because of its high theoretically specific capacity, as shows in figure 6 and low cost and abundance in the Earth's crust of sulfur material.

However, during the charge and discharge process, as the sulfur is reduced by lithium into low order polysulfides the total number of species dissolved in the electrolyte increases. This leads to increased viscosity and reduced conductivity, which leads to significant changes in the resistance of the cell. Particularly at the end of charging process, the polysulfide solubility reaches its peak value. Figure 14 shows polysulfide shuttle effect in a schematic way. The long chain lithium polysulfides produced during charging ($Li_2^+S_n^{2-}$) would be reduced to shorter chain lithium polysulfides ($Li_2^+S_{n-x}^{2-}$) when it contacts Li metal at anode or interact with insoluble lithium polysulfides. [47]

In addition the mobile high order polysulfides ($Li_2^+S_8^{2-}$ and $Li_2^+S_6^{2-}$) can diffuse to the anode and react with lithium directly, leading to very high self-discharge rates, and a phenomenon called the 'shuttle' [16]. The shuttle occurs during charging where the high order polysulfides diffuse to the anode where they are reduced to low order polysulfides, which diffuse back to the cathode where they are oxidised again, at best leading to low coulombic efficiencies and difficulties in estimating SOC, and at worst can continue indefinitely meaning a cell can never be fully charged. Figure 13 shows a typical Li-S battery charge/discharge voltage behaviour as well as the solubility/resistance change of the polysulfides. [36] The shuttle mechanism repeats itself and contributes significantly to heat generation, and the process is not fully reversible. As a consequence, the shuttle effect leads to the challenges that Li-S cells have a high self-discharge, relatively rapid capacity fade, low charging efficiency and difficulty estimating SOC. [16]

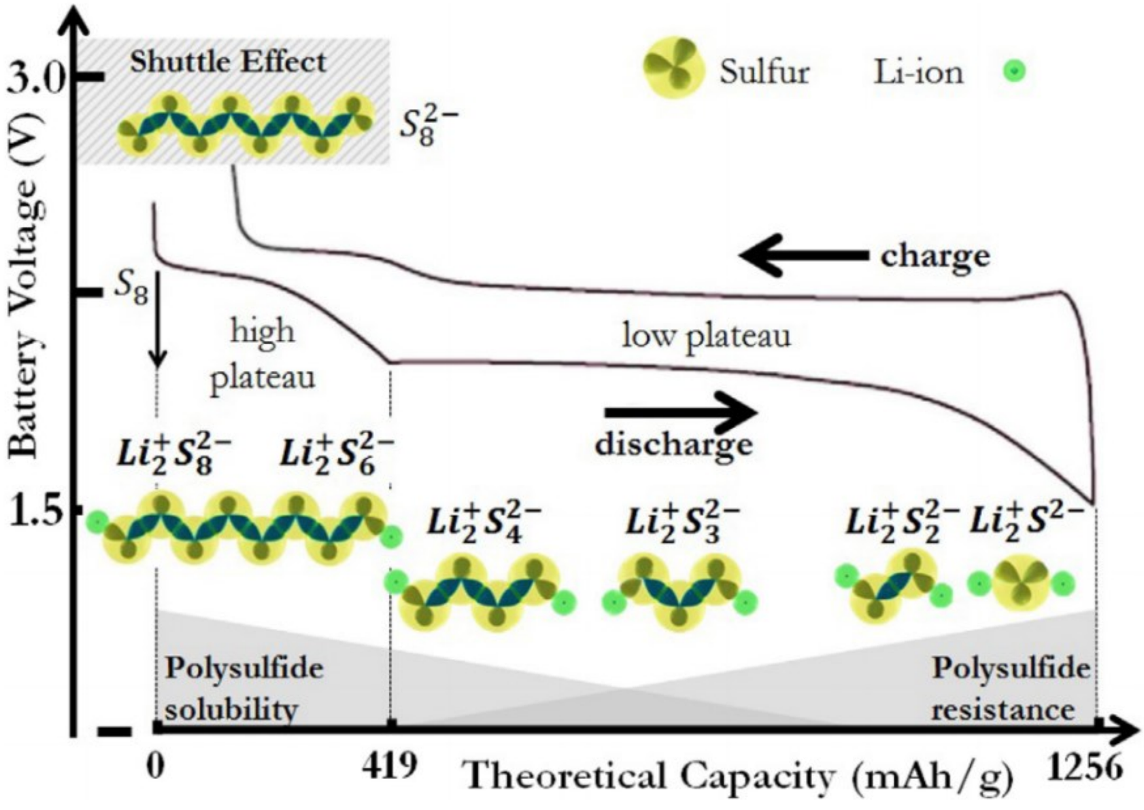

*Figure 13 Basic voltage behaviour Li-S battery with changed Polysulfide solubility and Polysulfide resistance.*[36]

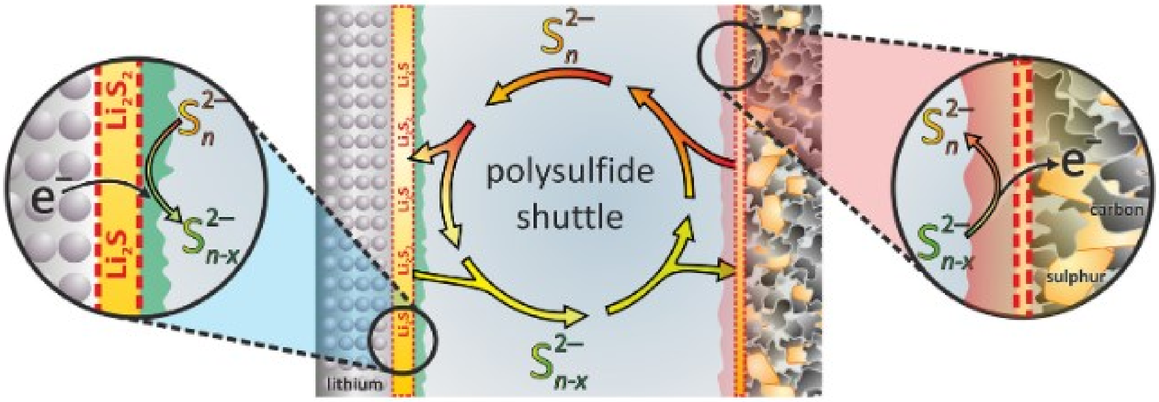

*Figure 14 Schematic illustration of the parasitic polysulfide shuttle effect in a liquid electrolyte based Li/S8-cell.*[48]

## 2.3.2. Anode/Negative Electrode

At the beginning (70s and 80s in last century) of lithium ion battery research and development, lithium metal was used as anode/negative-electrode material. However, lithium metal forms dendrites which can lead to short circuiting. As a consequence, thermal runaway can occur and ultimately batteries catch fire. [32] Therefore, secondary anode materials were needed to overcome this safety issue. A good anode material should have similar characteristics with cathode materials, such as long cycle life, low cost and higher specific capacities. In addition, a lower potential anode means a greater voltage difference between cathode and anode (aka. Open-Circuit-Voltage OCV), which contributes towards a higher energy and power density. In figure 15 (d), it shows the potential differences and specific capacity of lithium titanium oxide (LTO), Graphite, Silicon and magnesium oxide (MnO).

Nowadays, the carbon (essentially graphite) anode is widespread used in lithium ion batteries because graphite is equipped with advantaging anode characteristics such as low cost, low delithiation potential, high specific capacity and so on. In the graphite anode, each atom of lithium is stabilised by 6 carbon atoms, as shown in figure 15 (a). This stable structure gives it mechanical stability and low volume expansion, which enable a battery with a high cycle life. [49]

Lithium titanate oxide (LTO) is another commercially available anode material. It has higher potential vs Li/Li+ compares with graphite anode (1.55V vs Li as shown in figure 15 (d)). This allows LTO to be operated above 1V, which avoids the formation and growth of the anode Solid-Electrolyte-Interface (SEI). Higher potential operating window also prevent Li dendrite formation, even at high rates. LTO has a good thermal stability, relative high volumetric capacity and high cycle life due to its negligible volumetric expansion upon lithiation. [32,50–52] Thus, although LTO does not have particularly high Li diffusivity or electrical conductivity, it is a good material for lower energy, but high power high cycle life Li-ion batteries. That's why LTO is quite often used in grid-energy storage applications.

Silicon is also used in anodes, and Figure 15 (c) demonstrates the crystal structure of the lithiation of silicon and figure 15 (d) shows that silicon has the highest specific and volumetric capacity. Nevertheless, it has the disadvantages of large volume expansions with lower cycle life. Therefore one solution is to blend carbon with small amounts (less than 10%) of silicon to have the benefits of higher specific capacity with acceptable volume expansions. [53]

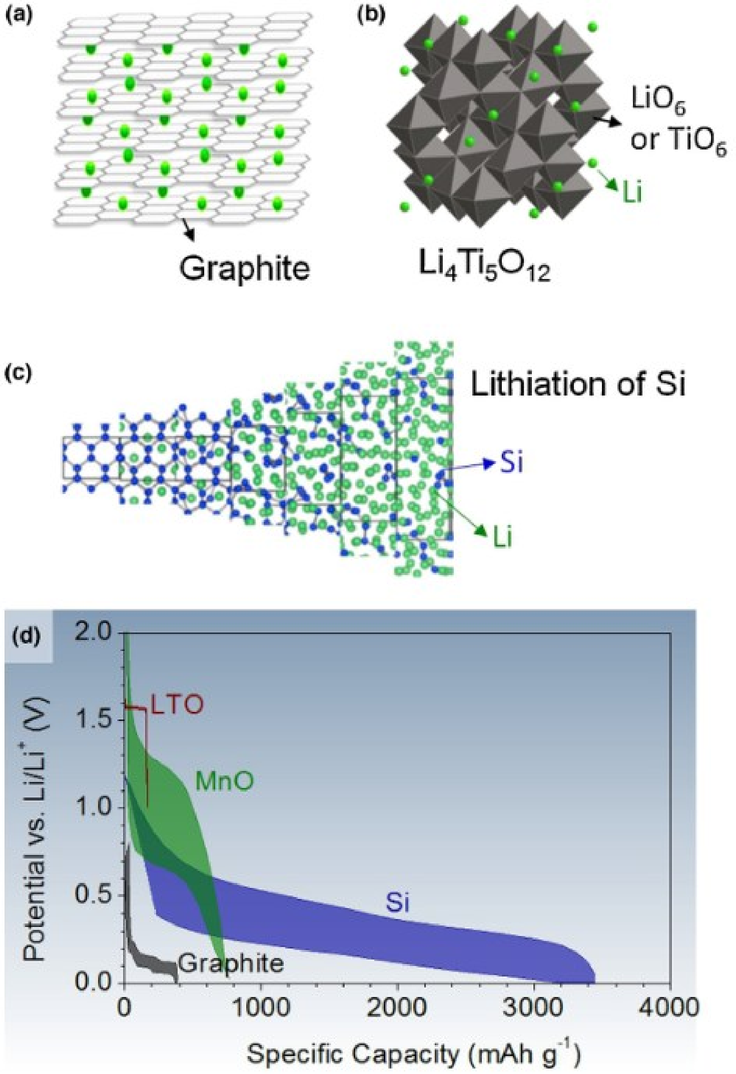

*Figure 15 Crystal structures of (a) lithiated graphite (b) lithium titanate (LTO) (c) silicon during lithiation and (d) charge-discharge profiles at low charge/discharge rates for LTO, MnO, Si and Graphite.* [32]

## 2.4. Current Collector

In lithium ion batteries, the electrode materials are attached to the current collectors to transport electrons and power to/from the external devices/ battery cyclers. There are a few critical requirements for the current collectors. First requirement is the good electrical conductivity to reduce heat generation and increase efficiency. The second is that it should be thin and light. As a current collector may be considered as 'inactive' mass and volume in a battery, its usage reduces the gravimetric and volumetric energy densities of the battery. The last but not the least, it must be electrochemically stable in contact with the battery anode/cathode & electrolyte materials across the operating voltage windows of each electrodes. Therefore, for anode and cathode, the current collectors are different due to their various operating voltage windows. [54]

Nowadays, in the majority of the commercial li-ion batteries, copper foil Cu is used for anode current collector and aluminium foil Al is used for cathode current collector. The aluminium foil is a good cathode current collector candidate, which is inexpensive, with high conductivity and electrochemically stable in contact with cathode material. The oxidation potential of Al is around 4.7 V with respect to Li/Li+, and the operation voltage of the cathode is around 3-4.7 V, it is therefore safe and stable. Cu is a good anode current collector, as current collector corrosion can occur by reactions with electrolyte components or if the potential of the anode gets too positive versus Li/Li+. Cu fits this operating potential window (0 V-2.5 V). If corrosion does occur this can result in gradual increase in internal resistance, gradual capacity fade and internal short circuit. The more detailed studies on current collectors are conducted in: [54–56].

## 2.5. Lithium-ion battery construction and configuration

There are 3 major types of lithium ion batteries that are commercially available, which are prismatic, cylindrical and pouch. All 3 types of batteries are made of cathode aluminium current collector laminate, anode copper current collector laminate and separator, but with different packaging methods, or in other words encapsulation methods, and different wounding methods (e.g. laminated or jelly roll structure).

Prismatic cell has the cell core of the laminated electrode stack structure or the jelly roll structure, encapsulated with a hard aluminium housing. For the jelly roll structure, the electrode current collectors are wound and flattened, as shown in figure 16. The prismatic cell enhances the space utilisation and allows flexible design, however due to its large thickness and volume for a single cell, it can be harder to thermally manage compared with cylindrical and pouch cells. [28,57,58]

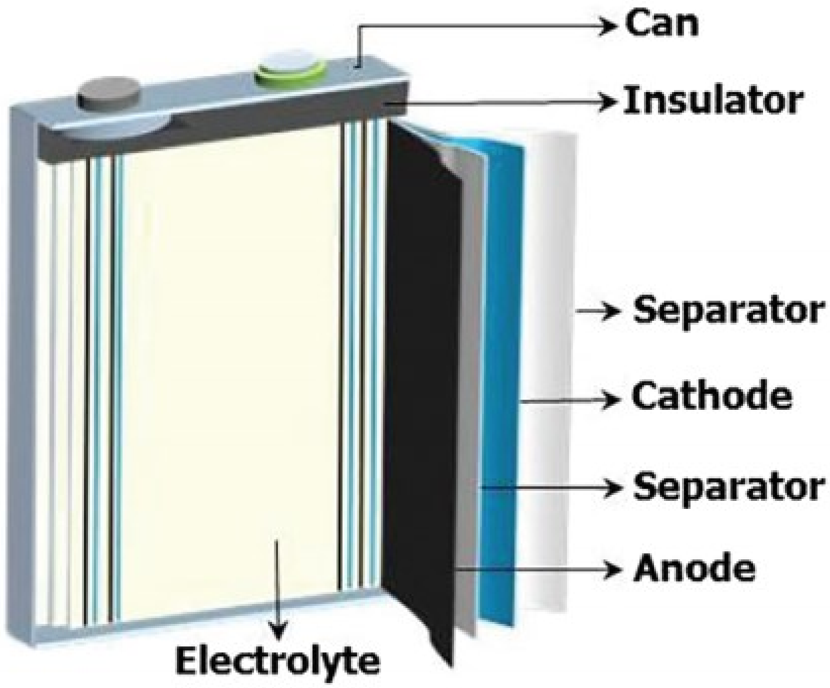

*Figure 16 Cross Section of a prismatic cell.* [59]

Cylindrical cell is one of the most widely used packaging style for lithium-ion batteries, used by many EV OEMs (e.g. Telsa). The jelly-rolled electrode current collector laminates are spiral wound inside a cylindrical housing, normally steel or aluminium as shown in figure 17.

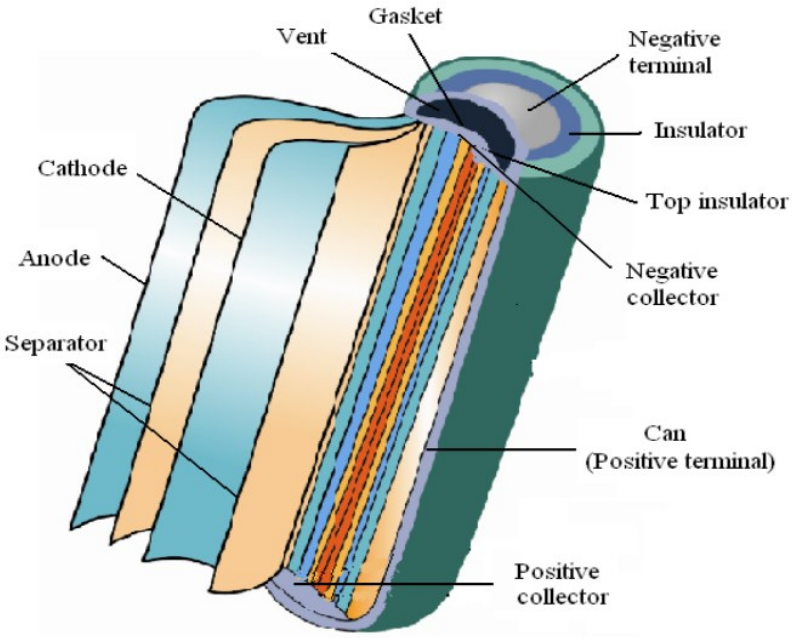

*Figure 17 Cross Section of a cylindrical cell.*[60]

Pouch cells have a lightweight laminated pouch material as the external case. The cathode and anode foil tabs are welded to the electrodes and brought to the outside in a fully sealed way. The layered laminated electrode stacks are encapsulated within the housing (e.g. aluminium laminated film), as shown in figure 18.

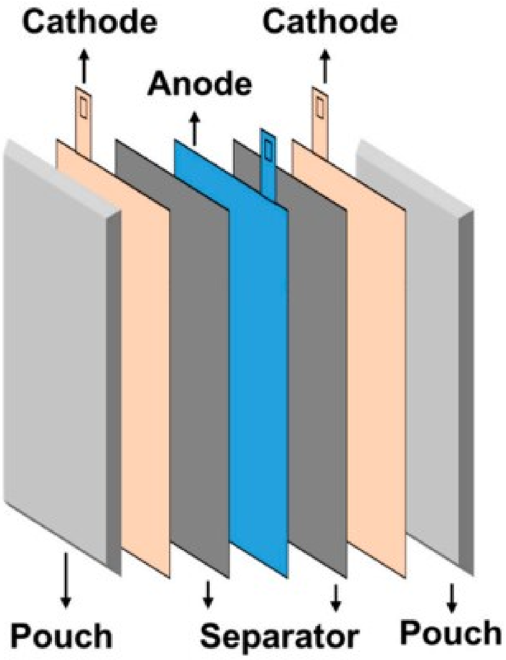

*Figure 18 Cross Section of a pouch cell.*[61]

Different form factors are designed and used in different applications, depending on which requirement takes the design priority. For example, pouch cell is less robust than prismatic and cylindrical batteries due to its soft case, but it delivers the benefits of high volumetric and gravimetric density of the system. Moreover, within the same form factor, different cell configuration designs can affect system efficiency particularly due to thermal management requirements. [62]

## 2.6. Essential Electrochemical & Key Heat Generation Equations

In this section, some essential electrochemical equations as well as heat generation equations are introduced. The nature of the electrochemical reactions are the interactions between reaction rate, current, potential and temperature. The following sections is referenced from the electrochemistry textbook: '*Electrochemical Methods: Fundamentals and Applications, 2nd Edition*' by Allen J. Bard et al and Larry R. Faulkner et al. [63]

### 2.6.1. Nernst Equation

The Nernst equation is introduced for the cell thermodynamics at equilibrium, as below:

$$E = E^{0'} + \frac{RT}{nF} ln \frac{(C_i^*)_{LHS}}{(C_i^*)_{RHS}} \qquad (16)$$

here:

$E$ = Cell Potential (Electromotive Force, EMF) at the temperature of interest, T

$E^{0'}$ = Standard electrode potential

$R$ = Universal gas constant

$T$ = Temperature in kelvins

$F$ = Faraday constant, the number of coulombs per mole of electrons

$n$ = the number of electrons transferred in the cell reaction

$\frac{(C_i^*)_{LHS}}{(C_i^*)_{RHS}}$ = known as $Q_r$, which is the reaction quotient of the cell reaction

$(C_i^*)_{LHS}$ = Bulk concentration of species $i$ at left hand side of reaction equation,

$(C_i^*)_{RHS}$ = Bulk concentration of species $i$ at right hand side of reaction equation

In the equilibrium state, there is no current flowing, where the electrode potential can be governed using the Nernst equation.

### 2.6.2. Arrhenius Equation

The Arrhenius equation defines the relationship between the operating temperature with the internal reaction rates:

$$k_r = Ae^{-\frac{E_a}{R_g T}} \tag{16}$$

where:

$k_r$ = rate constant, which is the frequency of the collisions resulting in a reaction

$T$ = absolute temperature, in Kelvins

$A$ = the pre-exponent factor, a constant for each chemical reaction

$E_a$ = the activation energy for the reaction

$R_g$ = the universal gas constant

The cell internal reaction rate defines the impedance of the cell, or what is known as phase-dependent resistance. A higher operating temperature links with higher reaction rate, with lower cell impedance. As a result, higher achievable power is enabled at higher temperature due to the rate of reaction is increased.

The operating temperature of a cell is linked with the overpotential as well, where the overpotential $\eta = E - E_{eq}$, which is the difference between the cell potential $E$ with thermodynamic potential, $E_{eq}$. A higher temperature leads to lower resistance of the cell, and therefore a smaller overpotential. As a result, higher achievable capacity is enabled at higher temperature due to the decreased overpotential (the cell terminal voltage hits the cut-off voltage at a later point).

Temperature is a key operating condition for Lithium-ion battery, where it correlates with internal reaction rate, internal resistance and therefore overpotentials. It also relates to multiple degradation modes as well as safety concern, which will be expressed in the later sections.

### 2.6.3. Butler-Volmer Equation

The Butler-Volmer equation describes how the electrical current that occurs at an electrode, is a result of the potential difference between the electrode and the bulk electrolyte. It is assumed that a redox reaction, essentially both anodic and cathodic reaction occur at the same electrode but the rates are different giving rise to a net reaction rate in one direction.

$$j = j_0 \cdot \left\{ exp\left[\frac{\alpha_a nF}{RT}\left(E - E_{eq}\right)\right] - exp\left[-\frac{\alpha_c nF}{RT}\left(E - E_{eq}\right)\right]\right\} \tag{17}$$

where:

$j$ = Electrode current density

$j_0$ = Exchange current density

$E$ = Electrode potential

$E_{eq}$ = Electrode potential at equilibrium

$T$ = Absolute temperature in kelvins

$n$ = the number of electrons involved in the electrode reaction

$F$ = Faraday constant

$R$ = Universal gas constant

$\alpha_a$ = Anodic charge transfer coefficient, dimensionless ($0 \leq \alpha_a \leq 1$)

$\alpha_c$ = Cathodic charge transfer coefficient, dimensionless ($0 \leq \alpha_c \leq 1$)

The first exponential term in the Butler-Volmer equation presents the contribution of the anodic reaction (oxidation), and the seconds is cathodic reaction (reduction). The exchange current density is the background current when there is an equilibrium state (e.g. zero net current). From the Butler-Volmer equation, the relationship between the current density of the cell and the overpotential is described, where a higher current density results in higher overpotential. As a result, it describes how a higher current with higher overpotential would leads to sooner cut-off voltage of the cell during charging and discharging, or in other words there is a natural trade-off between power achieved (e.g. achievable current density) with energy (e.g. capacity).

## 2.6.4. Heat Generation Equation

The heat generation of a Lithium ion battery during operation can be separated into 2 parts, which are reversible and irreversible processes. [18,64–69] The reversible is dominated by the entropy change due to the material phase changes within the cell. Meanwhile, the irreversible heat generated is associated with the losses caused by the difference between the cell OCV and the operating cell terminal potential. The irreversible heat generation is caused by 2 types of interactions, which are long-range interactions and short-range interactions respectively. The transport of charge and species in the solid and electrolyte phases cause the long range interactions, and therefore ohmic heat generation. The charge-transfer reactions at the interphase cause the short range interactions, which leads to the kinetic heat generation. There is one study that summarises the above heat generation in a simple format conducted by *Bernardi* et al.[70]:

$$\dot{Q}_{\mathrm{irr}} = I \cdot (E_{OCV} - E) = R \cdot I^2 \tag{18}$$

$$\dot{Q}_{\mathrm{rev}} = I \cdot T \cdot \frac{dE_{OCV}}{dT} \tag{19}$$

$$\dot{Q} = \dot{Q}_{\mathrm{irr}} + \dot{Q}_{\mathrm{rev}} = \ I \cdot (E_{OCV} - E) + I \cdot \left(T \cdot \frac{dE_{OCV}}{dT}\right) = R \cdot I^2 + +I \cdot \left(T \cdot \frac{dE_{OCV}}{dT}\right) \tag{20}$$

where:

$\dot{Q}_{\mathrm{irr}}$ = Irreversible heat generation

$\dot{Q}_{\mathrm{rev}}$ = Reversible heat generation

$I$ = Applied current into the cell

$E_{OCV}$ = Open Circuit Voltage

$E$ = Cell terminal potential

$T$ = Operating temperature of the cell, in kelvins

$R$ = Internal equivalent resistance of the cell

As stated in the heat generation equation, the heat generation of an operating Lithium ion battery (cell and/or pack) is associated with the current applied. Therefore, the positive feedback loop of the current magnitude, heat generation, operating temperature, battery internal resistance/impedance, cell potential & overpotential is formed.

## 2.6.5. Li-S Shuttle Heat Generation Equation

Lithium Sulfur batteries have different heat generation mechanisms, compared with conventional Lithium ion batteries (e.g. NMC, NCA, LFP cells). A study by *Mikhaylik* et al [16] proposed a positive feedback between shuttle and cell temperature: and assumed shuttle to be the only heat generation mechanism, and exponentially dependent on temperature. In order to quantitatively study the shuttle heat generation, a few other equations were introduced:

$$\frac{d[S_H]}{dt} = \frac{I}{q_H} - k_s[S_H] \tag{21}$$

where:

$S_H$ = High polysulfide amount (high plateau polysulfide concentration)

t = Time.

$I$ = Charge/discharge current

$q_H$ = Specific capacity of sulfur to high voltage plateau

$k_S$ is shuttle constant or heterogeneous reaction constant.

The equation above assumes that the rate of reduction of high polysulfide on the Li anode surface is directly proportional to the concentration $S_{H.}$ Then, the solution for this differential equation is derived as:

$$\frac{I - q_H k_s[S_H]}{I - q_H k_s[S_H^0]} = e^{-k_s t} \tag{22}$$

where:

$S_H^0$ = the polysulfide concentration when $t$ equals 0 at high plateau

The Li-S battery self-heating during charge, increases the interaction rate of polysulfide with lithium anode.[16] Consequently, there is an increase of the shuttle constant $k_S$ in Eq.23 and

Eq 24. The Arrhenius equation can be considered to describe the relationship between the cell Temperature T (T0 is the temperature where a charge process starts) and the shuttle constant $k_{S,}$ where A is the shuttle activation energy (0.56 eV).

$$k_s(T) = k(T_0)\exp\left[-\frac{A}{R}\left(\frac{1}{T}-\frac{1}{T_0}\right)\right] \tag{23}$$

When charging, the terminal voltage gradually increases and heat generation is formed because of an increasing $S_H$. Consequently, the heat generated due to shuttle effect exceeds the heat dissipated and forms a thermal gradient, such temperature change is described as:

$$\frac{dT}{dt} = \frac{1}{mc_h}[k_s(T)q_H[S_H]V_H - \alpha(T - T_0)] \tag{24}$$

where:

$m$ = the cell mass

$c_h$ = the cell heat capacity

$V_H$ = voltage at high plateau

$\alpha$ = cell heat-transfer coefficient

Here, as described in Eq 21 to Eq 22, shuttle constant kS is temperature dependent, or in other words the Li-S cell behaviour (e.g. voltage behaviour) is sensitive to small amount of operation temperature change, on top of the heat generation Eq 23-24.

## 2.7. Degradation

Lithium ion battery would experience highly thermal dynamic usage or physical interplay over the entire lifetime, while the complex physical and chemical mechanisms cause the degradation of the battery. There are essentially 2 types of degradation, which are thermodynamic degradation and kinetic degradation, which are both caused by various reasons and lead to one of or both degradation effects: capacity fade and power fade. [71] The decrease in the loss of useable/fundamental cell capacity measured in Ah (ampere hour) is called capacity fade. Normally, the experimental method to identify capacity fade is to conduct a simple slow rate discharge on a fully charged cell. This capacity fade quantifies the cells' ability to store energy. Further, the power fade represents the ability of the cell to meet the power demand for a system, identified by measuring the cell over potential. The kinetic degradation caused by the rise in internal resistance/impedance, which leads to power fade. Also, an increase in resistance would contribute more heat generation, and also decrease the useful cell capacity due to hitting the voltage cut-off sooner. [71]

The thermodynamic degradation has essentially 3 major degradation mode, which are 1) Loss of lithium inventory (LLI); 2) Loss of active material of the Negative Electrode ($LAM_{NE}$); 3) Loss of active material of the Positive Electrode ($LAM_{PE}$). In Figure 19 and Figure 20, the mechanisms of degradation in various locations, the causes and effects are introduced. [71] There are limited amount of lithium ions, which means the consumption of the lithium ions is irreversible. Therefore, in LLI mode, such as Solid Electrolyte Interface (SEI) growth, SEI and electrolyte decomposition and lithium plating/dendrite formation, the lost lithium ions are no longer participating in the redox reactions between the positive and negative electrodes, causing a decrease in the total amount of energy that can be stored. The cause of LLI in operation including time (calendar aging), high temperature, high voltage /SOC range and high operating current loads.

The loss of active material, at both positive and negative electrodes deliver the degradation modes $LAM_{PE}$ and $LAM_{NE}$ respectively. For negative electrode, the active mass is lost and not available for the insertion of lithium ion due to loss of electrical contact, particle cracking, structural disordering and resistive surface layers (block of active sites). These degradation reactions lead to both capacity fade and capacity fade.

Degradation remains as a major and critical research topic, and a few other good reviews in addition to the one conducted by Birkl et al., are from Vetter et al. and Palacin et al. [55,71,72]

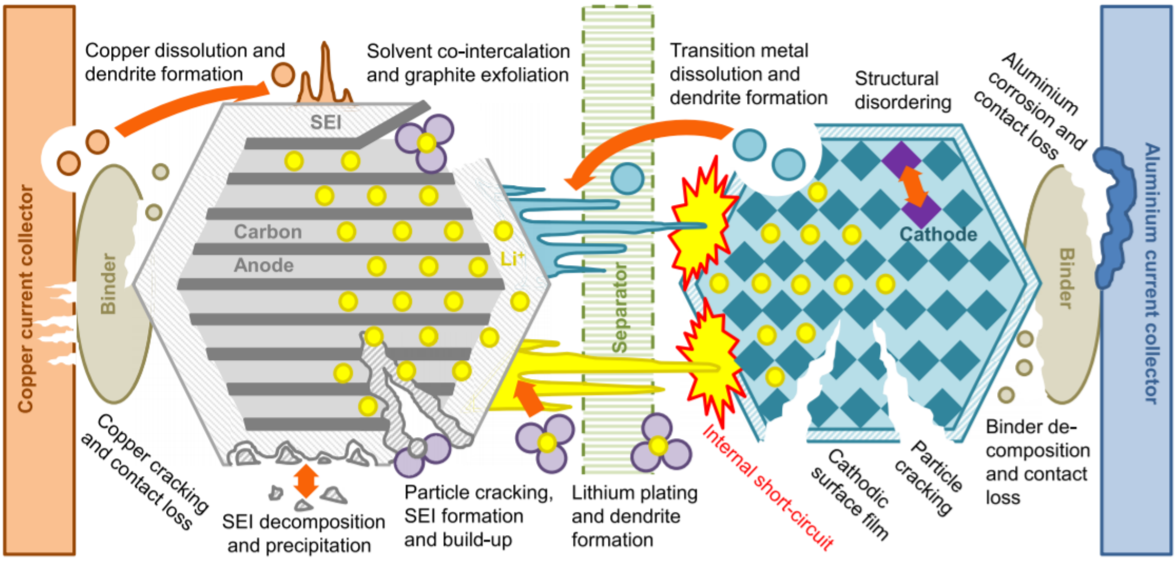

*Figure 19 Degradation mechanisms in Li-ion cells.*[71]

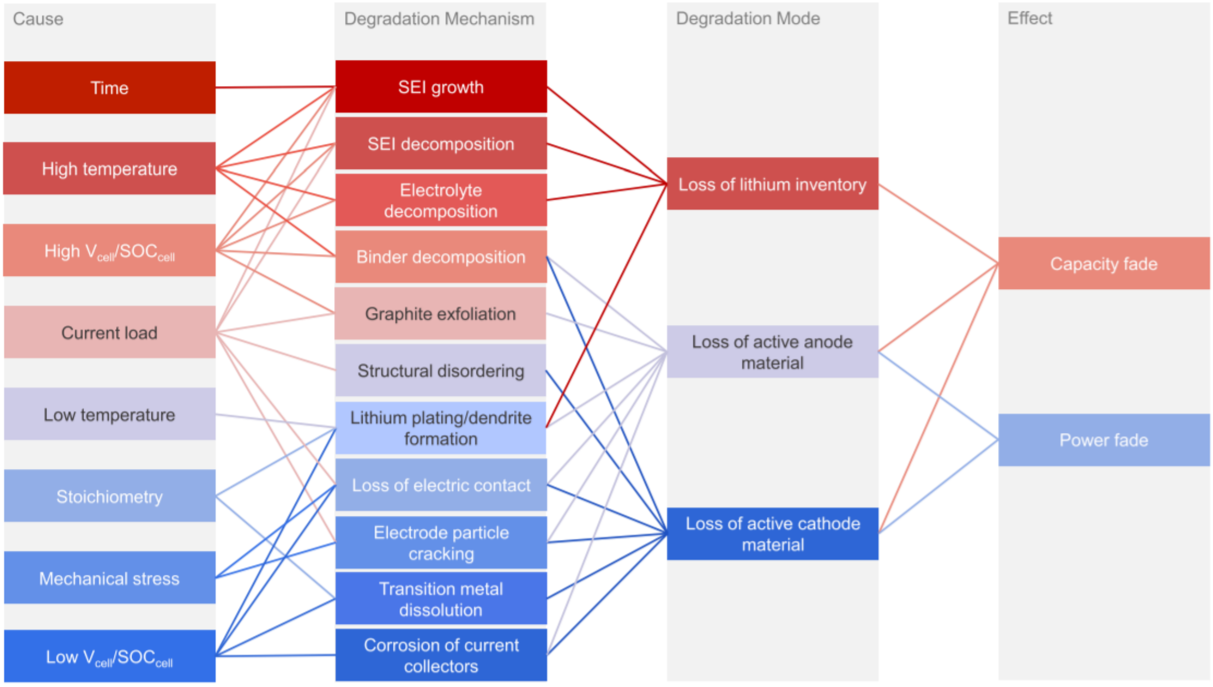

*Figure 20 Causes and effect of degradation mechanisms and associated degradation modes.* [71]

## 2.8. Safety

One of the critical reasons for the thermal studies of Lithium ion battery is safety concern. As the battery is generating heat while operating with a load, both in charging and discharging. The high capacity and large serial-parallel numbers in many thermal dynamic applications (e.g. automotive) of Lithium-ion battery make safety an essential issue for the industry. Figure 21 and Figure 22, demonstrate the temperature operating windows for lithium ion battery as well as the different stages for the thermal runaway at various temperatures. [73,74]

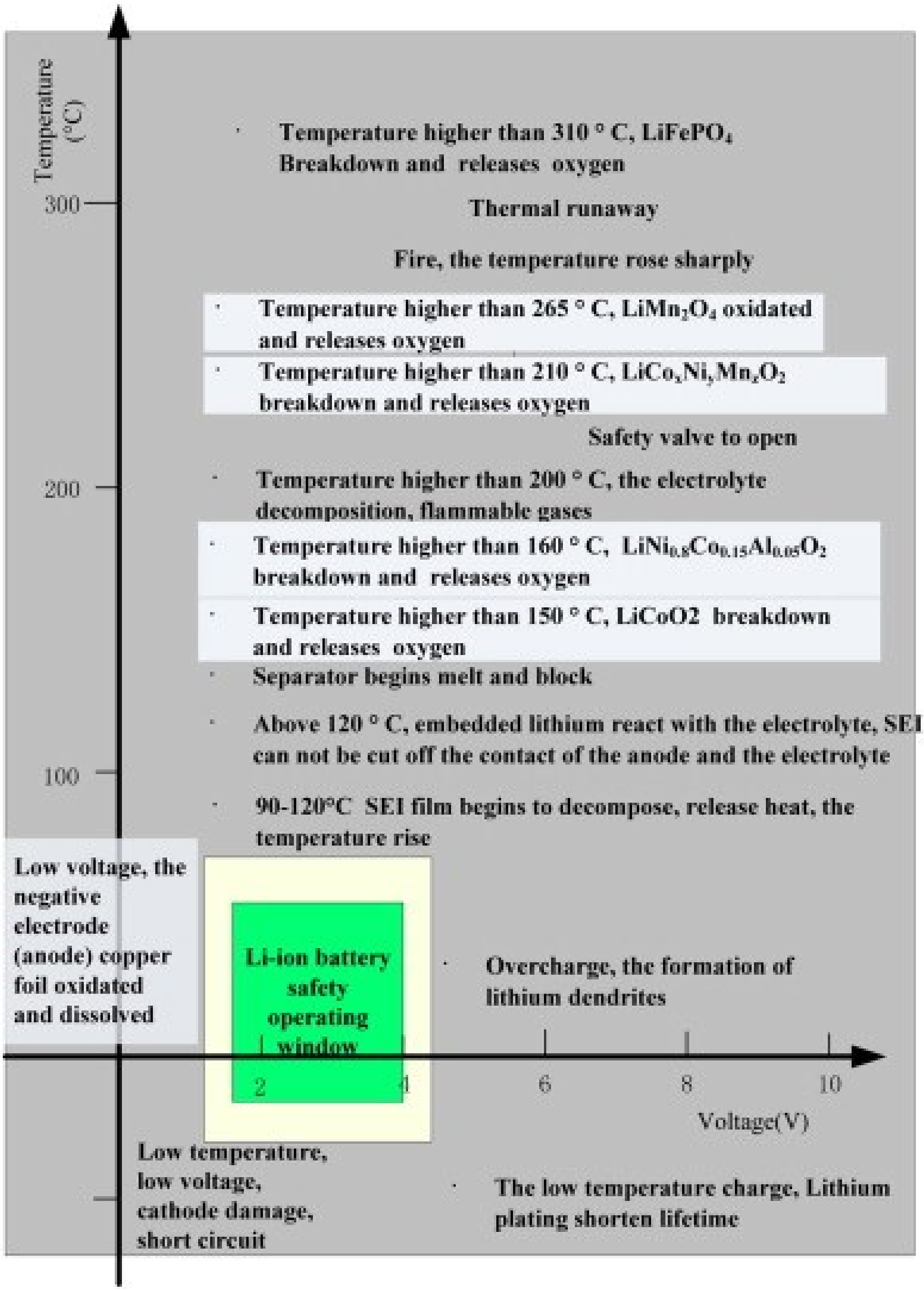

*Figure 21 Safety operating window for lithium ion battery.*[74]

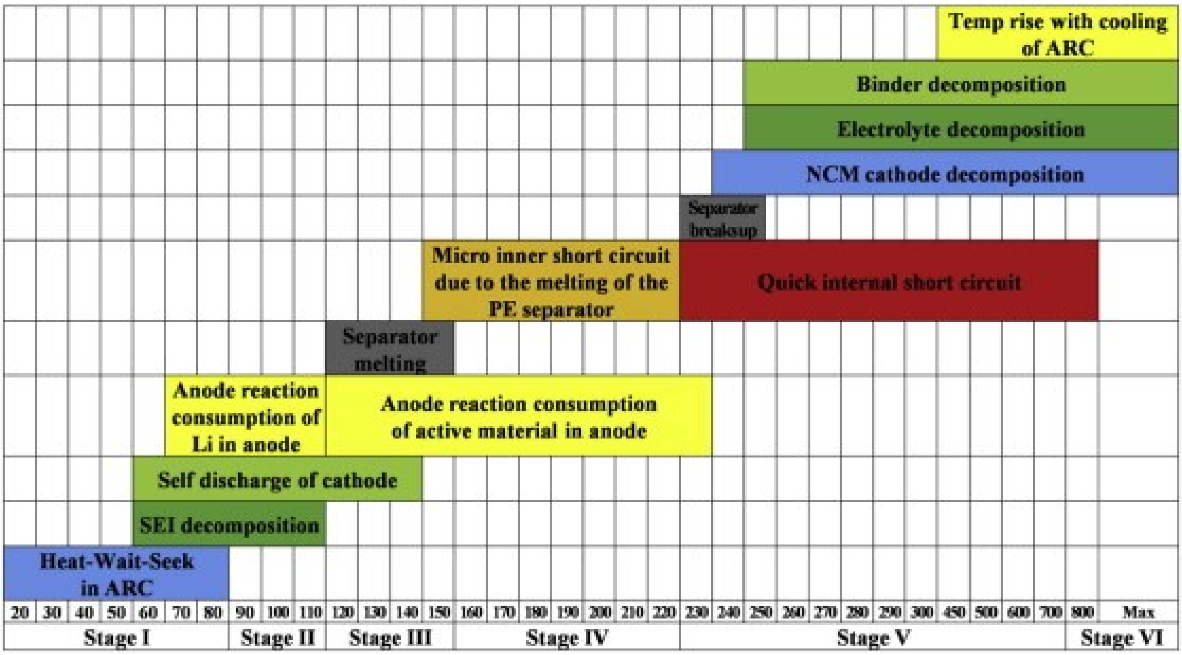

*Figure 22 Temperature ranges for different stages of thermal runaway test using EV-ARC.*[73]

As previously mentioned, high operating temperature would cause degradation of the battery. In the extreme cases, the battery becomes status, leading to heat generation without an external load or heating sources. Consequently, this thermal runaway effect causes significant safety issues for all the applications.

In the Figure 21 and Figure 22, the temperature operating window with corresponds thermal runway stages are presented:

***Stage 1***: High operating temperature causes capacity fades, while the lithium ion is deintercalated from anode. [75–79]

***Stage 2***: When temperature is above 50 °C, the capacity fade is happening while the SEI decomposition occurs. [80,81] As a consequence, the anode loses its protection layer, therefore starts to react with electrolyte and certain amount of heat is generated and detectable. [80,82,83]

***Stage 3***: Temperature is between 120 °C and 140°C, the separator is melting. [73,84]

***Stage 4***: When temperature below 240 °C, the micro internal short circuit is happening, while the anode reaction continues. The active materials is consumed, leads to self-discharging. [73,80,85]

***Stage 5 & 6***: When the temperature is above 240 °C, the electrolyte, binder and remaining components are decomposed due to one complete internal short circuit. A significant amount of heat will be released. [86–88]

Once again, in the safety concern domain, the thermal characterisation represents an essential topic for Lithium ion battery research. As introduced by Feng et al. and Lu et al. in [73,74], all the thermal runaway is starting from the higher end of 'normal' operating window, around 50 °C. Therefore, essential experimental and modelling tools need to be developed, parameterised and validated to implement the understanding captured from the thermal literature review.

## 2.9. Key Thermal Evaluation and Diagnostic Experimental techniques

Within Lithium-ion battery research fields, experimental techniques always play an irreplaceable role, to provide cell thermal and voltage responses in real-time. Here, 2 of the essential in-situ experimental techniques, Differential Thermal Voltammetry (DTV) and Cell Cooling Coefficient (CCC) have been reviewed and discussed in detail. These techniques are developed further in this thesis.

### 2.9.1. Thermal Diagnostic Technique: Differential Thermal Voltammetry

There are a range of diagnostic techniques, which enable measuring capacity loss without inserting a reference electrode (decoupling anode and cathode [89–91]). However, for automotive applications, integrating a reference electrode is impractical to implement, as it incurs extra cost and can influence the cell behaviour. [92] Therefore, there is a need for non-destructive diagnostics, which can monitor degradation. A few examples include: Electrochemical Impedance Spectroscopy (EIS) [93,94], Slow Rate Cyclic Voltammetry (SRCV) [93], differential voltage analysis (dV/dQ) [95–98], Incremental Capacity Analysis (ICA, dQ/dV) [99–101]. However, no single technique is able to provide all the required information to decouple physical mechanisms for a whole cell. [102] Additionally, the majority of the diagnostic techniques require isothermal experimental conditions, which is nearly impossible to achieve in an operational Electric Vehicle. Therefore, a diagnostic experimental technique which is in-operando, doesn't require isothermal requirement, non-destructive, only needs few simple operational parameters (e.g. Voltage & Cell temperature) was needed.

A novel method of extracting the same information as SRCV, using galvanostatic operating modes (faster than SRCV), and enabled the monitoring of battery degradation through phase transitions (and therefore entropic heat, occur in the electrodes), was developed and presented by Wu et al. and Merla et al. [46,102,103], and called Differential Thermal Voltammetry. This technique only requires voltage and single cell surface temperature to conduct the diagnosis without requiring isothermal experimental conditions. The technique has been demonstrated for NMC [103], LFP [46] and battery packs, [104] demonstrating the tracking of phase transitions is meaningful and quantifiable for State-of-Health (SOH) estimation purposes.

As described above, the thermal and heat generation behaviour of Li-S battery is relatively unique amongst batteries. Instead of ohmic and entropic heat generation dominating, the shuttle effect is the most important factor of heat generation for Li-S battery. Therefore, a strong candidate for study was can DTV be usefully demonstrated for Li-S batteries, and particularly:

1. ***Could one in-situ experimental diagnostic tool (e.g. DTV) quantify, track Li-S shuttle effect?***
2. ***Could this diagnostic tool, DTV, be used as a charging cut-off tool to minimise shuttle?***

*The detailed answers are presented in the Chapter 3 in this thesis.*

### 2.9.2. Thermal Evaluation Technique: Cell Cooling Coefficient

Before the invention of Cell Cooling Coefficient (CCC), there was no universal and quantifiable standard to evaluate a lithium-ion battery's capability to reject heat. [17,105] The recent Lithium ion battery development is driven by the energy/power densities, and battery heat rejection capabilities are generally overlooked. This leads to elevated operating temperature with large thermal gradient inside a cell, a module and a battery pack. To change the behaviour of the battery industry, a standardised metric to evaluate different cell's heat rejection capability was required, or in other words, the degree of difficulty to be thermally managed.

The empirically determined cell cooling coefficient (unit W/K) is measured using the total measured heat rejection rate Q during steady operation of a cell whilst thermally managing particular surfaces (surface cooling or tab cooling), divided by the largest thermal gradient measured from the thermally managed surface (cell tabs, cell surface) to the hottest location (cell centre, uncooled surface). The metric quantifies how much heat can be removed for a 1K thermal gradient within the tested cell. This thermal evaluation metric is independent of cycling rates, cell chemistries. Therefore, this tool provides a simple and easy way to evaluate how easy or not it is to cool a cell.

The previous studies conducted by Hales et al. Diaz et al. and Marzook et al. [17,105] investigated the CCC for an NMC pouch cell. None of the studies have focused on the large format prismatic cell, which generates relative more heat and results in a larger value of thermal gradient. Thus, an additional research questions needed answering:

3. ***Could CCC metric be capable of providing better thermal gradient understanding for large format LFP prismatic cells?***

*The detailed answers are presented in the Chapter 5 in this thesis.*

## 2.10. Key Modelling Tools

From a systems engineering perspective, there is a feedback loop in lithium ion battery development, where there are essentially 4 tasks interacting with each other: Experimental Validation, Model Development, Simulation and Optimisaiton. [106] Scientific research on full battery engineering often starts with experimental studies. In the absence of an existing approach to optimise, exploration is the key initial task and this must be done experimentally. As mentioned previously, DTV on Li-S cells and the CCC on prismatic LFP cell had not been done before, therefore they were initially explored experimentally. However, the next step was to develop corresponding models, which simulate the various responses of the battery (voltage, temperature, capacity fade etc.), providing simulation tools to enable the optimisation by the battery manufacturer and end users.

The models are distinguished into 2 major types, empirical models and electrochemical models. [62,107,108]

### 2.10.1. Discretised ECM Model

#### *ECM modelling*

Empirical models use experimental data to simulate the future battery responses, without consideration of physicochemical principles. Passive electrical circuit elements such as resistors and capacitors are often used, where the model type is termed as 'Equivalent Circuit Models (ECM)' The ease of implementation and computational simplicity enables fast computations, with known error margins. There is an apparent trade-off between complexity and accuracy, as the fitting experimental data is only validated for certain specific sets of operating conditions, leading to poor battery behaviour prediction for other operating conditions. [106] Such models are considered to be useless for the design or understanding of new battery chemistries or materials, quoted by Ramadesigan and Subramanian et al. [106] such as Li-S cells.

On the other hand, ECM has the potential to be scaled up to a 2 or 3 dimensional model, which is desirable for a large format lithium-ion battery due to its ease of implementation. The work conducted by Newman, Tiedemann, Gu and Kwon (NTGK) et al. [108–111] shows that such models can solve the potential and current distribution within the electrode plane, which in other words, is capable of providing lost power of heat generation in a distributed way. Zhao et al, established a few works using two-dimensional ECM model, which were thermally coupled and used look-up tables of resistances and capacitances parameterised at different ambient temperatures. The model was able to provide cell design optimisation guide on a two dimensional simulation phase, for a small format (5 Ah Kokam) NMC pouch cell.[62,108] However, the lack of three dimensional simulation domain limited the ultimate potential for the discretised ECM model by only providing cell optimisation guide on a single flat surface. Also, the parameterisation method was simple and only useful for these certain types of batteries. An inevitable upgrade is needed for a large format discretised three-dimensional ECM model. Therefore, the following research questions were identified as important:

4. ***Could the CCC be used as a novel method for thermal parameterisation of an ECM?***
5. ***Could the discretised Electro-thermal ECM model have developed together with embedded CCC boundary conditions be used for cell optimisation?***

6. ***Could changes in cell configuration affect the large format LFP prismatic cells thermal behaviours? And decrease the difficulties of thermal management for such large format cells?***

*The detailed answers are presented in the Chapter 5 in this thesis.*

***ECM parameterisation***

The parameter identification method (PIM) is critical for the ECM model accuracy. The model accuracy is correlated with what and how PIM is used for the certain Li-ion battery. A recent study conducted by Lai et al [112] compared 9 different popular PIMs for 9 different ECM models in the entire SoC area, including genetic algorithm (GA) [113,114], particle swarm optimization (PSO) algorithm [115–117], and the least-squares method [113,118]. It demonstrated the importance of the PIM to the model accuracy. The tuning factors of the model accuracy in existing studies can be distinguished into 1) number/order of RC networks 2) parameter dependency on the state of charge (SoC) range, temperature and current loads.

The number of RC networks affects the accuracy of the model, as the RC networks characterise the battery transient responses with different time-constants associated with the diffusion and charge-transfer processes. The typical ECM studies in the literature are: 1RC: [119–121], 2RC: [122,123] and up to 5 RC pairs in [124]. The number may vary depending on the dynamics of the load profile, model accuracy and the cell chemistry.

Moving forward, the PIMs should capture the parameter dependence on the operating condition, such as SoC, temperature and current directions, etc. The first method for describing the parameter dependency is to divide the entire operating window, e.g., 0-100% SoC, into several levels, e.g., 10% SoC per level. A local model with constant parameters can then be trained for each SoC level [125–128]. The same method can be applied to capture the temperature dependency [128–130]. This method is widely adopted due to its ease of implementation. However, the disadvantage is that each local model is only valid for the local SoC window, and the model accuracy during transition between neighbouring SoC levels is not guaranteed. Another disadvantage is the identification of the local model generally ignores some prior knowledge about the battery dynamics. For example, the battery resistance value increases as temperature drops. The prior knowledge can be a useful parameter constraint to generate a physically interpretable global model, leading to improved accuracy. The second method to capture the parameter dependency is to use global optimization algorithms to estimate at-once all the model parameters under full operating window [131,132]. However, this involves tens of parameters with high computational complexity, and the chance of finding a global minimum is often low. The third method to capture the parameter dependency is to use adaptive parameter estimation algorithms such as recursive least squares methods and the dual Kalman filter algorithms [133–136]. However, the robustness and convergence of the adaptive algorithms are difficult to establish [137]. In particular, poor algorithm tuning can lead to estimation divergence [138].

Another dependency factor for ECM parameters that is generally overlooked are the types of current loads. Different current profiles have been used for ECM parameter estimation, such as the pulsed current test [126,127,139,140], drive cycles [137,141] and constant-current charging and discharging [131,142,143]. However, few works have considered the effect of choosing different current profiles on the identified parameters and the model accuracy [137,141].

Therefore, in order to achieve a sufficiently accurate ECM model (in chapter 5), the following research questions were identified:

7. ***Could the conventional ECM parameterisation method fulfil the ECM parameters need for a large format lithium ion battery?***
8. ***If not, what changes are required to maintain certain model accuracy?***
9. ***Will the load dependent parameter identification method deliver better model accuracy for equivalent circuit model?***

*The detailed answers are presented in the Chapter 4 in this thesis.*

### 2.10.2. Zero-dimensional Li-S Electrochemical Model

Electrochemical models often have more accurate predictions than the empirical models, due to the incorporation of the chemical and electrochemical kinetics and transport phenomena, such as charge conservation and lithium diffusion via the Nernst equation and the Butler-Volmer equation. [106,107,144] Representative works conducted by Newman, Doyle and Fuller et al. [145,146] present the physics based modelling for 1D based mathematical framework.

Nevertheless, electrochemical models are a double edged sword. The critical issues with all electrochemical models are difficulties in parameterisation and intense computational requirements.[107,108] There are more than 30 parameters needed to be fitted and parameterised including salt concentration, electrode/separator thickness, conductivity of electrolyte etc. [107,147–152]. Quite often the parameters in the physics-based model require ex-situ experimental measurements which are time/cost inefficient. [153,154] Also, the computational speed is another disadvantage of this type of models. Further, it is challenging to scale such model into multi-dimensional or pack level analysis. [108,151,155]

Cutting edge models try to address the disadvantages of electrochemical models, by reducing the order of the model, which simplifies the computational tasks. A few examples of reduced-order electrothermal models are conducted by Stetzel et al. Lee et al. and Plett et al. [156,157]

As discussed in the Empirical Modelling section, when a new battery chemistry is invented, the electrochemical models are more suitable for the purpose of understanding the internal reaction mechanisms. Thus, for Li-S cells, electrochemical models are developed. The first published Li-S model was conducted by Mikhaylik and Akridge et al. [16], which focuses on the relationship between charging current and polysulfide shuttle effect. The 2-step reaction zero dimensional with an expansion on the Nernst equation is conducted by Moy et al. [158] The adding of the intermediate reaction steps in the chain of polysulfide reduction increased the accuracy of the model in the region of discharge curve. [144] State-of-the-art zero dimensional models developed by Marinescu et al. studied diffusion limitations, precipitation/dissolution of polysulfides and kinetic limitations, which improved the voltage response for Li-S cells (e.g. flatness of the voltage plateaus). However, with all of the mentioned models, none of them has been combined with a diagnostic technique, to quantify and track the most essential challenge of Li-S cells, the shuttle. Combining with the thermal diagnostic tool DTV, the zero dimensional model has the potential to be thermally coupled (based on Eq 21-24, that shuttle is the only heat generation source at the end of charging). Therefore, the following research question was waiting to be answered:

10. ***Could thermally-coupled 0-Dimentinal LiS model provide optimal charging algorithms?***

*The detailed answers are presented in the Chapter 3 in this thesis.*

# 3. DTV technique on LiS cell and corresponding 0D modelling

## 3.1. Introduction

This chapter is based on the journal publication by Xiao Hua, Teng Zhang, Gregory Offer and Monica Marinescu. '*Towards online tracking of the shuttle effect in lithium sulfur batteries using differential thermal voltammetry*' *Journal of Energy Storage, 21 (2019), pp. 765-772.* As described in detail in section 1.4 in the Chapter 1.

From the literature review in Chapter 2, the polysulfide shuttle effect for lithium sulfur battery and its subsequent drawbacks are discussed: Lithium sulfur (Li-S) batteries are an important next generation high energy density battery technology. However, the phenomenon known as the polysulfide shuttle causes accelerated degradation, reduced Coulombic efficiency and increased heat generation, particularly towards the end of charge. The real-time detection of the onset of shuttle during charge would improve the safety and increase cycle life of Li-S batteries in real applications. In this chapter, the Differential Thermal Voltammetry (DTV) is demonstrated to act as one technique which can be used for tracking shuttle during Li-S charging. By combining voltage and temperature measurements, DTV is shown to be sensitive to the magnitude of shuttle. There are significant differences in the DTV curves for Li-S cells charged at different currents and temperatures. Quantitative interpretations of the experimental DTV curves are performed through a thermally coupled zero-dimensional Li-S model. The DTV technique, together with the model, is a promising tool for real-time detection of shuttle in applications, to inform control algorithms for deciding the end of charging, thus preventing excessive degradation and charge inefficiency.

This chapter answers following research questions:

1. ***Could one in-situ experimental diagnostic tool (e.g. DTV) quantify, track Li-S shuttle effect?***
2. ***Could this diagnostic tool, DTV, be used as a charging cut-off tool to minimise shuttle?***
3. ***Could thermally-coupled 0-Dimentinal LiS model provide optimal charging algorithms?***

## 3.2. Backgrounds

Lithium-Sulfur (Li-S) batteries are a promising next generation battery chemistry due to their high theoretic gravimetric energy density of 2500-2600 Wh kg-1, which converts to a practical value of 500-600 Wh kg-1 [14,159]. In comparison to conventional lithium-ion batteries, Li-S also promise economic advantages, because sulfur is cheap, abundant, and non-toxic [160]. Nevertheless, there are still significant challenges to overcome before widespread commercialisation, particularly associated with capacity fade, low columbic efficiency and self-discharge [25]

Many of these challenges are associated with the polysulfide shuttle, caused by the high solubility of long-chain polysulfides [27,161]. Long-chain lithium polysulfides produced during charging ($Li_2^+S_n^{2-}, n > 4$) have a high mobility through the electrolyte and can reach the surface of the Li metal anode, where they are reduced to shorter chain lithium polysulfides ($Li_2^+S_n^{2-}, n < 4$). These shorter chain lithium polysulfides diffuse back to the cathode, where they are oxidised back to long-chain polysulfides [26]. This back and forth shuttle of polysulfides is sustained during charging, leading to low charge efficiency at high states of charge (SoC) [47] and cell self-heating [162], associated irreversible capacity fade [163].

A study by Mikhaylik et al [162] proposed a positive feedback between shuttle and cell temperature: shuttle is assumed to be the only heat generation mechanism, and exponentially dependent on temperature. Thus, cell self-heating due to shuttle increases the shuttle rate, which in turn produces more heat. Consequently, the amount of shuttle and the associated degradation are directly linked to the cell’s temperature, and to the possibility of thermal runaway. Given the importance of minimising both degradation and thermal runaway in any real-world application, mitigating the amount of shuttle by devising appropriate safety cut-off criteria is key.

Given its importance to real life operation, there are relatively few studies published on diagnosing the amount of shuttle as a result of various operational conditions, such as temperature, current, or state of health. Most studies on shuttle focus on improving material properties [35,164], such as through lithium anode protection [165]. From an application perspective, however, there is value in developing a set of tools to diagnose shuttle, that will enable current Li-S batteries to be more performant in applications. Such tools should maintain their usefulness in the future, even for shuttle-protected battery formulations, as it is unlikely the shuttle will be removed completely.

One study assumes the shuttle is equal to the steady-state current achieved during constant voltage hold, thus offering a direct method of measuring shuttle [158]. This technique assumes the cell is maintained at a constant SoC during the voltage hold. Due to the significant duration of the voltage hold, this technique is not suitable for on-line shuttle diagnosis. Based on this shuttle current measurement, an open circuit voltage model of Li-S was developed to include temperature-dependent self-discharge during shuttle [166]. This model, however, is only validated during discharge. In real applications, the shuttle occurring during charging must be quantified, under different operational conditions, and preferably in real time, in order to avoid its detrimental effects.

All-solid-state lithium-sulfur batteries (ASSLSBs) are considered as one of the solution to eliminate the polysulfide shuttle. [167] However, the performance of ASSLSBs is far worse that the liquid-electrolyte lithium-sulfur batteries, in the aspects of : 1. Sulfur utilisation, 2. cycling life and 3. rate performance. [168–170] The main challenges come from 1. Poor electronic and ionic conductivities of sulfur, and 2. Large stress within the sulfur electrode in the ASSLSBs. Therefore, despite the promising findings on the elimination of shuttle, the focus on the thermal characterisation rather has higher priority in this work, to solve the shuttle issue fast and cheap.

In this study, we propose a fast, cost-effective method to detect and quantify shuttle during the charge of a Li-S cell using differential thermal voltammetry (DTV). We demonstrate this method is applicable for a range of charging currents and ambient temperatures. The DTV value is obtained as the ratio between the cell temperature and voltage differentials, during galvanostatic charge [171]:

$$\mathrm{DTV} = \frac{dT}{dt} \div \frac{dV}{dt} = \frac{dT}{dV} \tag{1}$$

The utility of DTV has been proven in tracking degradation of Li-ion battery [172]. It was shown to be faster than Slow Rate Cyclic Voltammetry and works in conditions where the cell generates significant heat, making the method particularly suitable to implementation in real applications. Its usefulness on tracking degradation mechanisms of the Nickel Manganese Cobalt chemistry at both cell and pack level [104], and of the Lithium Iron Phosphate (LFP) chemistry [46]. Due to the strong correlation between shuttle, cell voltage, and heat generation, DTV measurement are expected to yield information on the amount of shuttle in Li-S cells.

In this chapter, the DTV technique is applied to Li-S batteries to study the shuttle in Li-S cells for a range of charging currents and ambient temperatures, as might be encountered in an application. A zero-dimensional (0D) Li-S model is used to interpret the experimentally obtained DTV curves. The 0D model includes thermodynamics and kinetics for two electrochemical reactions, polysulfide precipitation and dissolution [144], and temperature coupling through a temperature-dependent shuttle and a shuttle-induced heat generation, as described by *Mikhaylik et al* [173]. The 0D model is shown to capture essential features of Li-S DTV, features which are shown to be correlated with the magnitude of shuttle. DTV in tandem with mechanistic modelling is therefore shown to be a fast and effective method for tracking shuttle, and thus a promising tool for optimising charging in Li-S cells by minimising shuttle.

## 3.3. Experimental details

A range of charge/discharge and DTV tests on a long-life 10Ah OXIS pouch cell (150×100×7.27 mm) were examined under various temperatures. Before experiments were carried out, the cell underwent three charge/discharge cycles for re-conditioning, and showed stabilised capacity. Various cells from the same cell manufacturer, same batch were tested to ensure repeatability of the test results. The cell was placed on an acrylic cell holder which sat individually in the centre of the bottom shelf of a thermal chamber (Binder, model KB 23). K-type thermocouple was placed and taped with Kapton® polyimide films tape on the centre of the pouch cell surface to measure surface temperature. An 8-channel battery cycling system (Bio-Logic, BCS-815) was used for charging/discharging the cell. The cell was pre-cycled 3 times using constant current 0.1C (1A) charge and 0.2C (2A) discharge. Two sets of DTV experiments were carried out in this study, as detailed below.

***Experiment #1: Variable ambient temperature DTV tests***

Firstly, 0.1C/0.2C charge/discharge was run under various ambient temperatures of 20 °C, 30 °C, 40 °C and 45 °C. In-between DTV test cycles, the cell was cycled once 0.1C/0.2C charge/discharge at 30 °C (referred to as standard conditions) to mitigate the effect of history effects [174].

***Experiment #2: Variable charging rates DTV tests***

Secondly, charging at different C-rates and discharging at 0.2 C was run at ambient temperatures of 30 °C and 40 °C. The charging rates were 0.1 C, 0.2C and 0.3C. As in experiment #1, the cell was cycled once at standard conditions in-between DTV test cycles.

### *Voltage & time limits*

In all experiments, the cell was cycled with voltage cut-offs of 1.5V and 2.45V, and an additional time limit of 12 hours during charging. After each DTV test cycle and before the standard conditions cycle, a rest period of one hour was introduced at the end of discharge, to allow for the cell temperature to equilibrate with the ambient temperature.

### *Test sequence*

Standard conditions: charge at 0.1C, discharge at 0.2C under ambient temperature of 30°C

1. Three standard condition cycles
2. 30°C tests: charge at 0.1C, 0.2C, 0.3C, discharge at 0.2C, with one standard conditions cycle after each DTV cycle.
3. Three standard conditions cycles.
4. 20°C test: charge at 0.1C, discharge at 0.2C.
5. Three standard conditions cycles.
6. 40°C tests: charge at 0.1C, 0.2C, 0.3C, discharge at 0.2C, with one standard conditions cycle after each DTV cycle.
7. Three standard conditions cycles.
8. 45°C test: charge at 0.1C, discharge at 0.2C.

| | **Ambient Temperature/°C** | **Charging Current/A** | **Discharging Current/A** |
|---|---|---|---|
| **#1 variable T** | | | |
| | 20 | 1 | 2 |
| | 30 | 1 | 2 |
| | 40 | 1 | 2 |
| | 45 | 1 | 2 |
| **#2 variable I** | | | |
| | 30 | 1 | 2 |
| | 30 | 2 | 2 |
| | 30 | 3 | 2 |
| | 40 | 1 | 2 |
| | 40 | 2 | 2 |
| | 40 | 3 | 2 |

*Table 1 Combinations of operational parameters considered in the DTV study of Experiment #1 & #2.*

## 3.4. Zero-dimensional model

The model fulfills two roles: helps identify which physical phenomena give rise to the experimentally observed DTV characteristics, and helps evaluate the potential of using DTV during charging to avoid capacity fade associated with shuttle and degradation. The latter is possible because the model allows direct access to the true capacity of the cell, information which is inaccessible from experiments, but is essential for determining charge efficiency and state of health.

A 0D Li-S model [144] is further developed to include heat generation and temperature-dependent behaviour, both required features for a comparison to DTV experimental data. The shuttle is assumed to be the only heat generation source, as in the work by *Mikhaylik et al* [162]. There, heat generation in the form of Ohmic heat from the shuttle current has been proposed in a lumped, thermally coupled electrochemical model.

While there is Ohmic heat generation associated with the internal resistance of the cell and entropic heat associated with phase changes occurring during charge, both these sources are assumed to be significantly smaller than the heat generated through shuttle. The maximum heat generated by the internal resistance of the cell can be estimated to be two orders of magnitude smaller than that generated due to shuttle at the end of charge. This value corresponds to a resistance of 0.15Ω, the maximum resistance during discharge, as obtained from a 0.1C discharge [175]. The Ohmic resistance during charge is expected to be smaller than that during discharge, possibly due to the electrolyte concentration remaining lower than during discharge [176]. The measured temperature during charge shows a significant increase at the end of charge, as seen in figure 23, which is not correlated to a significant increase in cell resistance [177], further justifying the assumption of shuttle being the only significant heat source.

The thermal-electrochemical model does not include the Ohmic resistance of a cell, which has been shown to have a significant contribution to the cell voltage [175], and thus to the heat generated in all regions where the shuttle is not prominent. The Ohmic heat generation is expected to exhibit a peak at the boundary between the two plateaus, in both charge [177] and discharge [178], according to the peak in Ohmic resistance. There is no visible peak in the temperature evolution of the charging cell, indicating that Ohmic heat is not significant. Heat generation could also be caused by the abrupt increase in charge transfer resistance [36], expected to be significant only at the end of discharge. Some of these contributions to heat generation have been accounted for in the model proposed by *Stroe et al.* [179], which omits heat from shuttle, thus limiting its utility to discharge. For studying shuttle, here we focus on the last section of charging, where all heat sources other than shuttle can be ignored.

## 3.5. Experimental results and discussion

The voltage and temperature during a 0.1C (1A) charge at 20 °C is illustrated in Figure 23a, whereas the DTV curve, obtained according to Eq 1, is shown in Figure 23b. The temperature data was smoothed by the Savitzky-Golay smoothing filter and the moving average method [172]. The cell surface temperature remains relatively constant during the lower plateau region of the charge curve. As the voltage approaches the higher plateau, a noticeable temperature-drop of around 0.2 °C is observed. This temperature dip during charge corresponds to the drop in heat flux reported previously by Kolosnitsyn et al [180], but not explained, and shifts to lower capacities for Li-S cells charged at increasing current rates. The same trend is observed here for all charging conditions. (as in Supplementary Data section) The location of the dip suggests it could be the effect of decreasing Ohmic heat generation[180], as it occurs after the peak in Ohmic resistance [177], followed by an increasing heat generation when advancing into the high plateau region. The significant temperature increase until the voltage cut-off is reached is assumed to be caused by shuttle, as the main heat generation mechanism in the region [162].

The cell surface temperature has a steep increase at the same time as the voltage plateaus. Then, there is a temperature plateau when dynamic equilibrium is reached between heat generation and transport. The voltage increase towards a cut-off, gives rise to a DTV peak towards the end of charge. In addition to this finite peak, two infinite peaks can be observed at the beginning of charge in the DTV curves. These peaks are a consequence of the local maxima and minima voltage points in the low SoC region, which lead to an infinitesimally small dV/dt (d_Voltage/d_Time) value. The charge voltage initially increases, due to the high overpotential caused by the surface passivation with $Li_2S$ precipitate [47,181,182]. As the dissolution overpotential drops, so does the cell voltage, increasing when the open-circuit voltage begins to dominate the charging behaviour. Other fluctuations of the DTV value, at times between 0.5-1.5 x $10^4$ s, are caused by temperature fluctuation (<0.05°C). These could be the effects of other heat generation sources, such as Ohmic and entropic, and are not related to shuttle. In this study, the focus is on the feasibility of identifying shuttle via the DTV peaks, and thus the other figures focus on the end of discharge only. Whole range charge data is plotted in Supplementary Data section, at the end of this chapter.

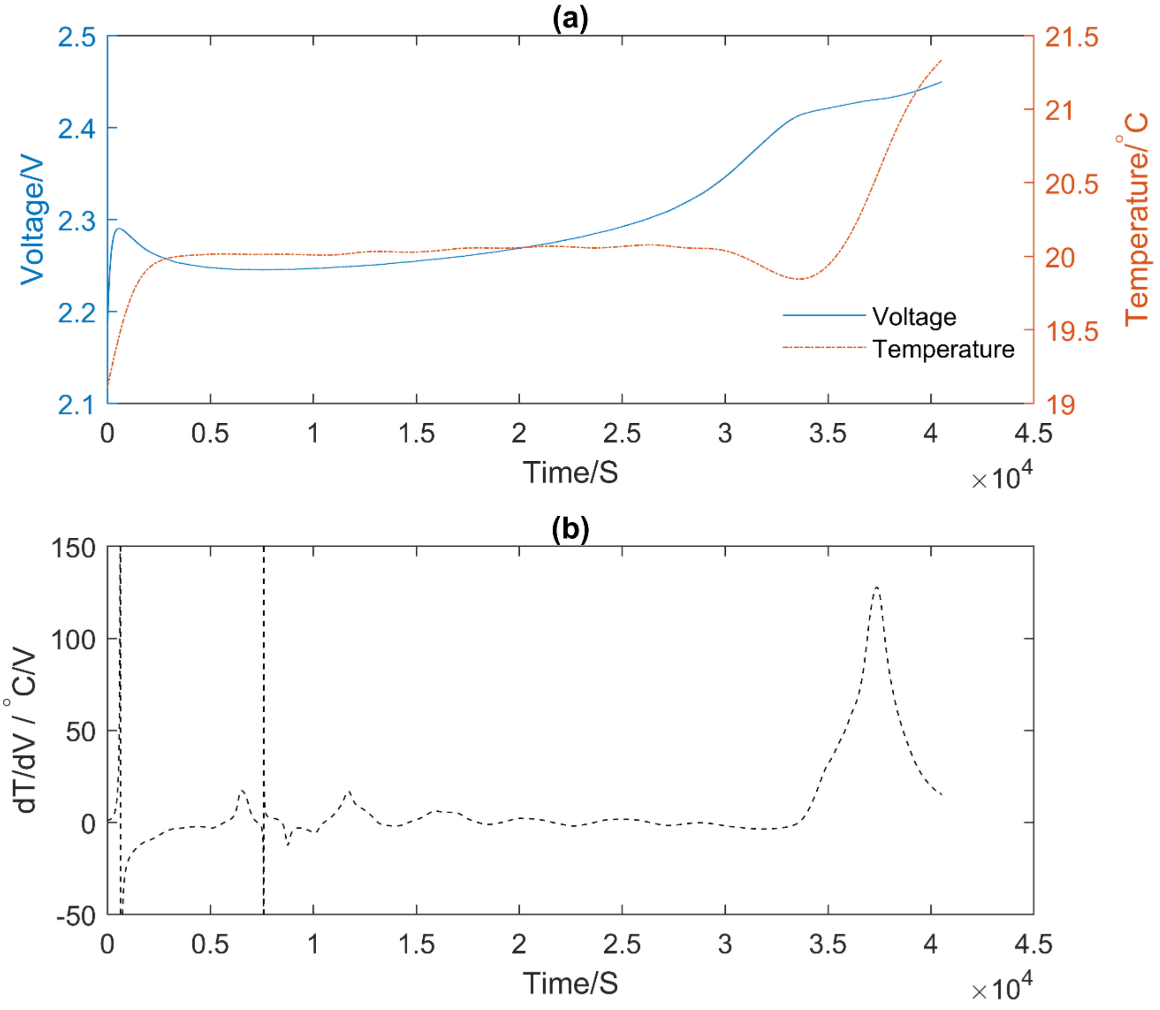

*Figure 23 The differential thermal voltammetry measurement during a constant current charge exhibits a peak in the high plateau. Charging of a 10Ah cell at 20 ℃ with 1A (0.1C) with 2.45V voltage cut-off. (a) Cell voltage and temperature, and (b) dT/dV as obtained by differentiating the data in (a).*

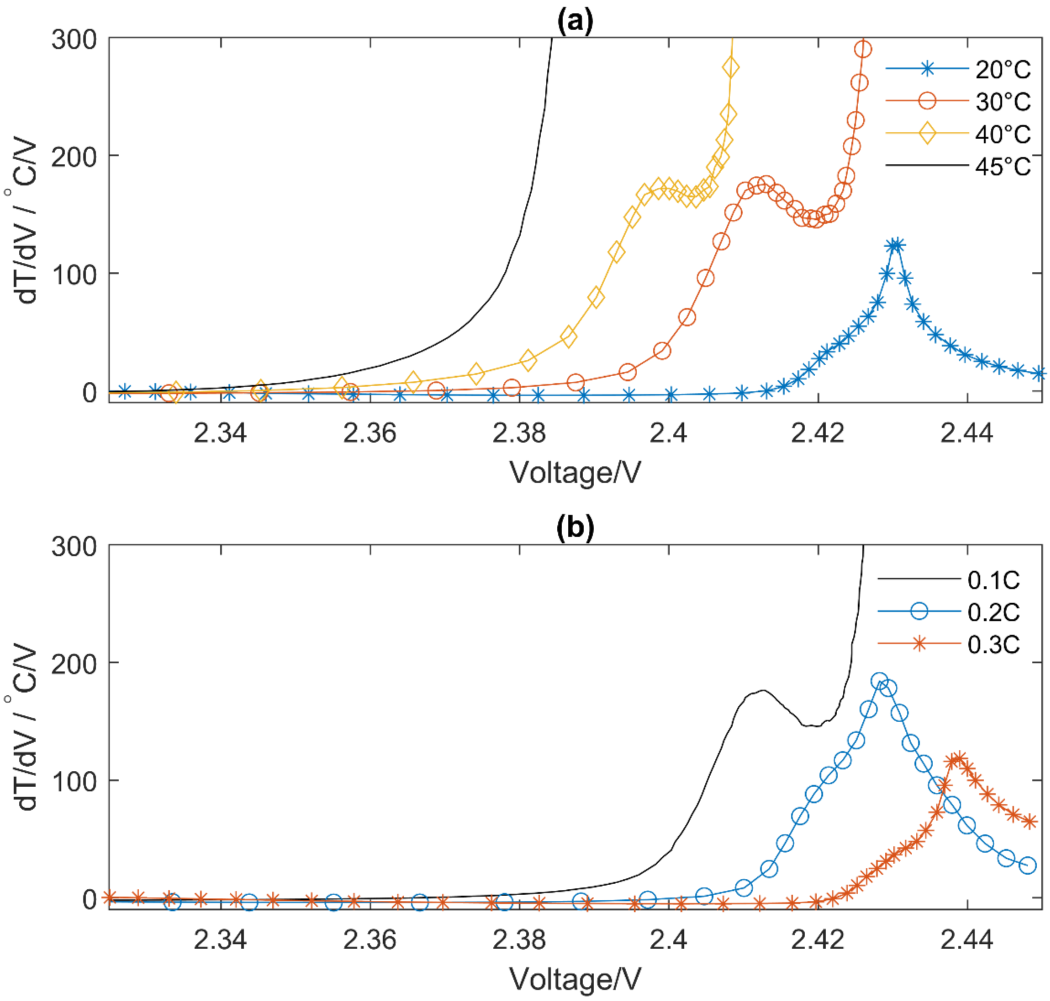

*Figure 24 The peaks of DTV measurements during constant current charge exhibit voltage shift and height change (a) under different ambient temperatures: Charging of a 10Ah cell at a range of temperatures (see legend) with 1A (0.1C) with 2.45V voltage cut-off. DTV peak shifts to smaller voltage position, increases peak magnitude when temperature rises. (b) Different charging rate: 10Ah cell at 30 ℃ with 1A (0.1C), 2A (0.2C), 3A (0.3C) with 2.45 V voltage cur-off. DTV peak shifts to smaller voltage position, increases peak magnitude when charging rate drops. Line symbols correspond to 1 in 300 measurements collected, to improve visibility.*

### *Rate and temperature dependence of DTV curves*

Figure 24 shows the DTV peaks at the end of charge curves for various temperatures and charge rates. Figure 24a illustrates the temperature dependence of DTV curves, as the peak pattern, height, and position varies under different ambient temperatures. The DTV curves can be categorised into three cases, showing: 1. a finite peak, 2. a finite peak followed by a subsequent infinite peak, and 3. an infinite peak. The finite peak case occurs for charging at the lower 20 °C ambient temperature, as has been explained in the previous section for figure 23. The second case appears when the ambient temperatures are increased to 30 °C and 40 °C, where a second, infinite peak appears following the first, finite peak. The third case occurs at the highest charging temperature of 45 °C. At higher ambient temperatures, higher solubility and mobility of polysulfides is expected, leading to increased shuttling of polysulfides[183] and an infinitely high DTV value as the voltage plateaus and dV becomes infinitesimally small.

Figure 24b demonstrates the DTV peaks for different charging currents (1A, 2A and 3A) at the ambient temperature of 30 °C. A finite peak (case 1) was observed at 0.2C and 0.3C charging rates, while a finite peak followed by an infinite peak (case 2) was observed at 0.1C. The finite peaks at 0.2C exhibited higher height compared to that at 0.3C. When the charge rate increases, the dissolution bottleneck of $Li_2S$ is expected to limit the amount of dissolved polysulfides at any given time during charge. Whether this limits the amount of sulfur that participates in shuttle [47,184] or increases it as shuttle can occur earlier, is not clear. The time spent in the shuttling region at the end of charge, however, certainly decreases with higher charging rates. The cells charged at a higher rate exhibit a reduced peak height, associated with this smaller effect of shuttle. On the other hand, the cells' polarization increases with increasing charge rate, causing the DTV peaks to shift to higher voltages, thus the positions of the peaks at 0.3C were at higher voltages compared to the peaks observed at 0.2C. The underlying mechanisms for the change in peak pattern, height, and location is further explored via comparison to model predictions in the next section.

Figure 25 shows the dT measurements at the end of charge curves for various temperatures and charge rates. Figure 25a demonstrates that, in the case of charges at different ambient temperatures, a similar trend is obtained from both dT and DTV: the peak height is proportional to the amount of shuttle expected at the end of charge. However, in the case of charging at different rates, the peak height of dT in figure 25b decreases at lower charging rates, despite more shuttle occurring. This is most probably a result of other heat generation sources becoming significant at the higher charging rates. Thus, the dT peak height is not a generally clear indication of the amount of shuttle, unlike the DTV peak height. Additionally, the magnitude of dT is on the order of $10^{-4}$ °C, compared to $10^{2}$ °C/V for DTV. This makes DTV more applicable and cost-effective, as in the real-world applications it is challenging to have such high precision measurements.

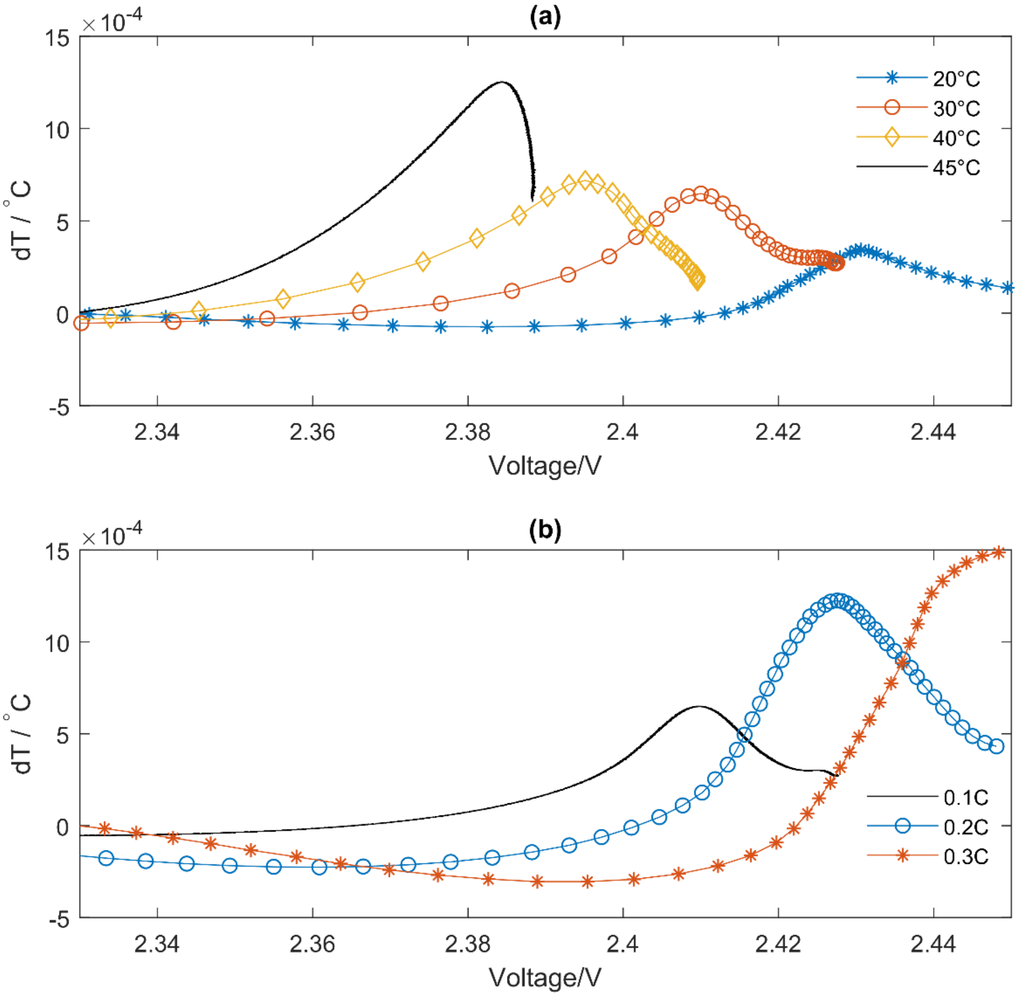

*Figure 25 The peaks of dT measurements during constant current charge exhibit voltage shift and height change (a) under different ambient temperatures: Charging of a 10Ah cell at a range of temperatures (see legend) with 1A (0.1C) with 2.45V voltage cut-off. dT peak shifts to smaller voltage position, increases peak magnitude when temperature rises. (b) Different charging rate: 10Ah cell at 30 ℃ with 1A (0.1C), 2A (0.2C), 3A (0.3C) with 2.45 V voltage cur-off. dT peak shifts to smaller voltage position, decrease peak magnitude when charging rate drops. Line symbols correspond to 1 in 300 measurements collected, to improve visibility.*

## 3.6. Model predictions and discussion

Model predictions obtained from the model are illustrated in figure 26 for a set of ambient temperatures between 20 °C and 45 °C at fixed charging rate. A peak is present in the DTV charging curve at high states of charge, with height and position comparable to those observed in experiments, in figure 24a. Charged at the lowest temperature, the cell reaches the cut-off voltage, and a finite peak is present. At higher temperatures, the cell is protected from overcharge, exhibits voltage plateaus, and thus infinite peaks in the DTV plot. At 30 °C, both finite and infinite peaks are visible, similar to the experimental data for 30 °C and 40 °C. The known shift in charging behaviour with increasing ambient temperature is retrieved by the model because of the addition of an Arrhenius-like dependence of the shuttle rate on temperature. This dependence also leads to a decrease in the upper plateau voltage with increasing temperature, and thus to a shift to lower voltages of the start of both finite and infinite peaks. Both trends can be observed in the experimental data in figure 24a. The peak height increases significantly with temperature in both modelling and experimental data; in the model this effect is caused by heat generation that is proportional to the amount of shuttling sulfur, which itself increases with temperature.

One feature of the experimental data that is not captured by the model is a shift of the finite peak to lower voltages when increasing temperature. This shift is most probably related to the contribution of the Ohmic potential drop to the cell voltage, which has been shown to be significant. [185] The Ohmic resistance is expected to decrease significantly with increasing temperature, leading to lower charging voltages. The current 0D model can only predict the terminal voltage qualitatively, and not quantitatively, because of the omission of the Ohmic resistance, whose experimental characterisation is beyond the scope of this work.

In both experimental and modelling results there is no direct way to predict whether the cell will follow the overcharge protection or voltage cut-off scenario from the temperature evolution. This lack of features distinguishing between the two cases indicates that a simple temperature detection algorithm is not sufficient to avoid degradation.

### *Model Equations*

Two electrochemical reactions occur simultaneously in the system, during both charge and discharge:

$$\mathrm{S_8^0} + 4\mathrm{e}^- \longleftrightarrow 2\mathrm{S_4^{2-}},$$
$$\mathrm{S_4^{2-}} + 4\mathrm{e}^- \longleftrightarrow 2\mathrm{S}^{2-}\downarrow + \mathrm{S_2^{2-}}. \quad (2)$$

In effect, due to the value of their standard potentials, each reaction dominates one of the two discharge plateaus. Due to the upper voltage limit of 2.45 V, solid $S_8$ is not expected to form in any significant quantity. Dissolved $S_8^0$ is the most oxidised species allowed in the system. As a result of the two reactions chosen in Equation 2, the theoretical capacity of the cell $c_{\mathrm{th}}$ that corresponds to the true state of charge, can be calculated. Each $S_8^0$ molecule contributes twelve electrons and each $S_4^{2-}$ four electrons to the cell capacity:

$$c_{\mathrm{th}}[\mathrm{Ah}] = \left(\frac{3n_4}{n_{\mathrm{S8}}}\frac{F}{M_{\mathrm{S}}}S_8^0 + \frac{n_4}{n_{\mathrm{S4}}}\frac{F}{M_{\mathrm{S}}}S_4^{2-}\right)\frac{1000}{3600} \quad (3)$$

where $F$ is Faraday's constant, $M_{\mathrm{S}}$ the molar mass of $S_8^0$, $n_4$ the number of electrons corresponding to each reaction, here both equal to four. $n_{S8}$ and $n_{S4}$ denote the number of sulfur atoms in each polysulfide species, and $S_8^0$ and $S_4^{2-}$ the amounts of the respective polysulfide in grams. The expression in Equation 3 would need to be changed, if a different electrochemical path were chosen.

The equilibrium potentials associated with the two reactions $E_{\mathrm{H}}$ and $E_{\mathrm{L}}$ are modelled via the Nernst equation:

$$E_{\mathrm{H}} = E_{\mathrm{H}}^0 + \frac{RT_{\mathrm{N}}}{n_4F}\ln\left(f_{\mathrm{H}}\frac{S_8^0}{(S_4^{2-})^2}\right),$$
$$E_{\mathrm{L}} = E_{\mathrm{L}}^0 + \frac{RT_{\mathrm{N}}}{n_4F}\ln\left(f_{\mathrm{L}}\frac{S_4^{2-}}{(S^{2-})^2S_2^{2-}}\right). \quad (4)$$

$E_H^0$and $E_L^0$ are the standard potentials for the reactions in Equation 2, respectively, $R$ is the gas constant, and $T_N$ the temperature at which the reaction occurs. Only the temperature dependence of the shuttle rate is considered here, such that $T_N$ is a constant, rather than equal to the cell temperature Tc, as it becomes apparent below and in Table3. $S_2^{2-}$ and $S^{2-}$ are the amounts of the respective polysulfides in grams. The factors $f_{\mathrm{L}}, f_{\mathrm{H}}$ convert species quantities measured in grams to units compatible with Equation 4:

$$f_{\mathrm{H}} = \frac{n_{\mathrm{S4}}^2 M_{\mathrm{S}} v}{n_{\mathrm{S8}}},$$
$$f_{\mathrm{L}} = \frac{n_{\mathrm{S}}^2 n_{\mathrm{S2}} M_{\mathrm{S}}^2 v^2}{n_{\mathrm{S4}}}. \quad (5)$$

Here $n_{\mathrm{S2}}$ and $n_{\mathrm{S}}$ denote the number of sulfur atoms in the respective polysulfide species, and $v$ is the electrolyte volume per cell. The cell current is the sum of the currents from the two electrochemical reactions, $I_{\mathrm{H}}$ and $I_{\mathrm{L}}$,

$$I = I_{\mathrm{H}} + I_{\mathrm{L}}, \quad (6)$$

as described by the Butler-Volmer approximation:

$$I_{\mathrm{H}} = -2 i_{\mathrm{H},0} a_{\mathrm{r}} \sinh \frac{n_4 F \eta_{\mathrm{H}}}{2RT_{\mathrm{N}}},$$
$$I_{\mathrm{L}} = -2 i_{\mathrm{L},0} a_{\mathrm{r}} \sinh \frac{n_4 F \eta_{\mathrm{L}}}{2RT_{\mathrm{N}}}. \quad (7)$$

Here $a_{\mathrm{r}}$ is the active interfacial area for the cell, here assumed to be constant, and $i_{\mathrm{H},0}$, $i_{\mathrm{L},0}$ are exchange current densities for the higher and lower plateau reactions.

The overpotentials $\eta_{\mathrm{H}}$, $\eta_{\mathrm{L}}$ of the two reactions are given by:

$$\eta_{\mathrm{H}} = V_{\mathrm{c}} - E_{\mathrm{H}}$$
$$\eta_{\mathrm{L}} = V_{\mathrm{c}} - E_{\mathrm{L}}. \quad (8)$$

$V$c is the cathode voltage, assume to be identical to the cell voltage in this model.

The various polysulfide species evolve with time as a result of electrochemical reactions, shuttle and precipitation/dissolution, as given by:

$$
\begin{aligned}
\frac{\mathrm{d}S_8^0}{\mathrm{d}t} &= -\frac{n_{\mathrm{S8}}M_{\mathrm{S}}}{n_4F}I_{\mathrm{H}} - k_{\mathrm{s}}S_8^0 \\
\frac{\mathrm{d}S_4^{2-}}{\mathrm{d}t} &= 2\frac{n_{\mathrm{S4}}M_{\mathrm{S}}}{n_4F}I_{\mathrm{H}} + k_{\mathrm{s}}S_8^0 - \frac{n_{\mathrm{S4}}M_{\mathrm{S}}}{n_4F}I_{\mathrm{L}} \\
\frac{\mathrm{d}S_2^{2-}}{\mathrm{d}t} &= \frac{n_{\mathrm{S2}}M_{\mathrm{S}}}{n_4F}I_{\mathrm{L}} \\
\frac{\mathrm{d}S^{2-}}{\mathrm{d}t} &= 2\frac{n_{\mathrm{S}}M_{\mathrm{S}}}{n_4F}I_{\mathrm{L}} - \frac{1}{v\rho_{\mathrm{S}}}k_{\mathrm{p}}S_{\mathrm{p}}\left(S^{2-} - S_*^{2-}\right) \\
\frac{\mathrm{d}S_{\mathrm{p}}}{\mathrm{d}t} &= \frac{1}{v\rho_{\mathrm{S}}}k_{\mathrm{p}}S_{\mathrm{p}}\left(S^{2-} - S_*^{2-}\right) \\
\frac{\mathrm{d}S_{\mathrm{s}}}{\mathrm{d}t} &= k_{\mathrm{s}}S_8^0 \\
\frac{\mathrm{d}T_{\mathrm{c}}}{\mathrm{d}t} &= \frac{1}{m_{\mathrm{c}}c_{\mathrm{h}}}\left[k_{\mathrm{s}}\frac{n_4F}{n_{\mathrm{S8}}M_{\mathrm{S}}}S_8^0V_{\mathrm{c}} - h\left(T_{\mathrm{c}} - T_{\mathrm{a}}\right)\right],
\end{aligned}
\qquad (9)
$$

where *S*p is the mass of precipitated sulfur, $\rho_S$ its density, and $S_*^{2-}$

the saturation mass of $S^{2-}$, assumed to be constant. Equation 9 describes the temperature evolution of the cell, as a result of heat generated by the shuttle, according to the first term on the right hand side, and heat convection between the cell and the ambient, as given by the second term. *T*a is the ambient temperature, *h* the heat transfer coefficient for the cell, $c_h$ the heat capacity for the cell, and $m_c$ the mass of the cell. The shuttle constant $k_s$ becomes a function of the cell temperature, according to the Arrhenius equation:

$$
k_{\mathrm{s}}(T_{\mathrm{c}}) = k_{\mathrm{s}}^0 \exp\left[-\frac{A}{R}N_A\left(\frac{1}{T_{\mathrm{c}}} - \frac{1}{T^0}\right)\right], \qquad (10)
$$

where $k_s^0 = k_s(T^0)$ corresponds to the shuttle rate at the reference temperature $T_0$. The addition of the Avogadro's number $N_A$ to the expression provided by Mikhaylik and Akridge serves to ensure units consistency under the exponential. As a result, all terms in Equation 9 where $k_s$ appears have a temperature dependence, on the value of $T_c$.

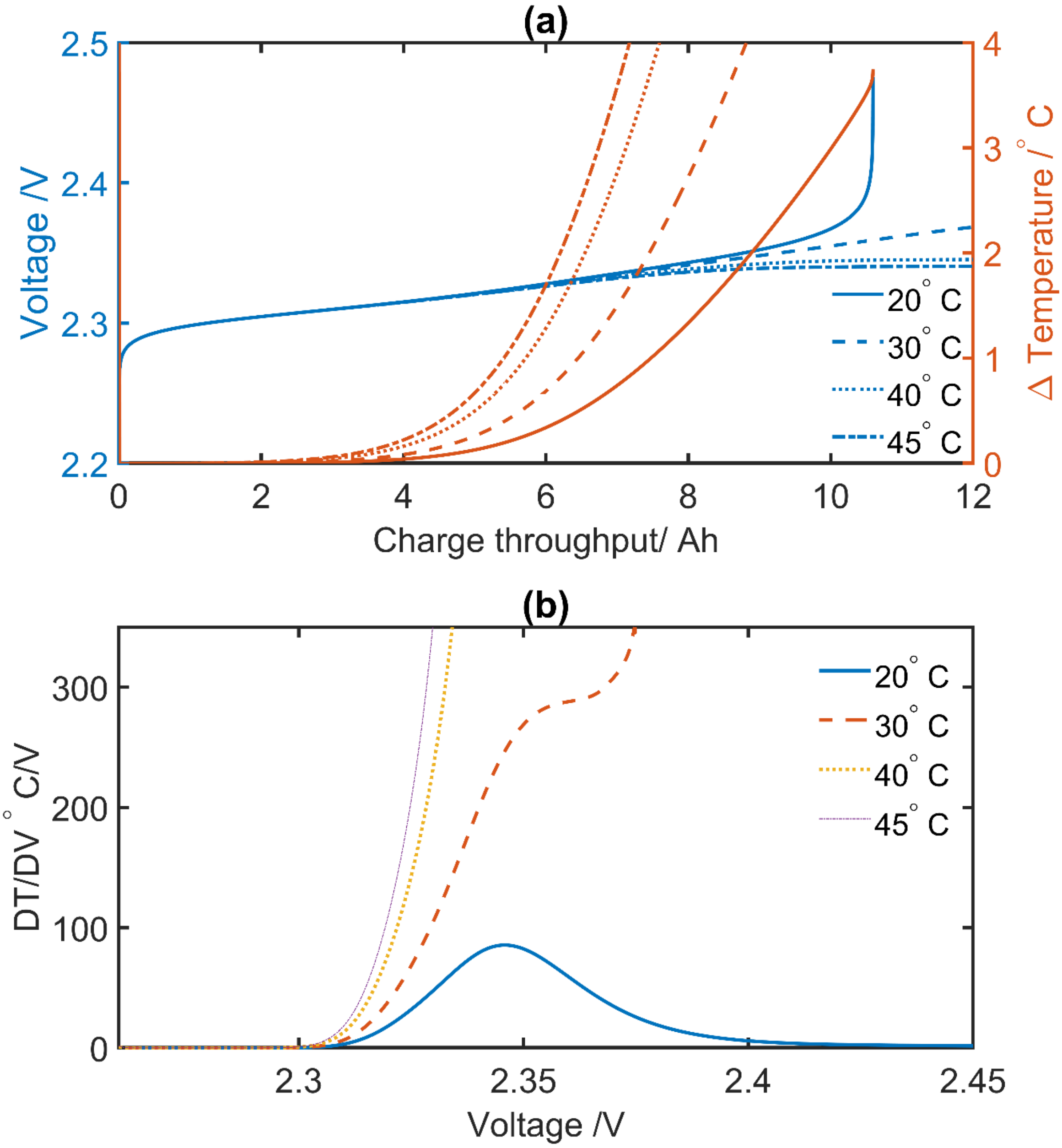

*Figure 26 Thermal voltammetry model predictions during a constant current charge exhibit a peak in the high plateau. Charging of a 10Ah cell at a range of temperatures with 1A (0.1C) and a 2.45V voltage cut-off. (a) Cell voltage and temperature, and (b) dT/dV as obtained by differentiating the data in (a).*

**Fixed ambient temperature, variable charge rate**

Model predictions for cell behaviour charged at different C-rates at fixed ambient temperature are shown in figure 27. The height of the DTV peaks can be explained with a similar reasoning to that used in the previous section: the larger DTV peaks correspond to the conditions in which the shuttle effect is larger. Charging with the smallest current allows the largest amount of material to shuttle, leading to a finite and an infinite peak. The position of the peak shifts towards higher voltages with higher charging rate. This is the combined effect of larger kinetic and dissolution over-potentials at larger C-rates, as can be seen from the fact that the voltage curves are shifted to higher values. The DTV peaks visibly broaden when the C rate increases, similarly to the experimental data shown in figure 24b.

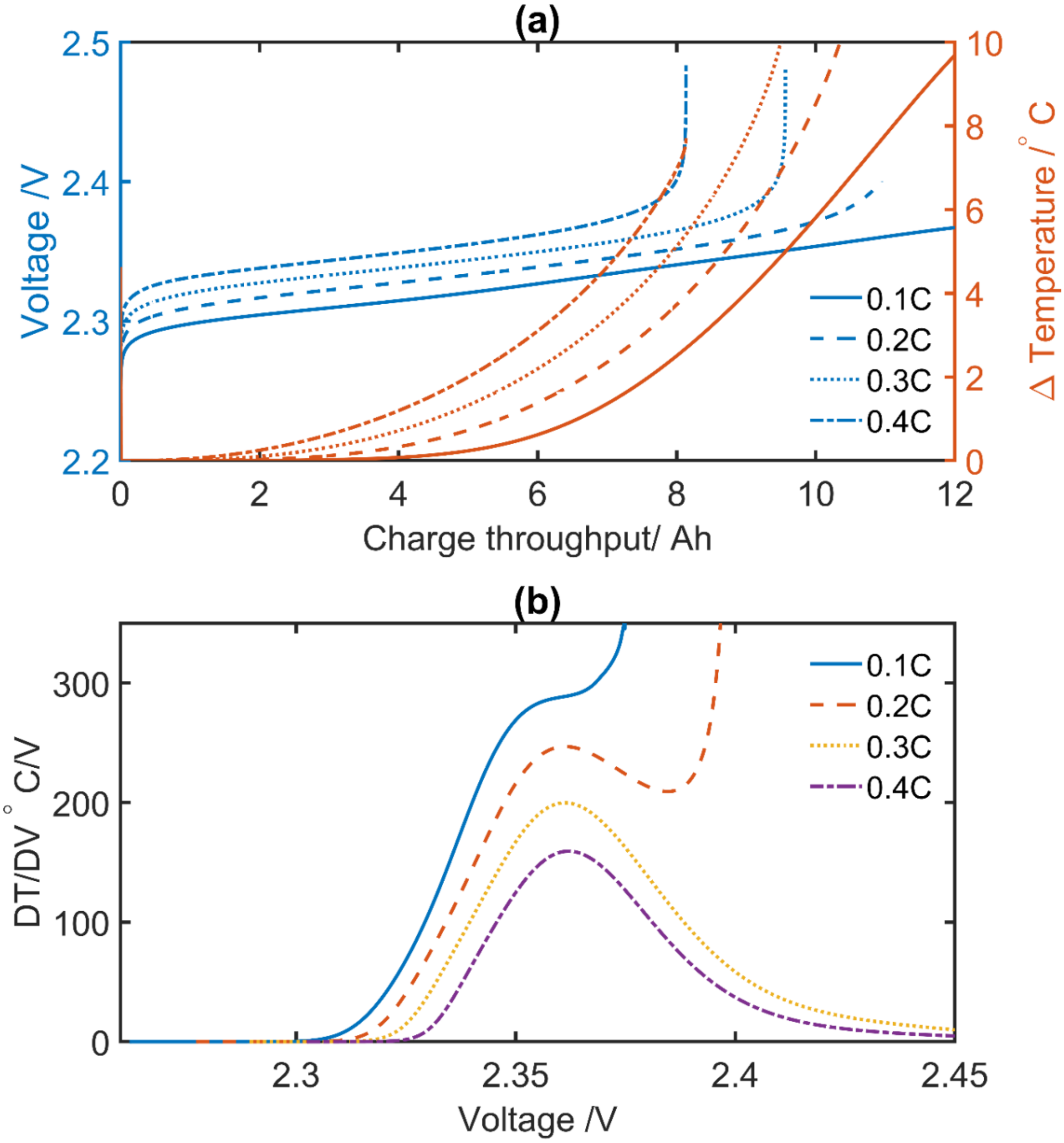

*Figure 27 Thermal voltammetry model predictions during a constant ambient temperature at different charging rates exhibit a peak in the high plateau. Charging of a 10Ah cell at 25 deg C with 2.45V voltage cut-off. (a) Cell voltage and temperature, and (b) dT/dV as obtained by differentiating the data in (a).*

Aside from providing a tool to verify causality between observed features and assumed mechanisms, a sufficiently complex validated LiS model also allows access to states of the cell that are not available in experiments. Crucially, it allows a separation between charge lost through shuttle and charge that contributes to raising the cell's state of charge. Obtaining this information is key to deriving a control algorithm to allow efficient, flexible charging protocols. These aspects are explored in the following sections.

### Charging efficiency

In the model, the concentrations of the various polysulfide species are tracked throughout operation, thus allowing direct access to the true capacity of the cell. The true capacity rise in the cell with charge throughput is given in figure 28. The incremental capacity is calculated as the charge that contributes to raising the cell capacity, as calculated from the predicted species concentrations in the model. As a result of the two reactions chosen in Equation 2, the theoretical capacity of the cell $C_{\mathrm{th}}$ that corresponds to the true state of charge, can be calculated. Each $S_8^0$ molecule contributes twelve electrons and each $S_4^{2-}$ four electrons to the cell capacity [144]:

$$C_{th}[Ah] = \left(\frac{3n_4}{n_{S8}}\frac{F}{M_S}S_8^0 + \frac{n_4}{n_{S4}}\frac{F}{M_S}S_4^{2-}\right)\frac{1000}{3600} \tag{11}$$

Where $F$ is Faraday's constant, $M_S$ the molar mass of $S_8^0$, $n_4$ the number of electrons corresponding to each reaction, here both equal to four. $n_{S8}$ and $n_{S4}$ denote the number of sulfur atoms in each polysulfide species, and $S_8^0$ and $S_4^{2-}$ the amounts of the respective polysulfide in grams. The expression in Equation 11 is valid strictly for the chosen set of governing electrochemical reactions.

The charge throughput corresponds to the capacity of the cell as wrongly calculated via coulomb counting, I·t. As the cell charges past the boundary between the two plateaus, a steep drop in the added capacity is present, as more charge is lost by shuttle. This drop occurs earlier in the charging cycle for higher ambient temperatures.

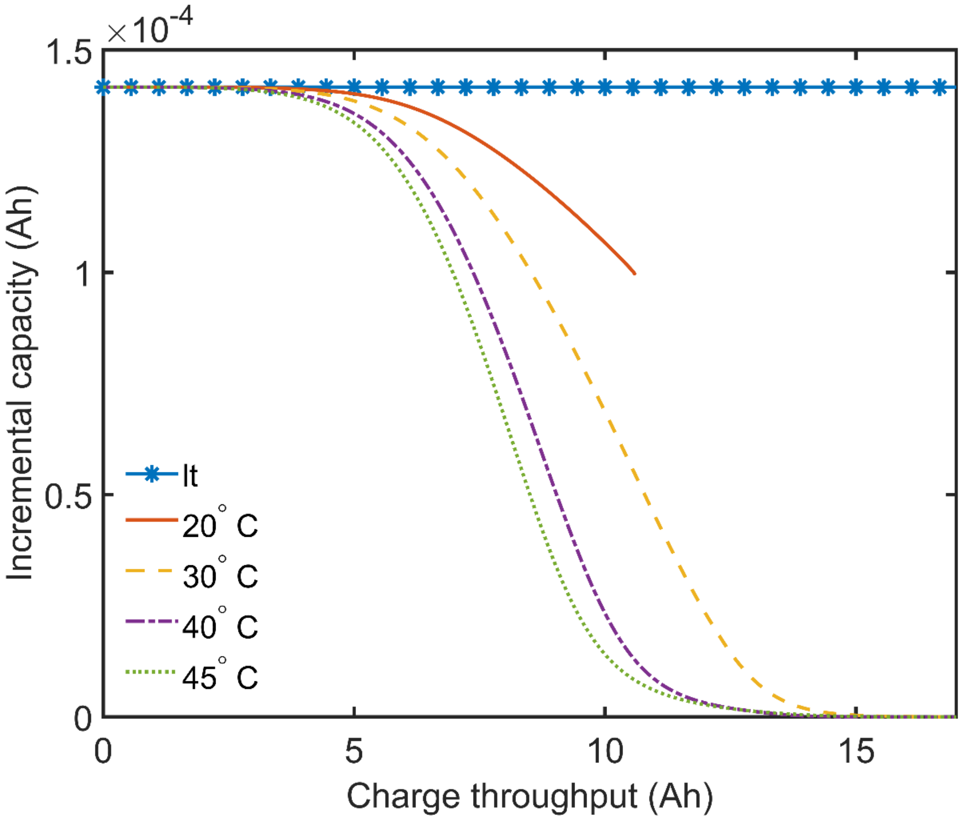

*Figure 28 Model predictions: As the cell is charged into the high plateau, the charge efficiency decreases abruptly, sooner and faster for higher ambient temperatures. Added charge per unit time for a charge at 0.1 C under the ambient temperatures given in the legend.*

Consequently, for a pre-decided value of the coulombic efficiency, given by the ratio between throughput charge and useful charge, the charging of a cell should be stopped much sooner if running in warmer conditions. The charging efficiency defined as the ratio between the true and assumed cell capacities is shown in figure 29 for a set of ambient temperatures and charging rates.

Figure 29a predicts that the colder cell reaches the highest ultimate true capacity, while incurring the least loss through shuttle. In reality, we expect a hotter cell to suffer considerably less from the dissolution bottleneck, as both the saturation concentration and the dissolution rate increase with temperature [186]. At charging conditions for which mass transport is limiting, diffusion of species decreases with decreasing temperature, also decreasing the achieved true capacity. These effects compete with the effect of reduced shuttle, such that a warm cell can have a higher achievable capacity than the colder one. In the current model, however, precipitation/dissolution mechanisms are not temperature dependent and diffusion limitations are ignored. Figure 29b illustrates that a higher charging capacity can be achieved by slow charging than fast charging, with the cost of much shuttle incurred, because of the trade-off between shuttle and dissolution bottleneck.

Star symbols in figure 29 & 30 denote the position of the DTV finite peak. No such peak is present when charging at 40ºC and 45ºC. The peaks occur at significantly different charging efficiencies, demonstrating that their position alone is not a good indicator of the opportune moment to stop charging. It is thus concluded that, in order to provide dedicated charging algorithms to minimise degradation, a reduced order model must be used alongside DTV measurements. The algorithm needs to take into account both position of peak and current and temperature at which the charging occurs. As the current model is a qualitative rather than a quantitative tool, it is the trend rather than the exact numbers in this section that is trustworthy. Clear future works can be found in section 6.2, where detailed upgradation of this model is described, in terms of transformation from 'qualitatively' to 'quantitatively'.

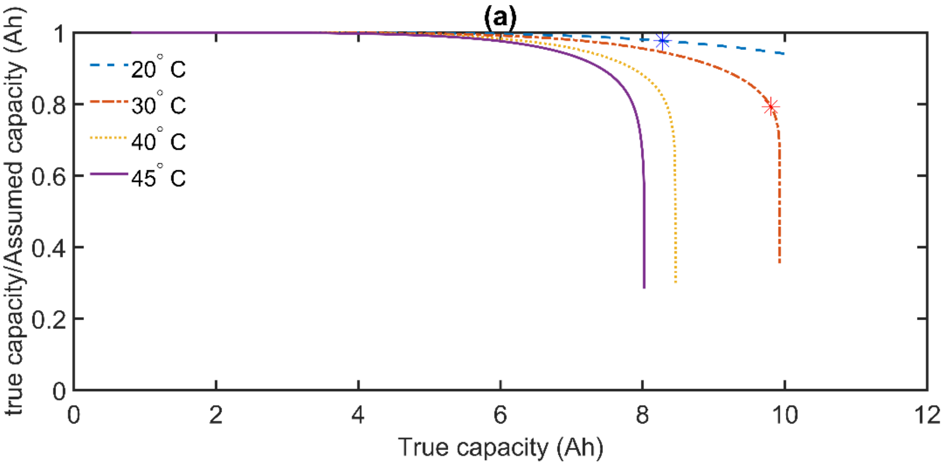

*Figure 29 Model predictions for the ratio between true capacity, corresponding to the useful charge, and the total charge throughput for a) constant current charge at 0.1 C under various ambient temperatures, as noted in the legend*

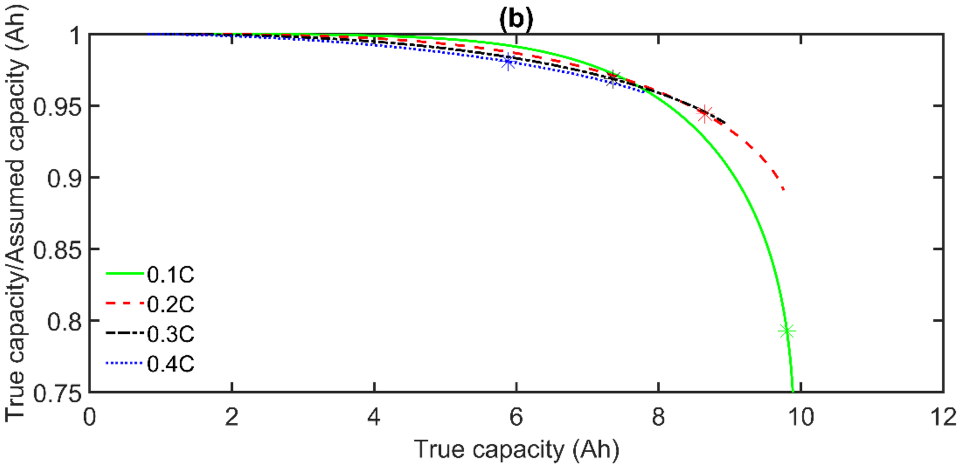

*Figure 30 Model predictions for the ratio between true capacity, corresponding to the useful charge, and the total charge throughput for b) constant current charge at various currents, as noted in the legend, under constant ambient temperature of 30 ℃. The circle symbols denote the location of the finite DTV peak. At 40 ℃ and 45 ℃ no such peaks are present.*

## 3.7. Supplementary data

The various experimental data are plotted in this section, as a supplementary material to this chapter, as a data reference.

### 3.7.1. Voltage and temperature experimental data

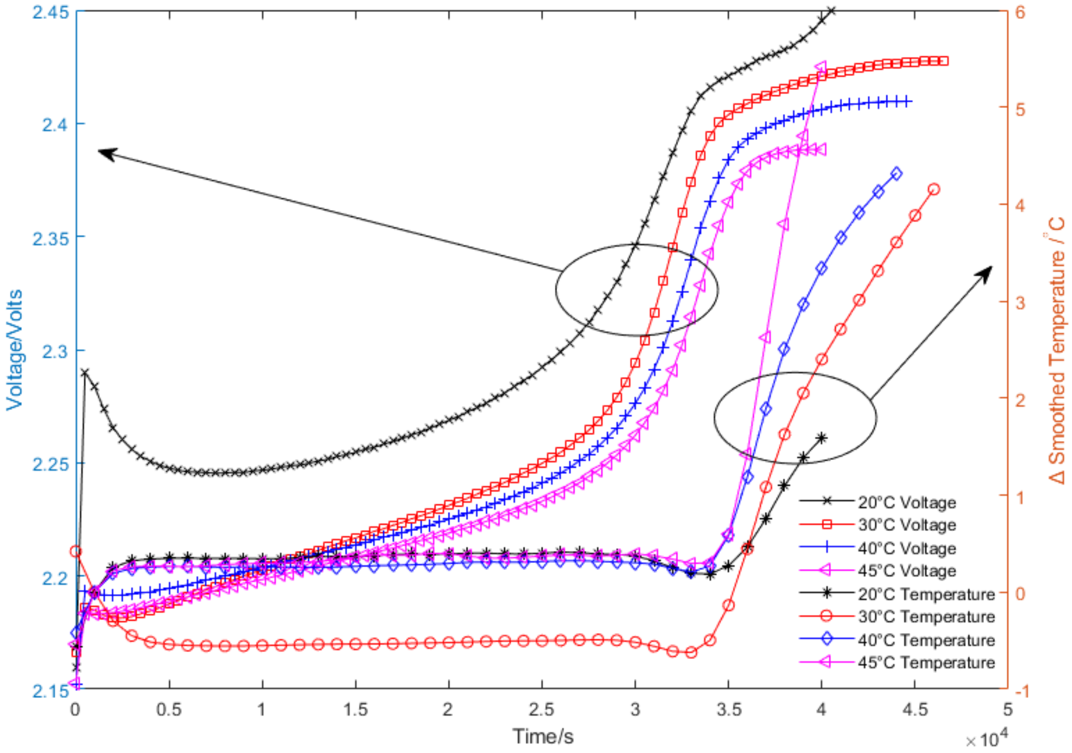

*Figure 31 The corresponding voltage and temperature plots during constant current charge (1A 0.1C) under different ambient temperatures (see legend). (a) The voltage curves show the trend of entering flat shuttle region in high voltage plateau for higher ambient temperature is sooner than lower ambient temperatures. (b) The ambient temperature curves show the temperature increase trend in higher ambient are quicker and larger that lower temperatures. Line symbols correspond to 1 in 300 measurements collected, to improve visibility. This figure corresponding to Figure 24.a.*

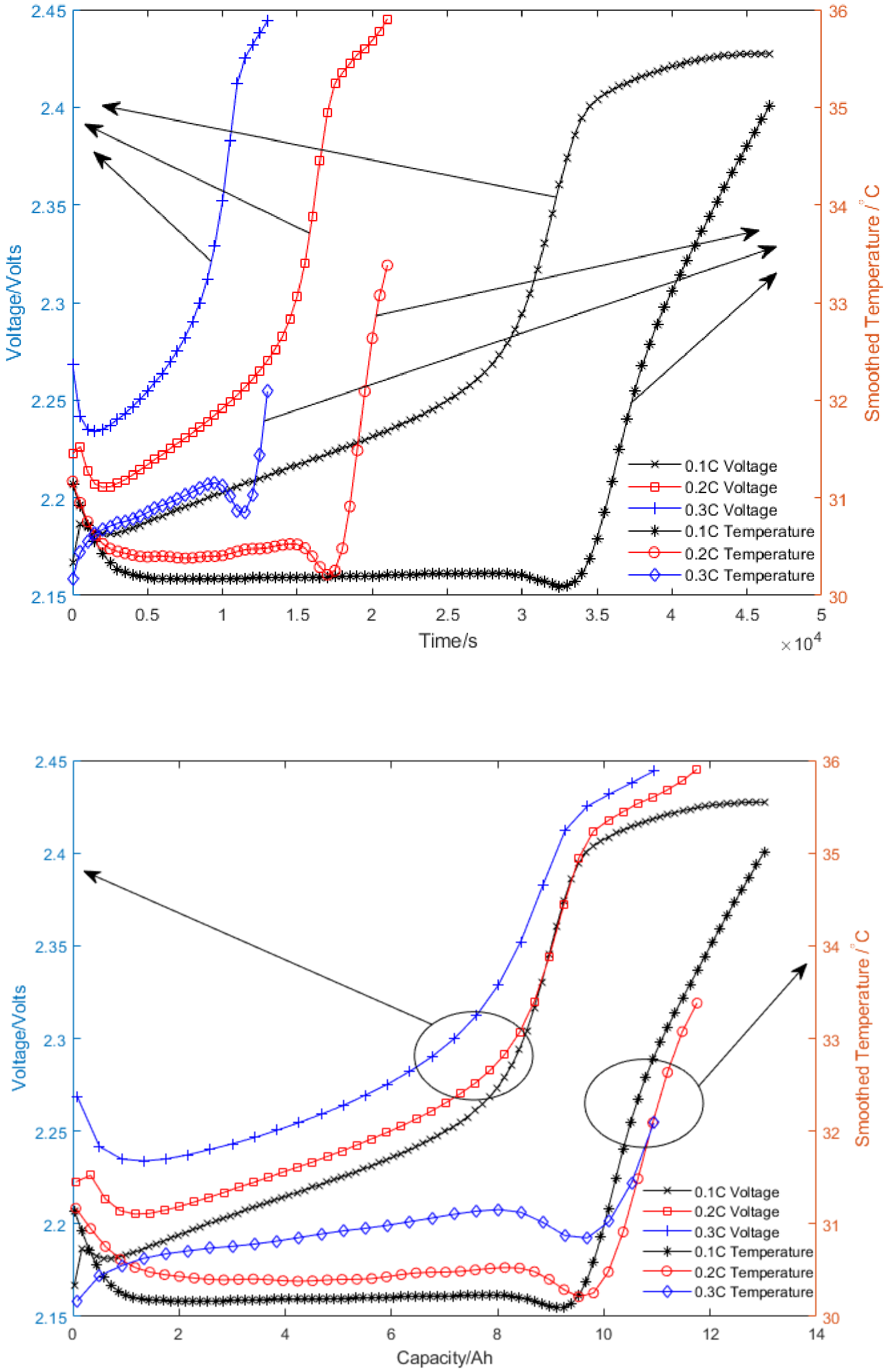

*Figure 32 The corresponding voltage and temperature plots during constant ambient temperature (30 ℃) with different constant current charge (1A (0.1C), 2A (0.2C), 3A (0.3C)). (a)The voltage curves show the trend of entering flat shuttle region in high voltage plateau for lower constant current charging rate is sooner than higher constant current rate. (b) The*

*ambient temperature curves show the temperature increase trend in lower constant current charging rate are quicker and larger than higher constant current rate. Line symbols correspond to 1 in 300 measurements collected, to improve visibility. This figure corresponding to Figure 24.a. and the 2 sub-figures show same group of date but plot against (1) time in second and (2) charge throughput (capacity) in Ah.*

### 3.7.2. 40 °C DTV data: voltage and temperature experimental data

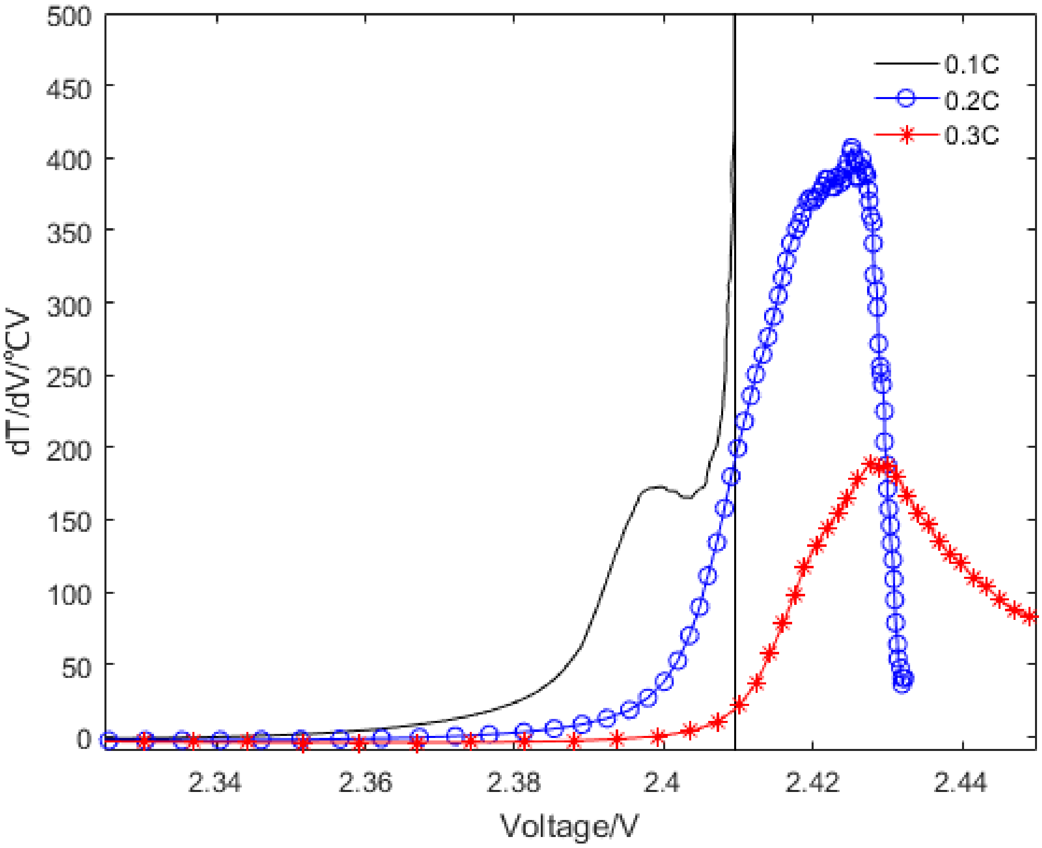

*Figure 33 The peaks of DTV measurements during constant current charge demonstrate voltage shift and pattern/shape/height change under different charging rate: 10Ah cell at 40 ℃ with 1A (0.1C), 2A (0.2C), 3A (0.3C) with 2.45 V voltage cur-off. DTV peak shifts to smaller voltage position, increases peak magnitude when charging rate drops. Line symbols correspond to 1 in 300 measurements collected, to improve visibility.*

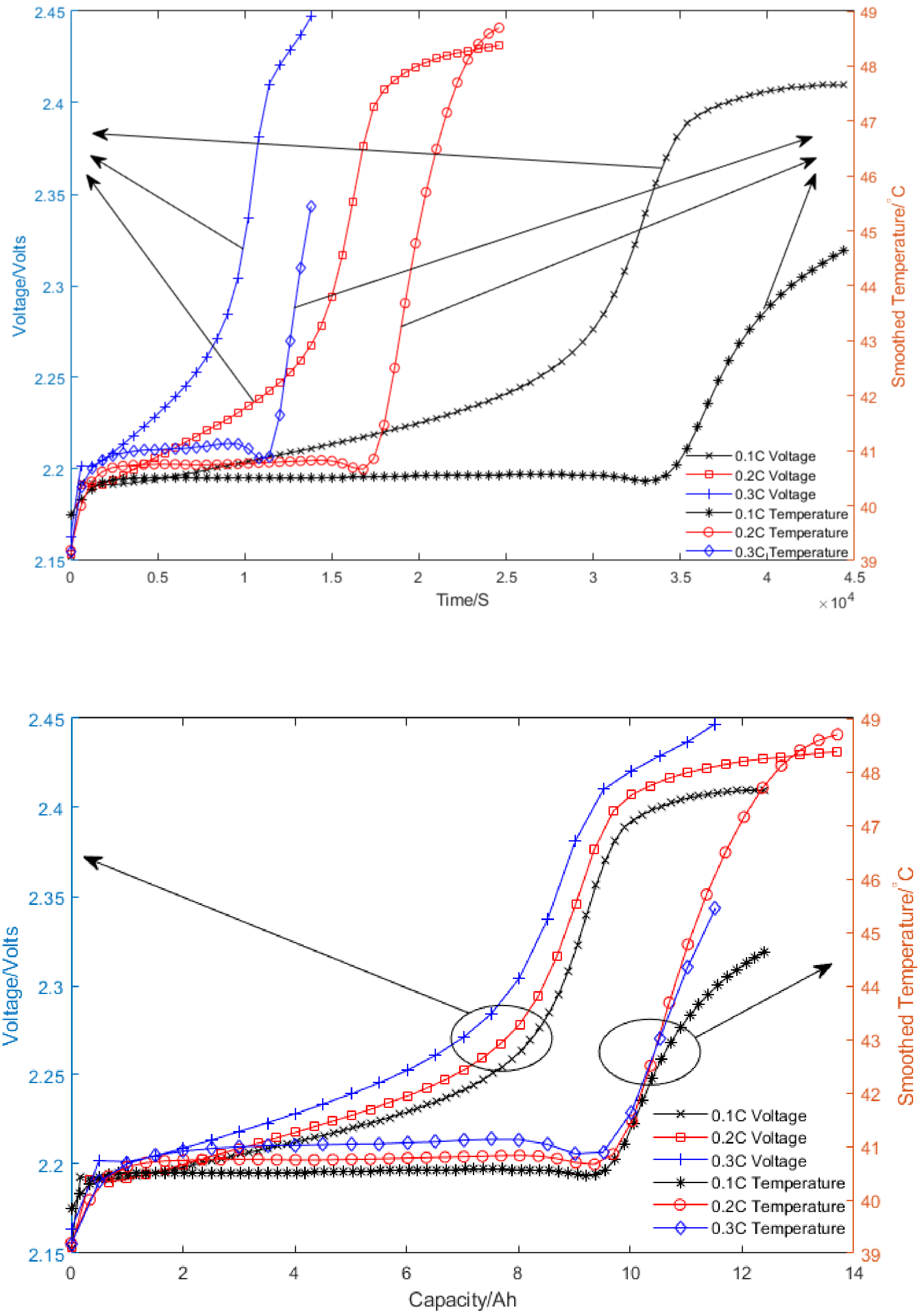

*Figure 34 The corresponding voltage and temperature plots during constant ambient temperature (40 ℃) with different constant current charge (1A (0.1C), 2A (0.2C), 3A (0.3C)). (a)The voltage curves show the trend of entering flat shuttle region in high voltage plateau for lower constant current charging rate is sooner than higher constant current charging rate. (b) The ambient temperature curves show the temperature increase trend in lower constant*

*current charging rate are quicker and larger than higher constant current rate. One special case is the 0.1C (1A) charge, which shows lower temperature increase with slower increase rate than higher charging rate (0.2C -2A & 0.3C -3A). Line symbols correspond to 1 in 300 measurements collected, to improve visibility. This figure corresponding to Figure 25. and the 2 sub-figures show same group of date but plot against (1) time in second and (2) charge throughput (capacity) in Ah.*

## 3.8. Modelling supplementary material

The modelling parameters are presented in this section, as a supplementary material to this chapter.

### *Nomenclature*

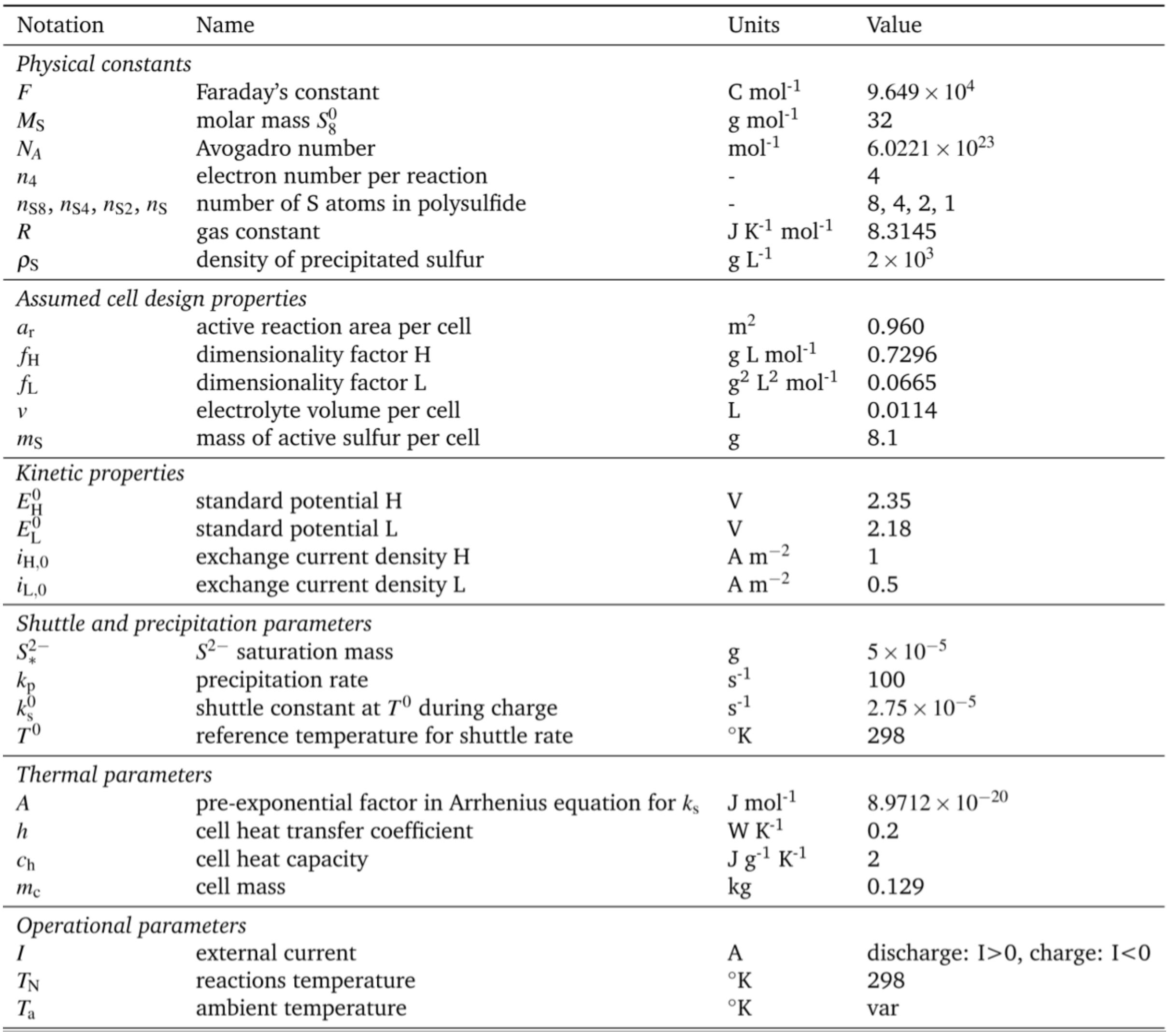

| Notation | Name | Units | Value |
|---|---|---|---|
| *Physical constants* | | | |
| $F$ | Faraday's constant | C mol$^{-1}$ | $9.649 \times 10^4$ |
| $M_S$ | molar mass $S_8^0$ | g mol$^{-1}$ | 32 |
| $N_A$ | Avogadro number | mol$^{-1}$ | $6.0221 \times 10^{23}$ |
| $n_4$ | electron number per reaction | - | 4 |
| $n_{S8}$, $n_{S4}$, $n_{S2}$, $n_S$ | number of S atoms in polysulfide | - | 8, 4, 2, 1 |
| $R$ | gas constant | J K$^{-1}$ mol$^{-1}$ | 8.3145 |
| $\rho_S$ | density of precipitated sulfur | g L$^{-1}$ | $2 \times 10^3$ |
| *Assumed cell design properties* | | | |
| $a_r$ | active reaction area per cell | m$^2$ | 0.960 |
| $f_H$ | dimensionality factor H | g L mol$^{-1}$ | 0.7296 |
| $f_L$ | dimensionality factor L | g$^2$ L$^2$ mol$^{-1}$ | 0.0665 |
| $v$ | electrolyte volume per cell | L | 0.0114 |
| $m_S$ | mass of active sulfur per cell | g | 8.1 |
| *Kinetic properties* | | | |
| $E_H^0$ | standard potential H | V | 2.35 |
| $E_L^0$ | standard potential L | V | 2.18 |
| $i_{H,0}$ | exchange current density H | A m$^{-2}$ | 1 |
| $i_{L,0}$ | exchange current density L | A m$^{-2}$ | 0.5 |
| *Shuttle and precipitation parameters* | | | |
| $S_*^{2-}$ | $S^{2-}$ saturation mass | g | $5 \times 10^{-5}$ |
| $k_p$ | precipitation rate | s$^{-1}$ | 100 |
| $k_s^0$ | shuttle constant at $T^0$ during charge | s$^{-1}$ | $2.75 \times 10^{-5}$ |
| $T^0$ | reference temperature for shuttle rate | °K | 298 |
| *Thermal parameters* | | | |
| $A$ | pre-exponential factor in Arrhenius equation for $k_s$ | J mol$^{-1}$ | $8.9712 \times 10^{-20}$ |
| $h$ | cell heat transfer coefficient | W K$^{-1}$ | 0.2 |
| $c_h$ | cell heat capacity | J g$^{-1}$ K$^{-1}$ | 2 |
| $m_c$ | cell mass | kg | 0.129 |
| *Operational parameters* | | | |
| $I$ | external current | A | discharge: I>0, charge: I<0 |
| $T_N$ | reactions temperature | °K | 298 |
| $T_a$ | ambient temperature | °K | var |

*Table 2 Values of zero dimensional model parameters*

Most parameters are chosen as in[3]. The value of $k_0$ s was chosen to obtain the transition between overcharge protection and ability to fully charge at the same value of current as in experiments, at the reference ambient temperature of 298 K. The value of $h$ can be experimentally calculated. Here, it is chosen to yield a similar magnitude for the DTV peak as seen in the experimental data.

## 3.9. Interim conclusion

In this chapter, the thesis has presented DTV as a fast, cost-effective and straightforward technique which is able to track and quantify the polysulfide shuttle effect of Li-S batteries during charge. DTV peaks correspond to instances of rapid cell temperature increase vs relatively constant voltage. Experimental data shows a strong dependence of the DTV peaks pattern and height on the ambient temperature and the magnitude of charging current. A zero-dimensional model with temperature-dependent shuttle constant and heat generation through shuttle was successfully used to interpret most of the observed features in the experimental data. It is concluded that the amount of shuttle current is strongly dependent on temperature and charging current, as it is directly correlated to the size of the DTV peak.

The polysulfide shuttle effect of Li-S is considerably stronger at higher ambient temperatures or low charging currents, corresponding to higher DTV peaks. It is suggested that the peak characteristics could be used as an adaptive safety cut-off criterion and/or to design advanced control algorithms to minimise degradation and maximise coulombic efficiency.

In the model, the true capacity of the cell is directly accessed by tracking the different polysulfide species. By plotting the true capacity and DTV peak positions together, it is shown that stopping charging at the DTV peak position alone is not sufficient to achieve a set charging coulombic efficiency. Therefore, a reduced order model, such as one based on the thermally coupled zero-dimensional model developed here, is recommended for implementation alongside the DTV diagnostic technique in the real-world applications.

# 4. Novel Equivalent circuit model parameterisation method for Li-ion batteries

## 4.1. Introduction

Chapter 4 is based on the journal publication by Xiao Hua, Cheng Zhang, Gregory Offer. '*Finding a better fit for lithium ion batteries: a simple, novel, load dependent, modified equivalent circuit model and parameterization method* 'under review in *Journal of Power Sources.* As described in detail in section 1.4 in the Chapter 1.

In the literature review chapter 2, the advantages and drawbacks of ECM have been expressed. In this chapter, the reasons for the choice of ECM as well as a novel ECM parameterisation method are presented for a Lithium iron phosphate (LFP) battery. The parameterization process proposed in this chapter serves as a critical role for the later discretised ECM modelling in chapter 5, as the developed model captures the SoC, temperature and load dependences, which fulfils the requirements for both thermal/load dynamic operating conditions.

As discussed, Equivalent circuit models (ECM) of lithium ion batteries are used in many applications because of their ease of implementation and low complexity. The accuracy of an ECM is critical to the functionality and usefulness of the battery management system (BMS). The ECM accuracy depends on the parametrization method, and therefore different experimental techniques and model parameter identification methods (PIM) have been widely studied. Yet, how to account for significant changes in time constants between operation under load and during relaxation has not been resolved.

In this chapter, a novel PIM and modified ECM is presented that increases accuracy by 77.4% during drive cycle validation and 87.6% during constant current load validation for a large format lithium iron phosphate prismatic cell. The modified ECM uses switching RC network values for the different load phases (underload & relaxation), these differences are significant for this cell and also at low state-of-charge for all lithium ion batteries. Different characterisation tests and the corresponding experimental data have been trained together across a complete State-of-Charge (SoC) and temperature range, which enables a smooth transition between identified parameters. Ultimately, the model created using parameters captured by the proposed PIM shows an improved model accuracy in comparison with conventional PIM techniques.

Therefore, this chapter answers the following research questions:

1. ***Could the conventional ECM parameterisation method fulfil the ECM parameters need for a large format lithium ion battery?***
2. ***If not, what changes are required to maintain certain model accuracy?***
3. ***Will the load dependent parameter identification method deliver better model accuracy for equivalent circuit model?***

## 4.2. Backgrounds

While researching and developing lithium-ion batteries, the usage of a robust battery model is pivotal at the application level. Models enable the battery management system (BMS) to improve battery performance and prolong lifetime. [187] There are predominantly 2 types of models in the literature, which are physics-based models and equivalent circuit models (ECM). The physics-based models capture the physical behaviours through solving equations such as lithium diffusion equations and charge conservation equations. Newman, Doyle, Fuller et al established the foundations for these physics-based model. [145,146,188] The main two drawbacks of physics-based models for BMS applications are 1. High complexity of parameterisation; 2. High computational power. There are more than 30 parameters needed to be fitted and parameterised including salt concentration, electrode/separator thickness, conductivity of electrolyte etc. [107,147–152]. Quite often the parameters in the physics-based model require ex-situ experimental measurements which are time/cost inefficient. [153,154] Also, the computational speed is another disadvantage of this type of models. Further, it is challenging to scale such model into multi-dimensional or pack level analysis. [108,151,155] Although these drawbacks can be mitigated through reduced order models (ROMs) ECMs are still the model of choice for many applications.

ECMs describe the battery terminal voltage-current dynamics using passive electrical components (resistors and capacitors) and measured/parameterised look-up tables or simple mathematical functions. The ease of implementation and low model complexity make ECM feasible in real-time applications such as integrated BMS systems, and they are regularly embedded in microprocessors and deliver precise simulation/feedback signals in real-time.[189]. The reader is referred to recent reviews by He et al. [190] and Hu et al.[191] on ECM models. Figure 35 shows a typical ECM which consists of the battery open circuit voltage (OCV) and a series ohmic resistor $R_0$ and several resistor-capacitor (RC) networks

[135]. The battery OCV can be measured directly from experimental data using low-rate constant current (CC) (dis)charge (giving a pseudo-OCV), or using a pulsed current (dis)charge with long rest periods between pulses (true OCV) [192]. The RC values, on the other hand, need to be identified by fitting the model's voltage prediction under current load to measurements using optimisation algorithms [128,136]. This represents the model parametrization procedure.

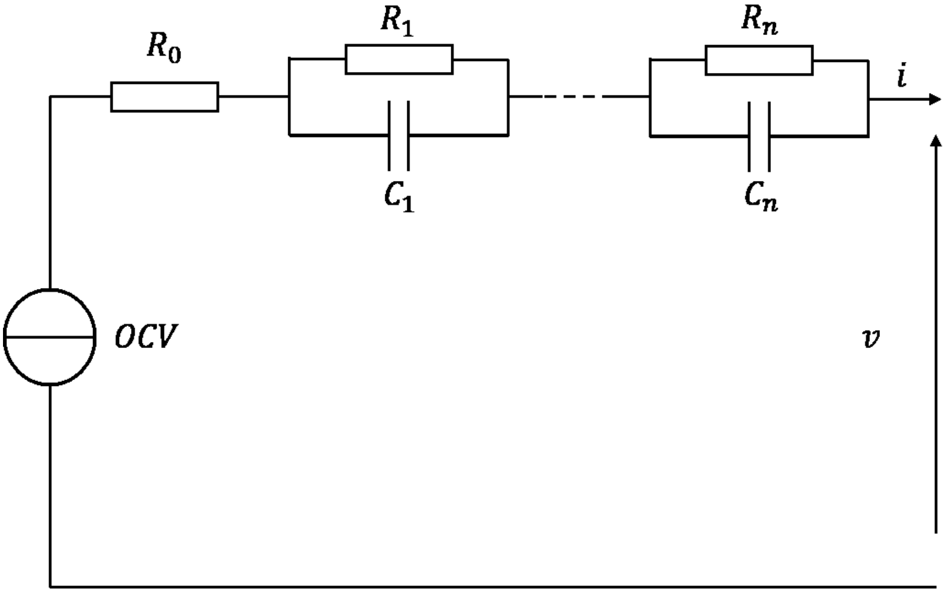

*Figure 35 Battery equivalent circuit model with n RC networks*

The parameter identification method (PIM) is critical for the ECM model accuracy. The model accuracy is correlated with what and how PIM is used for the certain Li-ion battery. There are various PIMs for ECM parametrization in the literature, including genetic algorithm (GA) [113,114], particle swarm optimization (PSO) algorithm [115–117], and the least-squares method [113,118]. A recent study conducted by Lai et al [112] compared 9 different popular PIMs for 9 different ECM models in the entire SoC area and demonstrated the importance of the PIM to the model accuracy.

The ECM parameters depend on the operating conditions. The popular methods for capturing this parameter dependency include offline parameterized look-up tables [125–128] and the online adaptive parameter estimation algorithms such as recursive least squares methods and the dual Kalman filter algorithms [133–136]. Existing PIMs mainly focus on capturing the parameter dependence on the SoC, temperature and current directions. However, another important dependency factor for ECM parameters that is generally overlooked is the type of current loads. Different current profiles have been used for ECM parameter estimation, such as the pulsed current test [126,127,139,140], drive cycles [137,141] and constant-current charging and discharging [131,142,143]. However, few works have considered the effect of choosing different current profiles on the identified parameters and the model accuracy [137,141]. The battery is an electrochemical system with complex internal dynamics, and ECM is an approximate reduced-order model. Therefore, different current excitations will reveal different system properties. As a result, the ECM parameters will vary under different load conditions [193]. There is one key difference in the current load that the studies in the literature were missing, which is the difference in the underload and the relaxation. Generally the model parameters were identified without distinguishing the two different working conditions and the underload and relaxation test data are used together for ECM parametrization [126,140]. However, the test data analysis on the chosen cell in this chapter shows that the battery performs distinctly differently during underload and relaxation, in terms of the scale of magnitude of time constants of the RC networks. It shows that using the same parameter set cannot capture both the underload and the relaxation dynamics accurately. Therefore, this chapter proposes a parameter switching scheme between underload and relaxation working conditions to address this problem.

Further, this chapter delivers a novel PIM that captures ECM parameter dependence on load switching, SoC (0-100%) and temperatures ($10°C$, $20°C$, $30°C$ and $40°C$). The novelty of the proposed PIM is that the time constants of the RC networks are independent from SoC and temperature. The rest parameters, i.e., the resistor values, then become linear-in-the-variable which can be readily obtained using computationally efficient least squares optimization solvers. This also enables the simultaneous estimation of all the resistor values under all SoC and temperatures levels with parameter constraints to ensure a smooth transition between different temperature levels. In theory, the battery internal resistance is reversely proportional with the operating temperature. However, in the conventional way of parameter identification, the resistance values might zig-zag across a range of temperatures without using parameter constrains [128]. The ultimate purpose of this novelty is to provide a temperature dependent ECN model e.g. [108], in many BMS and modelling applications, which is critical for the model accuracy. This proposed PIM shows a better fit for large current/large power/large heat generation applications. Unlike smaller cells, large format cells have significant heat generation challenges, therefore training the data the operating temperature window is important and inevitable.

## 4.3. ECM Equations

For the battery ECM depicted in figure 35, $v,\ i$ represent the battery terminal voltage and current, respectively. Denote $n_{rc}$ as the number of RC networks and define $v_j,\ i_j, j = 1,2,\ldots,n_{rc}$ as the voltage and current through $R_j$. Then, $v_j = R_j i_j$ . Let $\tau_j = R_j C_j$ be the time constant. Then

$$i_j(k+1) = a_j i_j(k) + (1 - a_j) i(k), \quad j = 1,2,\ldots,n_{rc} \tag{1}$$

where

$$a_j = exp(-T_s/\tau_j)$$

$i_j(k)$ stands for $i_j$ at the k-th sampling time, and $T_s$ is the sampling interval (s).

The battery SoC is obtained using the widely employed coulomb counting method [126,128],

$$SoC(k+1) = SoC(k) + \frac{T_s}{3600C_n} i(k) \tag{2}$$

where $C_n$ is the battery nominal capacity at 25°$C$ (unit: Ampere-hour). Next, the battery terminal voltage can be expressed as,

$$v(k) = OCV(k) + R_0 i(k) + \sum_{j=1}^{n_{rc}} R_j i_j(\mathrm{k}) \tag{3}$$

## 4.4. Experimental details

This section introduces the detailed experimental procedure of the battery characterisation, and the test data are used for identifying the OCV, $R_0$ and RC values. The data sampling rate is 1Hz under current load and during relaxation periods. The OCV hysteresis effect is not considered in this chapter, therefore only experimental data for discharge current was used for parameter training and validation. The OCV hysteresis is a battery behaves to the existence of seral possible thermodynamic equilibrium potentials at the same SoC. (a.k.a. OCV hysteresis) [192] In literature, it is found that positive electrodes with lithium iron phosphate as the active material are known to exhibit a hysteretic phenomenon. [192,194]

The experimental technique DTV mentioned in Chapter 3 is able to be applied onto charging process of the LFP batteries [46]. Similarly, the CCC technique can also be applied onto charging process of the LFP batteries, as detailed in Chapter 5. The parameterisation technique in this chapter is also applicable to charging, for a more comprehensive boundary conditions if OCV hysteresis is considered during real-time operations. (E.g. industrial EV data processing and algorithm implementation). However, is out of the scope for this thesis.

The battery is always charged using the same constant current constant voltage (CC-CV) test procedure to make sure the initial SoC of the battery is consistent between tests. The CC current is 1C (90A) and the CV voltage is 3.65V. The cut-off charging current of CV procedure is C/50 (1.8A). The cut-off voltage during discharge procedure is 2.5V.

A range of pulse discharge characterisation tests, on a high capacity 90Ah Lithium iron phosphate (LFP) cathode based, graphite anode battery with aluminium/prismatic shell (200.5 x 130.3 x 36.5 mm) were examined under various temperatures. Before characterisation tests were carried out, the cell underwent five 1C (90A) charge/discharge cycles for pre-conditioning and demonstrated stabilised capacity. After the pulse discharge characterisation tests, a range of validation tests were examined, including drive cycle discharge with noisy current load at $20°C$ and constant current discharge under various temperatures. The cell was evenly wrapped with nitrite rubber insulation material (RS Pro, thickness 25 mm, thermal conductivity 0.034 W/mK) across entire cell surface, as shown in the figure 36. The cell was placed in the centre of the bottom shelf of a thermal chamber (Binder, model KB23).

The thermal boundary condition has been designed in this format to approach a near 'adiabatic condition' by minimizing convection in the thermal chamber, this is done to minimize the internal thermal gradient of the cell being tested and to avoid the problems this can cause as described by Zhao et al.[108] The same thermal boundary condition was implemented in the model. K-type thermocouple was placed and taped with Kapton® polyimide films tape on the centre of the prismatic aluminium shell surface (200.5 x 130.3 mm) to measure surface temperature, as marked in figure 36. A single channel battery cycling system (BioLogic, HCP-1005) was used for charging/discharging the cell. One set of characterisation pulse discharge tests, one validation noisy load drive cycle test and one set of constant current discharge tests were carried out in this study, as detailed below.

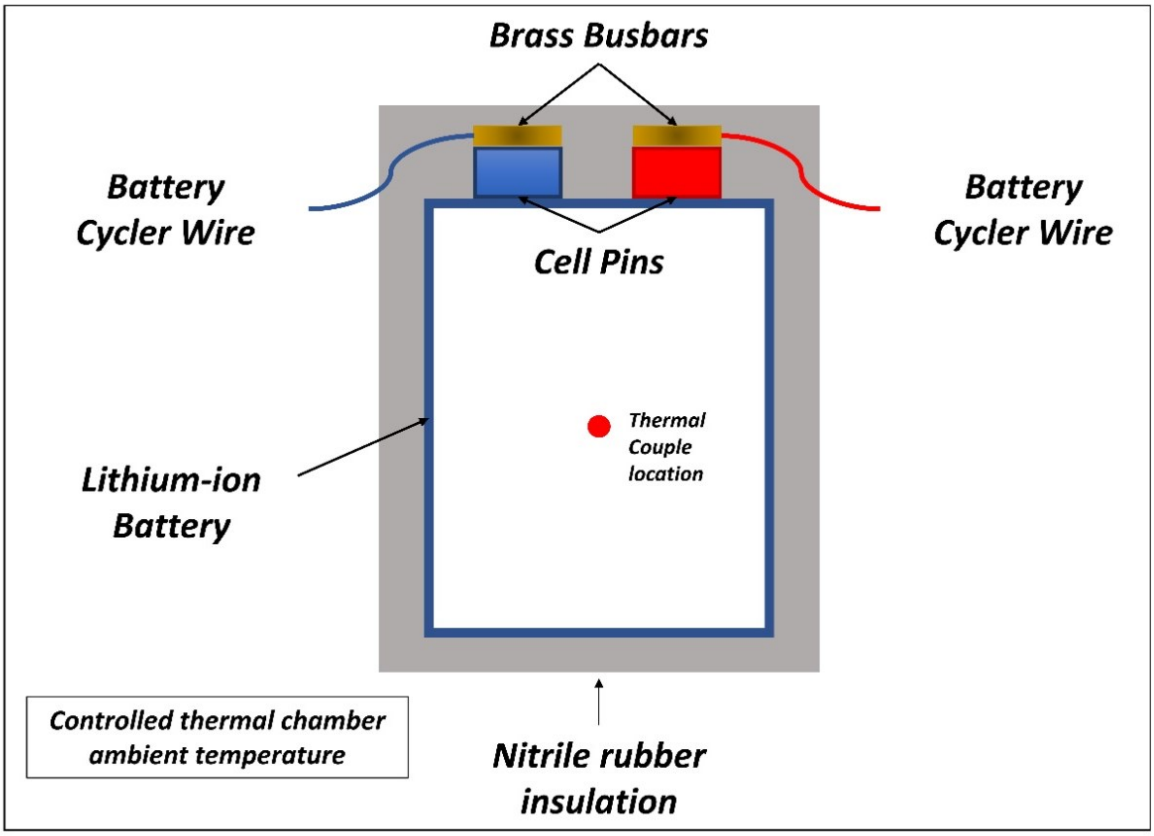

*Figure 36 Battery testing rig demonstration*

### 4.4.1. Experiment #1: variable ambient temperature characterisation pulse discharge tests

Characterisation pulse discharge (PD) tests were carried out to generate data for the PIMs in this work. The measurement involves repetitions of a constant current discharge pulse at 1C (90A) followed by a resting period of 2 hours. This process starts from 100% SoC and finished at 0% SoC. The SoC breakpoints step length is 1% (9Ah) for 0% -10%, 90% - 100% SoC, and 5% (4.5Ah) for 10% - 90%. The current input and the corresponding voltage response are shown in figure 37. Also, in figure 37(d), the cell surface centre temperature is presented, where a maximum temperature difference at different SoC is about 0.5 °C. The measurements were repeated for a range of temperatures ($10°C$, $20°C$, $30°C$ and $40°C$). Here, Figure 37 only shows data at $20°C$ as an example, and all the other data can be found in supplementary data section, which is at the end of this chapter.

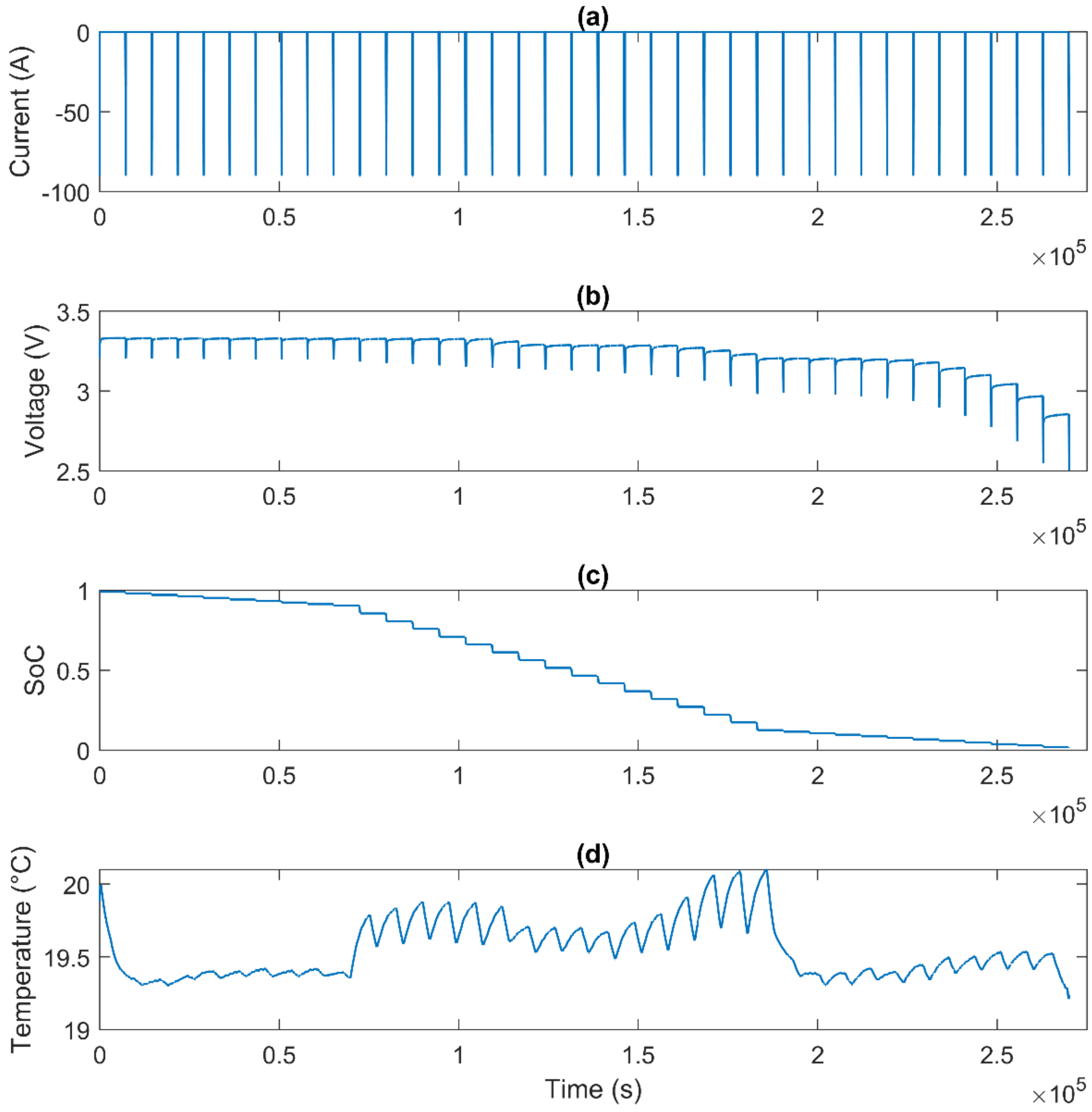

*Figure 37 Test data for the pulse discharge experiment at 20°C thermal chamber ambient temperature: (a) Input current, (b) Terminal voltage, (c) SoC profile, (d) Measured surface temperature.*

### 4.4.2. Experiment #2: validation noisy load drive cycle discharge test

The model and the parameters are validated using independent sets of experiment data. The first one is the bespoke designed noisy load discharge which based on the US06 drive cycle current profile with enlarged average current value and extended test time. The Figure 38 demonstrates the current profile examined, the voltage and cell surface temperature responses respectively.

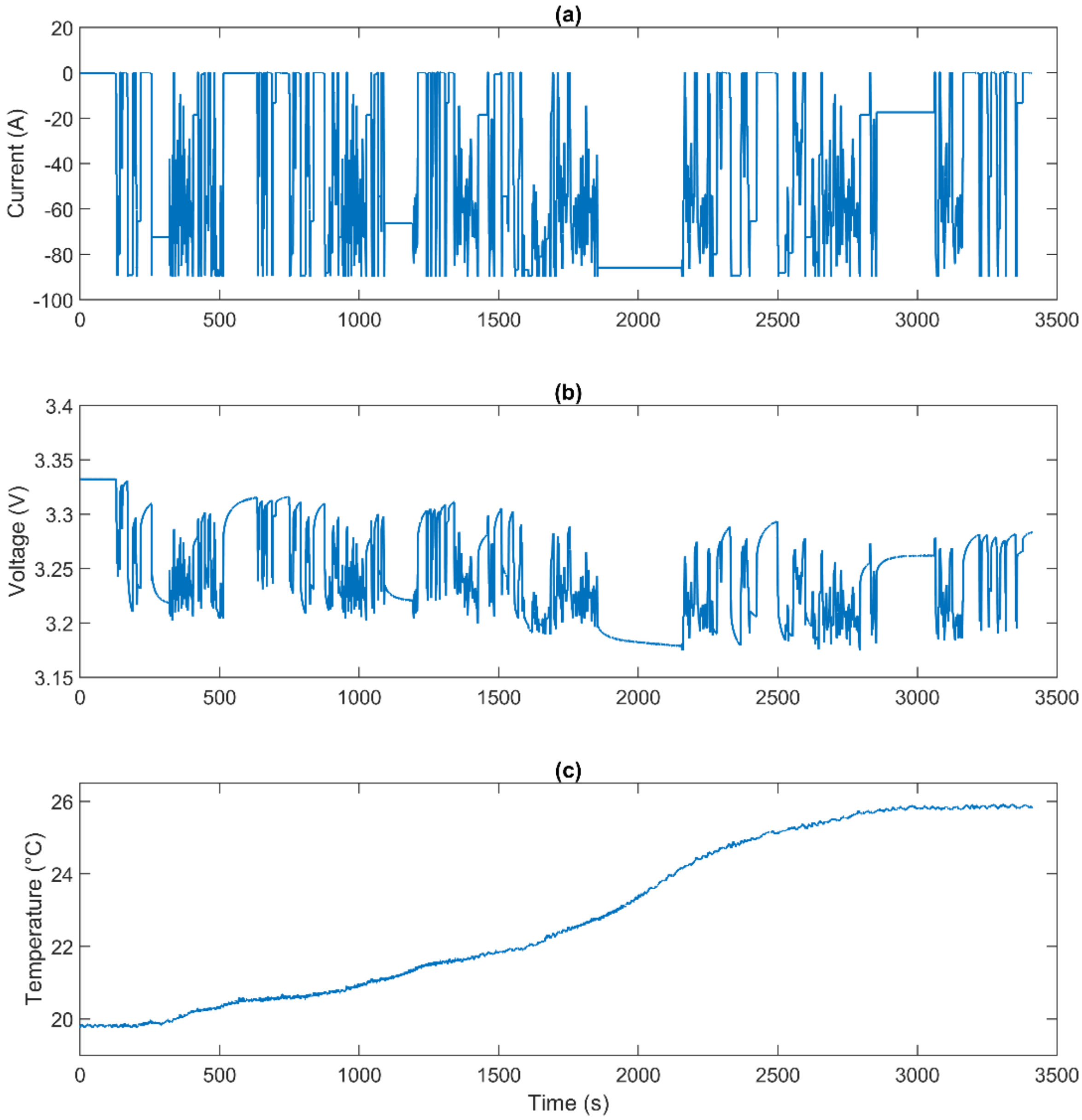

*Figure 38 Test data for the discharge drive cycle experiment at 20°C thermal chamber ambient temperature: (a) Input Current, (b) Terminal voltage, (C) Cell centre surface temperature.*

### 4.4.3. Experiment #3: variable ambient temperature validation constant current discharge tests

The second set of validation experiments are constant current discharge tests. The measurement involves a constant current discharge at 1C (90A). This process starts from 100% SoC and finished when the voltage reaches 2.5V. The current input and the corresponding voltage and cell surface temperature responses are shown in Figure 39. The measurements were repeated for a range of temperatures ($10°C$, $20°C$, $30°C$ and $40°C$). Here, the Figure 39 only shows $20°C$ as an example, and all the other data can be found in supplementary data section.

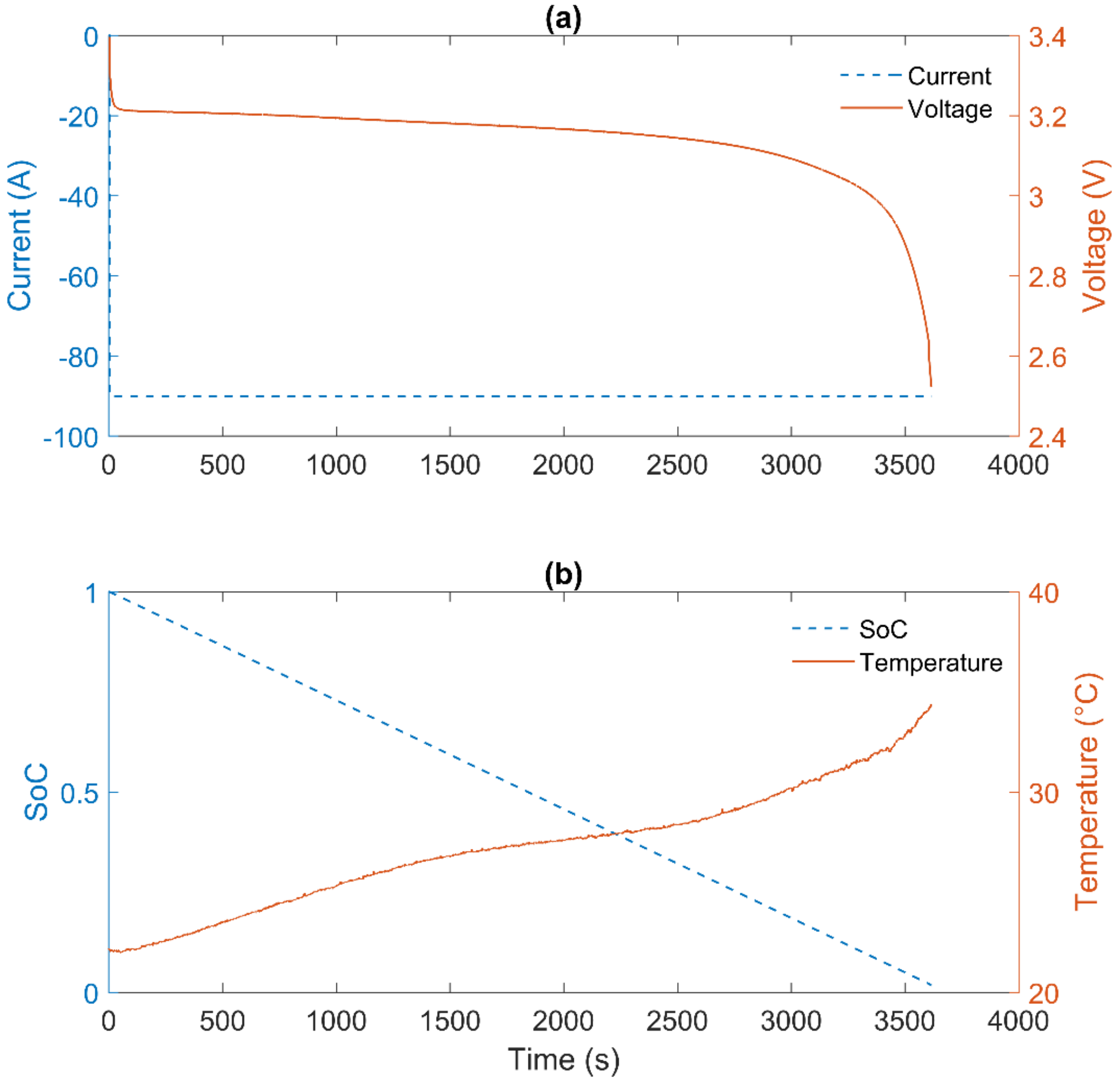

*Figure 39 Test data for the constant current discharge experiment at $20°C$ thermal chamber ambient temperature: (a) Input current & terminal voltage, (b) Cell centre surface temperature & SoC profile.*

## 4.5. Data analysis and ECM parameter estimation

### 4.5.1. Open circuit voltage measurement

The battery OCV is captured by the pulse discharge test followed by 2 hours rest. The test data is shown in figure 37. The battery OCV between the SoC breakpoints is calculated with the commonly used linear interpolation method [128][195]. Detailed OCV plots at various temperature are shown in the supplementary data section.

### 4.5.2. RC network characterisation

After collecting experimental data, it is essential to conduct a detailed data analysis to better understand the battery properties under study. A single pulse discharge data segment shown in figure 37 is used here for data analysis. The SoC value decreases from 50% to 45%. A detailed look is presented in the figure 40, which shows an underload period of 1C (90A) constant current discharge load for 180 seconds (5% SoC breakpoint step) followed by a 2-hour relaxation period.

Since both the SoC and temperature changes are small for this single pulse discharge, the model parameters are assumed to be constant. There are mature methods in the literature for selecting the number of RC networks, which for this study was chosen to be 3 following the procedure described in [126,140]. The ECM RC parameters, including the time constants in Eq (1) and the resistor values in Eq (3), are obtained following an optimization procedure to minimize the root mean square error (RMSE) between the model voltage output and the measurements. The Matlab function 'fminbnd' is used for the numerical optimization. This optimization involves only 6 parameters and is a standard procedure and therefore not detailed here.

The results give an indication that it is difficult to capture both the battery underload and relaxation voltage profiles accurately using a single parameter set. This is because large RC time constants are required to capture the 2-hour voltage relaxation, while only small RC time constants are required to capture the underload voltage profile. In this study, the LFP cell has a nominal capacity of 90Ah with a dimension of W200.5 x L130.3 x H36.5 mm. This large-size battery is an energy cell with thick electrodes. It is therefore hypothesized that the fast electrochemical reactions at the interface between the electrode and the electrolyte dominate the voltage response under load, while the slow diffusion dynamics inside the solid electrode particles dominate the voltage output during relaxation. Therefore, these two working conditions require RC time constants at different magnitudes. This data analysis process leads to the first novelty of this study, which captures the significant time constant difference between under load phase and relaxation phase using a parameter switching scheme, as follows,

$$\tau_j = \begin{cases} \tau_{j,u}, & if\ |i| > i_{th} \\ \tau_{j,r}, & if\ |i| \le i_{th} \end{cases}, j = 1,2,3 \tag{4}$$

where $\tau_{j,u}$ represents the underload time constant and $\tau_{j,r}$ the relaxation time constant. The current threshold value $i_{th} = 0.1A$ is used in this chapter. Note that there is no switching for the resistor values.

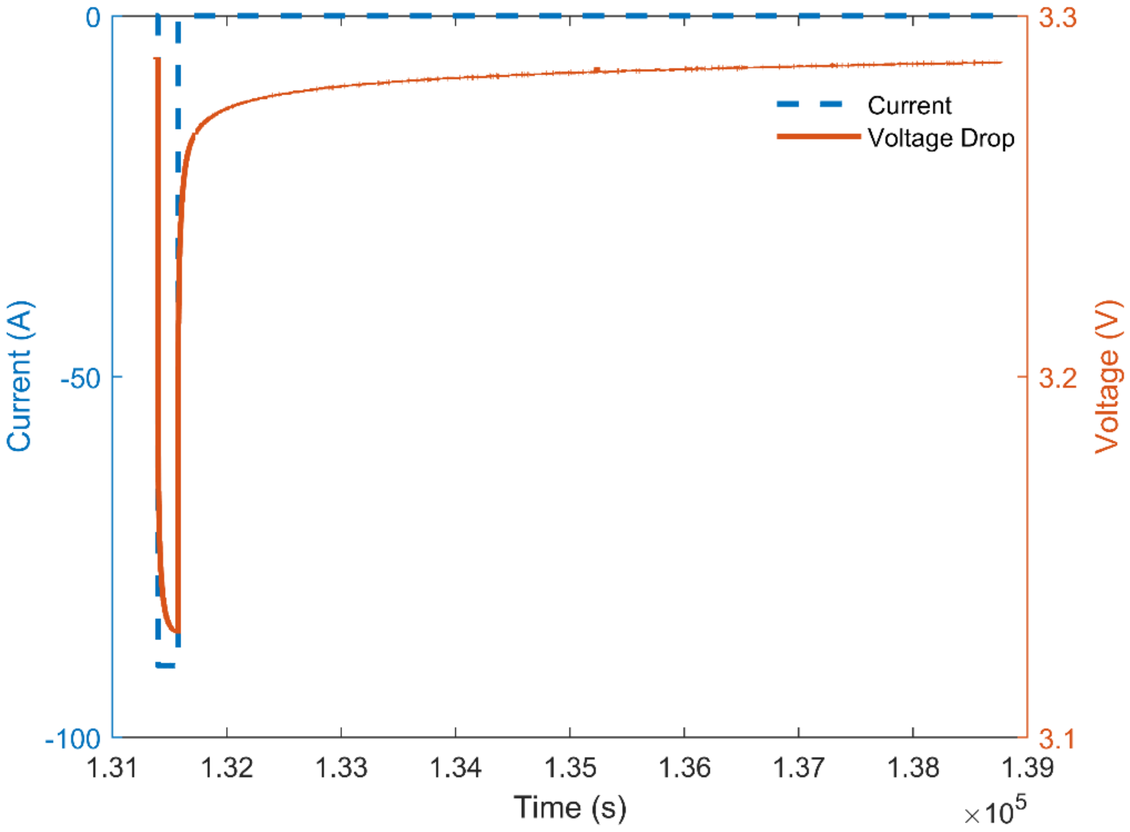

*Figure 40 Test data for the constant current discharge pulse experiment at 20°C thermal chamber ambient temperature, SoC starts at 50%, ends at 45%.*

To illustrate the comparison between the underload and relaxation dynamics, four parameter identification cases are compared. The first case uses only the underload data for parameter identification. The second case uses underload test data and 500-second relaxation period.

The third uses the underload with the full 2-hour relaxation data. The fourth case represents the proposed parameter switching scheme.

Table 4 introduces the time constants obtained in these four case studies, and the modelling results are given in figure 41 which compares the measured data with the simulation results. As it can be seen in Table 4, the time constants grow with the length of the relaxation period used for parameter identification. Using underload data alone for parameter identification in Case 1, the model can capture the underload dynamics with high accuracy. However, the model error during the relaxation period is high. This is because the maximum RC time constant is only 35.7s, which cannot reproduce a 2-hour voltage relaxation profile. The relaxation stage voltage profile can be better captured in Case 2 and 3, however, this comes at a cost of a larger underload modelling error. This can be clearly seen in figure 41(b), i.e., the zoomed segment at the end of the pulse discharge, where the model outputs of Case 2 and Case 3 produce an over-shoot error. It can be predicted that if the current pulse is longer, the underload modelling error will further increase. This is because, the three RC networks with high time constants ($\tau_3 = 2285.1s$) and large resistance values are needed in order to sustain the 2-hour voltage relaxation, which compromised the underload accuracy. This shows an apparent trade-off between the quality of fitting for underload region and the relaxation region, regardless of the length of the relaxation data being examined. The underload stage needs small RC time constants, while the relaxation stage needs long RC time constants. By using the proposed switching time constants in Eq (4), the results in Figure 7 (a)&(b) show good model accuracy for both underload and relaxation, which essentially solve this issue. It is noteworthy that not all lithium ion battery cells show such distinctive features between underload and relaxation stages across their full SOC range, but it is often observed at the extremes, particularly at low SOC when state estimation can be particularly important. Therefore, this study highlights the importance of considering the load dependency of the ECM parameters.

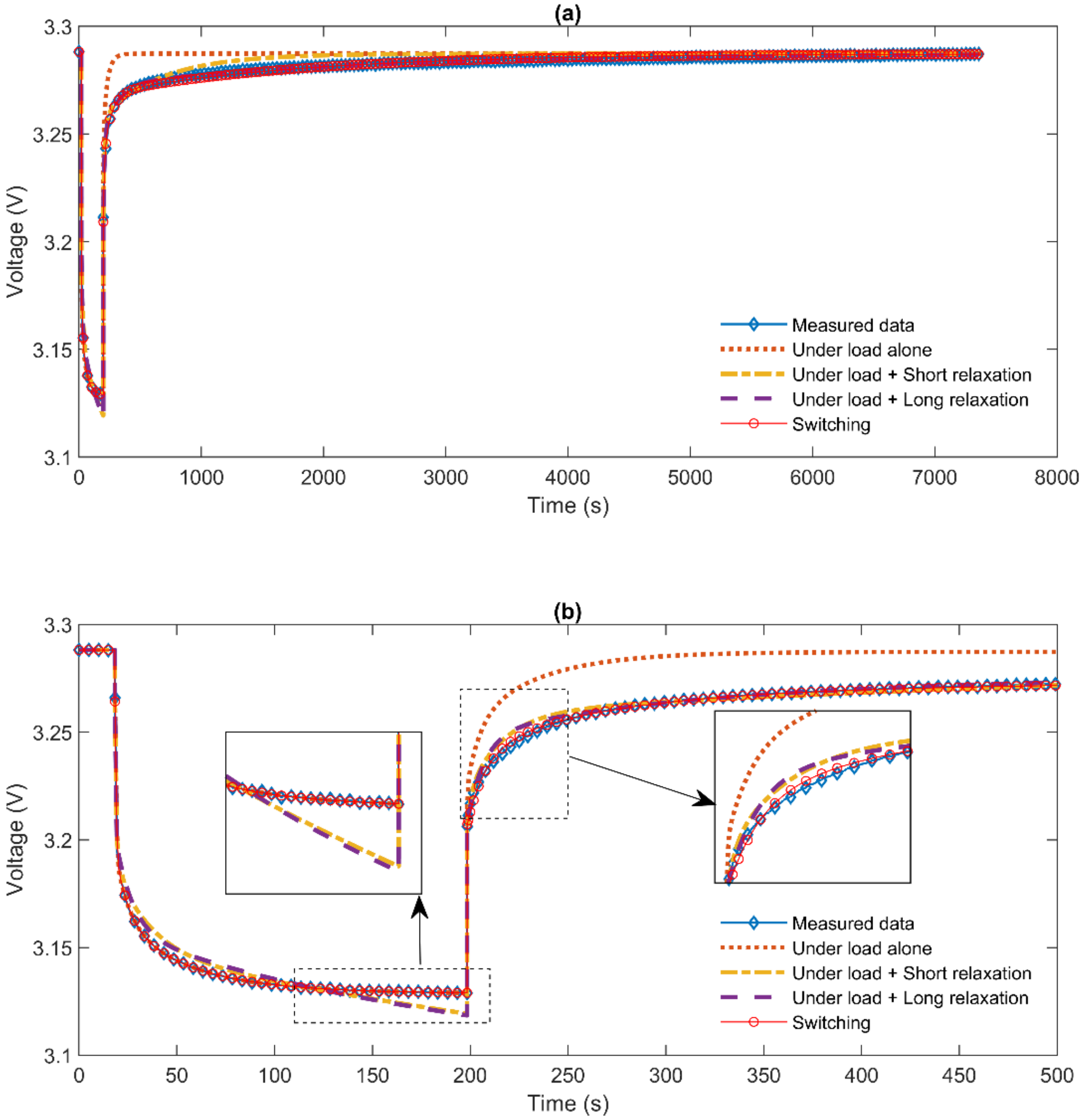

*Figure 41 Test data and simulation results for the constant current discharge pulse experiment at 20°C thermal chamber ambient temperature, SoC starts at 50%, ends at 45%. (a) Comparison between the measured data with simulation results using 1. Underload time constant 2. Underload + short relaxation (500 seconds) time constant 3. Underload + long relaxation (7200 seconds) time constant, (b) Zoomed look for (a).*

| Data Selected/ Tau No. | Time constant 1/s | Time constant 2/s | Time constant 3/s |
|---|---|---|---|
| Case 1: Underload alone | 0.21 | 6.4 | 35.7 |
| Case 2: Underload + 500s relaxation | 2.0 | 17.9 | 498.4 |
| Case 3: Underload + 7200s relaxation | 10.7 | 170.0 | 2285.1 |
| Case 4: Switching Taus | Underload: 0.2<br>Relaxation: 1653 | Underload: 6.4<br>Relaxation: 68.7 | Underload: 35.7<br>Relaxation: 9.3 |

*Table 3 Time constant used for the simulation results shown in Figure 41.*

### 4.5.3. ECM parameter identification

This section presents the full parameter identification procedure. The proposed method consists of two steps. The first step uses the underload test data to identify the underload RC time constants and the resistors values. The second step identifies the relaxation time constants using the relaxation region test data.

To reduce the complexity of the parameter optimization, the time constants of the RC networks are fixed throughout the entire SoC range and at various temperature levels. In this way, the resistor values become linear-in-the-variable parameters and can be solved using computationally efficient least squares tools. In literature, it is concluded by Hu et al. that the time constants of the RC networks can be considered as independent from SoC values. The benefit of this assumption is reducing the parameter identification complexity by finding the global minima of fewer parameters. The insensitivity of the variation of the capacitor values to the ECM-based SoC estimation accuracy further supports this assumption. [196] The RC time constants represent the time scale of interest for the voltage profile which can be considered independent from the working condition. The modelling results later show that this simplification doesn't lead to poor model accuracy.

#### *Step 1: identification of the underload time constants and resistors*

For a given set of the underload RC time constants, $\tau_{j,u}, j = 1,2,3$, the current passing through $R_j$ (i.e., $i_j$) can be calculated in Eq (1). Denote $i_0 = i$ to represent the current passing through $R_0$ (to be consistent with $i_j, j = 1,2,3$).

To capture the SoC dependency of the resistor values, the full SoC operating window is divided using breakpoints as follows,

$$0 < SoC_1 < SoC_2 < \cdots < SoC_{n_{soc}} < 100\% \tag{5}$$

where $n_{soc}$ is the number of SoC breakpoints. Next, define the triangle base function at each SoC breakpoint as follows,

$$f_1(SoC) = \begin{cases} 1, & if\ SoC < SoC_1 \\ \frac{SoC_2 - SoC}{SoC_2 - SoC_1}, & if\ SoC_1 \le SoC < SoC_2 \end{cases},$$

$$f_m(SoC) = \begin{cases} \frac{SoC - SoC_{m-1}}{SoC_m - SoC_{m-1}}, & if\ SoC_{m-1} \le SoC < SoC_m \\ \frac{SoC_{m+1} - SoC}{SoC_{m+1} - SoC_m}, & if\ SoC_m \le SoC < SoC_{m+1} \end{cases}, \quad \mathrm{m} = 2, \ldots, n_{soc} - 1 \tag{6}$$

$$f_{n_{soc}}(SoC) = \begin{cases} \frac{SoC - SoC_{n_{soc}-1}}{SoC_{n_{soc}} - SoC_{n_{soc}-1}}, & if\ SoC_{n_{soc}-1} \le SoC < SoC_{n_{soc}} \\ 1, & if\ SoC_{n_{soc}} \le SoC \end{cases}$$

The SoC dependency of the resistor values can now be expressed using linear interpolation as follows,

$$R_j = \sum_{m=1}^{n_{soc}} R_{j,m} f_m, \ \ j = 0,1,2,3 \tag{7}$$

Then from the terminal voltage in Eq (3), yielding,

$$v - OCV = \textstyle\sum_{j=0}^{n_{rc}} \left(\sum_{m=1}^{n_{soc}} R_{j,m} f_m\right) i_j \tag{8}$$

Here the time step indicator $(k)$ is dropped from the variables, e.g., $v(k)$. Denote $y = v - OCV$, and row vector $F = [f_1, f_2, \ldots, f_{n_{soc}}]$. Let row vector $p = [Fi_0, Fi_1, Fi_2, Fi_3]$ and $\theta = [R_{0,1}, R_{0,2}, \ldots, R_{0,n_{soc}}, \ldots, R_{3,1}, R_{3,2}, \ldots, R_{3,n_{soc}}]$ as the collection of all the resistor values. Eq (8) can then be reformulated as

$$y = p\theta$$

Denote the value of $y$ and $p$ at time $k$ as $y(k)$ and $p(k)$, respectively, and let

$$Y = \begin{bmatrix} y(1) \\ y(2) \\ \cdots \\ y(N) \end{bmatrix}, P = \begin{bmatrix} p(1) \\ p(2) \\ \cdots \\ p(N) \end{bmatrix}$$

Then from Eq (8) we obtain a least-squares formulation as follows,

$$Y = P\theta \tag{9}$$

Repeat the above procedure from Eq (5) to Eq(9) at the four different temperatures, and denote the $Y$, $P$ and $\theta$ at [10, 20, 30, 40]°C as $Y_{10}, Y_{20}, Y_{30}, Y_{40}$; $P_{10}, P_{20}, P_{30}, P_{40}$ and $\theta_{10}, \theta_{20}, \theta_{30}, \theta_{40}$ respectively.

Denote $P_s = blkdiag(P_{10}, P_{20}, P_{30}, P_{40})$ where '$blkdiag$' stands for block diagonal, $Y_s = [Y_{10}^T, Y_{20}^T, Y_{30}^T, Y_{40}^T]^T$ and $\theta_s = [\theta_{10}^T, \theta_{20}^T, \theta_{30}^T, \theta_{40}^T]^T$.

Then

$$Y_s = P_s\theta_s \tag{10}$$

The parameter constraints can be put as $\theta_{10} \geq \theta_{20} \geq \theta_{30} \geq \theta_{40}$ in elementwise. This comes from the prior knowledge that the resistance value decreases with temperature rise.

The optimal parameters to Eq (10), $\hat{\theta}_s$ can be obtained using least-squares solvers (here Matlab function 'lsqlin' is used). This is a convex optimization problem which can be solved efficiently. Then optimal resistor values can be calculated using the least squares method,

$$E_s = Y_s - P_s\hat{\theta}_s \tag{11}$$

and the modelling RMSE is $\sqrt{\frac{1}{N_s}E_s^T E_s}$, where $N_s$ is the length of $Y_s$. Note that this RMSE depends on the choices of the underload RC time constants, $\tau_{j,u}$. Then the optimal $\tau_{j,u}$ can be obtained by solving the following parameter optimization problem

$$\min_{\tau_{1,u}, \tau_{2,u}, \tau_{3,u}} \sqrt{\frac{1}{N_s}E_s^T E_s} \tag{12}$$

Here, with only three parameters to optimise, the chance of finding the global minimum is greatly increased compared with optimizing all the model parameters together using the Genetic algorithm [197]. The Matlab function 'fminbnd' is used in this work for finding the optimal underload RC time constants in Eq (12). The order of finding time constants and specific RC values is a non-linear approach. The base function and the least square shorten the entire process by linearising the process of finding resistance values. At the meantime, the time constants are found in a non-linear approach, ‘interior-point’ (default method by Matlab function ‘fmincon’), where the entire parameterisation process has fewer parameters to train and leave time constants as the only few non-linear parameters to be solved.

### *Step 2: identification of the relaxation time constants*

Note that in step1, only the underload test data are used. Next, the rest relaxation test data will be used for identification of the relaxation RC time constants.

First, the underload time constants and the resistor values obtained in step 1 are used to simulate the current values $i_j, j = 1,2,3$ under current load. Next, given the relaxation time constants $(\tau_{1,r}, \tau_{2,r}, \tau_{3,r})$, the model’s voltage profile during relaxation stage can be simulated using Eq (1) and Eq (3).

The model voltage during the relaxation stage will be compared with the measurements and the RMSE depends on the chosen relaxation time constants. This is an optimization problem similar to Eq (12). Again, with only three parameters $(\tau_{1,r}, \tau_{2,r}, \tau_{3,r})$ to optimise, the chance of finding the global minimum is high. The Matlab function ‘fminbnd’ is used again for parameter optimisation.

### *Comparison against PIM without parameter switching scheme*

In order to compare with the case that doesn’t consider the load dependency of the ECM parameters, another PIM is given here that uses the same RC time constants for both underload and relaxation stages. The PIM with no switching consists of only the optimization step in step 1 but uses different test data for parameter identification, i.e., both the underload and 2-hour relaxation test data are used for extracting the ECM parameters.

## 4.6. Modelling results vs validation results

In order to conduct a comparative study of the conventional PIM and the proposed PIM with switching, the model training results for the pulse discharge tests and 2 sets of validation tests are demonstrated in this section.

### 4.6.1. Model training results

The Figure 42 shows the model parameter training results for the two PIMs. Both PIMs perform under certain error bias within 20mV besides a few error spikes when the current jumps. In general, the PIM with no switching leads to better model accuracy during the relaxation stage and lower underload accuracy compared with the switching PIM, as it shows in figure 42 (c) & (d). It is noticeable that the model accuracy decreases under low SoC (<5%). Essentially, the training results show the overall RMSE errors are comparable, 2.4 mV and 3.4 mV for no switching and switching respectively. However, the underload phase RMSE errors are 7.1 mV and 1.8 mV for no switching and switching respectively, which demonstrates the benefits of using the switching PIM in this study. Figure 42 (c) & (d) shows a detailed investigation at SoC value of 85 % - 84%, where the cell underwent constant current discharge for 180s (5% SoC breakpoint step) followed by a 2-hour relaxation. The PIM with no switching illustrates a better performance on the relaxation phase but poorer fitting on the underload phase, by contrast to the switching PIM as detailed in figure 42 (c) & (d).

In figure 42 (b) subplot, PIM with no switching delivers a noticeable large error spike at SoC value of 90%, where the underload time for the constant current period changes from 36s (1% SoC breakpoint step) to 180s (5% SoC breakpoint step). The larger error generated from PIM with no switching (maximum error about 21 mV) compares to switching PIM (maximum error about 8mV) shows another advantage of the proposed switching PIM. As the underload phase and the relaxation phase are trained individually, therefore the RC networks values have greater potential to overcome current load fluctuation during characterisation tests, which fits the potential needs for various current load characterisation tests.

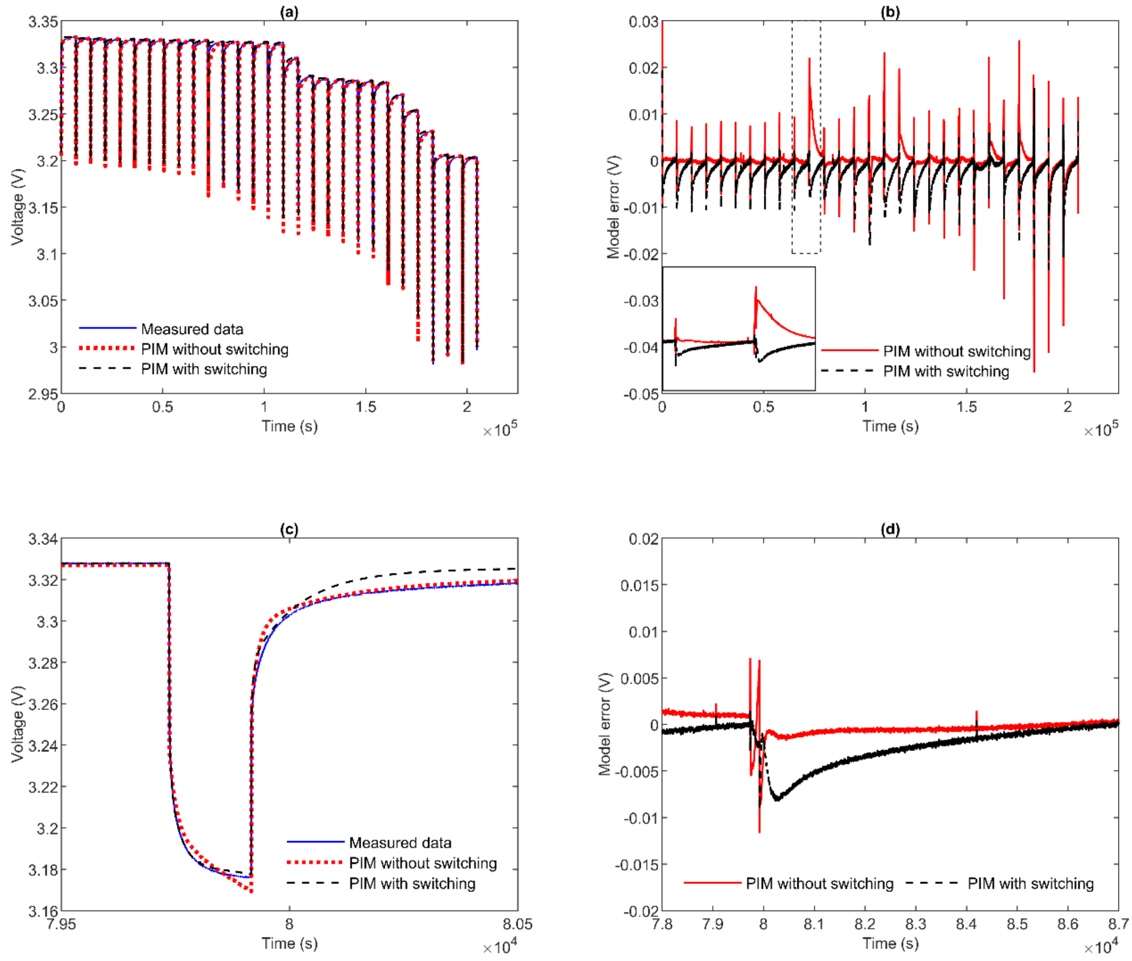

*Figure 42 Comparison of the two PIM methods using the 1% & 5% SoC pulse discharge data at 1C (90A) with a 120minutes relaxation period at 20 °C (a): battery voltage fitting results, (b) modelling error & a zoomed segment of the fitting error at SoC range 89% - 85%, (c): a zoomed segment of the battery voltage fitting results at SoC range 85% - 84%, (d) a zoomed segment of the modelling error at SoC range 85% - 84%.*

### 4.6.2. Validation results

In this chapter, there are 2 set of validation tests examined for both PIMs, which are constant current load and drive cycle noisy load. Normally if a set of parameters are trained from conventional PIM with pulse load as characterisation tests, then validation against constant current test data is typically not done, in many cases this is described as out of scope but is more likely because of poor agreement. Here, the proposed switching PIM is validated against both constant current and under load experimental data, to show its ability to reproduce a wide range of current loads.

### *Constant Current load validation*

Figure 43 (a) demonstrates the measured data together with simulated model results using both PIMs for a constant current discharge test at 1C (90A). The cell centre surface temperature acts as an additional input to the model. Figure 43 (b) demonstrates the error of both PIMs in voltage response. The overall modelling RMSE errors are 140.8 mV and 17.4 mV for PIM with no switching and switching PIM , respectively. The PIM with no switching shows a poor alignment between measured data and model simulation, where a constant error bias over 130 mV is observed. Meanwhile, the switching PIM delivers a good fit between measured data and simulation result. There is over 87.6% improvement on the error bias level from switching PIM.

This is because the PIM with no switching sacrifices partly the underload accuracy in order to improve the accuracy at the relaxation period, i.e., a trade-off. It is noteworthy that the model accuracy during the training step is acceptable, as shown in figure 42. This problem of underload accuracy deficiency only becomes outstanding under this constant current discharge. In another word, the model training results can be misleading without careful data analysis. The root cause to this problem is that the battery shows distinctive dynamics properties for underload and relaxation. This effect must be taken into consideration during ECM parametrization and application. It is therefore recommended that the training data set for ECM parametrization should have similar characteristics with the intended application of the model. In particular, if the intended application of the model includes constant current discharge, then a similar load profile should be used for ECM parametrization. This is a general recommendation for identifying a reduced order model from a highly complex or nonlinear system [193], which is however, generally overlooked in the ECM modelling field. The proposed PIM method using the parameter switching scheme effectively avoids this trade-off which would otherwise reduce the model underload accuracy.

There are similar features at low SoC region (<10%), where error is accumulated. This may be caused by the severe nonlinearity of the battery dynamics at this low SoC range, making constant-parameter ECM unsuitable for capturing the voltage profiles under different current profiles. The model accuracy at low SoC could be improved by taking into consideration of the difference between the surface and bulk concentrations of the battery electrode [198]. This, however, uses a different model structure from ECM and increases the model parametrization complexity. The low SoC accuracy of the ECM modelling will be explored in future work, however this is out of the scope for this study.

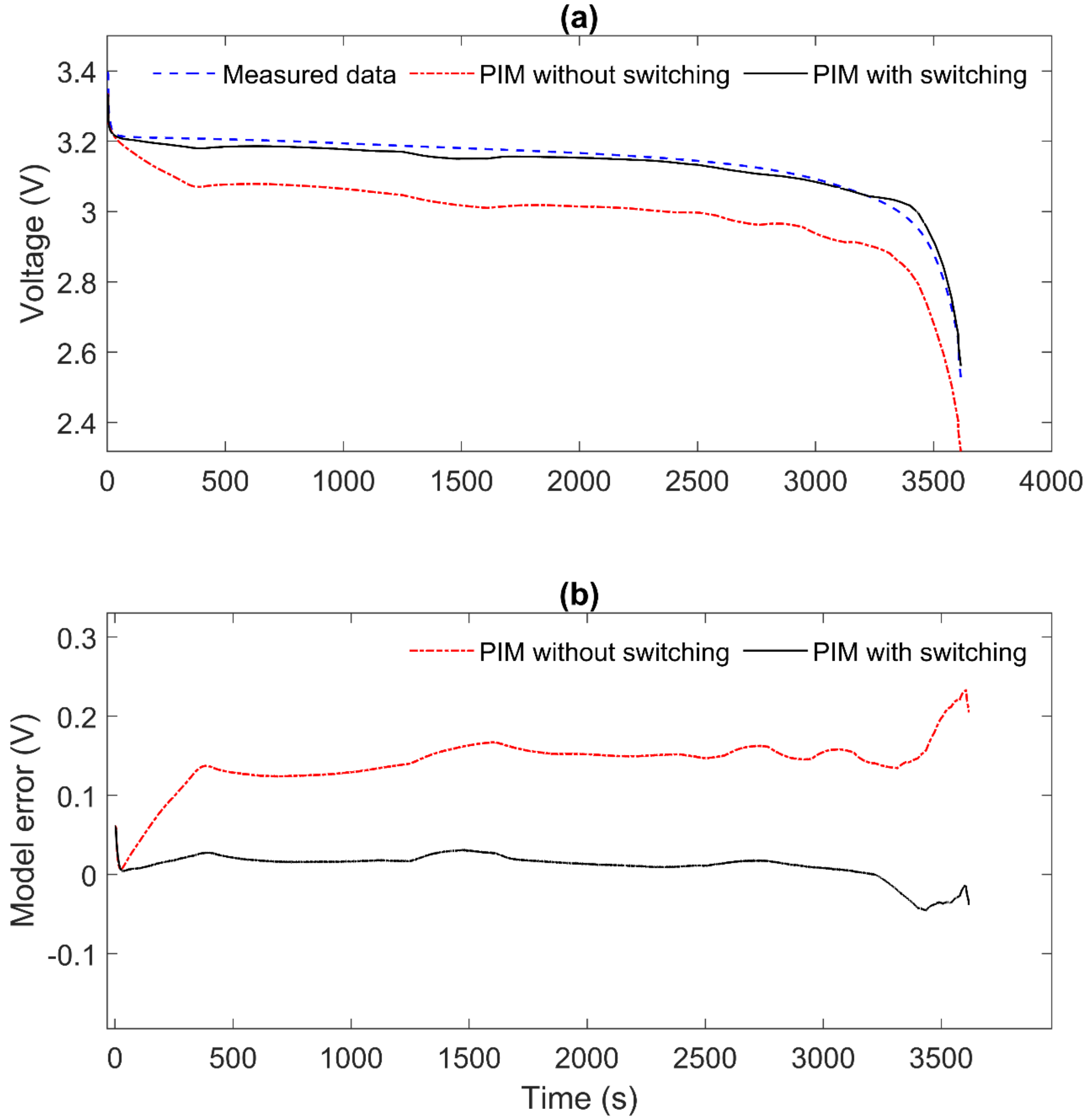

*Figure 43 Comparison of the two PIM methods using the Constant Current discharge load at 1C (at 20 °C as starting thermal chamber ambient, cell centre temperature data is considered as an input for model simulation, (a): battery voltage fitting results; (b) modelling error*

## Drive cycle validation

A bespoke designed drive cycle based on a US06 drive cycle is subjected to the cell, where the input current is shown in figure 38 (a). Figure 44 (a) demonstrates the measured data together with simulated model results using both PIMs. The cell centre surface temperature acts as an additional input to the model. Figure 44 (b) demonstrates the error of both PIMs in voltage response. The modelling overall RMSE errors are 78.2 mV and 17.7 mV for PIM with no switching and switching PIM, respectively. Also, the underload phase RMSE errors are 81.4 mV for PIM with no switching and 7.7 mV for switching PIM, where the switching PIM delivers 10 times less error (improved 90.5% for underload phase, and 77.4% for overall simulation) in this validation scenario. It is clear to see a constant error bias level about 75mV for the results generated from PIM with no switching, while the switching PIM offers an error bias level less than 10mV. The less error and more accurate model performance that uses the parameters generated from switching PIM proves the necessity of this PIM, especially for this type of battery. The reason for the difference of the model accuracy is similar to that in figure 43.

All the PIMs trained the parameters across the entire SoC bandwidth together with 4 characterisation test temperatures. As shown in Figure 38 (c) and 39 (b), the cell centre surface temperature grows from 20 °C to 26 °C for drive cycle test and 20 °C to 35 °C, respectively. Training all the data together gives the model a smooth transition on these thermally dynamic scenarios.

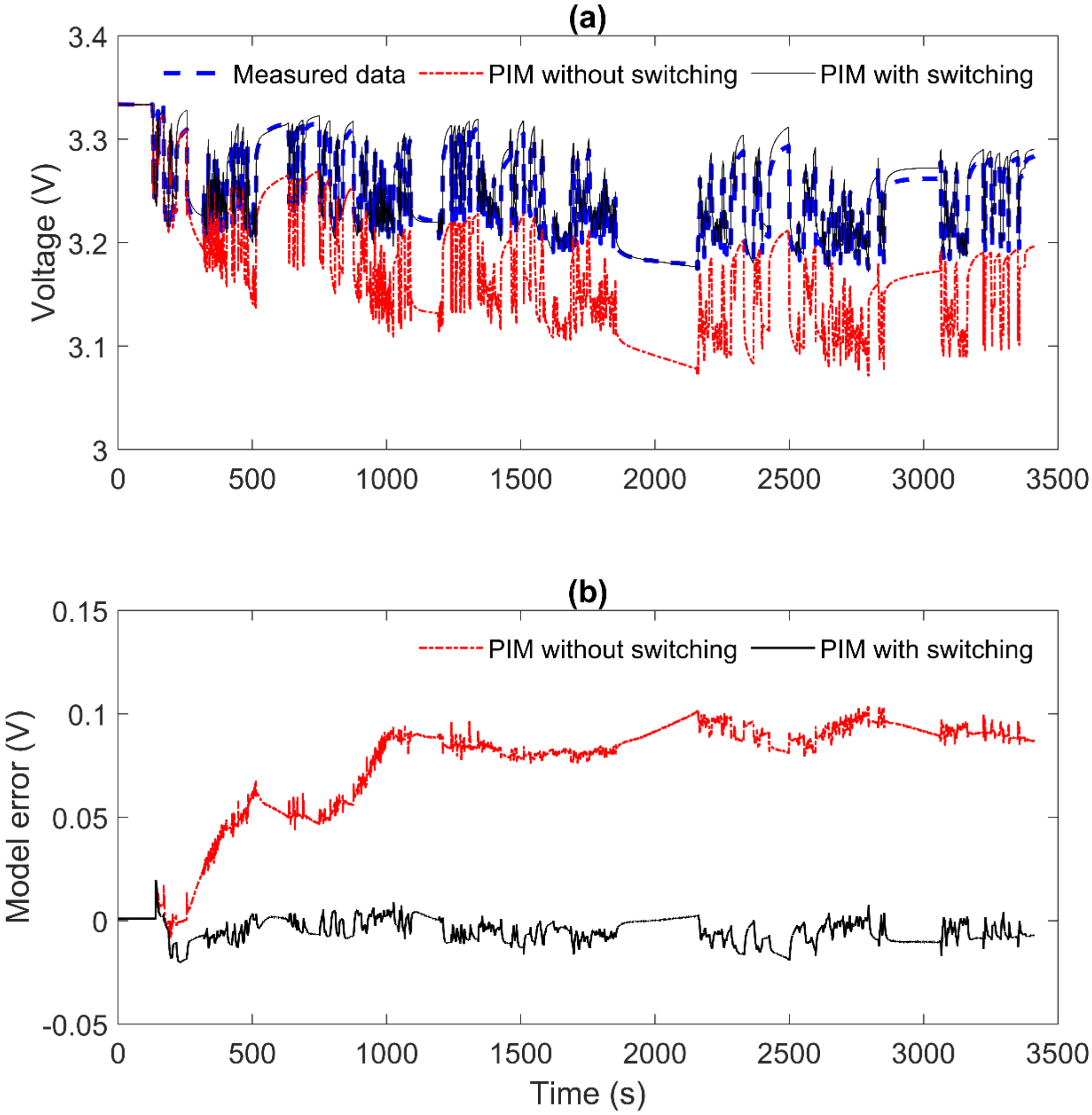

*Figure 44 Comparison of the two PIM methods using the Drive cycle discharge load (input current is shown in Figure 4(a)) at 20 °C as starting thermal chamber ambient, cell centre temperature data is considered as an input for model simulation, (a): battery voltage fitting results; (b) modelling error*

## 4.7. Supplementary data

In the main body of this work, 20 °C experimental data and its corresponding training and validation results are demonstrated for a clear story line. Here, in the supplementary data section, the 10 °C, 30 °C and 40 °C results are presented.

The reason to show these results is simple but essential. In figure 38 (c) and figure 39 (b) of the main chapter, the temperature for the validation tests of constant current load and drive cycle noisy load is not constant. Therefore, a range of characterisation tests covering the temperature range of interest is essential for training the model parameters for such thermally dynamic scenarios. In the following section, the model training results as well as the constant current validation rests are presented. The results align with the main chapter, which the switching PIM delivers better training and validation rests than PIM without switching. The overall RSME and under load phase RSME are also introduced in each figure captures accordingly. Also, the open-circuit voltage (OCV) measured and linear interpolated under 10 °C, 20°C, 30 °C and 40 °C are presented here as well.

### 4.7.1. 10 °C, 30 °C and 40 °C pulse discharge experimental tests and corresponding parameter training results:

#### *#1. 10 °C pulse discharge experimental tests and corresponding parameter training results.*

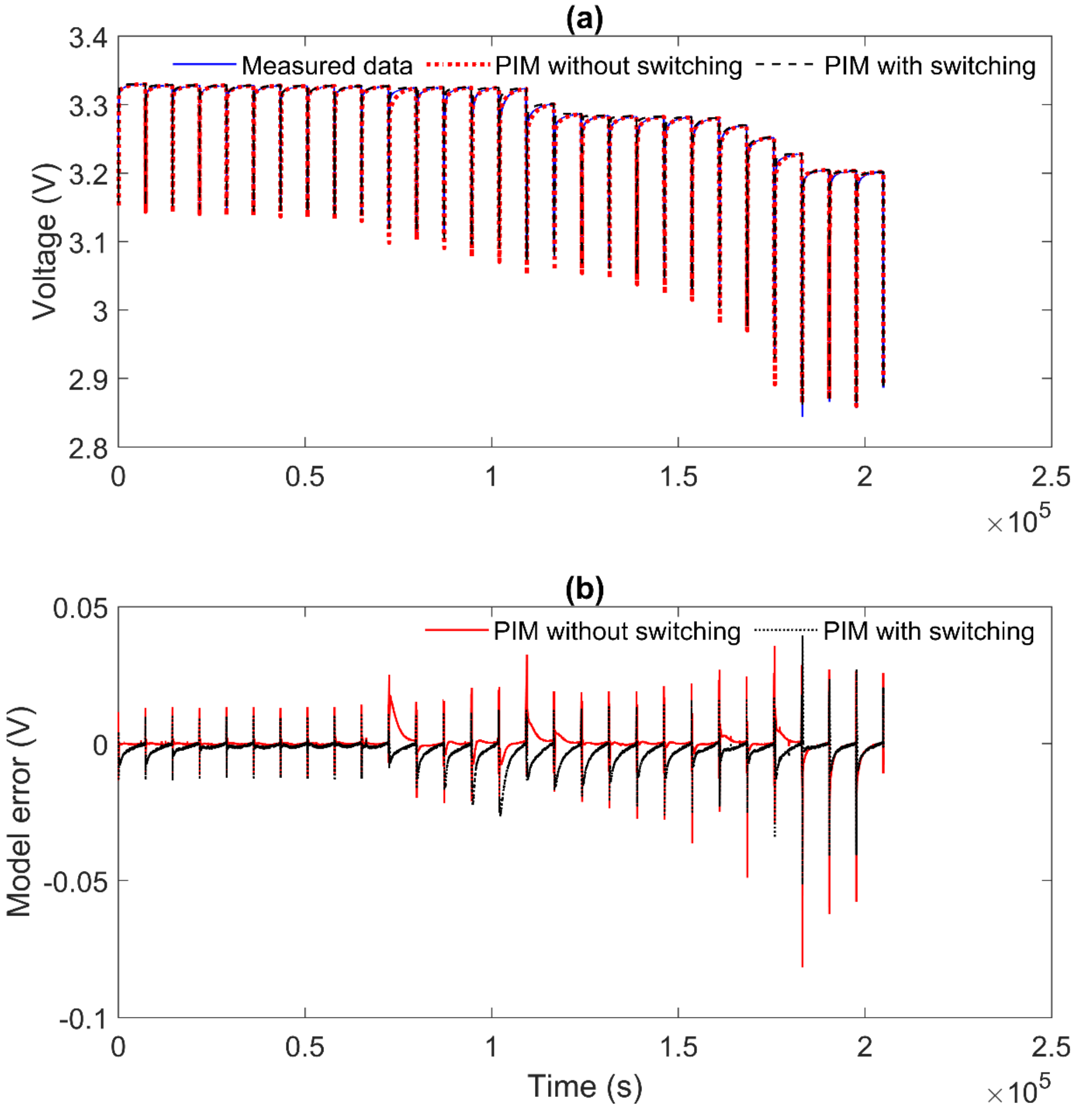

*Figure 45 Comparison of the two PIM methods using the 1% & 5% SoC pulse discharge data at 1C (90A) with a 120minutes relaxation period at 10 °C (a): Experimental data & battery voltage fitting results for PIM without switching and switching PIM (b) modelling error: Overall RMSE: PIM without switching: 3.3mV; Switching PIM: 4.4mV, Under load phase RMSE: PIM without switching: 9.9mV; Switching PIM: 2.9 mV.*

## *#2. 30 °C pulse discharge experimental tests and corresponding parameter training results.*

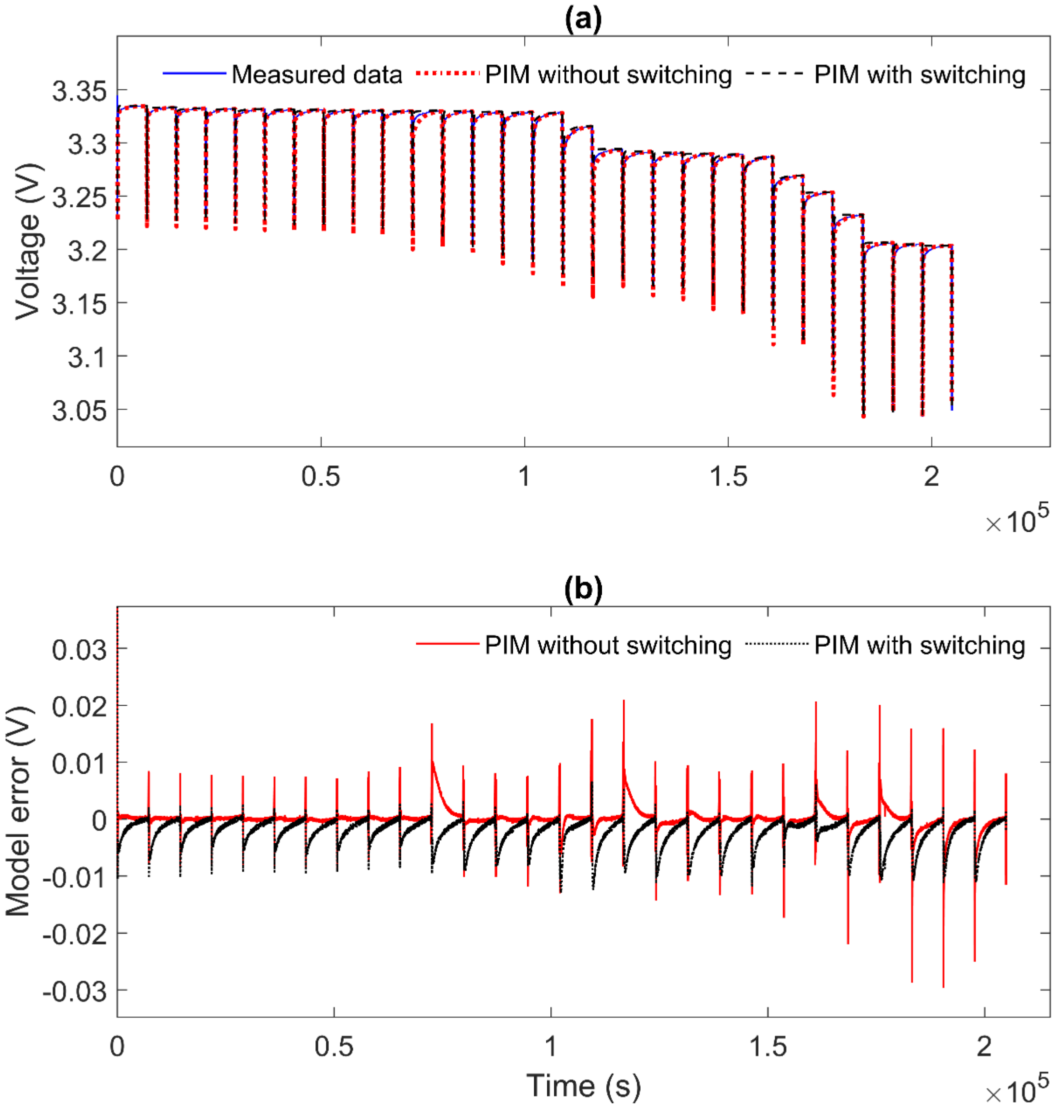

*Figure 46 Comparison of the two PIM methods using the 1% & 5% SoC pulse discharge data at 1C (90A) with a 120minutes relaxation period at 30 °C (a): Experimental data & battery voltage fitting results for PIM without switching and switching PIM (b) modelling error: Overall RMSE: PIM without switching: 1.8mV; Switching PIM: 3.1mV, Under load phase RMSE: PIM without switching: 6.7mV; Switching PIM : 3.3 mV.*

### #3. 40 °C pulse discharge experimental tests and corresponding parameter training results.

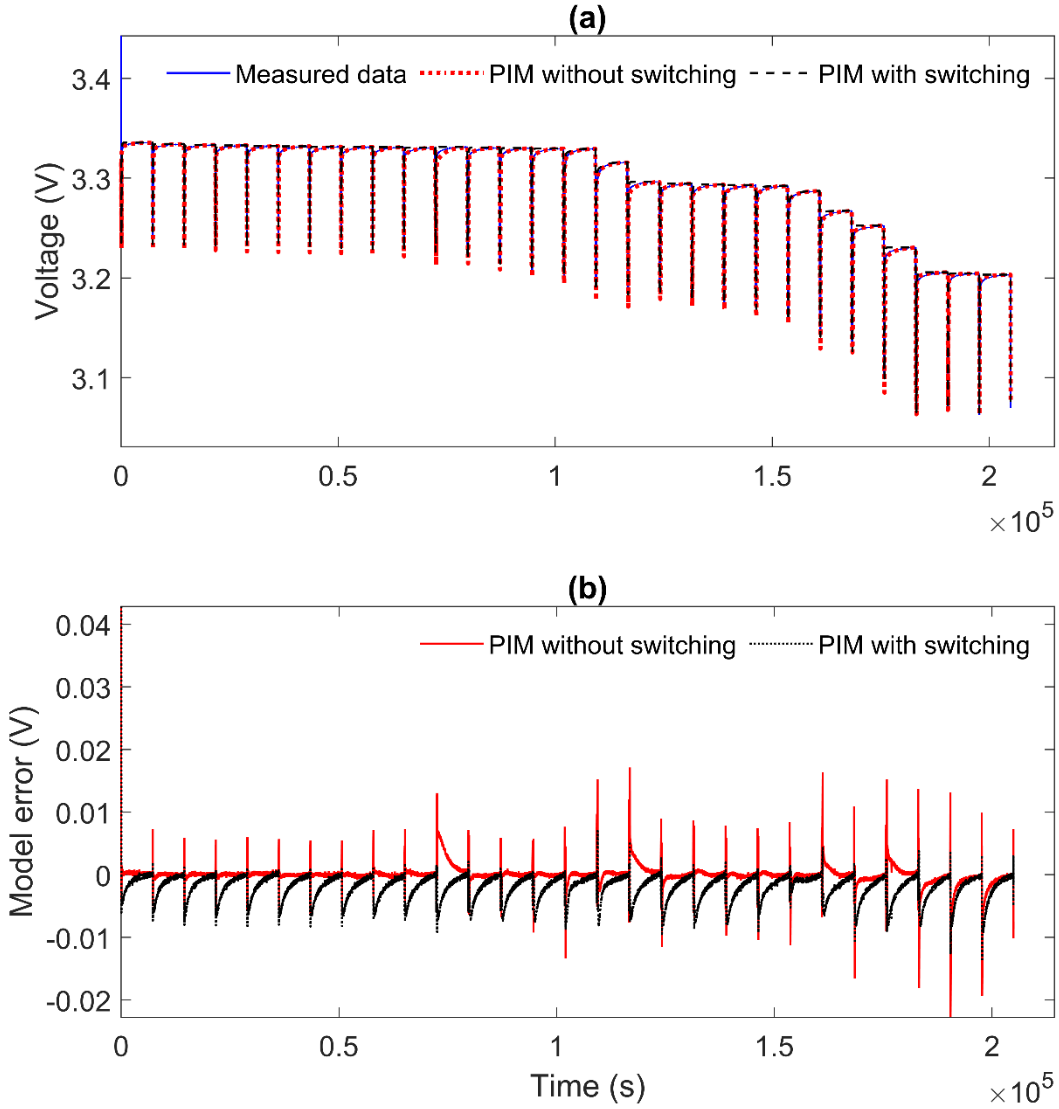

*Figure 47 Comparison of the two PIM methods using the 1% & 5% SoC pulse discharge data at 1C (90A) with a 120minutes relaxation period at 40 °C (a): Experimental data & battery voltage fitting results for PIM without switching and switching PIM (b) modelling error: Overall RMSE: PIM without switching: 1.6mV; Switching PIM: 2.8mV, Under load phase RMSE: PIM without switching: 8.4mV; Switching PIM : 6.9 mV.*

## 4.7.2. 10 °C, 30 °C and 40 °C constant current discharge experimental tests and corresponding validation results.

### *#1. 10 °C constant current discharge experimental tests and corresponding validation results.*

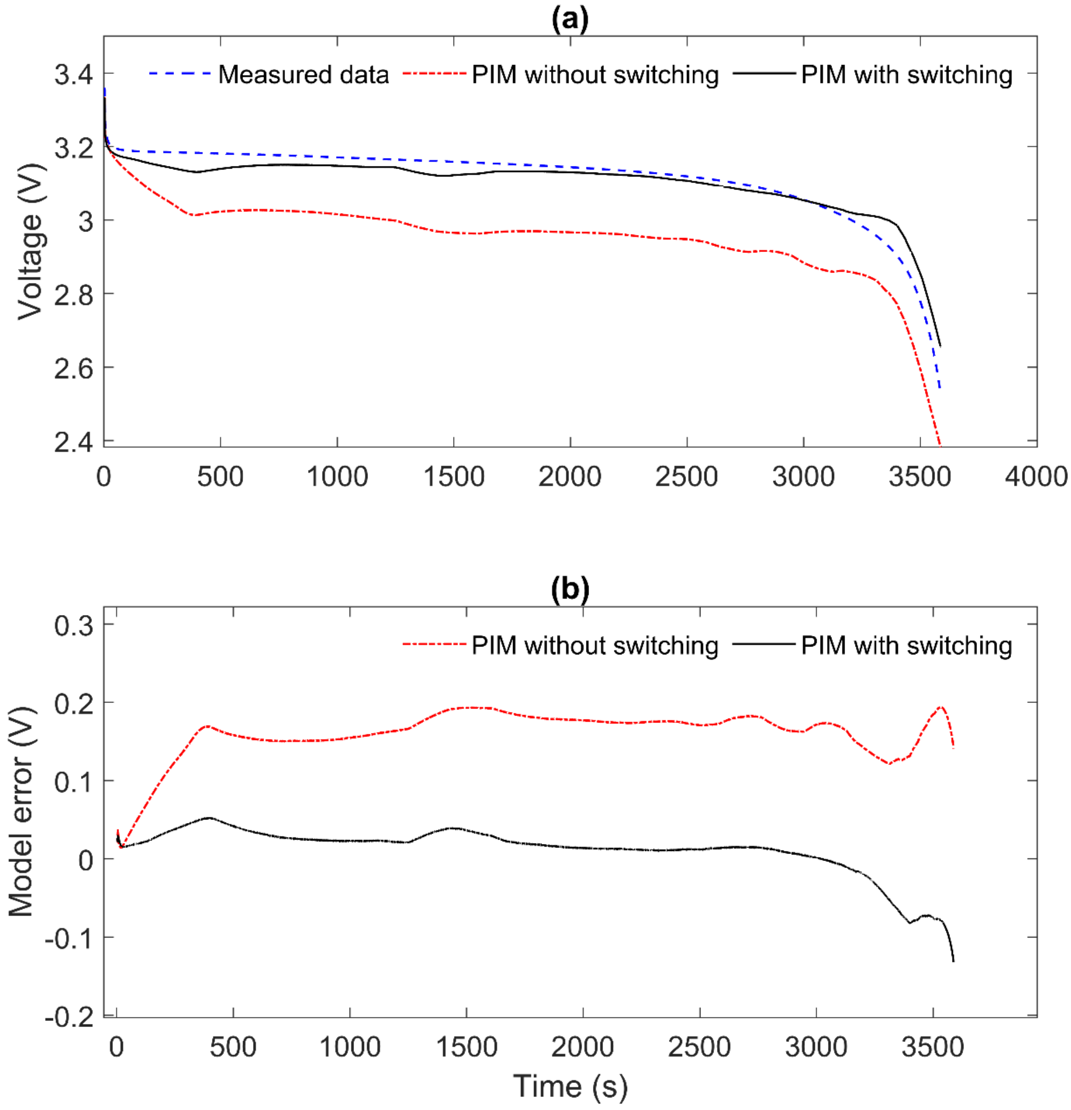

*Figure 48 Comparison of the two PIM methods using the constant current discharge at 1C (90A) at 10 °C (a): Experimental data & battery voltage fitting results for PIM without switching and switching PIM (b) modelling error: Overall RMSE: PIM without switching: 163.5mV; Switching PIM: 25.3mV.*

### *#2. 30 °C constant current discharge experimental tests and corresponding validation results.*

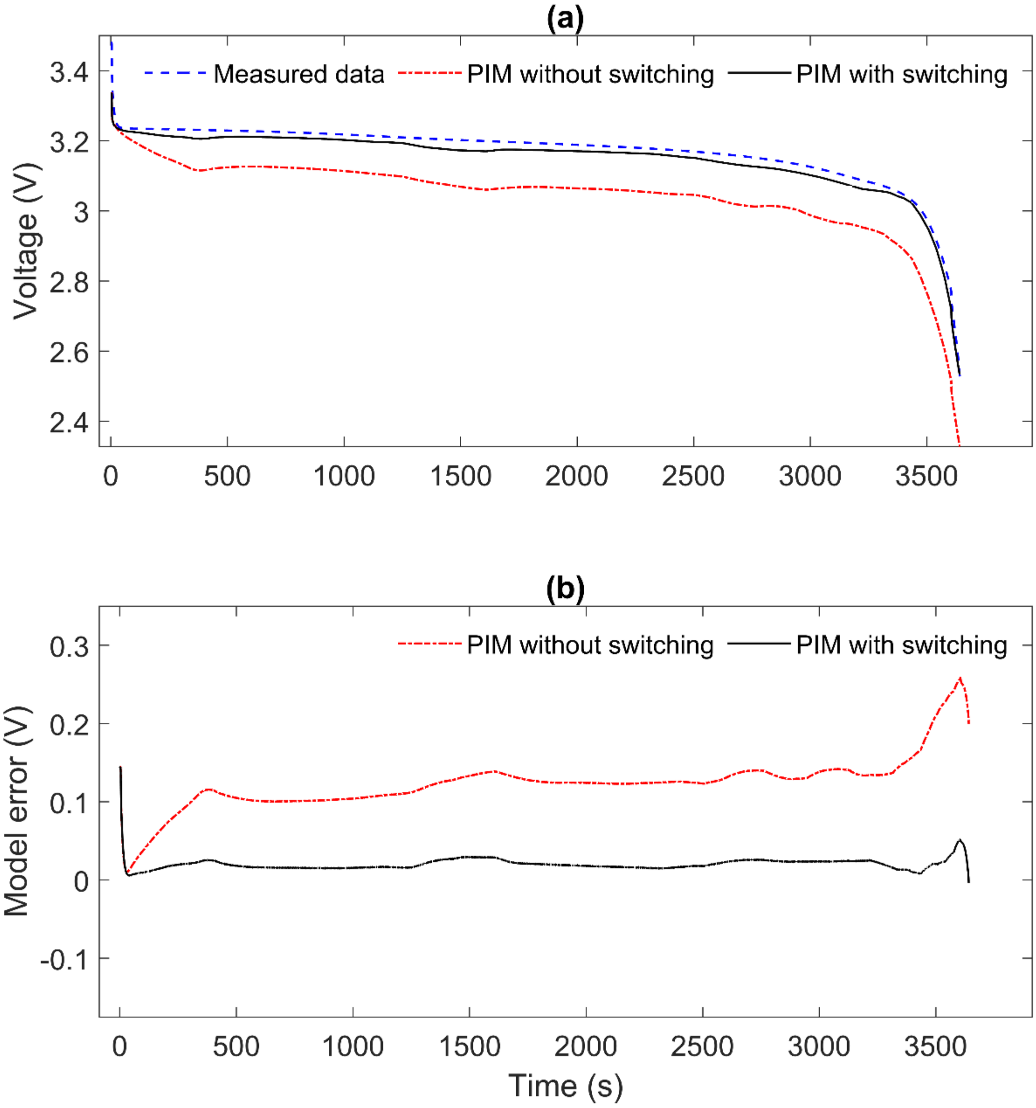

*Figure 49 Comparison of the two PIM methods using the constant current discharge at 1C (90A) at 30 °C (a): Experimental data & battery voltage fitting results for PIM without switching and switching PIM (b) modelling error: Overall RMSE: PIM without switching: 118.5mV; Switching PIM: 21.6mV.*

## *#3. 40 °C constant current discharge experimental tests and corresponding validation results.*

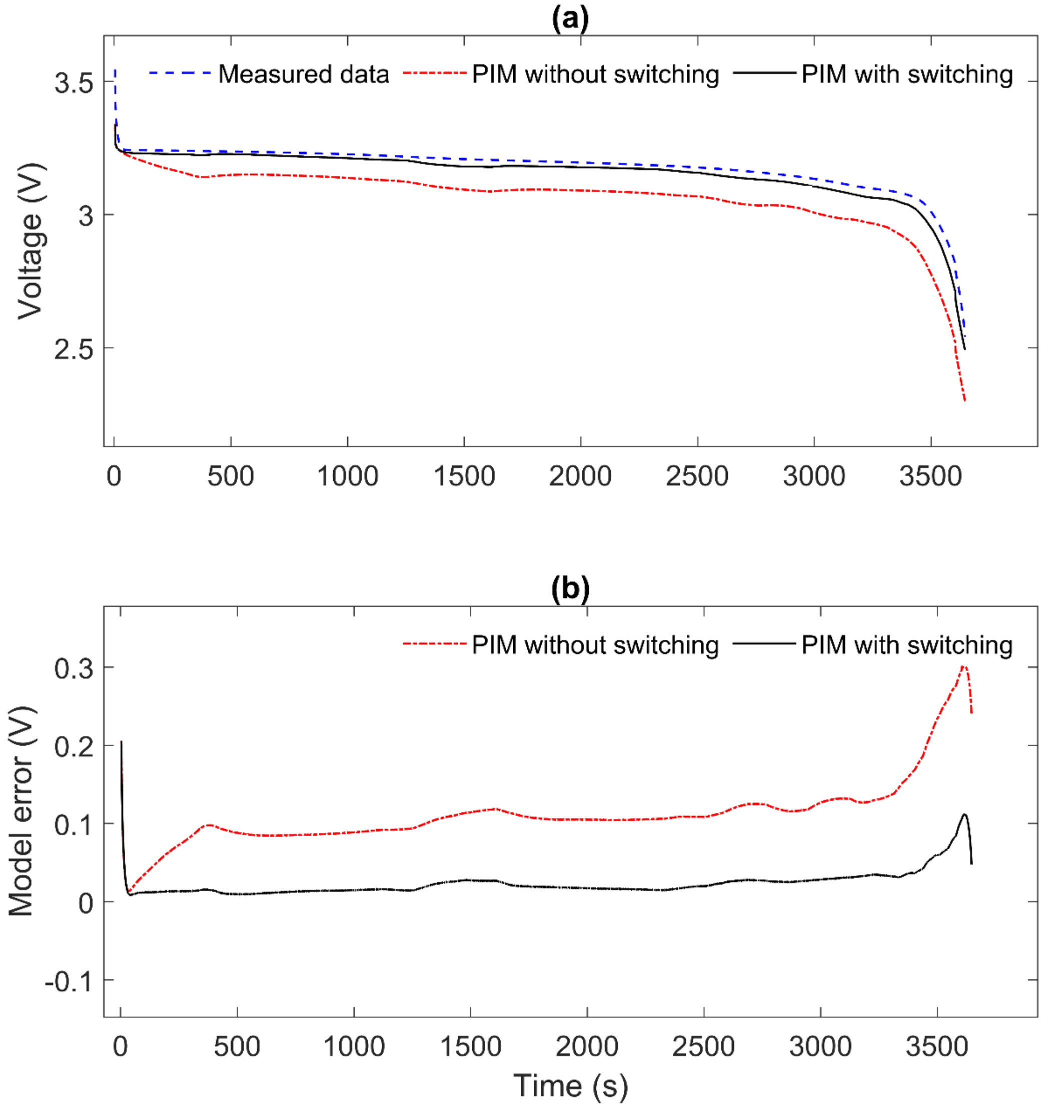

*Figure 50 Comparison of the two PIM methods using the constant current discharge at 1C (90A) at 40 °C (a): Experimental data & battery voltage fitting results for PIM without switching and switching PIM (b) modelling error: Overall RMSE: PIM without switching: 103.7mV; Switching PIM: 22.9mV.*

### 4.7.3. 10 °C, 20°C, 30 °C and 40 °C OCV results

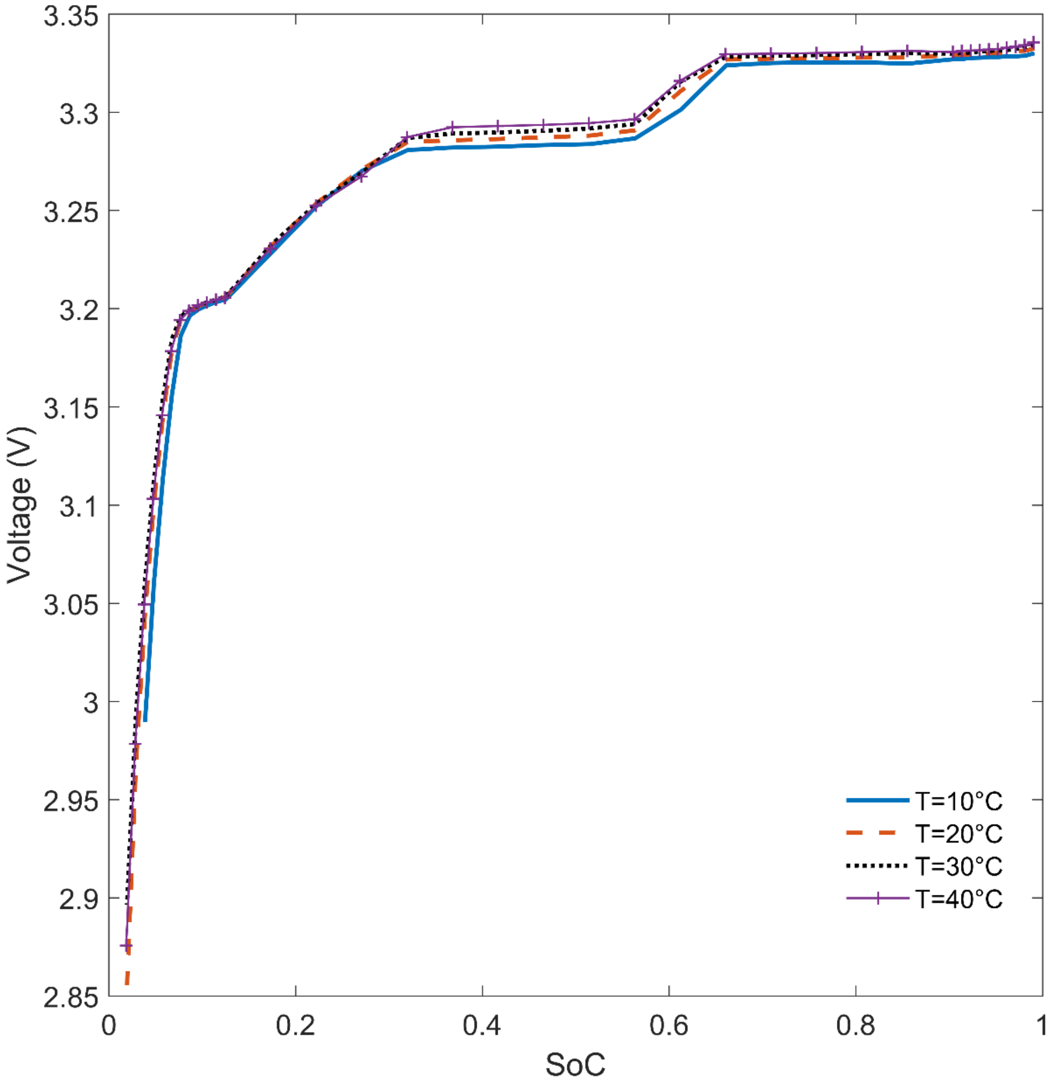

*Figure 51 Open-circuit voltage results at 10 °C, 20°C, 30 °C and 40 °C.*

## 4.8. Interim conclusion

A novel modified equivalent circuit model and parameter identification method is presented which takes into account the fact that many lithium ion batteries exhibit different time constants during underload operation compared to relaxation. The model switches between RC values for different current profiles. This is particularly pronounced in the large prismatic with lithium iron phosphate cathode studied in this chapter but is also seen at the extremes of SOC in other lithium ion batteries, particularly at low SOC where state estimation can be particularly difficult yet even more important. The approach presented in this thesis demonstrates significant improvements over a conventional equivalent circuit model without switching time constants. The work should be of interest to application engineers, battery management system developers, and control engineers.

Further, this chapter shows that an inevitable requirement for a good parameter identification method, especially for highly thermally dynamic operations. This chapter serves as a critical role for the next chapter, which presents the discretised Electro-thermal ECM modelling for the Li-ion battery. The quality of the PIM leads to the accuracy of the lost power, therefore the heat generation rate inside each thermal element within the model. The understanding of the PIM in this chapter builds great fundamentals for ECM modelling.

# 5. $CCC_{Surf}$ technique on LFP cell and corresponding Discretised ECM modelling

## 5.1. Introduction

Chapter 5 is based on the journal publication by Xiao Hua, Claas Heckel, Nils Modrow, Cheng Zhang, Alastair Hales, Justin Holloway, Anmol Jnawali, Shen Li, Yifei Yu, Melanie Loveridge, Paul Shearing, Yatish Patel, Monica Marinescu, Liang Tao, Gregory Offer. '*The Prismatic Surface cell cooling coefficient: a novel cell design optimisation tool & thermal parameterisation method for a 3D discretised Electro-Thermal Equivalent-Circuit Model 'under review in Journal of eTransportation.* As described in detail in section 1.4 in the Chapter 1.

As detailed in the literature review and previous chapters, a novel metric (CCC) to evaluate the cell's capability to be thermally managed is needed. Also, with the developed ECM parameterisation method presented in chapter 4, a precise loss power could be delivered to thermal model, forming a good electro-thermal simulation network. Such model that embeds with CCC as a key boundary condition could understand more about thermal management of large format prismatic lithium ion batteries, which is challenging due to significant heat generation rates, long thermal 'distances' from the core to the surfaces and subsequent thermal gradients across the cell.

In this chapter, the application of CCC has been introduced to prismatic cells with a 90Ah prismatic lithium iron phosphate cell with aluminium alloy casing. Further, a parameterised and discretised 3-dimentional electro-thermal equivalent circuit model is developed in a commercially available software environment, Dymola. The model is thermally and electrically validated experimentally against data including drive cycle noisy load and constant current CCC square wave load, with particular attention paid to the thermal boundary conditions. A quantitative study of the trade-off between cell energy density and surface CCC, and into casing material selection has been conducted here. The CCC enables comparison between cells, and the model enables a cell manufacturer to optimise the cell design and a systems developer to optimise the pack design. It is recommended this is done together holistically. This chapter offers a cost-effective, time-efficient, convenient and quantitative way to achieve better and safer battery designs for multiple applications.

This chapter answers following research questions:

1. ***Could the CCC metric be capable of providing better thermal gradient understanding for large format LFP prismatic cells?***
2. ***Could the discretised Electro-thermal ECM model have developed together with embedded CCC boundary conditions be used for cell optimisation?***
3. ***Could changes in cell configuration affect the large format LFP prismatic cells thermal behaviours? And decrease the difficulties of thermal management for such large format cells?***

## 5.2. Backgrounds

The thermal management system (TMS) is a critical sub-system of an electric vehicles (EVs) design. Firstly, if a LIB generates more heat than can be dissipated this can lead to thermal runaway. [84,199] Secondly, large temperature deviations can cause accelerated degradation and/or require de-rating of performance. [22,200,201] A TMS clearly cannot be avoided. However, thermal management will cause a thermal gradient across a LIB due to the finite and anisotropic thermal conductivity.[202] This combined with the strong temperature dependence on the impedance means different layers/regions will have different values of impedance. As a consequence, current inhomogeneities are caused which exacerbate the thermal gradients in a positive feedback mechanism.[21] Such thermal inhomogeneities caused by different thermal management methods (e.g. surface cooling or tab cooling) can be a significant contributor towards accelerated LIB degradation. [108,203]

TMSs broadly fall into two categories, convective air cooling and conductive liquid cooling. Nowadays, air cooling is restricted to low discharge rate applications, as high volumetric heat generation limits the usage of air-cooling. [105,204,205] Cooling can also be applied to different cell thermal interfaces, such as tabs, side surfaces or bottom surfaces. With the current generation of cell designs, surface cooling is typically the only feasible cooling method for most automotive applications, due to the high heat rejection rates achievable. [206–209] For simplicity, the majority of the TMS designs cool only one side of the cell, in order to achieve higher pack level performance. [210,211]

To understand and study the importance of TMS design on LIB performance, models are required. A robust LIB model should be able to capture both the voltage and thermal response of the battery. Multi-node 2D/3D electro-thermal coupled equivalent circuit models (ECM) are often chosen for their capability of predicting the internal current and thermal inhomogeneities within LIBs. [108,212] They are easier to implement and easier to parameterise compared to physics based models, and require less computational power to scale from a lumped cell model to a multi-dimensional model [108] as pioneered by Newman, Tiedemann et al and others.[109,110,146] Parameterisation is critical for good accuracy and can be achieved through simple pulse discharging (PD). [112,128,136] Two reviews of ECM models are recommended for further reading.[190,191] Previous work by some of the authors used an ECM model as a design tool, which showed that increasing cell tab width, thickness and position could significantly improve the performance of a LIB pouch cell.[62]

In the same way that volumetric energy density is defined by a single metric, Wh.L$^{-1}$, when designing a cell, it is useful to have a single comparable metric to compare how easy it is to thermally manage a cell. The Cell Cooling Coefficient (CCC), with units of W.K$^{-1}$ was introduced by Hales et al. in response to this need. It describes the rate of heat transfer that will occur due to the thermal gradient from the hottest point of a cell and its cooled surface, whilst it is generating heat throughout its volume. The CCC is a new cell evaluation standard for quantifying the rate of heat rejection. [202,203] A cell will have a different CCC for each surface that can be managed, and each can be measured empirically without any internal knowledge of the cell. The CCC allows the comparison of different cell formats, geometries, sizes and chemistries experimentally, just like volumetric or specific energy density can be compared. Cell tab and cell surface cooling for pouch cells have been previously defined. [105,202]

In this study, a large format prismatic Lithium iron phosphate (LFP) battery is examined. The prismatic form factor is favoured by some EV manufacturers due to its ease of manufacturing using a jellyroll design, and more robust packing assembly because of its metallic hard casing. [213] This study describes how to measure the CCC for a prismatic cell for the first time. The measured values are then compared to a discretised thermally coupled ECM. The three-dimensional discretised thermally coupled ECM is developed using ‘Dymola’ software in collaboration with Dassault Systèmes. The CCC experimental data provides a novel validation method in addition to the usual independent validation against realistic drive cycles.

The ECM is then used as a design tool to explore how changes to the cell design affect the CCC. Various cell design choices including changing the casing materials (e.g. pure aluminium, aluminium alloy, steel, aluminium laminated film), and cell physical geometries (e.g. thickness) are evaluated. Such analysis enables a clear and quantifiable way of studying the trade-offs between the volumetric energy density and specific energy with the CCC surface (*CCC<sub>surf</sub>*) values and therefore the degree of difficulty implementing a TMS.

## 5.3. Model Development

### 5.3.1. Overview

A three-dimensional (x,y,z) discretised electro-thermal ECM model is developed and implemented, which enables the simulation of cell internal states in all directions, including temperature distribution, current density and voltage response. A network of electric and thermal models represents the simulated battery, where the electric and thermal networks are exchanging the temperature and heat generated in each of the discretised volumes. The model is developed and implemented in Dymola [214] (Dynamic Modelling Laboratory), a tool for modelling and simulation of complex multi-domain systems. Dymola uses the object-oriented, acausal and component-oriented modelling language, termed Modelica.[215,216] The Battery Library, a Modelica based library for the design of battery systems, builds the base for the development and implementation, while both Dymola and the Battery Library are commercial tools from Dassault Systèmes.

### 5.3.2. Electric Model – Equivalent circuit model

As shown in Figure 52., the electric model is a network of parallel-connected ECMs, where each ECM consists of a voltage source, representing the open-circuit voltage (OCV) $U_{\mathrm{oc}}$, a serial resistor $R$ and two R-C branches connected in series. The resistors are described by Ohm's law in Eq1, the capacitors are described by Eq 2 and the cell terminal voltage is given by Eq 3:

$$U_i = R_i \cdot I_i \tag{1}$$

$$I_i = C_i(t) \cdot \frac{dU_i}{dt} \tag{2}$$

$$V_{terminal} = U_{\mathrm{oc}} - \sum_{j=1}^{2} U_{RC} - IR \tag{3}$$

Where $V_{terminal}$ is the cell terminal votlage, $I$ is the applied current and $U_{RC}$ is the voltage loss at each R-C branch. $U_i$, $R_i$, $I_i$ and $C_i$ is the voltage, resistance, current and capacitance values for each individual component $i$ respectively within the ECM networks.

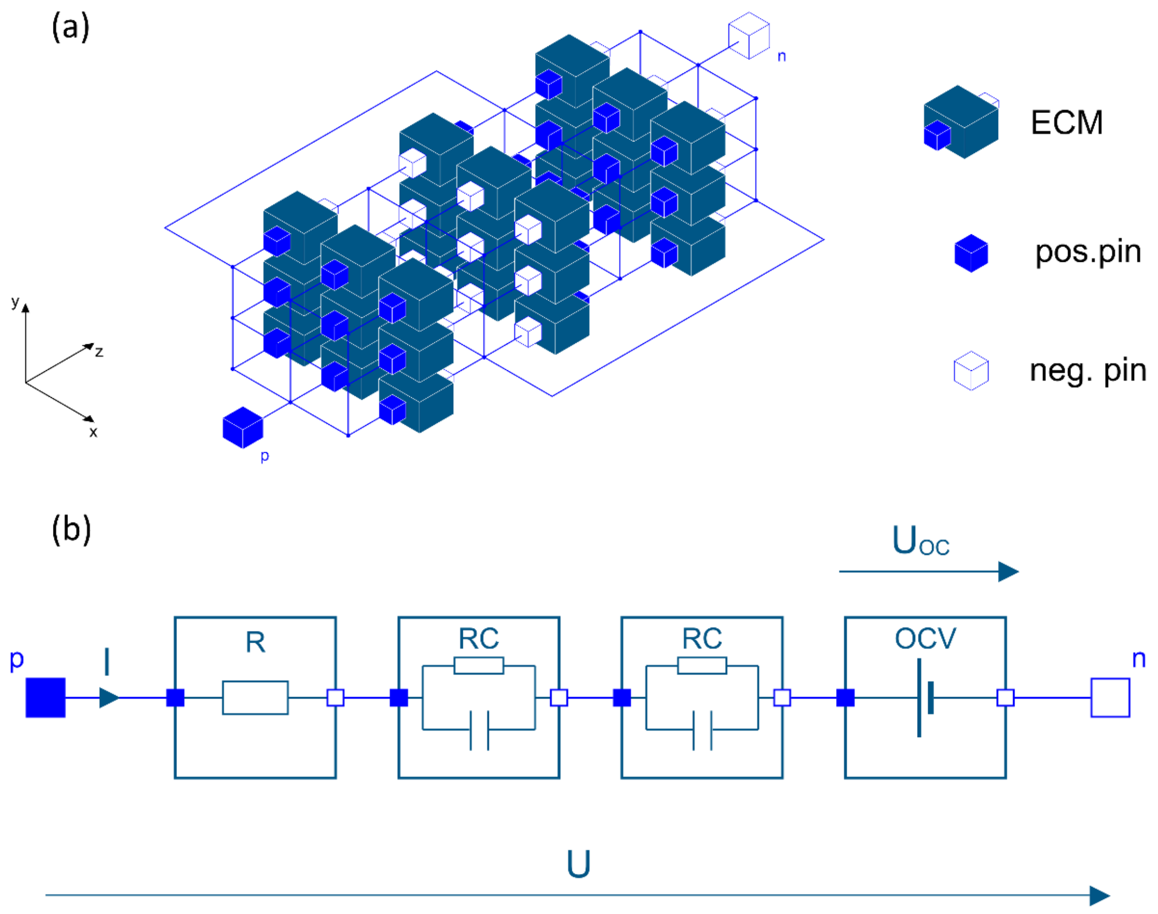

*Figure 52 (a)Electrical Model demonstration, in three dimensional, (x, y, z), (b)Battery equivalent circuit model with 2 R-C branches.*

All components of the ECM use lookup tables with state of charge (SoC) and temperature $T$ as inputs. The SoC is calculated from the ECM current $I_{ECM}$ and the nominal capacity $C_{nom}$ of the ECM:

$$SoC = SoC(t = 0) + \frac{1}{C_{nom}} \int I_{ECM} dt \tag{4}$$

The total heat flow generated by each ECM $\dot{Q}_{loss}$ is contributed from the reversible heat generation $\dot{Q}_{\mathrm{rev}}$ and irreversible heat generation $\dot{Q}_{\mathrm{irr}}$:

$$\dot{Q}_{loss} = \dot{Q}_{\mathrm{irr}} + \dot{Q}_{\mathrm{rev}} \tag{5}$$

The irreversible heat is calculated from the open circuit voltage $U_{OC}$ and the current $I_{ECM}$ and the voltage $U_{ECM}$ of each ECM element, while the reversible heat is calculated from the derivative of the open circuit voltage with respect to the temperature. The state of charge dependent derivative is adopted from [213] where it was measured on a similar chemistry. This reversible heat is caused by the entropy changes in electrodes at different SoC, where the CCC validation only generate heat at a single SoC point. The entropic heat generation cancel each other when the input current is a switching square wave, therefore the value from literature is taken to simplify the development procedure. The sum of the irreversible and reversible heat leads to the total heat flow generated by each ECM as described by Eq 6-8:

$$\dot{Q}_{\mathrm{irr}} = (U_{ECM} - U_{OC}) \cdot I_{ECM} \tag{6}$$

$$\dot{Q}_{\mathrm{rev}} = I_{ECM} \cdot T \cdot \frac{\partial U_{OC}}{\partial T} \tag{7}$$

$$\dot{Q}_{loss} = (U_{ECM} - U_{OC}) \cdot I_{ECM} + I_{ECM} \cdot T \cdot \frac{\partial U_{OC}}{\partial T} \tag{8}$$

The electrical properties are assumed to be homogenous throughout the entire cell. This allows scaling of the resistances and capacitances from cell level to each ECM for nth ECMs by:

$$R_{ECM} = n \cdot R_{cell} \tag{9}$$

$$C_{ECM} = \frac{C_{cell}}{n} \tag{10}$$

where $R_{ECM}$, $C_{ECM}$, $R_{cell}$ and $C_{cell}$ are the ECM resistance & capacitance and unit cell resistance and capacitance respectively.

## 5.3.3. Thermal Model

As shown in Figure 53 (a)., the thermal network consists of several thermal elements. The cuboid element has a few subcomponents, including the jellyroll element and the casing element for all 6 sides. The number of elements in x, y and z direction can be determined by setting the corresponding model parameters. The edge lengths of the elements are uniformly adjusted according to the overall length of the cell dimensions and to the selected degree of discretisation.

The basic thermal elements are modelled according to the finite volume method (FVM). Their heat capacity $C$ is assumed to be concentrated in the centre. It is calculated according to:

$$C = V \cdot \rho \cdot c_p \tag{11}$$

where $V$ is the volume of the element, $\rho$ is the density of the element and $c_p$ is the specific heat capacity of the element.

The material properties are assumed to be constant over temperature as the temperature range in which the model is used is relatively small. In Figure 53 (a)., the heat $\dot{Q}_{cond}$ is conducted in all three dimensions in the form of 1D heat conduction between its centre and the according side faces (essentially 6 directions for a cuboid element):

$$\dot{Q}_{cond} = k \cdot \frac{A}{x} \cdot \Delta T \tag{12}$$

where $k$ is the thermal conductivity of the element, $A$ is the cross-sectional area of the element, $x$ is the distance of the heat conduction range of the element and $\Delta T$ is the temperature difference at both end at the heat conduction of the element. Therefore, the heat balance of the basic thermal element is described by Eq 13 and Eq 14:

$$C_{cc,i} \frac{\partial T}{\partial t} = \sum_{i=1}^{6} \dot{Q}_{cond\_CC,i} \tag{13}$$

$$\rho_i c_{p,i} \frac{\partial T}{\partial t} = \sum_{i=1}^{6} k_i A \frac{\partial T}{\partial x} \tag{14}$$

where $C_{cc,i}$ is heat capacity of current collector elements, $\dot{Q}_{cond\_CC,i}$ is the heat conduction rate of current collector element in $i$ direction.

As shown in Figure 53 (a)., the jellyroll consists of layers of positive & negative current collectors and electrochemical elements that are alternately connected to each other in the z-direction. The number of layers of electrochemical elements in z-direction equals the desired discretisation in z-direction ($n_z$). Since the first and the last layer of the jellyroll model is a pure current collector layer, there are $n_z + 1$ current collector layers.

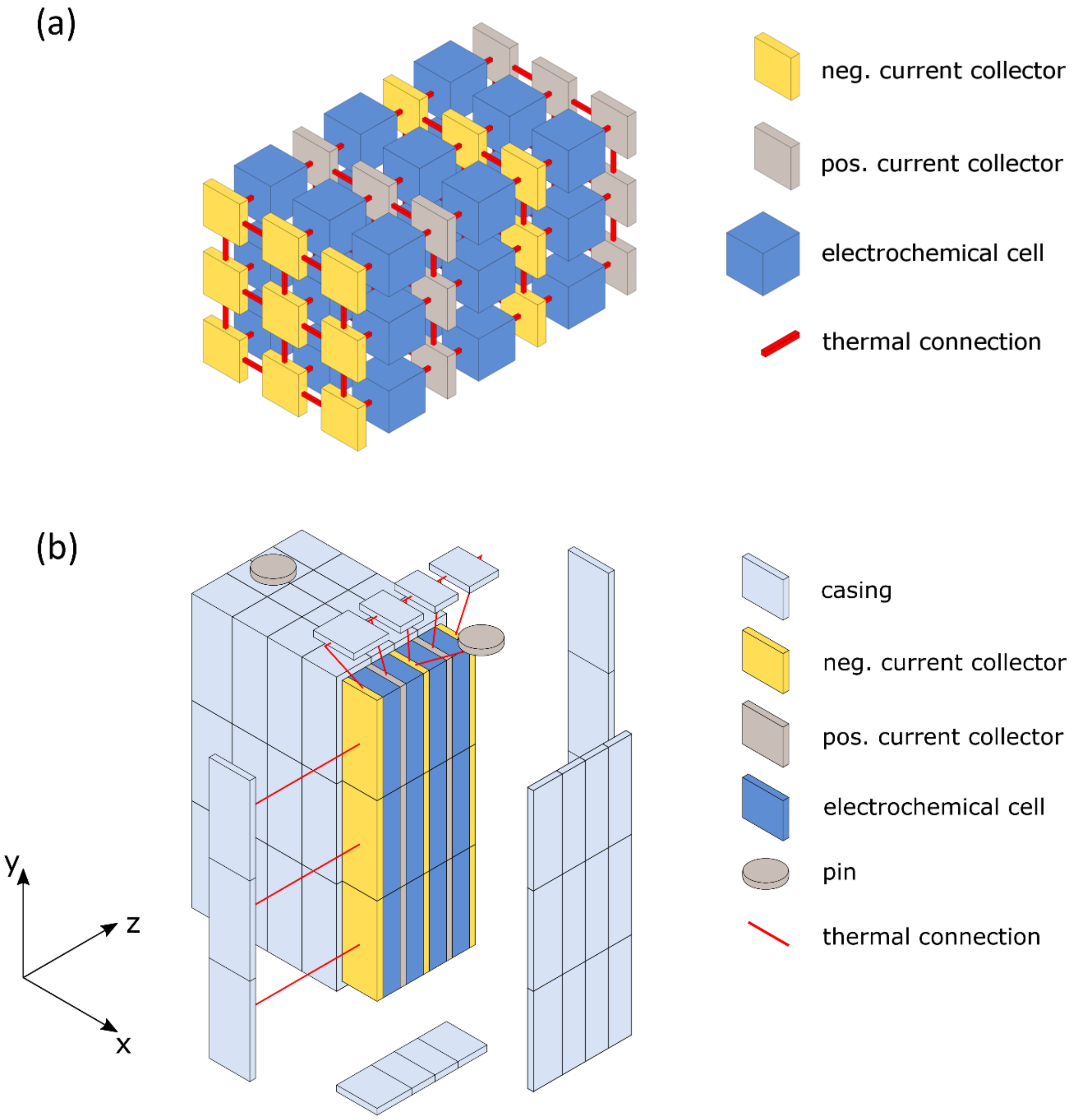

*Figure 53 (a)Thermal Model demonstration of electrode stack, in three dimensional, (x, y, z), (b) Cell level Thermal Model schematic, in three dimensional, (x, y, z)*

The electrochemical cell element consists of the anode, the cathode and the separator. The electrode stack is assumed as a single homogeneous mixture of materials. An assumption is made in the thermal connection here: as the thermal conductivity of the electrochemical cell elements are relatively small in comparison to the current collectors, the heat conduction in-plane for the electrochemical cell elements is assumed to have negligible influence on the thermal behaviours and is therefore ignored.

Therefore, besides from Eq 13 & 14, another thermal balance equation is implemented in the thermal network, where the heat is only conducted between the electrochemical cell elements and current collector elements. This simplification reduces the total number of the heat transfer equations to be solved, and therefore, an optimised simulation performance with less required computational force is achieved. The corresponding heat balance equation is described as in Eq 15 & 16:

$$C_{cell,i}\frac{\partial T}{\partial t} = \sum_{i=1}^{2} \dot{Q}_{cond\_cell,i} + \dot{Q}_{loss} \tag{15}$$

$$\rho_i c_{p,i}\frac{\partial T}{\partial t} = \sum_{i=1}^{2} k_i A\frac{\partial T}{\partial x} + \dot{Q}_{loss} \tag{16}$$

where the $\dot{Q}_{loss}$ is the heat generated by the electrical model, therefore coupling the electrical model network with the thermal model network. $C_{cell,i}$ is heat capacity of electrochemical cell elements, $\dot{Q}_{cond\_Cell,i}$ is the heat conduction rate of current collector element in $i$ direction.

The heat balance has an additional heat flow rate $\dot{Q}_{loss}$ added because every electrochemical cell element has an associated ECM element in the electrical model. Information is exchanged between these pairs of elements. The ECM element calculates the amount of heat generated in the corresponding part of the cell and this information is passed on to the thermal element. The temperature of the thermal element, in turn, is passed to the ECM and interacts with the calculation of the internal resistance and thus the heat generation.

In Figure 53 (b)., the electrochemical cell elements of the jellyroll are only in thermal contact with the current collectors, where it is not directly connected to the casing. The casing elements are connected to the current collectors, respectively. Like the actual cell, the pins have a cylindrical shape, where the heat conduction is modelled through FVM in y-direction. The welding region is modelled here, as a connection between the pins and the current collectors, where the welding electrical counterpart is used to calculate the heat generation of the welding. The ohmic resistance of the welding regions are considered constant, which is independent of the operating temperatures. The pins are located at the same end of the cell, and are not directly connected to the casing as there is electrical insulation and therefore thermal insulation between the pins and the casing. The welding regions are connected to the inner half of the corresponding current collectors, like the actual cell configuration.

As listed in Table 5 & Table 6, the thermal conductivities and the heat capacities of the current collectors, the casing material and the pin models are calculated based on the geometric measurements of the thermal elements, and material properties from literature.[58,62,108,203] The thermal conductivity and the specific heat capacity of the electrochemical elements, on the other hand, have been determined using parameter fitting, where the test bench has been rebuilt in Dymola, which is described in section 3.2. The fitted thermal parameters are based on original electrode stack parameters from literature [108,111], where Kim et al. and Zhao et al. considered the positive/negative electrode material and separator independently. Here, the electrode stack has been considered as a single thermal element in each discretised thermal element, therefore a fitting algorithm is necessary to validate the parameter. The fitted thermal conductivity & heat capacity of electrode stack are close to the values in the literature, with same order of magnitude. The measured current, voltage and temperature signals, including the ambient temperature signal, are imported into the model. The current and ambient temperature signals are used as boundary conditions during the simulation, while the measured cell surface and pin temperatures are used for comparison with the corresponding signals of the cell model and thus to calculate the optimisation objective. This model, converted to a Functional Mock-up Unit (FMU) [217], is used in a Python script to determine the optimal material values of the electrochemical cell elements. To run the FMU the python package *FMPy* [218] is used. For the parameter optimisation the differential evolution algorithm from the package *scipy.optimize* is used.[219] It is assumed that the fitted material data take into account the cell-internal heat transfer resistances and therefore do not need to be considered separately.

| **Material** | **Thermal conductivity [W/(mK)]** | **Density [kg/m³]** | **Specific heat capacity [J/(kgK)]** | **Comment** |
|---|---|---|---|---|
| Aluminium, pure | 180 | 2700 | 910 | From [58,203], used for current collectors |
| Aluminium, Alloy | 77 | 2700 | 910 | Fitted, used for casing |
| Copper | 398 | 8960 | 385 | From [58,62,108,203], used for current collectors |
| Brass (CA121) | 123 | 8470 | 380 | From [105,202], used for busbars |
| Jellyroll (Anode + Separator + Cathode) | 0.164 | 1900 | 693 | Density: datasheet from cell manufacturer<br>Thermal Conductivity & spec. heat capacity: fitted based on [108,111], used for electrochemical cell |

*Table 4 Material properties used in the thermal model.*

| Component | Thickness (of one layer) [mm] | Comment |
|---|---|---|
| Neg. current collector | 0.0154 | Number of layers = 52 |
| Pos. current collector | 0.0195 | Number of layers = 52 |
| JR layer (Anode, Separator, Cathode) | 0.3216 | Number of layers = 103 |
| Casing | 0.779 | |
| Neg. welding | 26 * 0.0154 | |
| Pos. Welding | 26 * 0.0195 | |

*Table 5 Cell component dimensions, measured from cell dismantling experiment*

## 5.4. Experimental

### 5.4.1 ECM parameterisation experiments

The ECM parameterisation experiments are identical to the tests in the Chapter 4, including ambient temperatures set-up, thermal chamber, battery cycler, pre-cycle set-up, testing profile and thermal insulation condition set-up. The surface temperature and the cell pin temperatures (TC_C1- C5 & TC_P1-P2) are measured using the same data recording method.

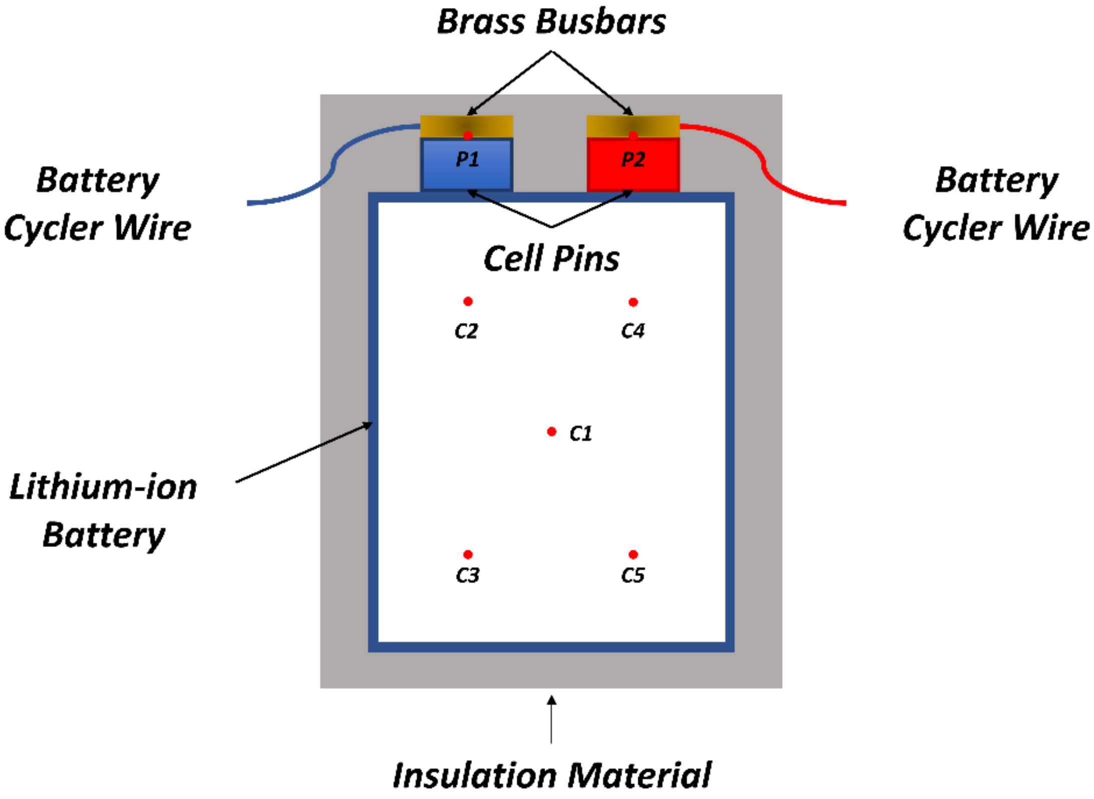

*Figure 54 Parameterisation experiments & Drive cycle experiment testing rig demonstration*

The pulse discharge tests were carried out to generate data for the ECM parameter identification in this work. The test involves repetitions of a constant current discharge pulse at 1C (90A) followed by a resting period of 2 hours. This process starts from 100% SoC and finishes till the voltage reaches 2.5V. The SoC step length is 1% (9Ah) for 0% -10%, 90% - 100% SoC, and 5% (4.5Ah) for 10% - 90%. The current input and the corresponding voltage response are shown in Figure 42 in chapter 4.

The model training results are given in Figure 42 in chapter 4. The 10 °C, 30 °C and 40 °C experimental data, model training results, the detailed parameter identification procedure, a detailed data analysis and mathematical equations are given in the chapter 4.

### 5.4.2. Adiabatic condition validation experiment: Drive cycle

On the same testing rig, as shown in Figure 54., the model and the parameters (both electrical and thermal parameters) are validated against a bespoke noisy load based on the US06 drive cycle current profile but with an enlarged average current value and extend test time. The Figure 56. in section 5.5.1 demonstrates the current profile examined, the measured and simulated voltage and cell surface temperature responses, respectively. The cell was pre-charged to 100% SoC, with a 1C (90A) CC-CV charge.

### 5.4.3. Cell cooling coefficient experiments

A same but brand new cell (same manufacturer & same batch) is investigated in this section. A schematic of the experimental testing rig used for the CCC experiments is shown in Figure 55. The cell pins are connected with 2 brass busbars and sit within the bottom insulation shell. All the thermocouples attached to the testing rig were adhered using thermal epoxy (1.22 $W.m^{-1}K^{-1}$), unless specifically stated. Temperature mesurements were recorded using 4 Pico Technology data loggers (Model: TC-08) with K-type thermocouples. The entire testing rig sat on the bottom shelf of a thermal chamber (Binder, model KB400), with forced convective air control. One end of each brass busbars is connected to the cell, using ring terminals. On the other end, the busbars are connected to the battery cycler (Maccor, Model: Series 4000) with ring terminals attached to 2 copper wires (insulated copper wires with a radius of 7.5 mm) accordingly. At both ends of the brass busbars, the set-up was tightened using set screws, to a 12 Nm with a torque wrench. This configuration set-up was found to minimise electrical resistance. In the results and discussion section, the featured model still considers the extra electrical resistance caused by the set-up.

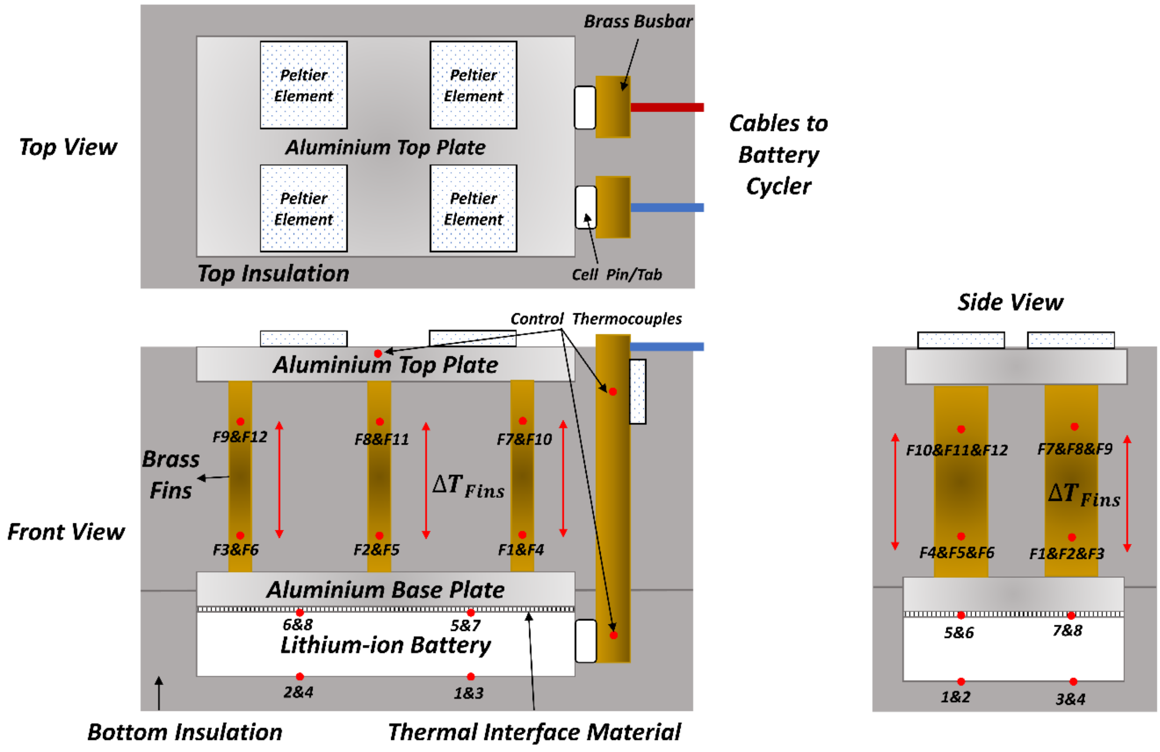

*Figure 55 Experimental testing rig for Cell Cooling Coefficient tests and thermocouple locations for the cell.*

There are 4 thin-leaf K-type TCs (TC 6-8) placed on the top surface and held in place with thermally condictive kapton tape. TC 6-8 had a thickness of just 50 µm and a width of 3.2mm. Such small thickness ensures a flat and even contact between the aluminium base plate and the cell. There is also a layer of 0.5 mm thick thermal interface gel (8 $W.m^{-1}K^{-1}$) between these 2 interfaces for an improved consistency. The TC 1-4 were adhered to the bottom surface of the cell.

The top and bottom aluminium plates are identical, with the same surface area as the cell (200.5 x 130.3 mm), and a thickness of 19 mm. These aluminnium plates (Aliminium alloy 6082T6) have a high thermal conductivity (180 $W.m^{-1}K^{-1}$), which ensure a uniform cell surface temperature and uniform heat distribution through 6 fins. The 6 brass fins were adhered into the base and top plates slots (5mm), with a length of 90 mm individually. Therefore, the adjacent faces of the top and base aluminium plates are 80 mm away from each other. Each cell side TC ( TC_F1-6) are located 65 mm from its corresponding control-side TC (TC_F7-12).

The insulation material used was milled Styrofoam (0.033 $W.m^{-1}K^{-1}$), to ensure a purely conductive system bounded by the insulation's exposed faces. The Peltier elements (PE) were attached and adhered to the top surface of the top aluminium plate as well as the top end of the brass busbars. PE were used to set the control temperature of the system. The PE on the aluminium cooling plate maintain a consistent thermal boundary condition. The PE on the busbars aim to match the cell temperature, in order to minimise heat transfer along the busbars (i.e. avoidable errors). Unavoidable heat loss through the insulation, wires, gaps/holes for wires was minimised but accounted in the simulation and data analysis.

The experimental procedure is based on previous work. [105,202] where the cell underwent a square wave pulsing current profile for heat generation, with a zero average current input. Therefore the SoC of the tested cell oscillates within a narrow range around a constant of 50%. A total of 6 current magnitude are tested in this study, which induced varying rates of heat generation in the tested cell. The current magnitudes are 0.67 C (60A), 1C (90A), 1.11C (100A), 1.22C (110A) and 1.33C (120A).

The cell was rested for 16 hours, to ensure a thermal equilibrium at control temperature. The controlled temperature $T_{con}$ is applied to the top aluminium plate. The thermal chamber is held at $T_{con}$ to minimise the variance of the insulation losses. The OCV of the tested cell was measured at beginning and end of each test at the controlled temperature, which ensures there was no SoC change after each test. Also, at the end of each test, there is a capacity check to ensure there was no noticeable degradation to the tested cell. The test procedure is detailed below:

1. 16 hours rest, to ensure thermal equilibrium at $T_{con}$ across entire testing rig
2. Square wave current pulsing at 1 Hz, centred around zero and with test specific current magnitude, for 6 hours. The time duration of each CC charge and discharge within the square wave is 5 seconds
3. 2 hours rest to reach consistent thermal conditions prior to capacity check
4. 1C (90A) CC-CV charge to 3.65 V with a C/50 (1.8A) cut-off, flowed by 2 hours rest
5. 1C (90A) CC discharge to 2.5 V, followed by 2 hours rest
6. 1C (90A) CC-CV charge to 3.65 V with a C/50 (1.8A) cut-off, flowed by 2 hours rest
7. 1C discharge to 50% SOC, followed by a 2 hours rest

## 5.5. Results and discussion

### 5.5.1. Adiabatic condition validation

The boundary conditions detailed in section 5.4.2 & 5.4.3 were reproduced in the simulation, with a cell discretisation of L4 x W6 x T8 (192 nodes). Detailed modelling boundary conditions are attached in the Appendix 2. In Figure 56a., the input current is shown, Figure 56b. and 56c. demonstrate the corresponding measured & simulated terminal voltage data and simulated results. For the electrical model, a good alignment between experimental data and the simulated results is shown, which delivers an overall RMSE of 8mV. The large error spikes at time step of 2500s (29.81 mV) and 3400s (23.97 mV) are from long resting periods with no current input. The priority of this work was accuracy under load, when heat is generated, to validate the discretised thermal model. Therefore, the electrical model is considered acceptable.

Figure 57a. & 56b. present the measured and simulated cell surface thermal behaviours, specifically at the cell surface centre and the cell positive & negative terminals (TC_C1, TC_P1-P2 in Figure 54.). It is shown that across the entire cell surface, the model is able to capture the temperature distribution well with a RMSE of 0.16 °C, 0.38 °C and 0.99 °C at cell surface centre, cell positive terminal and negative terminal, respectively. The results indicate that the overall cell stack heat capacity (together with the insulation and power cables) simulated in the model matches well with the experimental set-up. Therefore, the model is considered acceptable for implementing the more dynamic thermal analysis for the CCC.

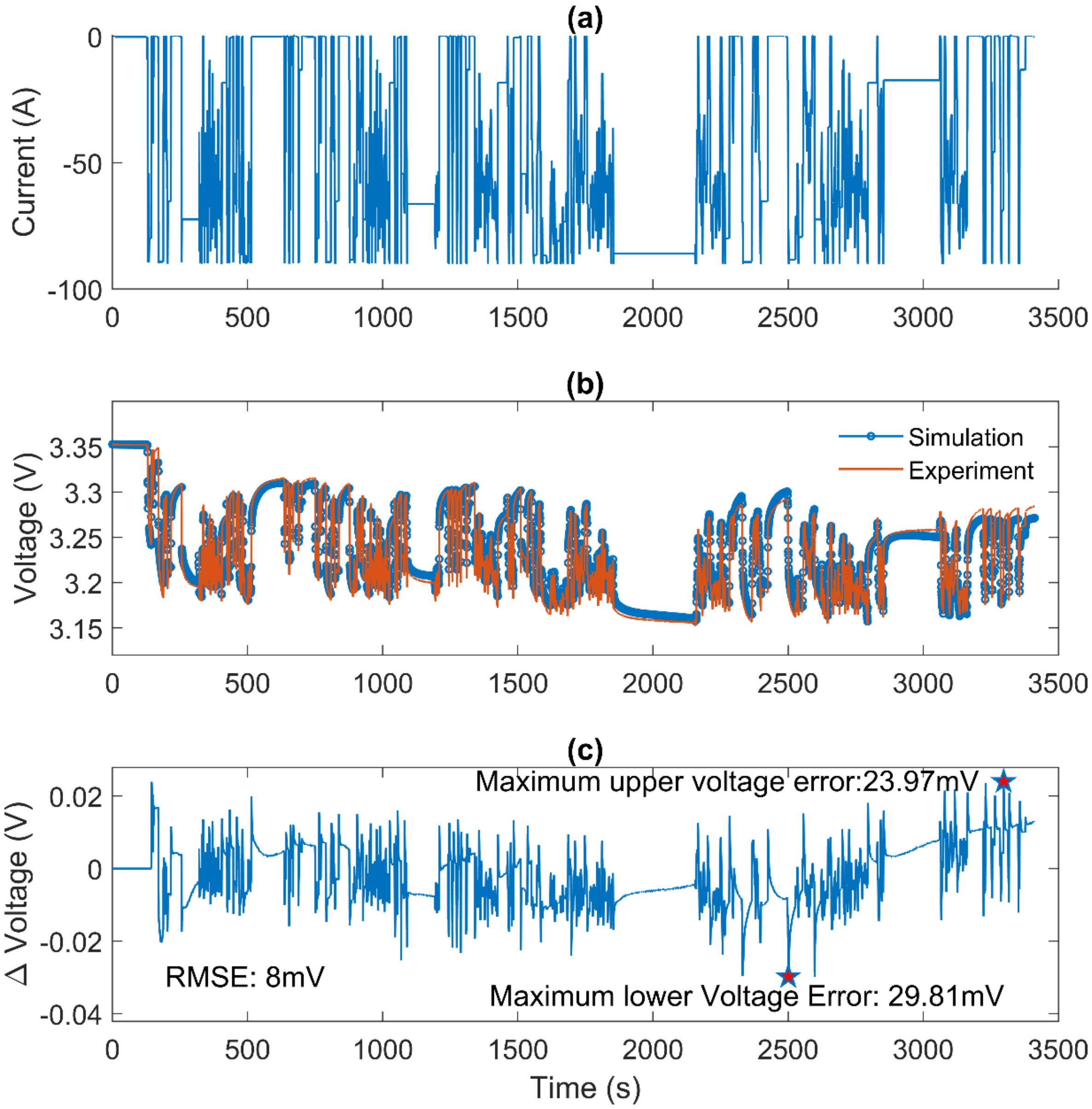

*Figure 56 Validation results for adiabatic condition, where a RMSE of cell terminal voltage of 8mV is achieved: (a) Input Current, (b) Terminal Voltage: Experimental data vs model simulation, (c) Delta voltage error between simulation and experimental data.*

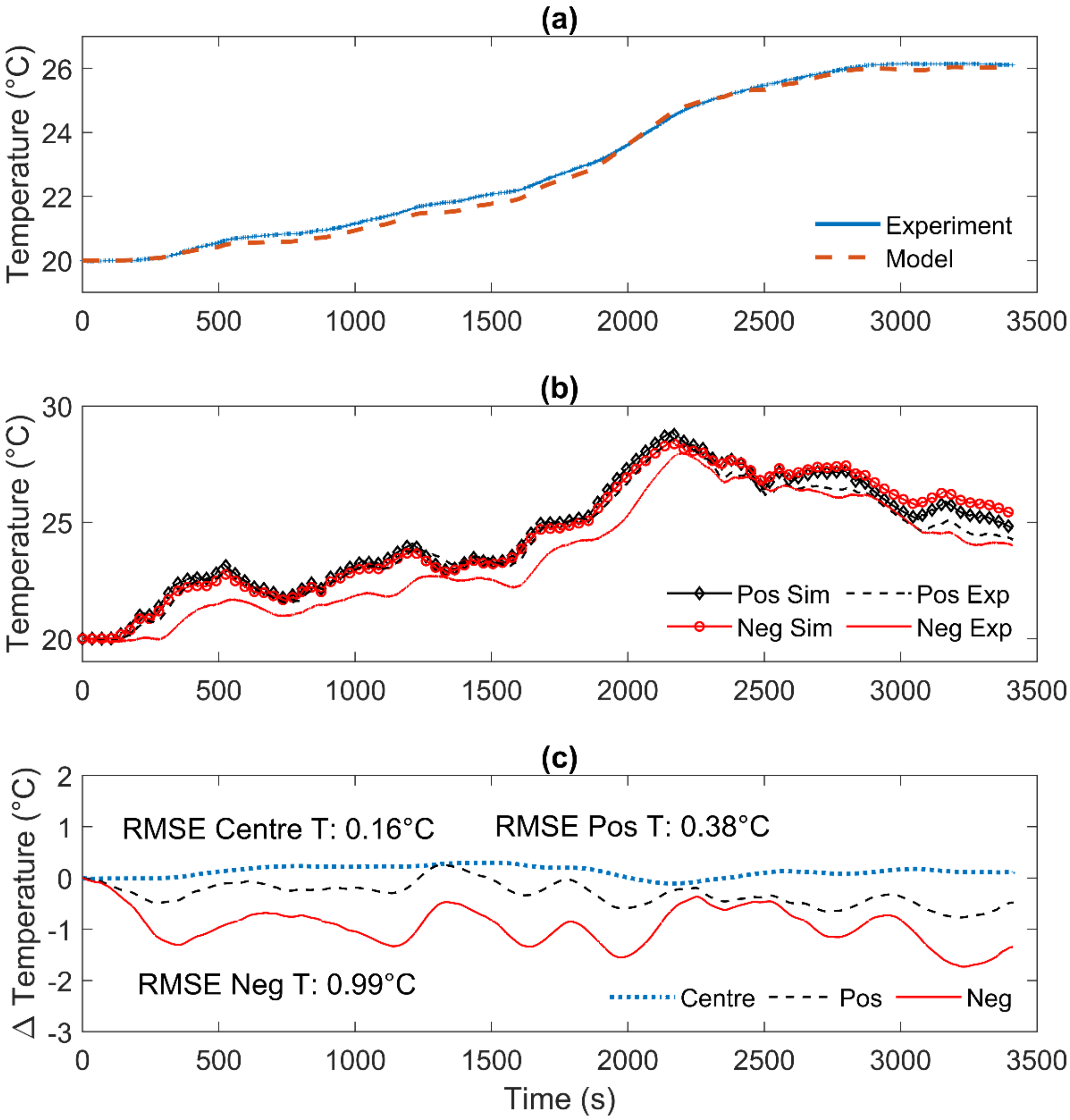

*Figure 57 Validation results for adiabatic condition, where the cell surface temperature RMSE of 0.16 °C, positive pin temperature RMSE of 0.38 °C and negative pin temperature RMSE of 0.99 °C are achieved: (a) Cell surface centre temperature Experimental data vs model simulation, (b)Cell terminal temperatures Experimental data vs model simulation, (c) Delta temperature error between simulation and experimental data for (a) and (b).*

With the benefits of 3-dimensional modelling, the ability to investigate thermal gradients in different directions is achieved. Figure 58a. & 58b. describe the 2D internal temperature profiles shown in Figure 59. & Figure 60. accordingly. Figure 59 presents the thermal distribution of the central jellyroll layer (e.g. x-y axis). At the beginning of the drive cycle, the cell is fully charged and reaches thermal equilibrium at 20 °C. While the cell underwent the drive cycle input current, the entire internal temperature level rises while the hottest region gradually evolves near the top part of the cell, as indicate in Figure 59b. This large amount of heat is generated from the large value of current load through the internal resistance of the cell terminal & power cables. At the end of the drive cycle shown in Figure 59c., the heat is generated, accumulated and propagated to the centre of the cell. In Figure 60, the cross-sectional thermal distribution (e.g. x-z axis) is demonstrated. Similar phenomena are overserved here, where the hottest region is the centre of the jellyroll. However, the largest thermal gradient is less than 0.2 °C in such near adiabatic condition. In the CCC analysis, larger thermal gradient is artificially generated for a better understanding of thermal management under more aggressive operating conditions.

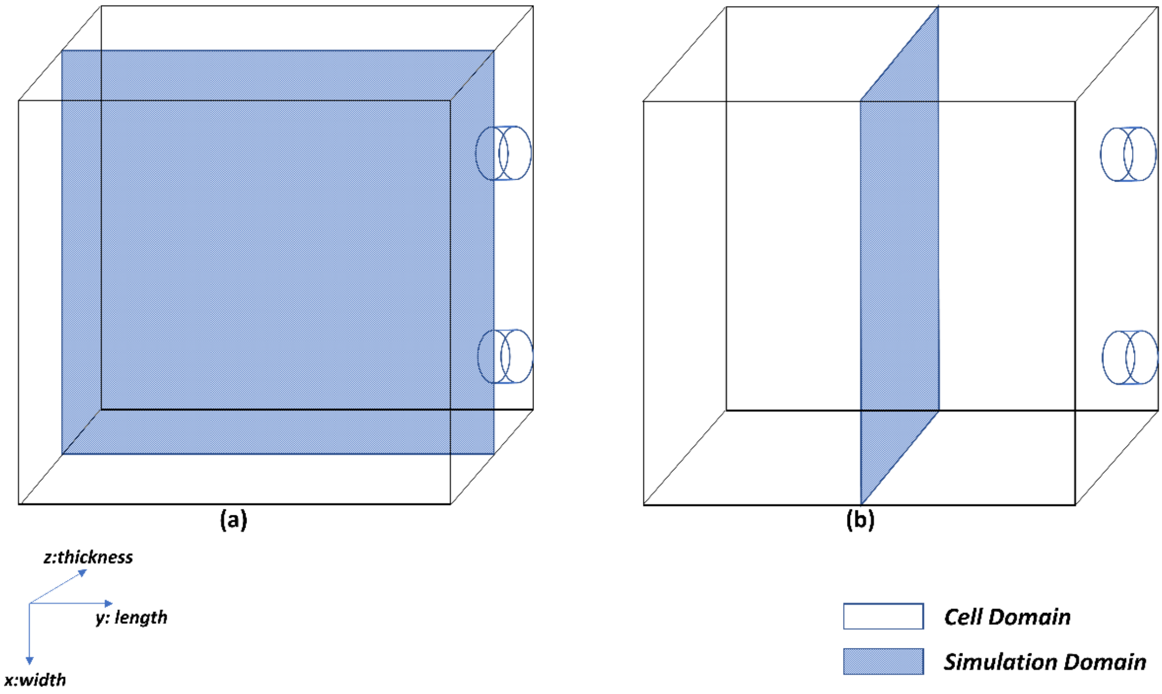

*Figure 58 Cell internal state domain & simulation domain demonstration: (a) x-y axis interface, (b) x-z axis interface*

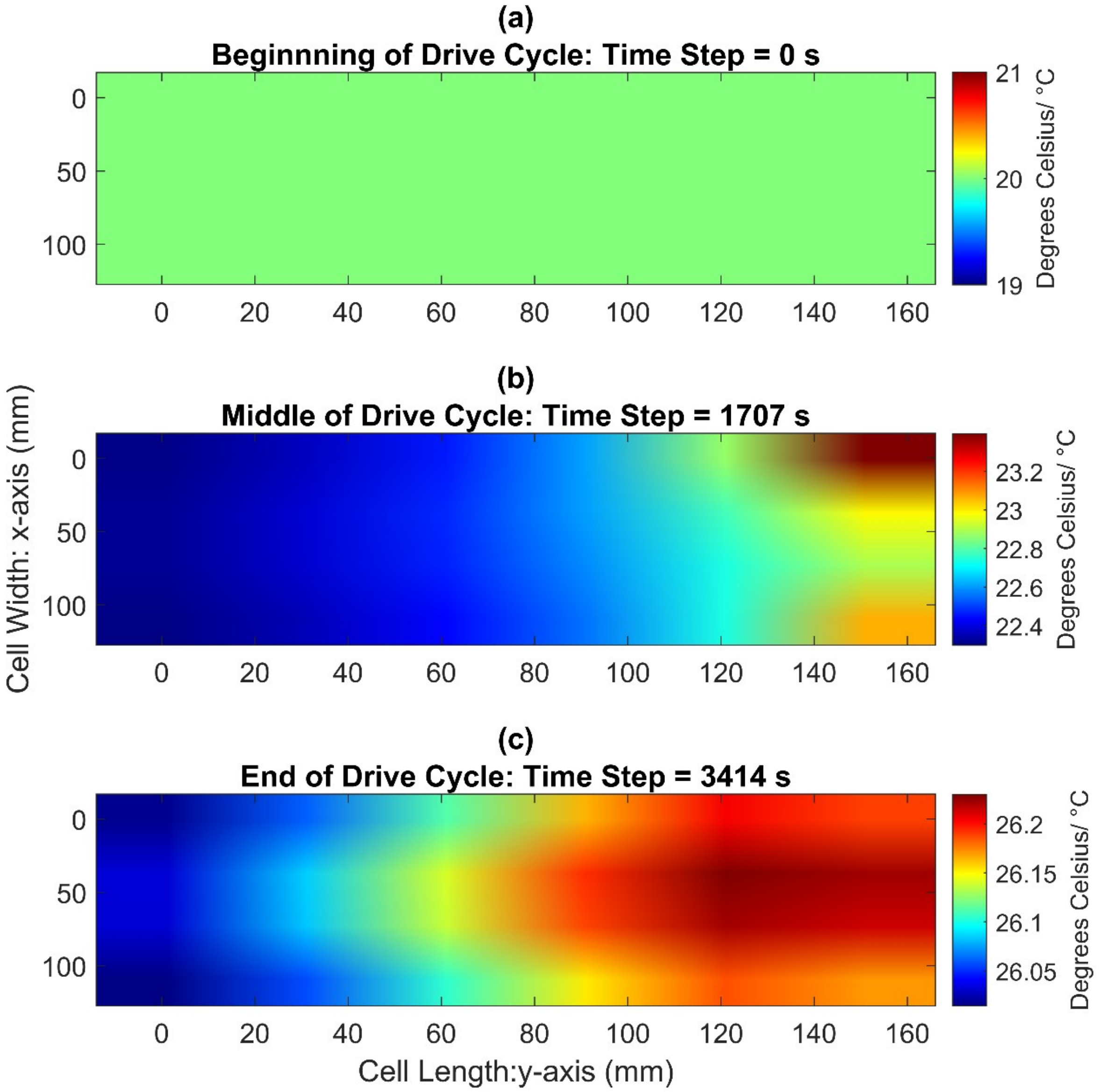

*Figure 59 Simulation results for adiabatic condition, cell internal temperature distribution in x-y axis domain (a) at beginning of the drive cycle, where t = 0 s, (b) at middle of the drive cycle, where t = 1707 s, (c) at end of the drive cycle, where t = 3414 s*

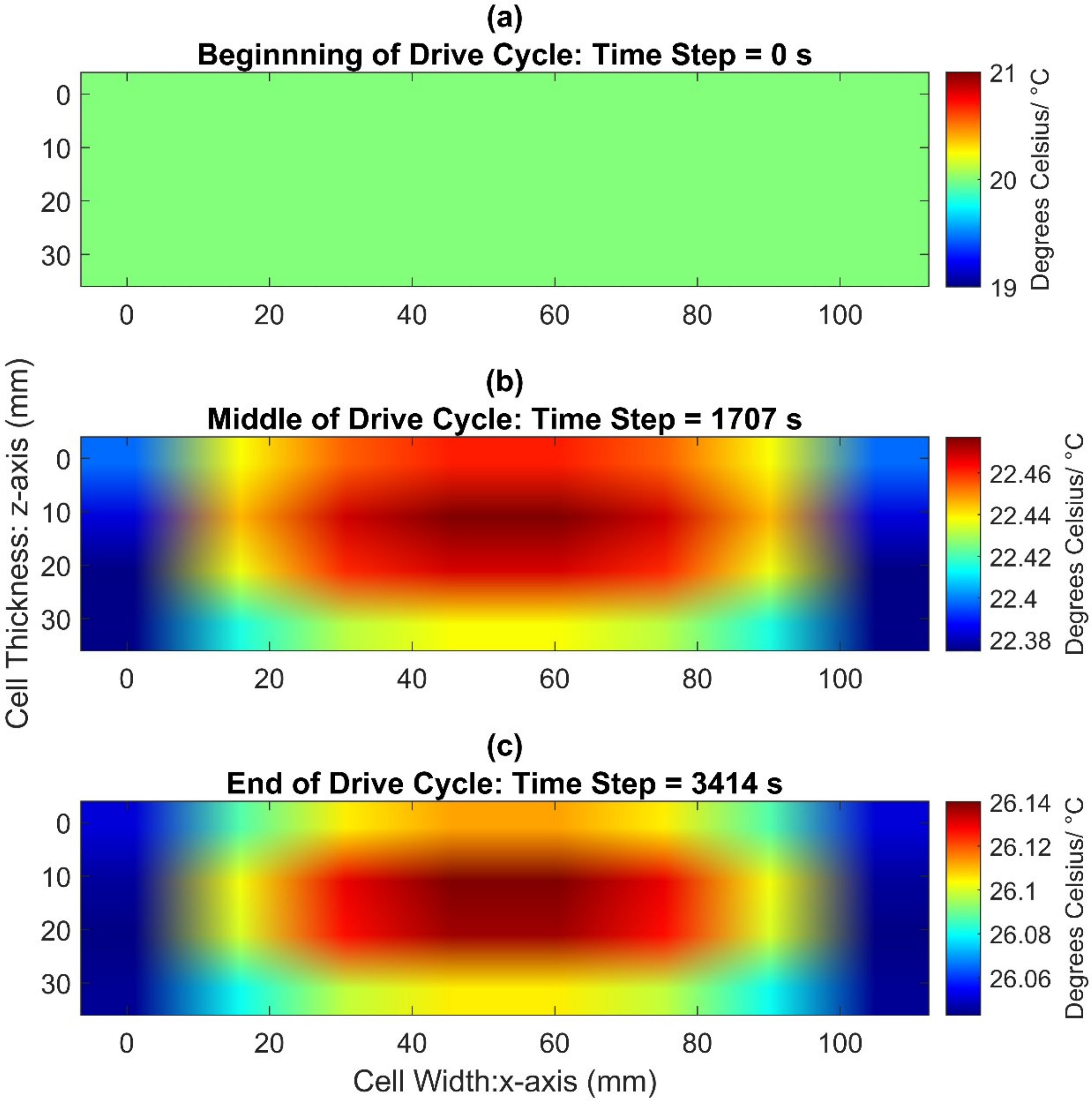

*Figure 60 Simulation results for adiabatic condition, cell internal temperature distribution in x-z axis domain (a) at beginning of the drive cycle, where t = 0 s, (b) at middle of the drive cycle, where t = 1707 s, (c) at end of the drive cycle, where t = 3414*

## 5.5.2. Cell cooling coefficient validation

The cell has been tested using CCC square wave heat generation testing procedure, using currents from 45A to 120A, while the model has been amended into the same boundary conditions as showed in Figure 55. The inputs for the model include as follows: input current recorded from the battery cycler, the ambient temperature of the thermal chamber, the controlled temperature at the aluminium top plate and the loss to the environment of the cell heat generation, due to the imperfect insulation.

The apparatus is characterized in the same method as the previous works, achieving a 76.3% efficiency of desired heat pathways compared to undesired. [105,202] This is significantly lower than previous measurements for a pouch cell with smaller surface area (94.6% for a 5Ah Kokam High Power Pouch cell SLPB11543140H5 [105], based on similar apparatus with a smaller size). This is because the large surface area and the higher thermal conductivity of the metallic casing of prismatic cells introduces significantly larger undesired losses. However, these losses can still be accounted for. In this work, low currents were used to reduce the heat generation rate, and therefore achieve a more precise heat generation rate captured through the brass fins.

In Figure 61, the experimental data and simulation results for the voltage response for the pulsing current are presented, with a good match between measured and simulated values where a RMSE of 2.6 mV is achieved. As mentioned in the parameterisation section in the supplementary material A, the underload RC network parameters deliver good fitting for the test like CCC (pure constant current underload), as the focus of this work is essentially on the estimation of loss power generation, and therefore heat generation.

In Figure 61c., the shrinking voltage range over time is due to the relationship between the cell internal resistance and temperature. As the heat generation pulsing test is ongoing, the average temperature of the cell increases, decreasing cell internal resistance. As a result, the voltage operating range decreased. After a certain amount of time (e.g. 20000 s), the cell reached the thermal steady state, where the cell average temperature, cell internal resistance and the voltage operating range stabilised. (Please note, for all the results in Chapter 5, the switching RC functioning parameterisation method is used, as for specific RC values for underload and relaxation differently, E.g. the CCC uses only the underload training results of RC values while the model developed in this chapter doesn’t support switching look-up table functions )

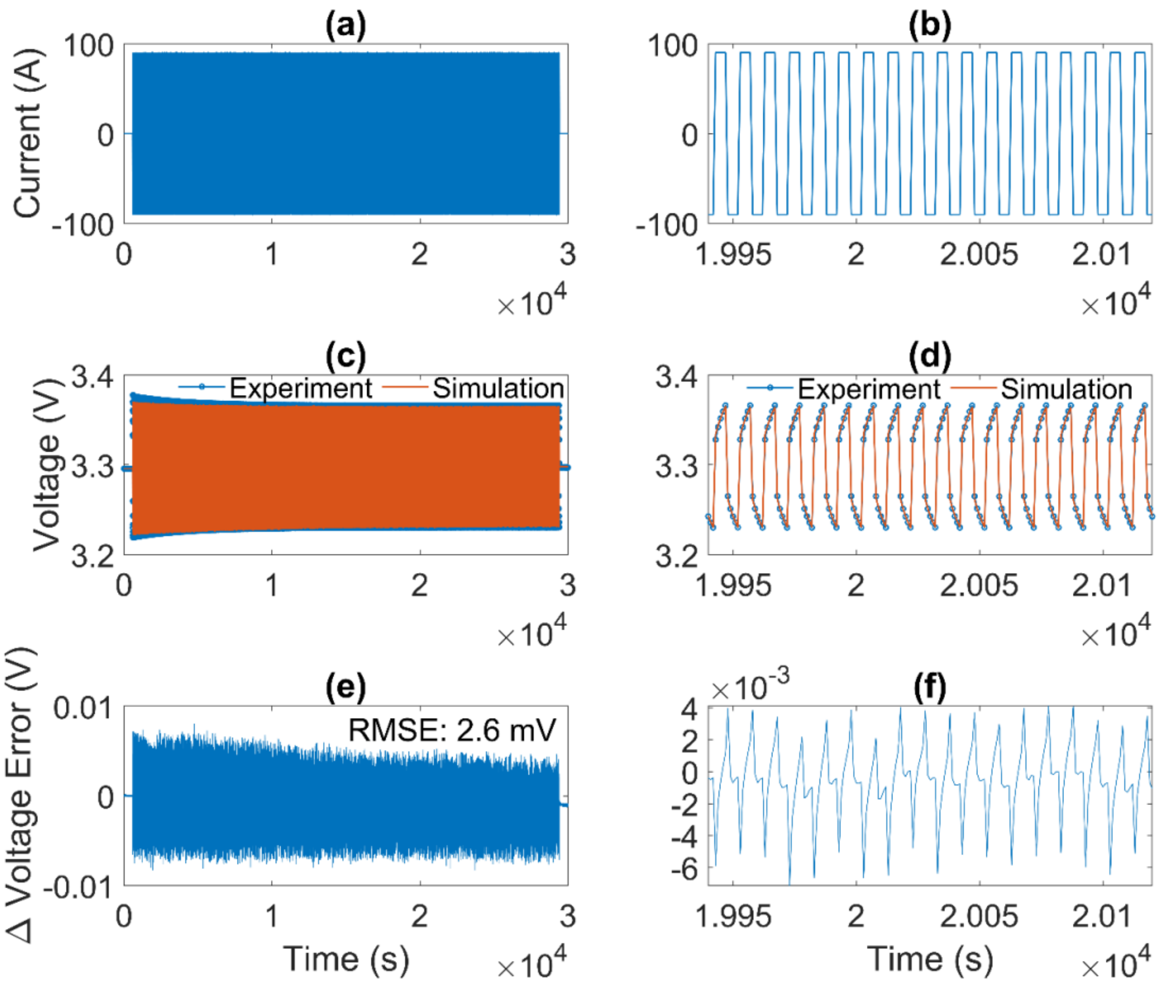

*Figure 61 Validation results for CCC Pulsing heat generation tests at 90A, where a RMSE of cell terminal voltage of 2.6mV is achieved: (a) Input Current, (c) Terminal Voltage: Experimental data vs model simulation, (e) Delta voltage error between simulation and experimental data; (b), (d) & (f) are the zoomed segment of data from Time = 19940 s to 20110 s for (a), (c) & (e) respectively.*

Determination of the CCC metric requires that the rate of heat generation within the cell is equivalent to the heat rejection from the cell when the system reaches its thermal steady state. Further, another critical assumption has been made in this work, based on previous published work[105], that the convective heat transfer is negligible within the apparatus. The airflow within the system (around the cell) was eliminated by the insulation, making this assumption justified. This boundary condition has been set into the model as well.

The average cell surface back and front temperature $\bar{T}_{Back}$ and $\bar{T}_{Front}$ can be calculated in Eq. 17 and Eq. 18:

$$\bar{T}_{Back} = \frac{T_{TC1} + T_{TC2} + T_{TC3} + T_{TC4}}{4} \tag{17}$$

$$\bar{T}_{Front} = \frac{T_{TC5} + T_{TC6} + T_{TC7} + T_{TC8}}{4} \tag{18}$$

The temperature difference across the cell, $\Delta T_{Cell}$, is the difference between mean back surface temperature with the mean front surface temperature:

$$\Delta T_{Cell} = \bar{T}_{Back} - \bar{T}_{Front} \tag{19}$$

Equation 20 and 21 summarise the rate of heat transfer through each fin (1-6), and the sum of the heat rates from all the fins delivers the conductive heat transfer through the front surface of the cell, $\dot{Q}_{Surf}$:

$$\dot{Q}_{fn} = \frac{k_{fn}}{x_{fn}} \times A_{fn} \times \Delta T_{fn}, n = 1 - 6 \tag{20}$$

$$\dot{Q}_{Surf} = \sum_{6}^{n=1} \dot{Q}_{fn} \tag{21}$$

The ratio of the front surface heat transfer rate with the thermal gradient across such cell defines the cell cooling coefficient for single surface cooling, $CCC_{surf}$:

$$CCC_{surf} = \frac{\dot{Q}_{Surf}}{\Delta T_{Cell}} \tag{22}$$

There is a good fit overall for the entire experiment, in both transient and steady state region. The model quantitatively simulated the heat generation as well as the temperature gradient of the tested cell. Figure 62 & 63. demonstrates the experimental and simulated thermal results for the 90A CCC test. The temperature gradient generated from the testing apparatus is shown in Figure 62a. It is shown that with 1C charge and discharge pulsing rate, there is a 1.51 °C thermal gradient across the cell thickness in z-axis. The simulation and experimental results align well with each other with a RMSE below 0.4 °C for both surfaces. The thermal gradient simulation shows a good fit of RMSE below 0.1 °C, which builds a foundation for an accurate CCC simulation. The CCC simulation shows a 0.4 W/K RMSE due to the relatively large error occur in the heat transfer rate simulation, where the RMSE of $\dot{Q}_{Surf}$ is 0.49W.

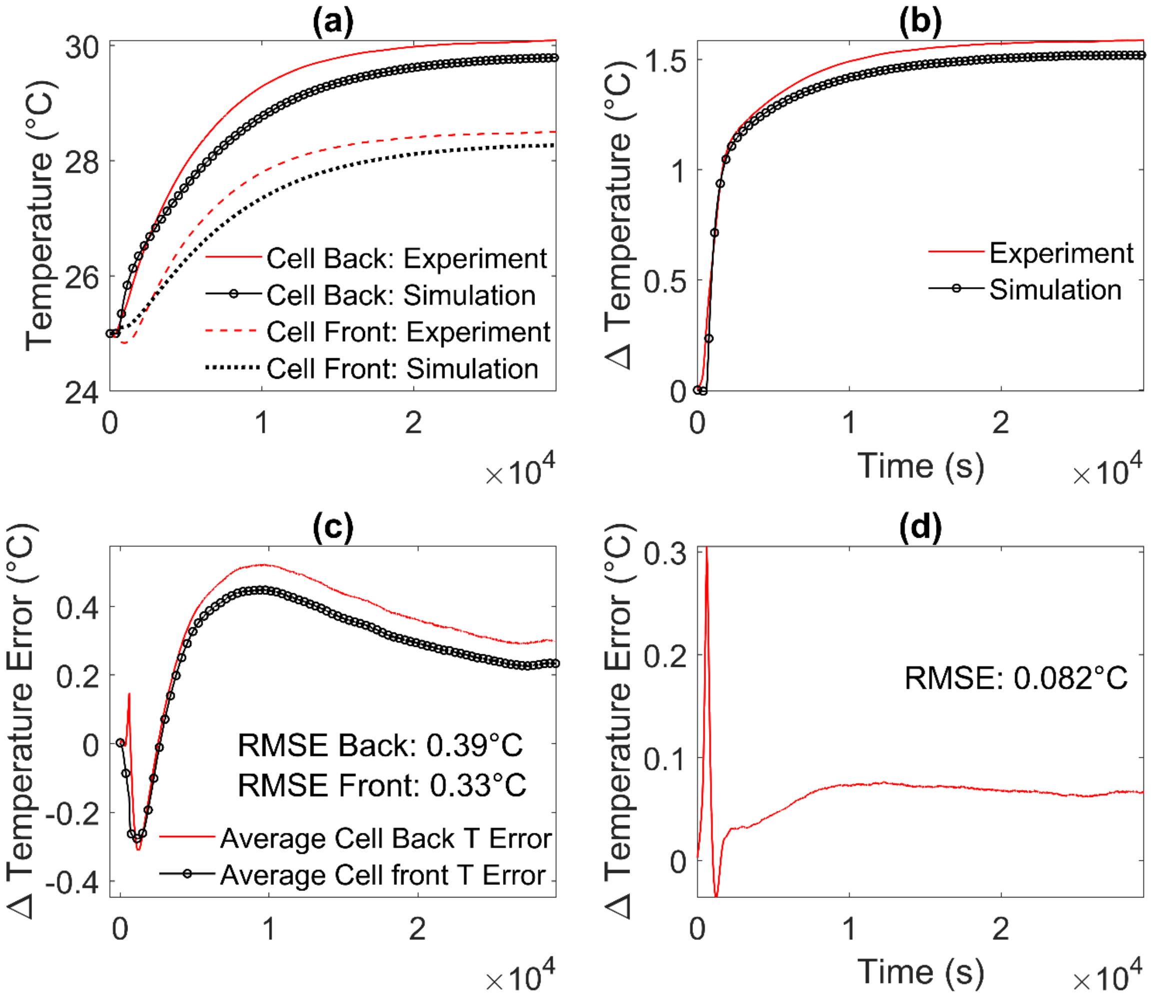

*Figure 62 Validation results for CCC Pulsing heat generation test at 90A, where a RMSE of cell front & back temperature of 0.33 °C & 0.39 °C are achieved, where the RMSE of the delta T of 0.082 °C is achieved: (a) Cell front and back temperature: Experimental data vs model simulation, (b) Delta temperature between cell front and back temperature: Experimental data vs model simulation, (c) & (d): corresponding error plots for (a) & (b)*

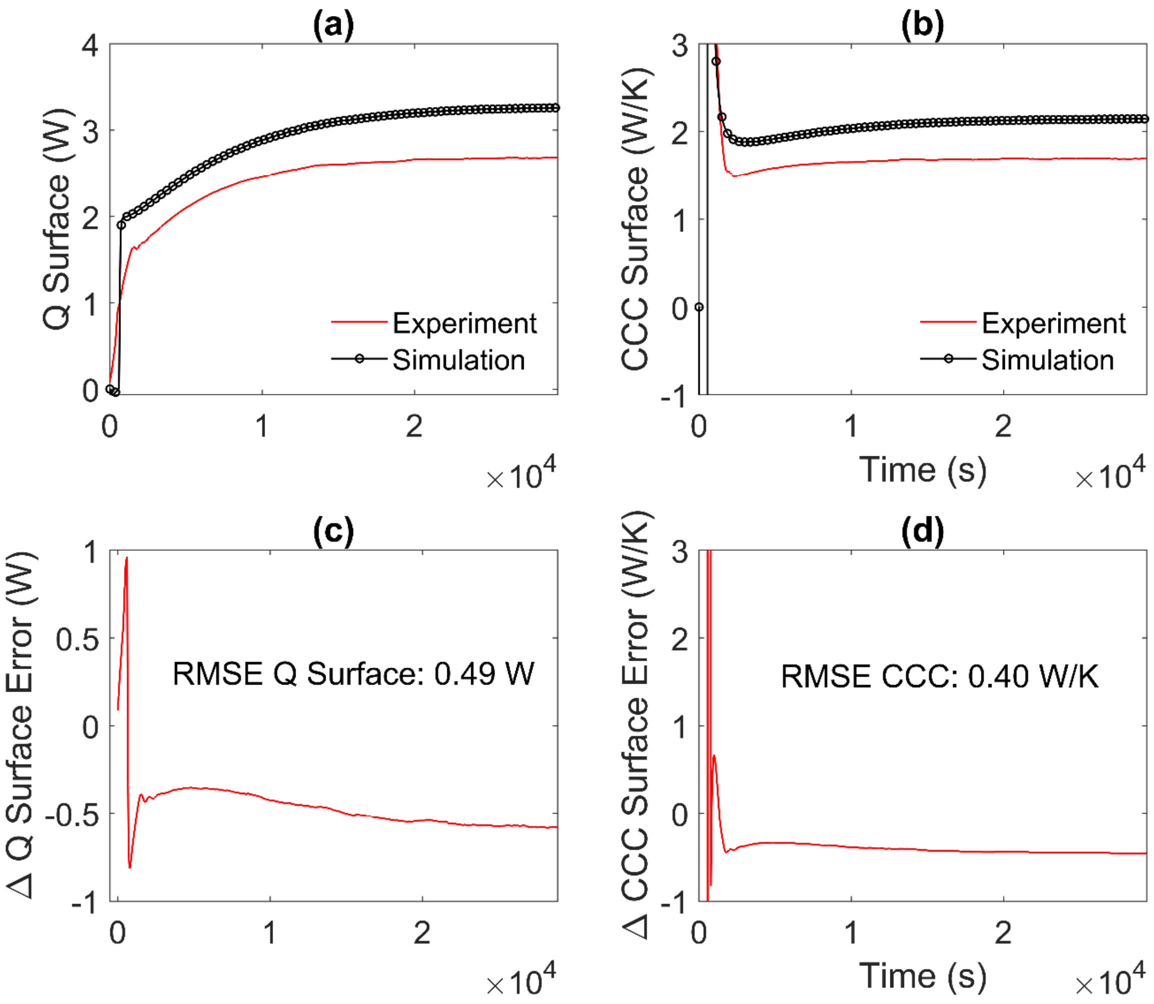

*Figure 63 Validation results for CCC Pulsing heat generation test at 90A, where a RMSE of Q Surface of 0.49 W, A RMSE of CCC surface of 0.4 W/K are achieved: (a) Sum of the Q surface through brass fins: Experimental data vs model simulation, (b) CCC surface of the cell: Experimental data vs model simulation, (c) & (d): corresponding error plots for (a) & (b)*

Figure 64 & 65 demonstrate the simulation domain & results for the internal thermal state of the 90A CCC experiments at time step of 25,000 s. The largest surface of the cell is attached to the CCC apparatus, where the heat rejection from the cell induces a thermal gradient across the cell thickness, z-axis. In Figure 65a, the model shows that an evenly distributed thermal gradient in the x-z domain has been simulated, with a validated $\Delta T_{Cell}$ above 1.5 °C. In Figure 65b, the model suggests that the region near the current collector welding points have the hottest operating temperature at thermal steady state. This is due to the large resistance of the welding, casing connection during manufacturing. The 4 control TCs and PEs on the busbar showed in Figure 55 aimed for a constant temperature at the busbar and therefore decreased the thermal gradient along the cell length to less than 1 K.

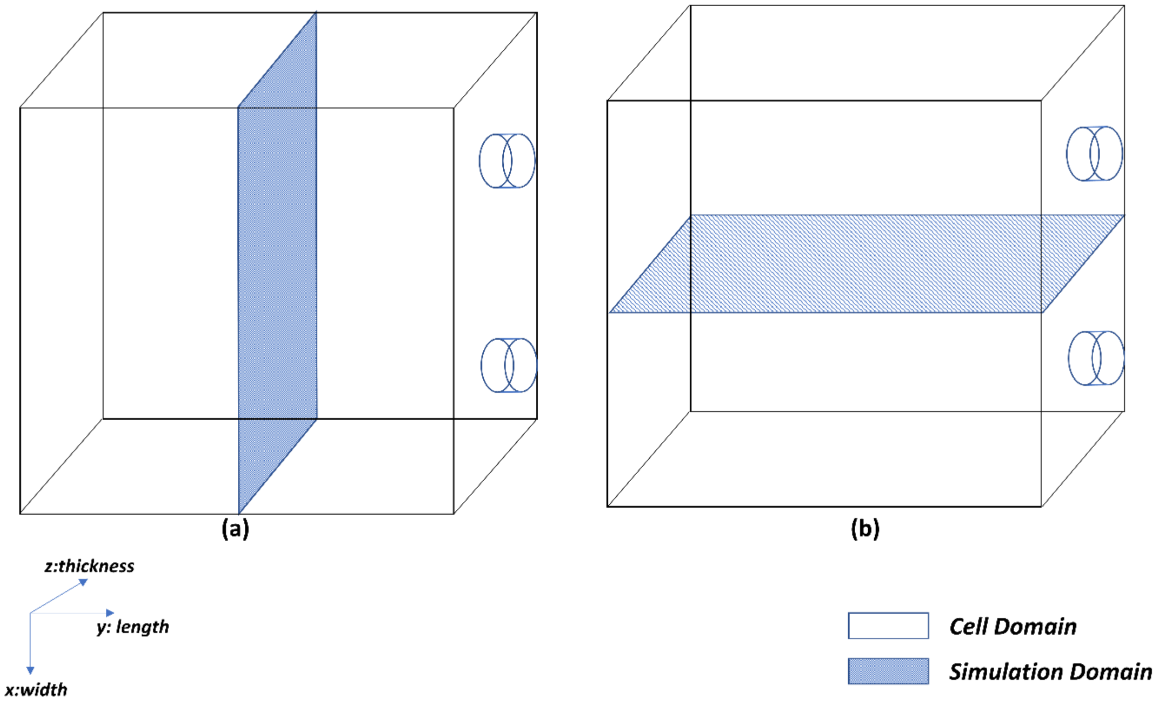

*Figure 64 Cell internal state domain & simulation domain demonstration: (a) x-z axis interface, (b) y-z axis interface*

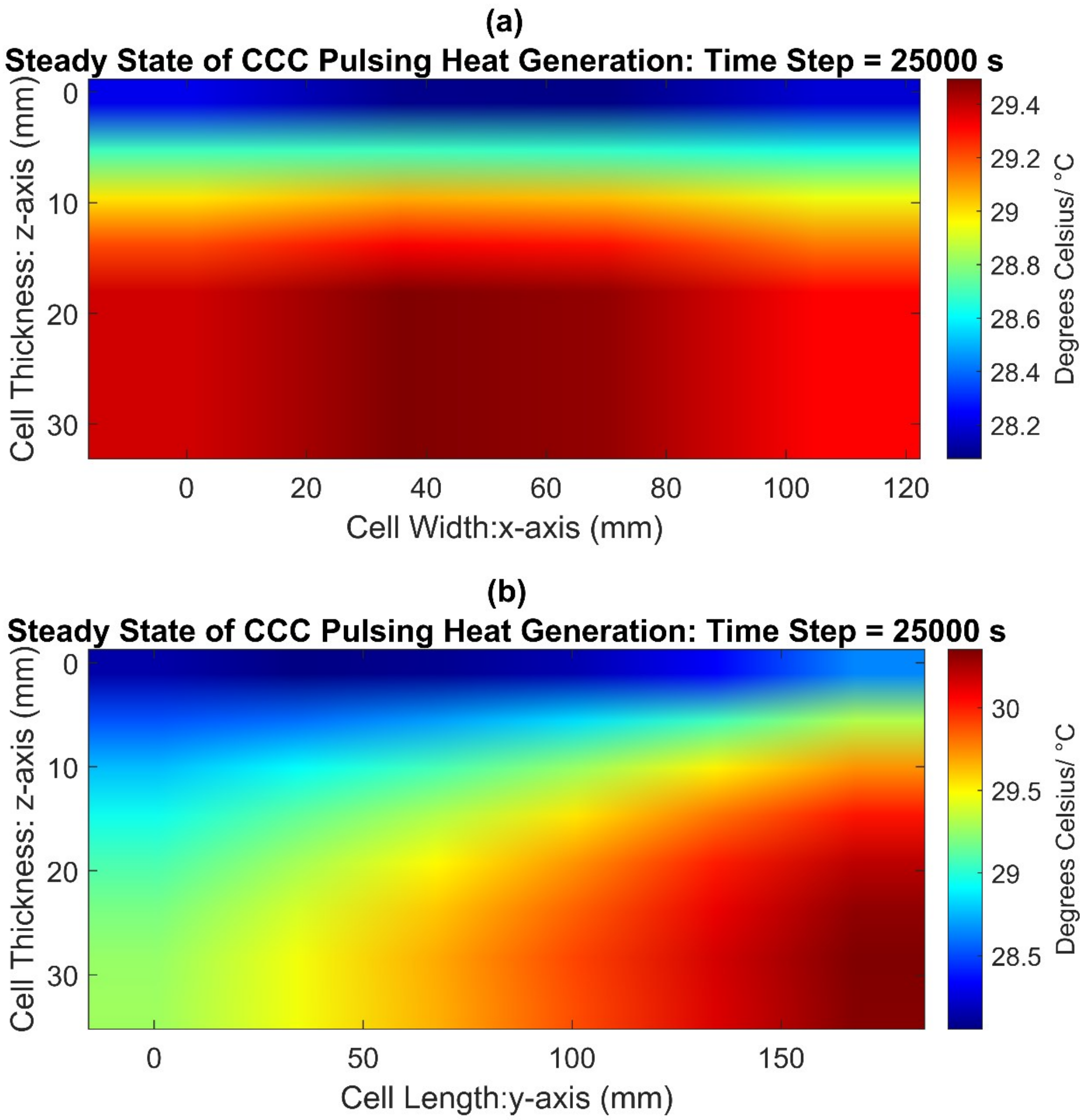

*Figure 65 Simulation results for 90A CCC pulsing heat generation, cell internal temperature distribution at thermal steady state where t = 25000 s, in (a) x-z axis domain (b) y-z domain*

However, the effect of the cell terminals cannot be entirely eliminated and therefore can still be seen in the simulation domain, particularly as both cell terminals are located on the same side of the cell. The trade-off between the manufacturing/battery pack assembling convenience with a thermal gradient along the cell length is therefore apparent. A previous study conducted by Zhao et al. [62] showed that cell terminals on opposite sides will significantly lower the thermal gradient along the cell length.

The simulated results of the internal thermal gradient suggest a similar logic, where the large format prismatic cells lead to large internal thermal gradients. Further, operating the cell at higher C rates lead to higher average operating temperature as well as higher thermal gradient across cell layers, which will therefore lead to accelerated degradation. Figure 66a demonstrates the simulated internal thermal gradient across the cell thickness in z axis at various currents. Figure 66b. shows a good agreement of the $\Delta T_{Cell}$ between simulations and experiments, with an overall RMSE of less than 0.9 K. The relationship between the pulsing current and the delta T is almost linear in both simulations and experiments.

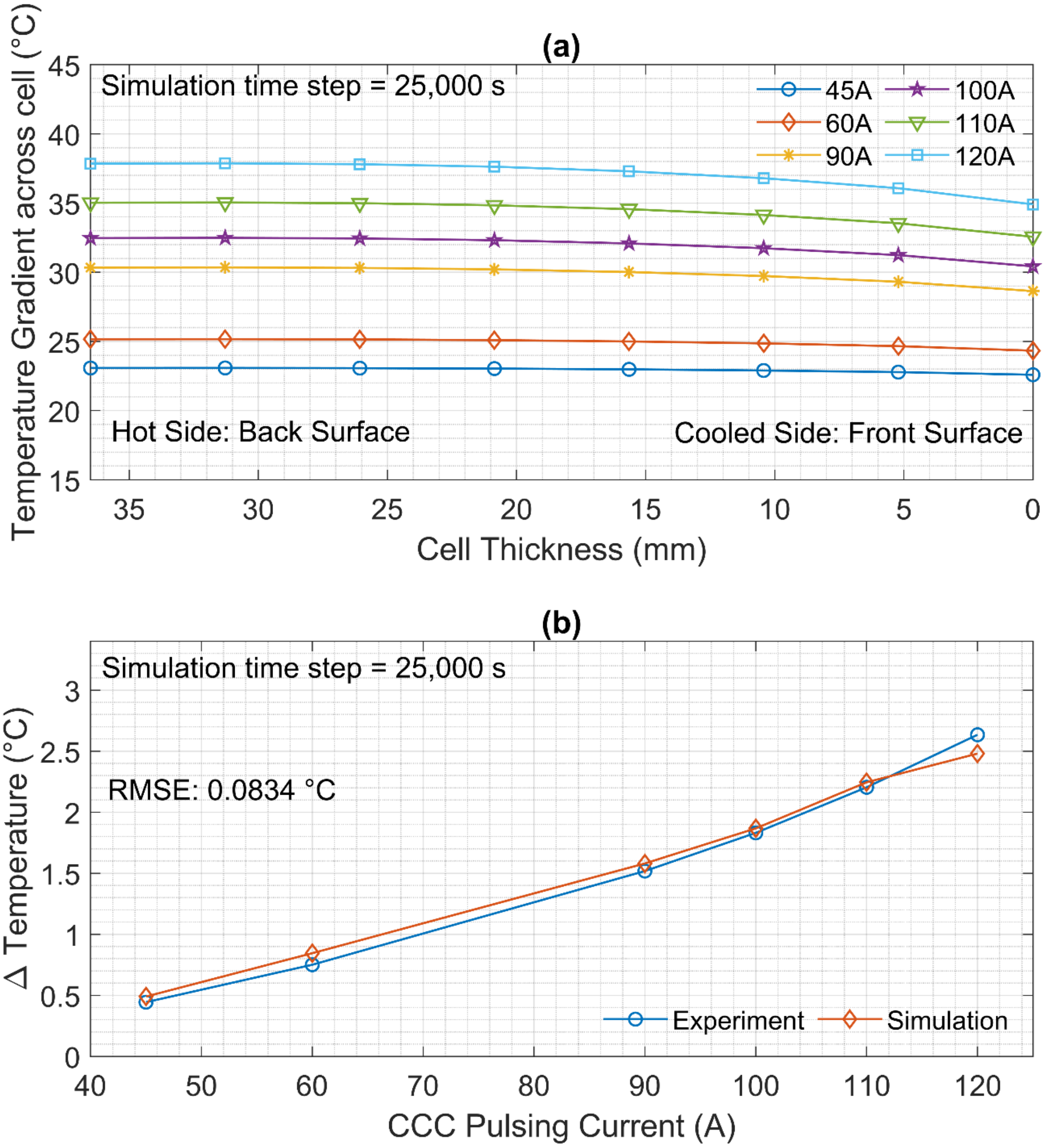

*Figure 66 Thermal gradient across cell surface in z-axis at 45A, 60A, 90A, 100A, 110A and 120A (a): Simulation results of internal thermal gradient for CCC pulsing heat generation, (b)Delta average surface temperature: Simulation vs Experiment.*

### 5.5.3. Cell cooling coefficient analysis and cell optimisation

#### *#1 Zero Ampere Cell cooling coefficient analysis*

In Figure 67, the experimental and simulated derived $CCC_{surf}$ values at various currents are shown. An overall RMSE of 0.41 W/K is achieved. A linear trend is captured for both cases: the CCC is negatively proportional to the pulsing current. Also, one noticeable phenomenon is observed that, in the large value of input currents (e.g. 90A, 100A, 110A & 120A), the change in both simulated and measured CCC is small. The vertical error bars indicate the errors from experimental measurements of the K-type thermocouples ($\pm$ 0.01 K), which results in a larger error in the $CCC_{surf}$ calculation when the Q surface is small (current input is small).

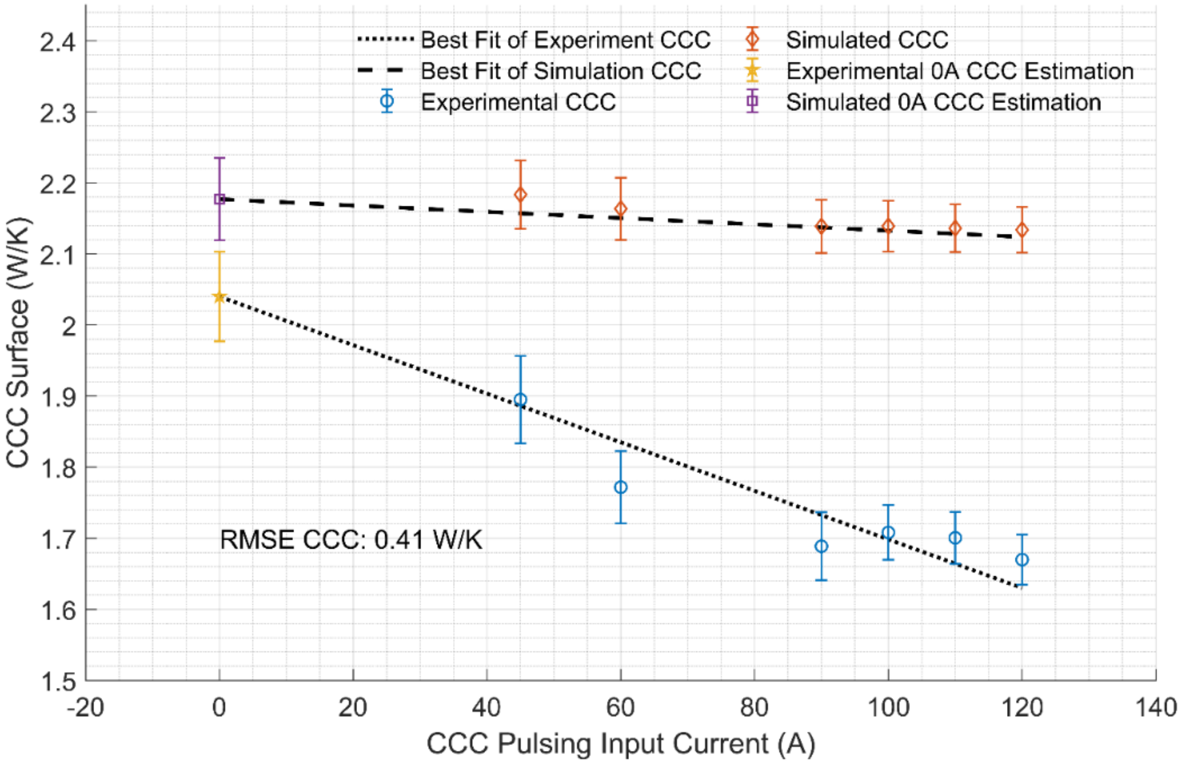

*Figure 67 The derived $CCC_{surf}$ for all experimental tests and simulation, plotted against the pulsing input currents at 45A, 60A, 90A, 100A, 110A and 120A with error bars. A linear least square line of best fit in included for each dataset, where the point of interactions with 0A input current are marked. The RMSE of $CCC_{surf}$ between experimental data and simulation is 0.41 W/K, the 0A $CCC_{surf}$ indicated a value between 2.04 to 2.18 W/K from experiments and simulation respectively.*

Similar to a previous work [105], the hotter bottom layers of the cell, as shown in Figure 65, reject a certain amount of heat through the tabs. This reduces the heat flux through the electrode-stack from the bottom layers to the top layers & subsequently the cell top surface. Consequently, a reduced $\Delta T_{Cell}$ presents higher values of $CCC_{surf}$ at lower input pulsing current (e.g. 45A & 60A). This explains the decreasing trends for both simulated and measured $CCC_{surf}$. Lower input pulsing current experiments achieved a higher value of $CCC_{surf}$, as the signal-to-noise ratio for higher current is high. This explains the different bias level & slopes of $CCC_{surf}$ between simulated and measured data in Figure 67. As in the model, the busbars are considered as passive heat dissipation components, where there is no heat flux transmitted into the cell. This leads to a smaller influence of the simulated busbars and therefore reduced difference in $CCC_{surf}$ magnitude in different C rates.

The non-linearity of the insulation efficiency causes the different slopes of $CCC_{surf}$ values in Figure 67. In all the CCC studies (including this one), the insulation efficiency is a single value which is used in various input currents and heat generation rates. In fact, larger heat generation causes a larger thermal gradient between the thermal chamber ambient temperature and the cell temperature, which leads to larger losses. This explains further why the simulation and the experiments deliver different slopes in CCC, as larger current experiment underwent a higher loss to the environment, where the simulation did not. A potential future work where a precise loss efficiency function is measured at different heat generation rates could be conducted to eliminate this issue.

The error analysis is validated through the linear extrapolation towards 0A of input current. (here Matlab function 'lsqlin' is used), assuming there is no heat generation from all the components in the apparatus, which eliminates all the errors. Values of 2.18 W/K and 2.04 W/K are captured for simulation and experiment respectively. These 0A $CCC_{surf}$ values or in other words the 'True $CCC_{surf}$' represent the cell's capability to be thermally managed, when external factors such as unwanted heat loss or ohmic heating at busbar contacts is eliminated. The model predicts the true $CCC_{surf}$ value with a RMSE of 0.14 W/K. It suggests that the model enhanced the CCC analysis by simplifying the true CCC identification process, and validated the experimental true CCC analysis method proposed previously [105] Here, a reliable true CCC value for the target cell is achieved through implementing few key boundary conditions into the model, with reduced cost and time.

## *#2 Cell Optimisation 1: Casing material analysis*

By modifying a few of the essential cell parameters within the developed model (e.g. casing material, cell thickness), cell optimisation can be conducted. The $CCC_{surf}$ can be used as the critical evaluation metric in order to redesign a cell for better thermal management.

In Figure 68a, four casing materials are investigated using the same battery jellyroll electrode stack, meaning the same internal heat generation rate at same input CCC pulsing currents. The detailed casing material thermal parameters are introduced in Table 7.

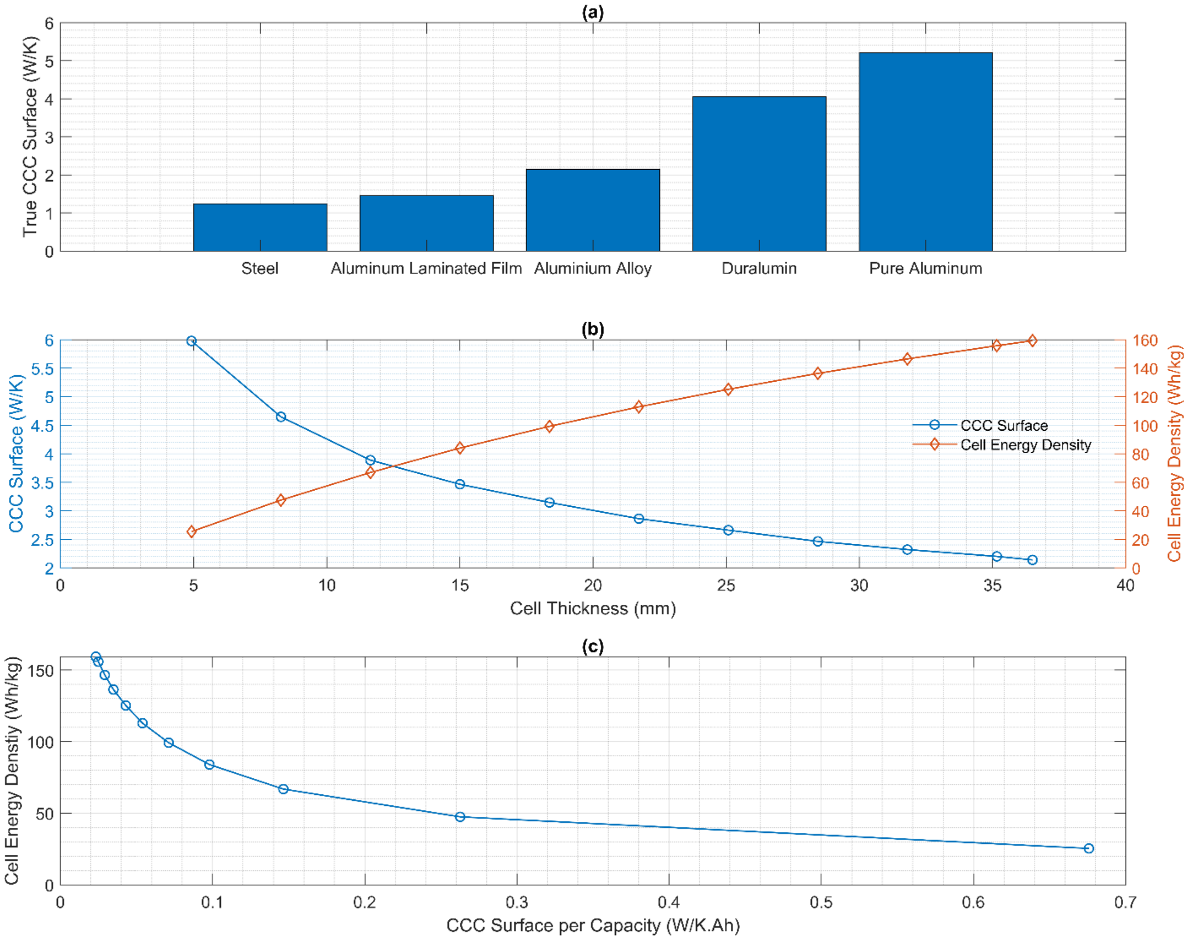

*Figure 68 Cell optimisation: (a) The derived true CCCsurf of simulation using different casing materials (Aluminium Alloy, Steel, Aluminium laminated film, Duralumin and Pure aluminium) with the same internal jellyroll electrode stack; The derived CCCsurf of simulation at different cell thickness: (b) The CCCsurf values and cell energy density at different cell thickness values, (c)the derived cell energy density plots against CCCsurf per Cell Capacity.*

The Steel casing has the largest value of density, which leads to low casing material mass to the active material ratio. Consequently, steel plays a minor role in the prismatic battery manufacturing due to the low energy density compares with other lighter material. The

$CCC_{surf}$ analysis demonstrates the effect of its low thermal conductivity, with a $CCC_{surf}$ value of around 1.24 W/K. By contrast, both pure aluminium and duralumin (aluminium alloy with improved strength) delivers significantly better $CCC_{surf}$ values, of 5.2 W/K and 4.1 W/K respectively. However, pure aluminium's hardness is low compared to many alloy materials, making alloy materials a better choice for prismatic cell casing, which considers both mechanical safety and thermal management capability. For comparison purposes, aluminium laminated film was also simulated, providing a $CCC_{surf}$ value around 1.45 W/K, which explains why pouch cells are typically far thinner than prismatic cells. These simulation results explain why a metallic casing for large format prismatic cells is necessary for thermal management, however it also provides ceiling on single cell energy density because of its weight. Therefore, a light, hard and with high thermal conductivity casing material is the ideal. The experimental validation of various casing material is out of this study's scope but would be interesting future work.

| **Casing Material** | **Density [kg/m³]** | **Thermal Conductivity [W/ (m.K)]** | **Specific Heat Capacity [J/(kg.K)]** | **True $CCC_{surf}$ [W/K]** |
|---|---|---|---|---|
| Duralumin [220] | 2770 | 177 | 875 | 4.1 |
| Pure Aluminium [62,220] | 2700 | 238 | 903 | 5.2 |
| Aluminium laminated film (0.112 mm) [62] | 2700 | 238 | 903 | 1.45 |
| Steel (1% C) [220] | 7801 | 43 | 473 | 1.24 |
| Aluminium Alloy (existing design) | 2700 | 77 | 910 | 2.14 |

*Table 6 Thermal Properties for different casing material*

### *#3 Cell Optimisation 2: Cell thickness analysis*

Figure 68b & 68c demonstrate the relationship between cell thickness with cell energy density and cell $CCC_{surf}$. (Using existing design: Aluminium Alloy) In Figure 68b, it is shown that, with reduced thickness, the cell energy density decrease is close to being linear. This is due to the increasing surface area to volume ration; the prismatic surface area (i.e. the can material) which takes a larger proportion of the cell mass at low thicknesses. By contrast, the decreased cell thickness delivers enhanced $CCC_{surf}$ values, due to the reduced number of layers of battery jellyroll, and therefore less temperature gradient across the cell thickness. In Figure 68c, the relationship between cell energy density and $CCC_{surf}$, normalised against capacity, is shown. There is an exponential decay in the normalised against capacity $CCC_{surf}$

versus cell energy density, showing that the trend towards thicker cells to achieve high energy density comes at the cost of large internal thermal gradients. This is not necessarily beneficial for OEMs nor the end users. Where is the optimum, is not known. The optimum will be a complicated function of cell design, how the cell is to be used, and thermal management system design. Hence, the development of a modelling tool capable of exploring these variables in this work, and the introduction of the CCC to be considered alongside energy density on the cell datasheet.

For example, if the cell thickness is decreased from 36.5 mm to 18.36 mm, then the $CCC_{surf}$ can be increased by 47% but at the cost of a 37% reduction in energy density. This may result in an increase in the pack level energy density if a more space and mass efficient thermal management system can be used. A detailed further experimental study on the various form factors of the cell could enhance and validate the above analysis, as a future work.

## 5.6. Interim conclusion

The study uses the revolutionary cell cooling coefficient (CCC) as an evaluation tool, together with a 3D thermally coupled discretised ECM, to deliver quantitative insights into lithium ion battery design and interactions with thermal management systems. The detailed model configuration and model development contribution explanation are attached as appendices at the end of this thesis.

The developed model is able to simulate the voltage and thermal responses for a given cell well. The RMSE of the voltage responses for drive cycle noisy load and constant current square wave load are 8 mV and 2.6 mV respectively. The thermal prediction for the noisy load across the entire cell surface and cell thickness is within 0.99 °C and 0.4 °C respectively. When simulating the surface Cell Cooling Coefficient, the RMSE for the thermal gradient across the cell thickness is below 0.09 °C and the RMSE for the empirically derived true $CCC_{surf}$ is 0.14 W/K, and $CCC_{surf}$ values of 2.04 and 2.18 W/K were measured experimentally and simulated respectively.

The CCC, as a cell evaluation metric, is used as a thermal parameterisation tool within the developed model. This single parameter delivers information on how well the cell is designed for thermal management, by quantifying the thermal gradient required across the thickness of the target cell, through the cell surface.

Here, for the first time, the relationship between the cell energy density and the ease of implementation for the thermal management system is concluded and quantified, through varying the cell thickness. By decreasing the cell thickness from 36.5 mm to 18.36 mm, an enhancement of 47% of the $CCC_{surf}$ is achieved, but at the cost of a 37% decrease in cell energy density. However, changing the casing material from aluminium alloy into aluminium with the same casing thickness would increase the CCC by 143%, with negligible impact on energy density (e.g. less than 0.1%).

# 6. Conclusion and future works

All the research questions introduced in Chapter 1 & 2 are answered in Chapter 3,4 & 5. Unlike many other studies in the literature, this thesis studies the thermal behaviour of two very different battery chemistries. It is shown that both well-commercialised LFP prismatic cells and next generation high energy density Li-S pouch cells require detailed thermal management studies, through engineering experimental techniques as well as modelling simulations. This thesis comprehensively proves that, for both new battery chemistries and even mature batteries that have been commercialised for decades, there are still significant improvements possible through a better understanding of thermal management.

## 6.1. DTV & 0D on Li-S

With the heat generation mechanism not fully understood for a certain type of future Lithium-ion battery candidate – Lithium sulfur battery, a thermal diagnostic technique Differential Thermal Voltammetry (DTV), which is widely used for conventional Lithium-ion batteries (NMC, LFP), was implemented and analysed. This kind of fast, cost-effective, easy-to-implement technique was able to track and quantify the most essential and critical challenges which restrict the development of Li-S cells, the polysulfide shuttle. It is shown that, the DTV spectra has a strong dependence on the cell temperature as well as the voltage of Li-S, giving rise to many different scenarios while charging. The DTV peaks and patterns were representative for the cell thermal state, charging rates as well as cell SoC, and therefore demonstrated the ability to provide quantitative information on the shuttle. The results showed that the polysulfide shuttle effect of Li-S is considerably stronger at higher ambient temperatures or low charging currents, corresponding to higher DTV peaks. It is suggested that the peak characteristics could be used as an adaptive safety cut-off criterion and/or to design advanced control algorithms to minimise degradation and maximise coulombic efficiency.

A physical electrochemical zero-dimensional model was upgraded to validate the experimental phenomena stated above and in Chapter 3. The model was made temperature-dependent through shuttle constant estimation, and therefore heat generation through shuttle. It was successfully used to interpret most of the observed features. The key contribution from the model is that it is capable of estimating the true capacity of the cell where is accessed by tracking the various polysulfide species. By plotting the true capacity and DTV peak positions together, it is shown that stopping charging at the DTV peak position alone is not sufficient to achieve a set charging coulombic efficiency. Therefore, a reduced order model, such as one based on the thermally coupled zero-dimensional model developed here, is recommended for implementation alongside the DTV diagnostic technique for real-world implementation.

## 6.2. Future work #1

Given the timeframe of the limited PhD time, as well as the closing of the Li-S research project (REVB) in 2017. The supply of the Li-S cells stopped when project closed. However, there are still few components are worthy to investigate further and of interest to continue:

1. An upgrade is suggested for the zero-dimensional model, to make shuttle constant a function of cycling number, and therefore degradation.
2. Using the generated shuttle constant at different cycling number to correlate the shape and evolution of DTV curves.
3. Embedding such combination of DTV and zero-dimensional onto an in-house Li-S battery pack in a BMS, to show its advantages of ease of implementation and cost-effective.

## 6.3. CCC & ECM on LFP

The thermal behaviour of the incumbent Lithium-ion batteries (e.g. LFP) is equally critical as the future candidates. While the heat generation mechanisms of such a type of battery are widely studied, new cell thermal evaluation experimental techniques, such as the Cell Cooling Coefficient (CCC) have recently been developed. The CCC can determine how well a cell is designed for the thermal management, by quantifying the thermal gradient required across the cell to achieve a required rate of heat rejection (or vice versa).

Empirical equivalent circuit models (ECM) were shortlisted and developed further in this thesis, both in the electrical parameter identification method (PIM) and thermal parameterisation (e.g. using CCC as a key thermal boundary condition). The ECM was selected due to its ease of implementation, low computational forces required and therefore great potential to be extended into multi-dimensional & multi-scale.

The proposed PIM in Chapter 4 identifies the fact that many lithium ion batteries exhibit different time constants during underload operation compared to relaxation. This is particularly pronounced in a large prismatic with lithium iron phosphate cathode studied in this thesis but is also seen at the extremes of SOC in other lithium ion batteries, particularly at low SOC where state estimation can be particularly difficult yet even more important. The approach presented in this thesis demonstrates significant improvements over a conventional equivalent circuit model without switching time constants (or with a given time constant choice during different operating conditions).

Taking the advantages from Chapter 4, the precise loss power which generates the irreversible heat in ECM, Chapter 5 presents a novel cell optimisation analysis. A fully parameterised and validated discretised Electro-Thermal ECM model is introduced. The model was used to quantify the degree of difficulty to thermally manage a Lithium ion battery through the cell surface, i.e. to derive the surface CCC using a model for the first time. A cell optimisation study based upon the CCC was then conducted to identify potential design improvements for prismatic cells to improve their thermal performance. The key conclusion is that, by varying the cell thickness and the cell casing material, the interaction between the energy density and thermal behaviour can be optimised.

The study uses the revolutionary cell evaluation tool, CCC, together with developed ECM, to delivers quantitative insights into lithium ion battery design and thermal management systems. The work should be of interest to application engineers, battery management system developers, and control engineers.

## 6.4. Future work #2

Empirical modelling has its own limitations, whilst its data-driven process is often time-consuming. Due to the limited time of the PhD, a few meaningful future works are suggested to be conducted in the near future:

1. It would be valuable to upgrade the existing thermally coupled, discretised ECM with a data-driven degradation ECM model, where the ECM embeds extra parameterisation domains: time (calendar ageing) and current throughput (cycle ageing).
2. Replacing the ECM model with a ‘fast-enough’ physical electrochemical model, to unlock more physical meaning within the cell model. A discretised electrochemical thermally coupled degradation model is proposed.
3. Extending the existing ECM, potential ECM degradation model, and potential discretised electrochemical degradation model from cell level into pack level, and ultimately power-

train level. Together with CCC technique again, evaluate and optimise the battery pack, thermal management system as a whole. Enhancing the product design for OEMs.

## 6.5. Message at the end

While the time of drafting this PhD thesis, the developed techniques (DTV and CCC) and developed models (0D and ECM) are disseminated through multiple pathways, through academic journal publications, academic and industry based conferences' presentations and poster. The ECM model is co-developed together with one of the major commercial modelling simulation companies, and soon will be available to both research community and industry OEMs. The outputs of this thesis (the articles, the models) are already in the on-going discussion with one top tier battery manufacturer and few top tier OEMs. The work, conducted and presented here is part of a paradigm shift for the industry on how to understand the thermal behaviour of lithium-ion batteries, and how to optimise and design new generations of batteries in a comprehensive, system engineering way.

# References

[1] Wikipedia, Phase-out of fossil fuel vehicles, (2020). https://en.wikipedia.org/wiki/Phase-out_of_fossil_fuel_vehicles (accessed January 17, 2020).

[2] H.Y. He Kebin, Zhang Qiang, Ming Dengli , Wu Ye , Catherine Witherspoon, Valentin Foltescu, Q.Y. , Cheng Jing, A Review of 20 years' Air Pollution Control in Beijing, Nairobi, Kenya, 2019. https://www.ccacoalition.org/en/news/beijing's-air-quality-improvements-are-model-other-cities.

[3] C. Mckerracher, Electric Vehicle Outlook 2019, (2019). https://about.bnef.com/electric-vehicle-outlook/ (accessed January 17, 2020).

[4] C. Mckerracher, Electric Vehicle Outlook 2019, (2019).

[5] T.W. Patrick Hertzke, Nicolai Müller, Stephanie Schenk, The global electric-vehicle market is amped up and on the rise, (2019). https://www.mckinsey.com/industries/automotive-and-assembly/our-insights/the-global-electric-vehicle-market-is-amped-up-and-on-the-rise (accessed January 17, 2020).

[6] T.W. Patrick Hertzke, Nicolai Müller, Stephanie Schenk, The global electric-vehicle market is amped up and on the rise, (2019).

[7] Ch.Z. Dana Hull, Elon Musk Set Up His Shanghai Gigafactory in Record Time, (2019). https://www.bloomberg.com/news/articles/2019-10-23/elon-musk-opened-tesla-s-shanghai-gigafactory-in-just-168-days (accessed January 17, 2020).

[8] H.Y. He Kebin, Zhang Qiang, Ming Dengli , Wu Ye , Catherine Witherspoon, Valentin Foltescu, Q.Y. , Cheng Jing, A Review of 20 years' Air Pollution Control in Beijing, Nairobi, Kenya, 2019.

[9] A.K. Padhi, K.S. Nanjundaswamy, J.B. Goodenough, Phospho-olivines as positive-electrode materials for rechargeable lithium batteries, J. Electrochem. Soc. (1997). https://doi.org/10.1149/1.1837571.

[10] S. Nishimura, G. Kobayashi, K. Ohoyama, R. Kanno, M. Yashima, A. Yamada, Experimental visualization of lithium diffusion in LixFePO4, Nat. Mater. 7 (2008) 707–711. https://doi.org/10.1038/nmat2251.

[11] D. Anseán, M. González, J.C. Viera, V.M. García, C. Blanco, M. Valledor, Fast charging technique for high power lithium iron phosphate batteries: A cycle life analysis, J. Power Sources. 239 (2013) 9–15. https://doi.org/10.1016/j.jpowsour.2013.03.044.

[12] B. Scrosati, J. Garche, Lithium batteries: Status, prospects and future, J. Power Sources. 195 (2010) 2419–2430. https://doi.org/10.1016/j.jpowsour.2009.11.048.

[13] D. Jugović, D. Uskoković, A review of recent developments in the synthesis procedures of lithium iron phosphate powders, J. Power Sources. 190 (2009) 538–544. https://doi.org/10.1016/j.jpowsour.2009.01.074.

[14] P.G. Bruce, S.A. Freunberger, L.J. Hardwick, J.-M. Tarascon, Erratum: Li–O2 and Li–S batteries with high energy storage, Nat. Mater. 11 (2012) 172–172. https://doi.org/10.1038/nmat3237.

[15] S. Urbonaite, T. Poux, P. Novák, Progress Towards Commercially Viable Li-S Battery Cells, Adv. Energy Mater. 5 (2015) 1–20. https://doi.org/10.1002/aenm.201500118.

[16] Y. V. Mikhaylik, J.R. Akridge, Polysulfide Shuttle Study in the Li/S Battery System, J. Electrochem. Soc. 151 (2004) A1969. https://doi.org/10.1149/1.1806394.

[17] A. Hales, L.B. Diaz, M.W. Marzook, Y. Zhao, Y. Patel, G. Offer, The Cell Cooling Coefficient: A Standard to Define Heat Rejection from Lithium-Ion Batteries, J. Electrochem. Soc. 166 (2019) A2383–A2395. https://doi.org/10.1149/2.0191912jes.

[18] H. Liu, Z. Wei, W. He, J. Zhao, Thermal issues about Li-ion batteries and recent progress in battery thermal management systems: A review, Energy Convers. Manag. 150 (2017) 304–330. https://doi.org/10.1016/j.enconman.2017.08.016.

[19] T.M. Bandhauer, S. Garimella, T.F. Fuller, A Critical Review of Thermal Issues in Lithium-Ion Batteries, J. Electrochem. Soc. 158 (2011) R1. https://doi.org/10.1149/1.3515880.

[20] T. Waldmann, M. Wilka, M. Kasper, M. Fleischhammer, M. Wohlfahrt-Mehrens, Temperature dependent ageing mechanisms in Lithium-ion batteries - A Post-Mortem

study, J. Power Sources. 262 (2014) 129–135. https://doi.org/10.1016/j.jpowsour.2014.03.112.

[21] Y. Troxler, B. Wu, M. Marinescu, V. Yufit, Y. Patel, A.J. Marquis, N.P. Brandon, G.J. Offer, The effect of thermal gradients on the performance of lithium-ion batteries, J. Power Sources. 247 (2014) 1018–1025. https://doi.org/10.1016/j.jpowsour.2013.06.084.

[22] P. Ramadass, B. Haran, R. White, B.N. Popov, Capacity fade of Sony 18650 cells cycled at elevated temperatures: Part II. Capacity fade analysis, J. Power Sources. 112 (2002) 614–620. https://doi.org/10.1016/S0378-7753(02)00473-1.

[23] M.R. Khan, M.J. Swierczynski, S.K. Kær, Towards an ultimate battery thermal management system: A review, Batteries. 3 (2017). https://doi.org/10.3390/batteries3010009.

[24] G. Offer, Y. Patel, A. Hales, L. Bravo Diaz, M. Marzook, Cool metric for lithium-ion batteries could spur progress, Nature. 582 (2020) 485–487. https://doi.org/10.1038/d41586-020-01813-8.

[25] T. Cleaver, P. Kovacik, M. Marinescu, T. Zhang, G. Offer, Perspective—Commercializing Lithium Sulfur Batteries: Are We Doing the Right Research?, J. Electrochem. Soc. 165 (2018) A6029–A6033. https://doi.org/10.1149/2.0071801jes.

[26] M.R. Busche, P. Adelhelm, H. Sommer, H. Schneider, K. Leitner, J. Janek, Systematical electrochemical study on the parasitic shuttle-effect in lithium-sulfur-cells at different temperatures and different rates, J. Power Sources. 259 (2014) 289–299. https://doi.org/10.1016/j.jpowsour.2014.02.075.

[27] Y. Diao, K. Xie, S. Xiong, X. Hong, Shuttle phenomenon-The irreversible oxidation mechanism of sulfur active material in Li-S battery, J. Power Sources. 235 (2013) 181–186. https://doi.org/10.1016/j.jpowsour.2013.01.132.

[28] X. Cheng, T. Li, X. Ruan, Z. Wang, Thermal runaway characteristics of a large format lithium-ion battery module, Energies. 12 (2019) 1–18. https://doi.org/10.3390/en12163099.

[29] C.H. Doh, Y.C. Ha, S. wook Eom, Entropy measurement of a large format lithium ion battery and its application to calculate heat generation, Electrochim. Acta. 309 (2019) 382–391. https://doi.org/10.1016/j.electacta.2019.04.026.

[30] U.D. of Energy, 2017 Tesla Model S AWD - 100D - Fuel Economy, (2017). https://www.fueleconomy.gov/feg/Find.do?action=sbs&id=38640 (accessed January 20, 2020).

[31] I. Tesla, Tesla Model S, Wikipedia, (2020). https://en.wikipedia.org/wiki/Tesla_Model_S#cite_note-150 (accessed January 20, 2020).

[32] N. Nitta, F. Wu, J.T. Lee, G. Yushin, Li-ion battery materials: Present and future, Mater. Today. 18 (2015) 252–264. https://doi.org/10.1016/j.mattod.2014.10.040.

[33] A.M. Colclasure, R.J. Kee, Thermodynamically consistent modeling of elementary electrochemistry in lithium-ion batteries, Electrochim. Acta. 55 (2010) 8960–8973. https://doi.org/10.1016/j.electacta.2010.08.018.

[34] C. Liu, Z.G. Neale, G. Cao, Understanding electrochemical potentials of cathode materials in rechargeable batteries, Mater. Today. 19 (2016) 109–123. https://doi.org/10.1016/j.mattod.2015.10.009.

[35] A. Manthiram, Y. Fu, S.H. Chung, C. Zu, Y.S. Su, Rechargeable lithium-sulfur batteries, Chem. Rev. 114 (2014) 11751–11787. https://doi.org/10.1021/cr500062v.

[36] K. Propp, M. Marinescu, D.J. Auger, L. O'Neill, A. Fotouhi, K. Somasundaram, G.J. Offer, G. Minton, S. Longo, M. Wild, V. Knap, Multi-temperature state-dependent equivalent circuit discharge model for lithium-sulfur batteries, J. Power Sources. 328 (2016) 289–299. https://doi.org/10.1016/J.JPOWSOUR.2016.07.090.

[37] M. Ghaznavi, P. Chen, Sensitivity analysis of a mathematical model of lithium-sulfur cells part I: Applied discharge current and cathode conductivity, J. Power Sources. 257 (2014) 394–401. https://doi.org/10.1016/j.jpowsour.2013.10.135.

[38] M. Ghaznavi, P. Chen, Sensitivity analysis of a mathematical model of lithium-sulfur cells: Part II: Precipitation reaction kinetics and sulfur content, J. Power Sources. 257 (2014) 402–411. https://doi.org/10.1016/j.jpowsour.2013.12.145.

[39] K. Kumaresan, Y. Mikhaylik, R.E. White, A Mathematical Model for a Lithium–Sulfur Cell, J. Electrochem. Soc. 155 (2008) A576. https://doi.org/10.1149/1.2937304.

[40] K. Mizushima, P.C. Jones, P.J. Wiseman, J.B. Goodenough, LixCoO2 (0<x<-1): A new cathode material for batteries of high energy density, Mater. Res. Bull. 15 (1980) 783–789. https://doi.org/10.1016/0025-5408(80)90012-4.

[41] A. Du Pasquier, I. Plitz, S. Menocal, G. Amatucci, A comparative study of Li-ion battery, supercapacitor and nonaqueous asymmetric hybrid devices for automotive applications, J. Power Sources. 115 (2003) 171–178. https://doi.org/10.1016/S0378-7753(02)00718-8.

[42] P. Kalyani, N. Kalaiselvi, Various aspects of LiNiO2 chemistry: A review, Sci. Technol. Adv. Mater. 6 (2005) 689–703. https://doi.org/10.1016/j.stam.2005.06.001.

[43] C.H. Chen, J. Liu, M.E. Stoll, G. Henriksen, D.R. Vissers, K. Amine, Aluminum-doped lithium nickel cobalt oxide electrodes for high-power lithium-ion batteries, J. Power Sources. 128 (2004) 278–285. https://doi.org/10.1016/j.jpowsour.2003.10.009.

[44] T. Ohzuku, Y. Makimura, Layered lithium insertion material of LiCo1/3Ni1/3Mn1/3O2 for lithium-ion batteries, Chem. Lett. (2001) 642–643. https://doi.org/10.1246/cl.2001.642.

[45] K.S. Nanjundaswamy, A.K. Padhi, J.B. Goodenough, S. Okada, H. Ohtsuka, H. Arai, J. Yamaki, Synthesis, redox potential evaluation and electrochemical characteristics of NASICON-related-3D framework compounds, Solid State Ionics. 92 (1996) 1–10. https://doi.org/10.1016/s0167-2738(96)00472-9.

[46] T. Shibagaki, Y. Merla, G.J. Offer, Tracking degradation in lithium iron phosphate batteries using differential thermal voltammetry, J. Power Sources. 374 (2018) 188–195. https://doi.org/10.1016/j.jpowsour.2017.11.011.

[47] C.E. Parfitt, Characterisation, modelling and management of lithium-sulphur batteries for spacecraft applications (PhD Thesis), University of Warwick, 2012. http://webcat.warwick.ac.uk/record=b2684478~S1.

[48] M.R. Busche, P. Adelhelm, H. Sommer, H. Schneider, K. Leitner, J. Janek, Systematical electrochemical study on the parasitic shuttle-effect in lithium-sulfur-

cells at different temperatures and different rates, J. Power Sources. 259 (2014) 289–299. https://doi.org/10.1016/j.jpowsour.2014.02.075.

[49] N.A. Kaskhedikar, J. Maier, Lithium storage in carbon nanostructures, Adv. Mater. 21 (2009) 2664–2680. https://doi.org/10.1002/adma.200901079.

[50] L. Aldon, P. Kubiak, M. Womes, J.C. Jumas, J. Olivier-Fourcade, J.L. Tirado, J.I. Corredor, C. Pérez Vicente, Chemical and electrochemical Li-insertion into the Li4Ti 5O12 spinel, Chem. Mater. 16 (2004) 5721–5725. https://doi.org/10.1021/cm0488837.

[51] S. Scharner, Evidence of Two-Phase Formation upon Lithium Insertion into the Li[sub 1.33]Ti[sub 1.67]O[sub 4] Spinel, J. Electrochem. Soc. 146 (1999) 857. https://doi.org/10.1149/1.1391692.

[52] M. Wagemaker, D.R. Simon, E.M. Kelder, J. Schoonman, C. Ringpfeil, U. Haake, D. Lützenkirchen-Hecht, R. Frahm, F.M. Mulder, A kinetic two-phase and equilibrium solid solution in spinel Li 4+xTi5O12, Adv. Mater. 18 (2006) 3169–3173. https://doi.org/10.1002/adma.200601636.

[53] V.G. Khomenko, V.Z. Barsukov, Characterization of silicon- and carbon-based composite anodes for lithium-ion batteries, Electrochim. Acta. 52 (2007) 2829–2840. https://doi.org/10.1016/j.electacta.2006.11.006.

[54] A.H. Whitehead, M. Schreiber, Current Collectors for Positive Electrodes of Lithium-Based Batteries, J. Electrochem. Soc. 152 (2005) A2105. https://doi.org/10.1149/1.2039587.

[55] J. Vetter, P. Novák, M.R. Wagner, C. Veit, K.-C. Möller, J.O. Besenhard, M. Winter, M. Wohlfahrt-Mehrens, C. Vogler, A. Hammouche, Ageing mechanisms in lithium-ion batteries, J. Power Sources. 147 (2005) 269–281. https://doi.org/10.1016/j.jpowsour.2005.01.006.

[56] S.T. Myung, Y. Hitoshi, Y.K. Sun, Electrochemical behavior and passivation of current collectors in lithium-ion batteries, J. Mater. Chem. 21 (2011) 9891–9911. https://doi.org/10.1039/c0jm04353b.

[57] M. Dubarry, B.Y. Liaw, M.S. Chen, S.S. Chyan, K.C. Han, W.T. Sie, S.H. Wu, Identifying battery aging mechanisms in large format Li ion cells, J. Power Sources. 196 (2011) 3420–3425. https://doi.org/10.1016/j.jpowsour.2010.07.029.

[58] P. Taheri, M. Bahrami, Temperature Rise in Prismatic Polymer Lithium-Ion Batteries: An Analytic Approach, SAE Int. J. Passeng. Cars - Electron. Electr. Syst. 5 (2012) 164–176. https://doi.org/10.4271/2012-01-0334.

[59] Y. Liang, C. Zhao, H. Yuan, Y. Chen, W. Zhang, J. Huang, D. Yu, Y. Liu, M. Titirici, Y. Chueh, H. Yu, Q. Zhang, A review of rechargeable batteries for portable electronic devices, InfoMat. 1 (2019) 6–32. https://doi.org/10.1002/inf2.12000.

[60] Z. Wang, J.U.N. Ma, L.E.I. Zhang, Finite Element Thermal Model and Simulation for a Cylindrical Li-Ion Battery, 5 (2017).

[61] S. Yoo, C. Hong, K.T. Chong, N. Seul, Analysis of pouch performance to ensure impact safety of lithium-ion battery, Energies. 12 (2019) 1–10. https://doi.org/10.3390/en12152865.

[62] Y. Zhao, L.B. Diaz, Y. Patel, T. Zhang, G.J. Offer, How to Cool Lithium Ion Batteries: Optimising Cell Design using a Thermally Coupled Model, J. Electrochem. Soc. 166 (2019) A2849–A2859. https://doi.org/10.1149/2.0501913jes.

[63] L.R.F. Allen J. Bard, Electrochemical Methods: Fundamentals and Applications, 2nd Edition, Wiley, 2000. https://www.wiley.com/en-us/Electrochemical+Methods%3A+Fundamentals+and+Applications%2C+2nd+Edition-p-9780471043720.

[64] T.M. Bandhauer, S. Garimella, T.F. Fuller, A Critical Review of Thermal Issues in Lithium-Ion Batteries, J. Electrochem. Soc. 158 (2011) R1. https://doi.org/10.1149/1.3515880.

[65] C.Y. Wang, V. Srinivasan, Computational battery dynamics (CBD)—electrochemical/thermal coupled modeling and multi-scale modeling, J. Power Sources. 110 (2002) 364–376. https://doi.org/10.1016/S0378-7753(02)00199-4.

[66] X. Zhang, Thermal analysis of a cylindrical lithium-ion battery, Electrochim. Acta. 56 (2011) 1246–1255. https://doi.org/10.1016/j.electacta.2010.10.054.

[67] M. Xiao, S.Y. Choe, Theoretical and experimental analysis of heat generations of a pouch type LiMn2O4/carbon high power Li-polymer battery, J. Power Sources. 241 (2013) 46–55. https://doi.org/10.1016/j.jpowsour.2013.04.062.

[68] Y. Lai, S. Du, L. Ai, L. Ai, Y. Cheng, Y. Tang, M. Jia, Insight into heat generation of lithium ion batteries based on the electrochemical-thermal model at high discharge rates, Int. J. Hydrogen Energy. 40 (2015) 13039–13049. https://doi.org/10.1016/j.ijhydene.2015.07.079.

[69] C. Heubner, M. Schneider, A. Michaelis, Detailed study of heat generation in porous LiCoO2 electrodes, J. Power Sources. 307 (2016) 199–207. https://doi.org/10.1016/j.jpowsour.2015.12.096.

[70] D. Bernardi, A General Energy Balance for Battery Systems, J. Electrochem. Soc. 132 (1985) 5. https://doi.org/10.1149/1.2113792.

[71] C.R. Birkl, M.R. Roberts, E. McTurk, P.G. Bruce, D.A. Howey, Degradation diagnostics for lithium ion cells, J. Power Sources. 341 (2017) 373–386. https://doi.org/10.1016/j.jpowsour.2016.12.011.

[72] M.R. Palacín, Understanding ageing in Li-ion batteries: a chemical issue, Chem. Soc. Rev. 47 (2018) 4924–4933. https://doi.org/10.1039/C7CS00889A.

[73] X. Feng, M. Fang, X. He, M. Ouyang, L. Lu, H. Wang, M. Zhang, Thermal runaway features of large format prismatic lithium ion battery using extended volume accelerating rate calorimetry, J. Power Sources. 255 (2014) 294–301. https://doi.org/10.1016/j.jpowsour.2014.01.005.

[74] L. Lu, X. Han, J. Li, J. Hua, M. Ouyang, A review on the key issues for lithium-ion battery management in electric vehicles, J. Power Sources. 226 (2013) 272–288. https://doi.org/10.1016/j.jpowsour.2012.10.060.

[75] K. Takei, K. Kumai, Y. Kobayashi, H. Miyashiro, N. Terada, T. Iwahori, T. Tanaka, Cycle life estimation of lithium secondary battery by extrapolation method and accelerated aging test, 98 (2001) 697–701. https://doi.org/https://doi.org/10.1016/S0378-7753(01)00646-2.

[76] R.P. Ramasamy, R.E. White, B.N. Popov, Calendar life performance of pouch lithium-ion cells, J. Power Sources. 141 (2005) 298–306. https://doi.org/10.1016/j.jpowsour.2004.09.024.

[77] Q. Zhang, R.E. White, Calendar life study of Li-ion pouch cells, J. Power Sources. 173 (2007) 990–997. https://doi.org/10.1016/j.jpowsour.2007.08.044.

[78] K. Amine, J. Liu, S. Kang, I. Belharouak, Y. Hyung, D. Vissers, G. Henriksen, Improved lithium manganese oxide spinel/graphite Li-ion cells for high-power applications, J. Power Sources. 129 (2004) 14–19. https://doi.org/10.1016/j.jpowsour.2003.11.007.

[79] K. Amine, J. Liu, I. Belharouak, High-temperature storage and cycling of C-LiFePO4/graphite Li-ion cells, Electrochem. Commun. 7 (2005) 669–673. https://doi.org/10.1016/j.elecom.2005.04.018.

[80] M.N. Richard, Accelerating Rate Calorimetry Study on the Thermal Stability of Lithium Intercalated Graphite in Electrolyte. II. Modeling the Results and Predicting Differential Scanning Calorimeter Curves, J. Electrochem. Soc. 146 (1999) 2078. https://doi.org/10.1149/1.1391894.

[81] D.D. MacNeil, Comparison of the Reactivity of Various Carbon Electrode Materials with Electrolyte at Elevated Temperature, J. Electrochem. Soc. 146 (1999) 3596. https://doi.org/10.1149/1.1392520.

[82] Z. Zhang, D. Fouchard, J.R. Rea, Differential scanning calorimetry material studies: Implications for the safety of lithium-ion cells, J. Power Sources. 70 (1998) 16–20. https://doi.org/10.1016/S0378-7753(97)02611-6.

[83] P. Biensan, B. Simon, J.P. Pérès, A. De Guibert, M. Broussely, J.M. Bodet, F. Perton, On safety of lithium-ion cells, J. Power Sources. 81–82 (1999) 906–912. https://doi.org/10.1016/S0378-7753(99)00135-4.

[84] X. Feng, X. He, M. Ouyang, L. Lu, P. Wu, C. Kulp, S. Prasser, Thermal runaway propagation model for designing a safer battery pack with 25 Ah LiNi x Co y Mn z O 2 large format lithium ion battery, Appl. Energy. 154 (2015) 74–91. https://doi.org/10.1016/j.apenergy.2015.04.118.

[85] M. Zhou, L. Zhao, S. Okada, J. Yamaki, Quantitative Studies on the Influence of LiPF 6 on the Thermal Stability of Graphite with Electrolyte, J. Electrochem. Soc. 159 (2011) A44–A48. https://doi.org/10.1149/2.066201jes.

[86] G.H. Kim, A. Pesaran, R. Spotnitz, A three-dimensional thermal abuse model for lithium-ion cells, J. Power Sources. 170 (2007) 476–489. https://doi.org/10.1016/j.jpowsour.2007.04.018.

[87] I. Belharouak, Y.K. Sun, J. Liu, K. Amine, Li(Ni1/3Co1/3Mn1/3)O2 as a suitable cathode for high power applications, J. Power Sources. 123 (2003) 247–252. https://doi.org/10.1016/S0378-7753(03)00529-9.

[88] J. Li, Y. Xu, X. Li, Z. Zhang, Li2MnO3 stabilized LiNi1/3Co1/3Mn1/3O2 cathode with improved performance for lithium ion batteries, Appl. Surf. Sci. 285 (2013) 235–240. https://doi.org/10.1016/j.apsusc.2013.08.042.

[89] B. Stiaszny, J.C. Ziegler, E.E. Krauß, J.P. Schmidt, E. Ivers-Tiffée, Electrochemical characterization and post-mortem analysis of aged LiMn 2O4-Li(Ni0.5Mn0.3Co 0.2)O2/graphite lithium ion batteries. Part I: Cycle aging, J. Power Sources. 251 (2014) 439–450. https://doi.org/10.1016/j.jpowsour.2013.11.080.

[90] C. Lim, B. Yan, L. Yin, L. Zhu, Simulation of diffusion-induced stress using reconstructed electrodes particle structures generated by micro/nano-CT, Electrochim. Acta. 75 (2012) 279–287. https://doi.org/10.1016/j.electacta.2012.04.120.

[91] B. Stiaszny, J.C. Ziegler, E.E. Krauß, M. Zhang, J.P. Schmidt, E. Ivers-Tiffée, Electrochemical characterization and post-mortem analysis of aged LiMn 2O4-NMC/graphite lithium ion batteries part II: Calendar aging, J. Power Sources. 258 (2014) 61–75. https://doi.org/10.1016/j.jpowsour.2014.02.019.

[92] T. Sasaki, T. Nonaka, H. Oka, C. Okuda, Y. Itou, Y. Kondo, Y. Takeuchi, Y. Ukyo, K. Tatsumi, S. Muto, Capacity-Fading Mechanisms of LiNiO[sub 2]-Based Lithium-Ion Batteries, J. Electrochem. Soc. 156 (2009) A289. https://doi.org/10.1149/1.3076136.

[93] B. Stiaszny, J.C. Ziegler, E.E. Krauß, J.P. Schmidt, E. Ivers-Tiffée, Electrochemical characterization and post-mortem analysis of aged LiMn2O4–Li(Ni0.5Mn0.3Co0.2)O2/graphite lithium ion batteries. Part I: Cycle aging, J. Power Sources. 251 (2014) 439–450. https://doi.org/10.1016/j.jpowsour.2013.11.080.

[94] B. Stiaszny, J.C. Ziegler, E.E. Krauß, M. Zhang, J.P. Schmidt, E. Ivers-Tiffée, Electrochemical characterization and post-mortem analysis of aged LiMn2O4–NMC/graphite lithium ion batteries part II: Calendar aging, J. Power Sources. 258 (2014) 61–75. https://doi.org/10.1016/j.jpowsour.2014.02.019.

[95] I. Bloom, A.N. Jansen, D.P. Abraham, J. Knuth, S.A. Jones, V.S. Battaglia, G.L. Henriksen, Differential voltage analyses of high-power, lithium-ion cells, J. Power Sources. 139 (2005) 295–303. https://doi.org/10.1016/j.jpowsour.2004.07.021.

[96] I. Bloom, J.P. Christophersen, D.P. Abraham, K.L. Gering, Differential voltage analyses of high-power lithium-ion cells. 3. Another anode phenomenon, J. Power Sources. 157 (2006) 537–542. https://doi.org/10.1016/j.jpowsour.2005.07.054.

[97] R. Fathi, J.C. Burns, D.A. Stevens, H. Ye, C. Hu, G. Jain, E. Scott, C. Schmidt, J.R. Dahn, Ultra High-Precision Studies of Degradation Mechanisms in Aged LiCoO 2 /Graphite Li-Ion Cells, J. Electrochem. Soc. 161 (2014) A1572–A1579. https://doi.org/10.1149/2.0321410jes.

[98] J.E. Harlow, D.A. Stevens, J.C. Burns, J.N. Reimers, J.R. Dahn, Ultra High Precision Study on High Capacity Cells for Large Scale Automotive Application, J. Electrochem. Soc. 160 (2013) A2306–A2310. https://doi.org/10.1149/2.096311jes.

[99] M. Dubarry, V. Svoboda, R. Hwu, B. Yann Liaw, Incremental Capacity Analysis and Close-to-Equilibrium OCV Measurements to Quantify Capacity Fade in Commercial Rechargeable Lithium Batteries, Electrochem. Solid-State Lett. 9 (2006) A454. https://doi.org/10.1149/1.2221767.

[100] A.J. Smith, J.R. Dahn, Delta Differential Capacity Analysis, J. Electrochem. Soc. 159 (2012) A290–A293. https://doi.org/10.1149/2.076203jes.

[101] X. Han, M. Ouyang, L. Lu, J. Li, Y. Zheng, Z. Li, A comparative study of commercial lithium ion battery cycle life in electrical vehicle: Aging mechanism identification, J. Power Sources. 251 (2014) 38–54. https://doi.org/10.1016/j.jpowsour.2013.11.029.

[102] B. Wu, V. Yufit, Y. Merla, R.F. Martinez-Botas, N.P. Brandon, G.J. Offer, Differential thermal voltammetry for tracking of degradation in lithium-ion batteries, J. Power Sources. 273 (2015) 495–501. https://doi.org/10.1016/j.jpowsour.2014.09.127.

[103] Y. Merla, B. Wu, V. Yufit, N.P. Brandon, R.F. Martinez-Botas, G.J. Offer, Novel application of differential thermal voltammetry as an in-depth state-of-health diagnosis method for lithium-ion batteries, J. Power Sources. 307 (2016) 308–319. https://doi.org/10.1016/j.jpowsour.2015.12.122.

[104] Y. Merla, B. Wu, V. Yufit, N.P. Brandon, R.F. Martinez-Botas, G.J. Offer, Extending battery life: A low-cost practical diagnostic technique for lithium-ion batteries, J. Power Sources. 331 (2016) 224–231. https://doi.org/10.1016/j.jpowsour.2016.09.008.

[105] A. Hales, M.W. Marzook, L. Bravo Diaz, Y. Patel, G. Offer, The Surface Cell Cooling Coefficient: A Standard to Define Heat Rejection from Lithium Ion Battery Pouch Cells, J. Electrochem. Soc. 167 (2020) 020524. https://doi.org/10.1149/1945-7111/ab6985.

[106] V. Ramadesigan, P.W.C. Northrop, S. De, S. Santhanagopalan, R.D. Braatz, V.R. Subramanian, Modeling and Simulation of Lithium-Ion Batteries from a Systems Engineering Perspective, J. Electrochem. Soc. 159 (2012) R31–R45. https://doi.org/10.1149/2.018203jes.

[107] Y. Merla, B. Wu, V. Yufit, R.F. Martinez-Botas, G.J. Offer, An easy-to-parameterise physics-informed battery model and its application towards lithium-ion battery cell design, diagnosis, and degradation, J. Power Sources. 384 (2018) 66–79. https://doi.org/10.1016/j.jpowsour.2018.02.065.

[108] Y. Zhao, Y. Patel, T. Zhang, G.J. Offer, Modeling the Effects of Thermal Gradients Induced by Tab and Surface Cooling on Lithium Ion Cell Performance, J. Electrochem. Soc. 165 (2018) A3169–A3178. https://doi.org/10.1149/2.0901813jes.

[109] U.S. Kim, C.B. Shin, C.S. Kim, Effect of electrode configuration on the thermal behavior of a lithium-polymer battery, J. Power Sources. 180 (2008) 909–916. https://doi.org/10.1016/j.jpowsour.2007.09.054.

[110] H. Gu, Mathematical Analysis of a Zn⁄NiOOH Cell, J. Electrochem. Soc. 130 (1983) 1459. https://doi.org/10.1149/1.2120009.

[111] U.S. Kim, C.B. Shin, C.-S. Kim, Modeling for the scale-up of a lithium-ion polymer battery, J. Power Sources. 189 (2009) 841–846. https://doi.org/10.1016/j.jpowsour.2008.10.019.

[112] X. Lai, W. Gao, Y. Zheng, M. Ouyang, J. Li, X. Han, L. Zhou, A comparative study of global optimization methods for parameter identification of different equivalent circuit models for Li-ion batteries, Electrochim. Acta. 295 (2019) 1057–1066. https://doi.org/10.1016/j.electacta.2018.11.134.

[113] K.C. Lim, H.A. Bastawrous, V.H. Duong, K.W. See, P. Zhang, S.X. Dou, Fading Kalman filter-based real-time state of charge estimation in LiFePO4 battery-powered electric vehicles, Appl. Energy. 169 (2016) 40–48. https://doi.org/10.1016/j.apenergy.2016.01.096.

[114] C. Zhang, J. Jiang, Y. Gao, W. Zhang, Q. Liu, X. Hu, Charging optimization in lithium-ion batteries based on temperature rise and charge time, Appl. Energy. 194 (2017) 569–577. https://doi.org/10.1016/j.apenergy.2016.10.059.

[115] W. Gao, Y. Zheng, M. Ouyang, J. Li, X. Lai, X. Hu, Micro-short-circuit diagnosis for series-connected lithium-ion battery packs using mean-difference model, IEEE Trans. Ind. Electron. (2019). https://doi.org/10.1109/TIE.2018.2838109.

[116] Y. Tian, D. Li, J. Tian, B. Xia, State of charge estimation of lithium-ion batteries using an optimal adaptive gain nonlinear observer, Electrochim. Acta. 225 (2017) 225–234. https://doi.org/10.1016/j.electacta.2016.12.119.

[117] T. Mesbahi, F. Khenfri, N. Rizoug, K. Chaaban, P. Bartholomeüs, P. Le Moigne, Dynamical modeling of Li-ion batteries for electric vehicle applications based on hybrid Particle Swarm-Nelder-Mead (PSO-NM) optimization algorithm, Electr. Power Syst. Res. 131 (2016) 195–204. https://doi.org/10.1016/j.epsr.2015.10.018.

[118] H. Dai, T. Xu, L. Zhu, X. Wei, Z. Sun, Adaptive model parameter identification for large capacity Li-ion batteries on separated time scales, Appl. Energy. 184 (2016) 119–131. https://doi.org/10.1016/j.apenergy.2016.10.020.

[119] H. Rahimi-Eichi, F. Baronti, M.Y. Chow, Modeling and online parameter identification of Li-Polymer battery cells for SOC estimation, in: IEEE Int. Symp. Ind. Electron., 2012. https://doi.org/10.1109/ISIE.2012.6237284.

[120] Y.-H. Chiang, W.-Y. Sean, J.-C. Ke, Online estimation of internal resistance and open-circuit voltage of lithium-ion batteries in electric vehicles, J. Power Sources. 196 (2011) 3921–3932. https://doi.org/10.1016/j.jpowsour.2011.01.005.

[121] J. Kim, B.H. Cho, State-of-charge estimation and state-of-health prediction of a Li-Ion degraded battery based on an EKF combined with a per-unit system, in: IEEE Trans. Veh. Technol., 2011. https://doi.org/10.1109/TVT.2011.2168987.

[122] T. Kim, W. Qiao, A hybrid battery model capable of capturing dynamic circuit characteristics and nonlinear capacity effects, IEEE Trans. Energy Convers. (2011). https://doi.org/10.1109/TEC.2011.2167014.

[123] M. Sitterly, L.Y. Wang, G.G. Yin, C. Wang, Enhanced identification of battery models for real-time battery management, IEEE Trans. Sustain. Energy. (2011). https://doi.org/10.1109/TSTE.2011.2116813.

[124] D. Andre, M. Meiler, K. Steiner, H. Walz, T. Soczka-Guth, D.U. Sauer, Characterization of high-power lithium-ion batteries by electrochemical impedance spectroscopy. II: Modelling, J. Power Sources. 196 (2011) 5349–5356. https://doi.org/10.1016/j.jpowsour.2010.07.071.

[125] W.D. Widanage, A. Barai, G.H. Chouchelamane, K. Uddin, A. McGordon, J. Marco, P. Jennings, Design and use of multisine signals for Li-ion battery equivalent circuit modelling. Part 2: Model estimation, J. Power Sources. 324 (2016) 61–69.

[126] C. Zhang, K. Li, L. Pei, C. Zhu, An integrated approach for real-time model-based state-of-charge estimation of lithium-ion batteries, J. Power Sources. 283 (2015) 24–36.

[127] S. Thanagasundram, R. Arunachala, K. Makinejad, T. Teutsch, A. Jossen, A cell level model for battery simulation, in: Eur. Electr. Veh. Congr., 2012: pp. 1–13.

[128] C. Zhang, K. Li, J. Deng, S. Song, Improved Realtime State-of-Charge Estimation of LiFePO4 Battery Based on a Novel Thermoelectric Model, IEEE Trans. Ind. Electron. 64 (2017) 654–663. https://doi.org/10.1109/tie.2016.2610398.

[129] Y. Hu, S. Yurkovich, Linear parameter varying battery model identification using subspace methods, J. Power Sources. 196 (2011) 2913–2923.

[130] W.D. Widanage, A. Barai, G.H. Chouchelamane, K. Uddin, A. McGordon, J. Marco, P. Jennings, Design and use of multisine signals for Li-ion battery equivalent circuit modelling. Part 1: Signal design, J. Power Sources. 324 (2016) 70–78.

[131] J. Brand, Z. Zhang, R.K. Agarwal, Extraction of battery parameters of the equivalent circuit model using a multi-objective genetic algorithm, J. Power Sources. 247 (2014) 729–737.

[132] Y. Hu, S. Yurkovich, Y. Guezennec, B.J. Yurkovich, Electro-thermal battery model identification for automotive applications, J. Power Sources. 196 (2011) 449–457. https://doi.org/https://doi.org/10.1016/j.jpowsour.2010.06.037.

[133] M. Verbrugge, B. Koch, Generalized recursive algorithm for adaptive multiparameter regression application to lead acid, nickel metal hydride, and lithium-ion batteries, J. Electrochem. Soc. 153 (2006) A187–A201.

[134] C. Campestrini, T. Heil, S. Kosch, A. Jossen, A comparative study and review of different Kalman filters by applying an enhanced validation method, J. Energy Storage. 8 (2016) 142–159. https://doi.org/https://doi.org/10.1016/j.est.2016.10.004.

[135] W. Allafi, K. Uddin, C. Zhang, R.M.R.A. Sha, J. Marco, On-line scheme for parameter estimation of nonlinear lithium ion battery equivalent circuit models using the simplified refined instrumental variable method for a modified Wiener continuous-time model, Appl. Energy. 204 (2017) 497–508.

[136] C. Zhang, W. Allafi, Q. Dinh, P. Ascencio, J. Marco, Online estimation of battery equivalent circuit model parameters and state of charge using decoupled least squares technique, Energy. 142 (2018) 678–688.

[137] H.P.G.J. Beelen, H.J. Bergveld, M.C.F. Donkers, On Experiment Design for Parameter Estimation of Equivalent-Circuit Battery Models, in: 2018 IEEE Conf. Control Technol. Appl., 2018: pp. 1526–1531. https://doi.org/10.1109/CCTA.2018.8511529.

[138] N. Wassiliadis, J. Adermann, A. Frericks, M. Pak, C. Reiter, B. Lohmann, M. Lienkamp, Revisiting the dual extended kalman filter for battery state-of-charge and state-of-health estimation: A use-case life cycle analysis, J. Energy Storage. 19 (2018) 73–87.

[139] C. Campestrini, Practical feasibility of Kalman filters for the state estimation of lithium-ion batteries, Technische Universität München, 2018.

[140] M. Ceraolo, J. Gazzarri, R. Jackey, P. Sanghvi, M. Saginaw, T. Huria, Battery Model Parameter Estimation Using a Layered Technique: An Example Using a Lithium Iron Phosphate Cell, SAE Tech. Pap. Ser. 1 (2013). https://doi.org/10.4271/2013-01-1547.

[141] X. Tang, F. Gao, C. Zou, K. Yao, W. Hu, T. Wik, Load-responsive model switching estimation for state of charge of lithium-ion batteries, Appl. Energy. 238 (2019) 423–434.

[142] M. Lenz, D. Jöst, F. Thiel, S. Pischinger, D.U. Sauer, Identification of load dependent cell voltage model parameters from sparse input data using the Mixed Integer Distributed Ant Colony Optimization solver, J. Power Sources. 437 (2019) 226880. https://doi.org/https://doi.org/10.1016/j.jpowsour.2019.226880.

[143] S.K. Rahimian, S. Rayman, R.E. White, Comparison of single particle and equivalent circuit analog models for a lithium-ion cell, J. Power Sources. 196 (2011) 8450–8462.

[144] M. Marinescu, T. Zhang, G.J. Offer, A zero dimensional model of lithium–sulfur batteries during charge and discharge, Phys. Chem. Chem. Phys. 18 (2016) 584–593. https://doi.org/10.1039/C5CP05755H.

[145] T.F. Fuller, Relaxation Phenomena in Lithium-Ion-Insertion Cells, J. Electrochem. Soc. 141 (1994) 982. https://doi.org/10.1149/1.2054868.

[146] M. Doyle, J. Newman, The use of mathematical modeling in the design of lithium/polymer battery systems, Electrochim. Acta. 40 (1995) 2191–2196. https://doi.org/10.1016/0013-4686(95)00162-8.

[147] R. Darling, Modeling a Porous Intercalation Electrode with Two Characteristic Particle Sizes, J. Electrochem. Soc. 144 (1997) 4201. https://doi.org/10.1149/1.1838166.

[148] P. Ramadass, B. Haran, R. White, B.N. Popov, Mathematical modeling of the capacity fade of Li-ion cells, J. Power Sources. 123 (2003) 230–240. https://doi.org/10.1016/S0378-7753(03)00531-7.

[149] R. Klein, N.A. Chaturvedi, J. Christensen, J. Ahmed, R. Findeisen, A. Kojic, Electrochemical model based observer design for a lithium-ion battery, IEEE Trans. Control Syst. Technol. (2013). https://doi.org/10.1109/TCST.2011.2178604.

[150] D.E. Stephenson, E.M. Hartman, J.N. Harb, D.R. Wheeler, Modeling of Particle-Particle Interactions in Porous Cathodes for Lithium-Ion Batteries, J. Electrochem. Soc. 154 (2007) A1146. https://doi.org/10.1149/1.2783772.

[151] M. Guo, G.-H. Kim, R.E. White, A three-dimensional multi-physics model for a Li-ion battery, J. Power Sources. 240 (2013) 80–94. https://doi.org/10.1016/j.jpowsour.2013.03.170.

[152] P.W.C. Northrop, V. Ramadesigan, S. De, V.R. Subramanian, Coordinate Transformation, Orthogonal Collocation, Model Reformulation and Simulation of Electrochemical-Thermal Behavior of Lithium-Ion Battery Stacks, J. Electrochem. Soc. 158 (2011) A1461. https://doi.org/10.1149/2.058112jes.

[153] M. Ecker, T.K.D. Tran, P. Dechent, S. Käbitz, A. Warnecke, D.U. Sauer, Parameterization of a Physico-Chemical Model of a Lithium-Ion Battery, J. Electrochem. Soc. 162 (2015) A1836–A1848. https://doi.org/10.1149/2.0551509jes.

[154] E. Prada, D. Di Domenico, Y. Creff, J. Bernard, V. Sauvant-Moynot, F. Huet, Simplified Electrochemical and Thermal Model of LiFePO 4 -Graphite Li-Ion Batteries for Fast Charge Applications, J. Electrochem. Soc. 159 (2012) A1508–A1519. https://doi.org/10.1149/2.064209jes.

[155] M. Guo, R.E. White, A distributed thermal model for a Li-ion electrode plate pair, J. Power Sources. 221 (2013) 334–344. https://doi.org/10.1016/j.jpowsour.2012.08.012.

[156] K.D. Stetzel, L.L. Aldrich, M.S. Trimboli, G.L. Plett, Electrochemical state and internal variables estimation using a reduced-order physics-based model of a lithium-ion cell and an extended Kalman filter, J. Power Sources. 278 (2015) 490–505. https://doi.org/10.1016/j.jpowsour.2014.11.135.

[157] J.L. Lee, L.L. Aldrich, K.D. Stetzel, G.L. Plett, Extended operating range for reduced-order model of lithium-ion cells, J. Power Sources. 255 (2014) 85–100. https://doi.org/10.1016/j.jpowsour.2013.12.134.

[158] D. Moy, A. Manivannan, S.R. Narayanan, Direct Measurement of Polysulfide Shuttle Current : A Window into Understanding the Performance of Lithium-Sulfur Cells, 162 (2015). https://doi.org/10.1149/2.0181501jes.

[159] S. Urbonaite, T. Poux, P. Novák, Progress Towards Commercially Viable Li-S Battery Cells, Adv. Energy Mater. (2015). https://doi.org/10.1002/aenm.201500118.

[160] X. Ji, L.F. Nazar, Advances in Li–S batteries, J. Mater. Chem. 20 (2010) 9821. https://doi.org/10.1039/b925751a.

[161] S. Xiong, K. Xie, Y. Diao, X. Hong, Characterization of the solid electrolyte interphase on lithium anode for preventing the shuttle mechanism in lithium-sulfur batteries, J. Power Sources. 246 (2014) 840–845. https://doi.org/10.1016/j.jpowsour.2013.08.041.

[162] Y. V Mikhaylik, J.R. Akridge, Polysulfide Shuttle Study in the Li/S Battery System, J. Electrochem. Soc. 151 (2004) A1969. https://doi.org/10.1149/1.1806394.

[163] J. Yan, X. Liu, B. Li, Capacity Fade Analysis of Sulfur Cathodes in Lithium-Sulfur Batteries, Adv. Sci. 3 (2016) 1600101. https://doi.org/10.1002/advs.201600101.

[164] D. Bresser, S. Passerini, B. Scrosati, Recent progress and remaining challenges in sulfur-based lithium secondary batteries--a review., Chem. Commun. (Camb). 49 (2013) 10545–62. https://doi.org/10.1039/c3cc46131a.

[165] G. Ma, Z. Wen, M. Wu, C. Shen, Q. Wang, J. Jin, X. Wu, A lithium anode protection guided highly-stable lithium–sulfur battery, Chem. Commun. 50 (2014) 14209–14212. https://doi.org/10.1039/C4CC05535G.

[166] V. Knap, D. Stroe, M. Swierczynski, R. Purkayastha, K. Propp, R. Teodorescu, E. Schaltz, A self-discharge model of Lithium-Sulfur batteries based on direct shuttle current measurement, J. Power Sources. 336 (2016) 325–331. https://doi.org/10.1016/j.jpowsour.2016.10.087.

[167] F. Han, J. Yue, X. Fan, T. Gao, C. Luo, Z. Ma, L. Suo, C. Wang, High-performance all-solid-state lithium-sulfur battery enabled by a mixed-conductive Li2S nanocomposite, Nano Lett. 16 (2016) 4521–4527. https://doi.org/10.1021/acs.nanolett.6b01754.

[168] M. Nagao, A. Hayashi, M. Tatsumisago, High-capacity Li 2S-nanocarbon composite electrode for all-solid-state rechargeable lithium batteries, J. Mater. Chem. 22 (2012) 10015–10020. https://doi.org/10.1039/c2jm16802b.

[169] Y. Yang, G. Zheng, Y. Cui, Nanostructured sulfur cathodes, Chem. Soc. Rev. 42 (2013) 3018–3032. https://doi.org/10.1039/c2cs35256g.

[170] L. Suo, Y.S. Hu, H. Li, M. Armand, L. Chen, A new class of Solvent-in-Salt electrolyte for high-energy rechargeable metallic lithium batteries, Nat. Commun. 4 (2013) 1–9. https://doi.org/10.1038/ncomms2513.

[171] B. Wu, V. Yu, Y. Merla, R.F. Martinez-botas, N.P. Brandon, G.J. Offer, Differential thermal voltammetry for tracking of degradation in lithium-ion batteries, 273 (2015) 495–501. https://doi.org/10.1016/j.jpowsour.2014.09.127.

[172] Y. Merla, B. Wu, V. Yu, N.P. Brandon, R.F. Martinez-botas, G.J. Offer, Novel application of differential thermal voltammetry as an in-depth state-of-health diagnosis method for lithium-ion batteries, 307 (2016) 308–319. https://doi.org/10.1016/j.jpowsour.2015.12.122.

[173] Y. V. Mikhaylik, J.R. Akridge, Low Temperature Performance of Li/S Batteries, J. Electrochem. Soc. 150 (2003) A306. https://doi.org/10.1149/1.1545452.

[174] M. Marinescu, L. O'Neill, T. Zhang, S. Walus, T.E. Wilson, G.J. Offer, Irreversible vs Reversible Capacity Fade of Lithium-Sulfur Batteries during Cycling: The Effects of Precipitation and Shuttle, J. Electrochem. Soc. 165 (2018) A6107–A6118. https://doi.org/10.1149/2.0171801jes.

[175] T. Zhang, M. Marinescu, L. O'Neill, M. Wild, G. Offer, Modeling the voltage loss mechanisms in lithium–sulfur cells: the importance of electrolyte resistance and precipitation kinetics, Phys. Chem. Chem. Phys. 17 (2015) 22581–22586. https://doi.org/10.1039/C5CP03566J.

[176] V.S. Kolosnitsyn, E.V. Kuzmina, S.E. Mochalov, Determination of lithium sulphur batteries internal resistance by the pulsed method during galvanostatic cycling, J. Power Sources. 252 (2014) 28–34. https://doi.org/10.1016/J.JPOWSOUR.2013.11.099.

[177] I.A. Hunt, T. Zhang, M. Marinescu, Y. Patel, R. Purkayasth, S. Kovacik, S. Walus, A. Sqiatek, G.J. Offer, The Effect of Current Inhomogeneity on the Performance and Degradation of Li-S Batteries, 165 (2017) 6073–6080. https://doi.org/10.1149/2.0141801jes.

[178] K. Propp, D.J. Auger, A. Fotouhi, S. Longo, V. Knap, Kalman-variant estimators for state of charge in lithium-sulfur batteries, J. Power Sources. 343 (2017) 254–267. https://doi.org/10.1016/J.JPOWSOUR.2016.12.087.

[179] D.I. Stroe, V. Knap, M. Swierczynski, E. Schaltz, Thermal Behavior and Heat Generation Modeling of Lithium Sulfur Batteries, ECS Trans. 77 (2017) 467–476. https://doi.org/10.1149/07711.0467ecst.

[180] V. Kolosnitsyn, E. Kuzmina, S. Mochalov, A. Nurgaliev, Effect of Current Density on the Heat Generation of Lithium-Sulphur Batteries during Charge and Discharge, Meet. Abstr. MA2014-04 (2014) 575–575. http://ma.ecsdl.org/content/MA2014-04/3/575.short (accessed July 5, 2018).

[181] V.S. Kolosnitsyn, E.V. Kuzmina, E.V. Karaseva, S.E. Mochalov, A study of the electrochemical processes in lithium–sulphur cells by impedance spectroscopy, J. Power Sources. 196 (2011) 1478–1482. https://doi.org/10.1016/J.JPOWSOUR.2010.08.105.

[182] T. Zhang, M. Marinescu, S. Walus, P. Kovacik, G.J. Offer, What Limits the Rate Capability of Li-S Batteries during Discharge: Charge Transfer or Mass Transfer?, J. Electrochem. Soc. 165 (2018) A6001–A6004. https://doi.org/10.1149/2.0011801jes.

[183] V.S. Kolosnitsyn, E. V. Karaseva, Lithium-sulfur batteries: Problems and solutions, Russ. J. Electrochem. 44 (2008) 506–509. https://doi.org/10.1134/S1023193508050029.

[184] M. Wild, L. O'Neill, T. Zhang, R. Purkayastha, G. Minton, M. Marinescu, G.J. Offer, Lithium sulfur batteries, a mechanistic review, Energy Environ. Sci. 8 (2015) 3477–3494. https://doi.org/10.1039/C5EE01388G.

[185] T. Zhang, M. Marinescu, S. Walus, G.J. Offer, Electrochimica Acta Modelling transport-limited discharge capacity of lithium-sulfur cells, 219 (2016) 502–508. https://doi.org/10.1016/j.electacta.2016.10.032.

[186] A.J. Bard, L.R. Faulkner, ELECTROCHEMICAL METHODS, 2001. https://doi.org/10.1016/B978-0-12-381373-2.00056-9.

[187] L. Lu, X. Han, J. Li, J. Hua, M. Ouyang, A review on the key issues for lithium-ion battery management in electric vehicles, J. Power Sources. (2013). https://doi.org/10.1016/j.jpowsour.2012.10.060.

[188] M. Doyle, Modeling of Galvanostatic Charge and Discharge of the Lithium/Polymer/Insertion Cell, J. Electrochem. Soc. 140 (1993) 1526. https://doi.org/10.1149/1.2221597.

[189] B. Pattipati, C. Sankavaram, K.R. Pattipati, System identification and estimation framework for pivotal automotive battery management system characteristics, IEEE

Trans. Syst. Man Cybern. Part C Appl. Rev. (2011). https://doi.org/10.1109/TSMCC.2010.2089979.

[190] H. He, R. Xiong, H. Guo, S. Li, Comparison study on the battery models used for the energy management of batteries in electric vehicles, Energy Convers. Manag. 64 (2012) 113–121. https://doi.org/10.1016/j.enconman.2012.04.014.

[191] X. Hu, S. Li, H. Peng, A comparative study of equivalent circuit models for Li-ion batteries, J. Power Sources. 198 (2012) 359–367. https://doi.org/10.1016/j.jpowsour.2011.10.013.

[192] A. Barai, W.D. Widanage, J. Marco, A. Mcgordon, P. Jennings, A study of the open circuit voltage characterization technique and hysteresis assessment of lithium-ion cells, J. Power Sources. 295 (2015) 99–107. https://doi.org/10.1016/j.jpowsour.2015.06.140.

[193] J. Schoukens, L. Ljung, Nonlinear System Identification: A User-Oriented Roadmap, ArXiv Prepr. ArXiv1902.00683. (2019).

[194] W. Dreyer, J. Jamnik, C. Guhlke, R. Huth, J. Moškon, M. Gaberšček, The thermodynamic origin of hysteresis in insertion batteries, Nat. Mater. 9 (2010) 448–453. https://doi.org/10.1038/nmat2730.

[195] G.L. Plett, Extended Kalman filtering for battery management systems of LiPB-based HEV battery packs: Part 2. Modeling and identification, J. Power Sources. 134 (2004) 262–276. https://doi.org/https://doi.org/10.1016/j.jpowsour.2004.02.032.

[196] C. Zhang, L.Y. Wang, X. Li, W. Chen, G.G. Yin, J. Jiang, Robust and Adaptive Estimation of State of Charge for Lithium-Ion Batteries, IEEE Trans. Ind. Electron. 62 (2015) 4948–4957. https://doi.org/10.1109/TIE.2015.2403796.

[197] A. Malik, Z. Zhang, R.K. Agarwal, Extraction of battery parameters using a multi-objective genetic algorithm with a non-linear circuit model, J. Power Sources. 259 (2014) 76–86. https://doi.org/https://doi.org/10.1016/j.jpowsour.2014.02.062.

[198] M. Ouyang, G. Liu, L. Lu, J. Li, X. Han, Enhancing the estimation accuracy in low state-of-charge area: A novel onboard battery model through surface state of charge determination, J. Power Sources. 270 (2014) 221–237. https://doi.org/10.1016/j.jpowsour.2014.07.090.

[199] B. Wu, V. Yu, M. Marinescu, G.J. Offer, R.F. Martinez-botas, N.P. Brandon, Coupled thermal e electrochemical modelling of uneven heat generation in lithium-ion battery packs, 243 (2013) 544–554. https://doi.org/https://doi.org/10.1016/j.jpowsour.2013.05.164.

[200] T. Waldmann, M. Wilka, M. Kasper, M. Fleischhammer, M. Wohlfahrt-Mehrens, Temperature dependent ageing mechanisms in Lithium-ion batteries - A Post-Mortem study, J. Power Sources. 262 (2014) 129–135. https://doi.org/10.1016/j.jpowsour.2014.03.112.

[201] T.G. Zavalis, M. Klett, M.H. Kjell, M. Behm, R.W. Lindström, G. Lindbergh, Electrochimica Acta Aging in lithium-ion batteries : Model and experimental investigation of harvested LiFePO 4 and mesocarbon microbead graphite electrodes, Electrochim. Acta. 110 (2013) 335–348. https://doi.org/10.1016/j.electacta.2013.05.081.

[202] A. Hales, L.B. Diaz, M.W. Marzook, Y. Zhao, Y. Patel, G. Offer, The Cell Cooling Coefficient: A Standard to Define Heat Rejection from Lithium-Ion Batteries, J. Electrochem. Soc. 166 (2019) A2383–A2395. https://doi.org/10.1149/2.0191912jes.

[203] I.A. Hunt, Y. Zhao, Y. Patel, J. Offer, Surface Cooling Causes Accelerated Degradation Compared to Tab Cooling for Lithium-Ion Pouch Cells, J. Electrochem. Soc. 163 (2016) A1846–A1852. https://doi.org/10.1149/2.0361609jes.

[204] J. Xun, R. Liu, K. Jiao, Numerical and analytical modeling of lithium ion battery thermal behaviors with different cooling designs, J. Power Sources. 233 (2013) 47–61. https://doi.org/10.1016/j.jpowsour.2013.01.095.

[205] M.M. K.J. Kelly and M. Zolot, Battery Usage and Thermal Performance of the Toyota Prius and Honda Insight for Various Chassis Dynamometer Test Procedures, 17th Annu. Batter. Conf. Appl. Adv. (2001). https://www.nrel.gov/transportation/assets/pdfs/2002_batteryusage.pdf.

[206] G. Xia, L. Cao, G. Bi, A review on battery thermal management in electric vehicle application, J. Power Sources. (2017). https://doi.org/10.1016/j.jpowsour.2017.09.046.

[207] D. Chen, J. Jiang, G.-H. Kim, C. Yang, A. Pesaran, Comparison of different cooling methods for lithium ion battery cells, Appl. Therm. Eng. 94 (2016) 846–854. https://doi.org/10.1016/j.applthermaleng.2015.10.015.

[208] Y. Deng, C. Feng, J. E, H. Zhu, J. Chen, M. Wen, H. Yin, Effects of different coolants and cooling strategies on the cooling performance of the power lithium ion battery system: A review, Appl. Therm. Eng. 142 (2018) 10–29. https://doi.org/10.1016/j.applthermaleng.2018.06.043.

[209] Q. Wang, B. Jiang, B. Li, Y. Yan, A critical review of thermal management models and solutions of lithium-ion batteries for the development of pure electric vehicles, Renew. Sustain. Energy Rev. 64 (2016) 106–128. https://doi.org/10.1016/j.rser.2016.05.033.

[210] L.W. Jin, P.S. Lee, X.X. Kong, Y. Fan, S.K. Chou, Ultra-thin minichannel LCP for EV battery thermal management, Appl. Energy. 113 (2014) 1786–1794. https://doi.org/10.1016/j.apenergy.2013.07.013.

[211] Y. Huo, Z. Rao, X. Liu, J. Zhao, Investigation of power battery thermal management by using mini-channel cold plate, Energy Convers. Manag. 89 (2015) 387–395. https://doi.org/10.1016/j.enconman.2014.10.015.

[212] Y. wei Pan, Y. Hua, S. Zhou, R. He, Y. Zhang, S. Yang, X. Liu, Y. Lian, X. Yan, B. Wu, A computational multi-node electro-thermal model for large prismatic lithium-ion batteries, J. Power Sources. 459 (2020) 228070. https://doi.org/10.1016/j.jpowsour.2020.228070.

[213] N. Damay, C. Forgez, M.P. Bichat, G. Friedrich, Thermal modeling of large prismatic LiFePO4/graphite battery. Coupled thermal and heat generation models for characterization and simulation, J. Power Sources. 283 (2015) 37–45. https://doi.org/10.1016/j.jpowsour.2015.02.091.

[214] DYMOLA Systems Engineering Introduction, (n.d.). https://www.3ds.com/products-services/catia/products/dymola/.

[215] The Modelica Association, (n.d.). https://www.modelica.org/.

[216] Industry Solitions - Modelica Libraries - Battery Library, (n.d.). https://www.3ds.com/products-services/catia/products/dymola/industry-solutions/.

[217] Contact@fmi-standard.org, Functional Mock-up Interface, (n.d.). https://fmi-standard.org/ (accessed May 22, 2020).

[218] S. T, GitHub:CATIA-Systems / FMPy, (2020). https://github.com/CATIA-Systems/FMPy (accessed May 22, 2020).

[219] T.S. Community, SciPy.org: scipy.optimize.differential_evolution, (2019). https://docs.scipy.org/doc/scipy/reference/generated/scipy.optimize.differential_evolution.html#scipy.optimize.differential_evolution (accessed May 22, 2020).

[220] T. David, Galat, Arnaud, Material Thermal Properties Databasee,University of Central Florida (UCF), (n.d.). https://ncfs.ucf.edu/burn_db/Thermal_Properties/material_thermal.html.

# Appendices

## Appendix 1: Permission to Republish Third Party Works

| *Usage in Thesis* | *Copyright Holder* | *Permission* | *Remark* |
|---|---|---|---|
| Figure 1 | International Energy Agency | Yes | Permitted according to the copyright holder's existing terms and conditions of use. |
| Figure 2 | International Energy Agency | Yes | Permitted according to the copyright holder's existing terms and conditions of use. |
| Figure 3 | International Energy Agency | Yes | Permitted according to the copyright holder's existing terms and conditions of use. |
| Figure 4 | United Nations Environment Programme | Yes | Permitted according to the copyright holder's existing terms and conditions of use. |
| Figure 5 | Nature Materials and Author(s) | Yes | Permission was given by the copyright holder. |
| Figure 6 | 2014 The Authors. Published by Elsevier Ltd. | Yes | Open access under Creative Commons CC-BY-NC-ND license. |
| Figure 7 | 2010 Elsevier Ltd. All rights reserved. | Yes | Permission was given by the copyright holder |
| Figure 8 | 2015 The Authors. Published by Elsevier Ltd. | Yes | Open access under Creative Commons CC-BY-NC-ND license. |
| Figure 9 | 2016 The Authors. Published by Elsevier B.V. | Yes | Open access under Creative Commons CC-BY-NC-ND license. |
| Figure 11 | 2014 The Authors. Published by Elsevier Ltd. | Yes | Open access under Creative Commons CC-BY-NC-ND license. |
| Figure 12 | 2014 The Authors. Published by Elsevier Ltd. | Yes | Open access under Creative Commons CC-BY-NC-ND license. |
| Figure 13 | 2016 The Authors. Published by Elsevier B.V. | Yes | Open access under Creative Commons CC-BY-NC-ND license. |
| Figure 14 | 2014 Elsevier B.V. All rights reserved. | Yes | Permission was given by the copyright holder |
| Figure 15 | 2014 The Authors. Published by Elsevier Ltd. | Yes | Open access under Creative Commons CC-BY-NC-ND license. |
| Figure 16 | 1999-2020 John Wiley & Sons, Inc. All rights reserved | Yes | Open access under Attribution 4.0 International (CC BY 4.0) |
| Figure 17 | 2020 IEEE - All rights reserved. | Yes | Permitted according to the copyright holder's existing terms and conditions of use. |
| Figure 18 | 1996-2020 MDPI (Basel, Switzerland) unless otherwise stated, Energies, the Authors. | Yes | Open access under Attribution 4.0 International (CC BY 4.0) |

## Appendix 2: Dymola Model Configuration

The model is developed, tested and validated in the software 'Dymola', and this section introduces layer by layer, the details of the model proposed in chapter 4 & 5 in this thesis. Ideally, with fully-functional Dymola Battery library, the model can be re-produced by accessing the chapter details and the model configuration figures below.

### *Layer 1: An overall user interface*

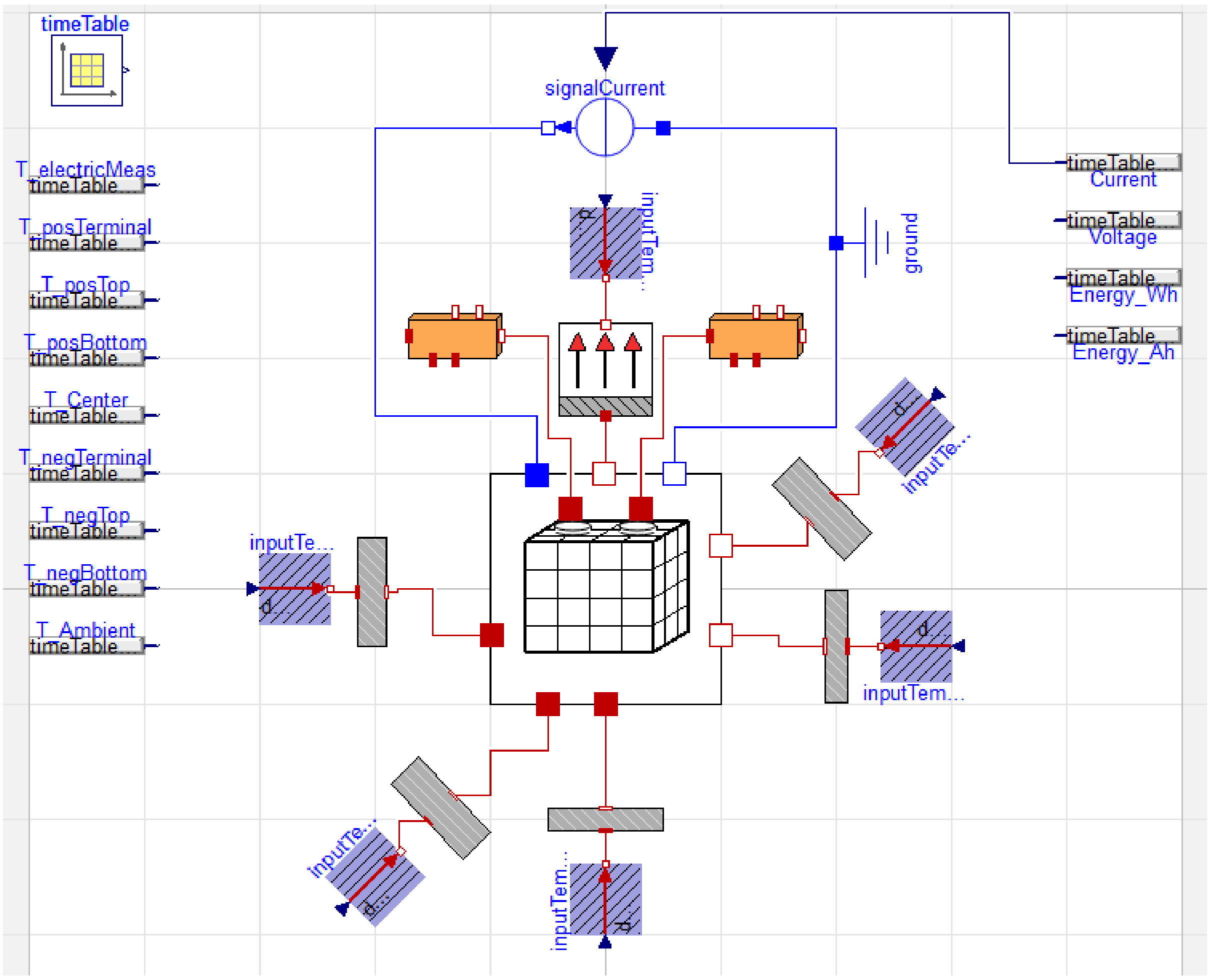

*Figure 69 Dymola user interface: overall structure of developed thermally coupled, discretised ECM.*

### Layer 1: basic model parameter selection interface (level of discretisation)

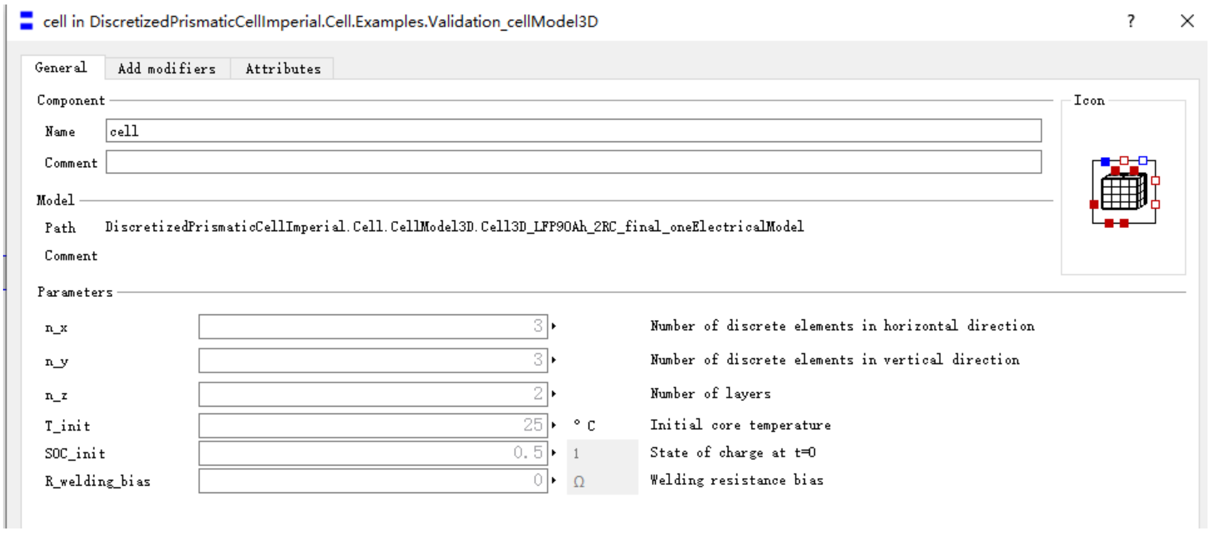

cell in DiscretizedPrismaticCellImperial.Cell.Examples.Validation_cellModel3D

Component

Name: cell

Comment:

Model

Path: DiscretizedPrismaticCellImperial.Cell.CellModel3D.Cell3D_LFP90Ah_2RC_final_oneElectricalModel

Comment:

Parameters

| | | | |
|---|---|---|---|
| n_x | 3 | | Number of discrete elements in horizontal direction |
| n_y | 3 | | Number of discrete elements in vertical direction |
| n_z | 2 | | Number of layers |
| T_init | 25 | °C | Initial core temperature |
| SOC_init | 0.5 | 1 | State of charge at t=0 |
| R_welding_bias | 0 | Ω | Welding resistance bias |

*Figure 70 Model parameter selection Layer 1*

### Layer 2: Cell model

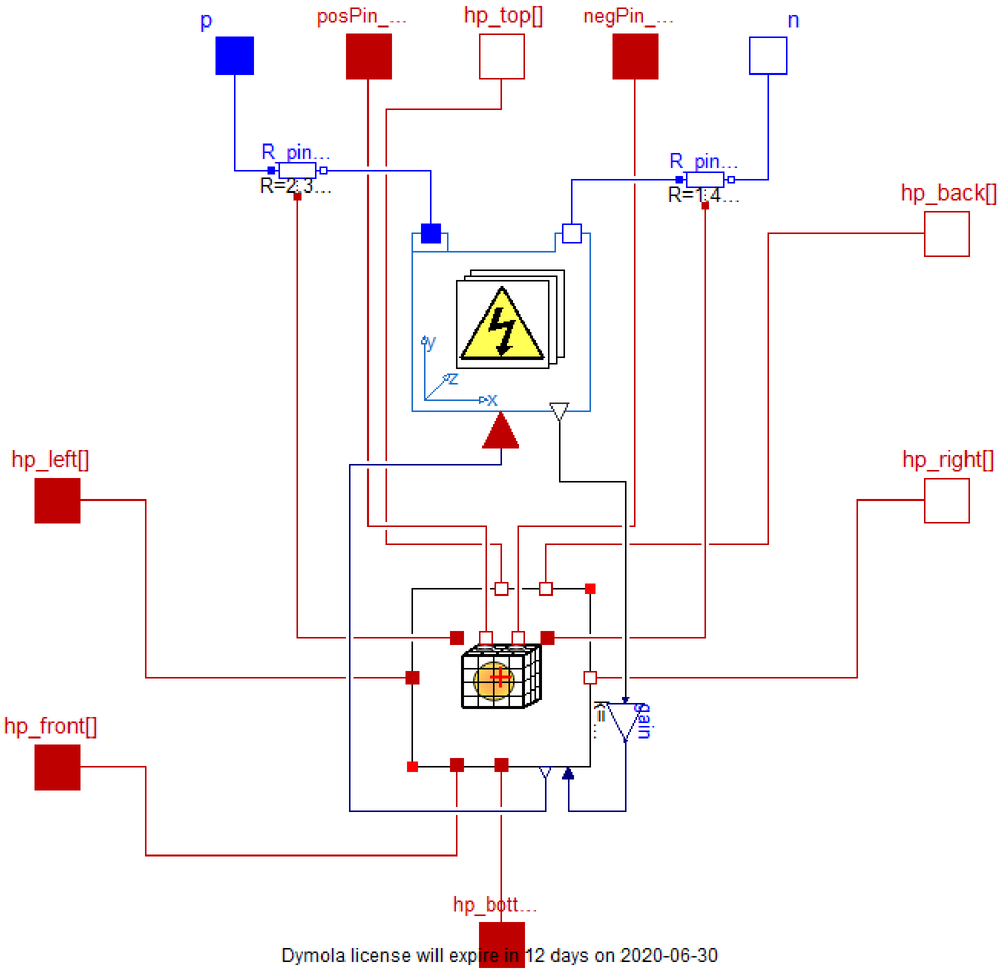

*Figure 71 Cell Model Overall structure: thermal-electric coupled.*

### Layer 3: Electric model 1_input

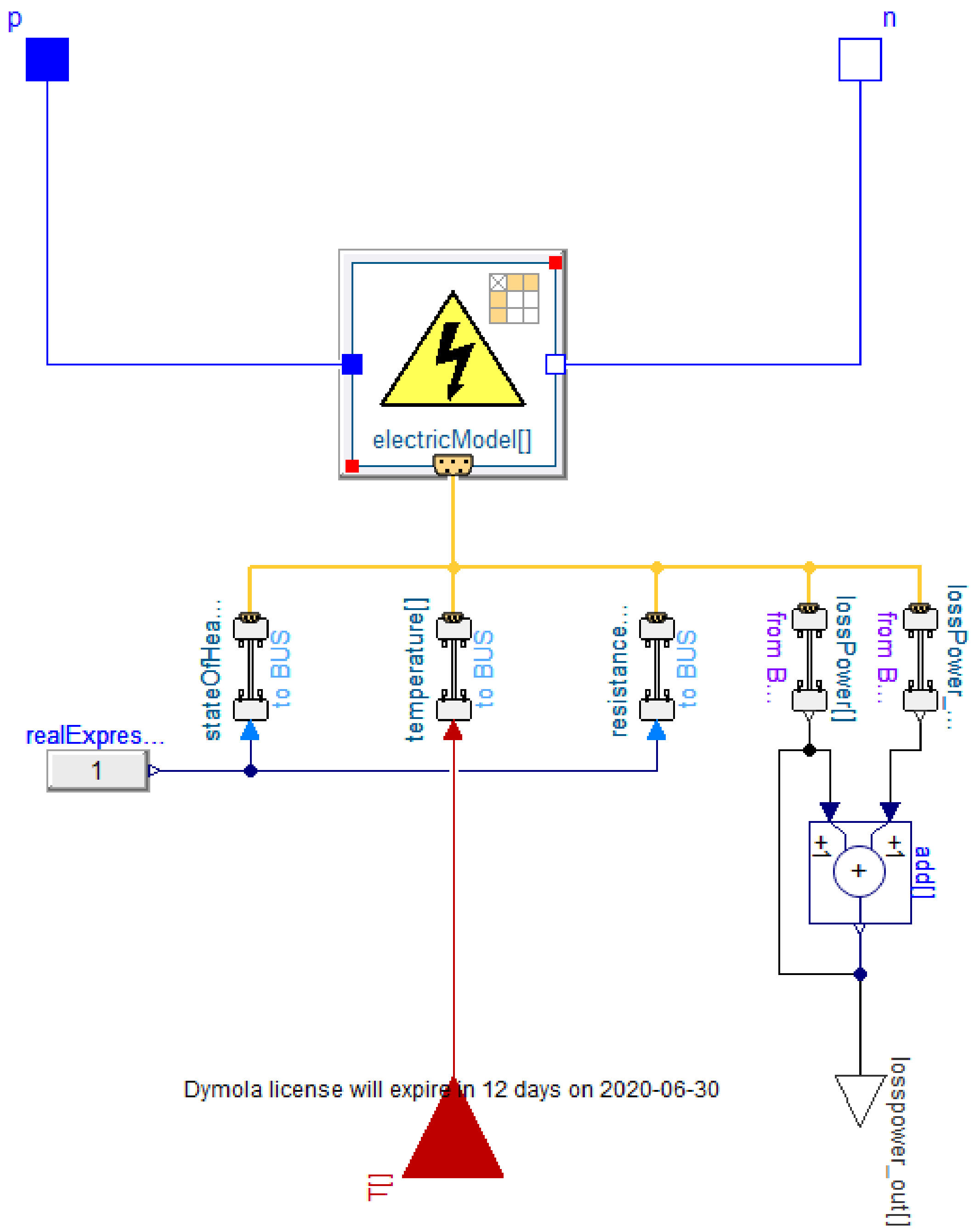

*Figure 72 Electric Model in Layer 3, model input busbars.*

## *Layer 4: Electric model 2_ECM*

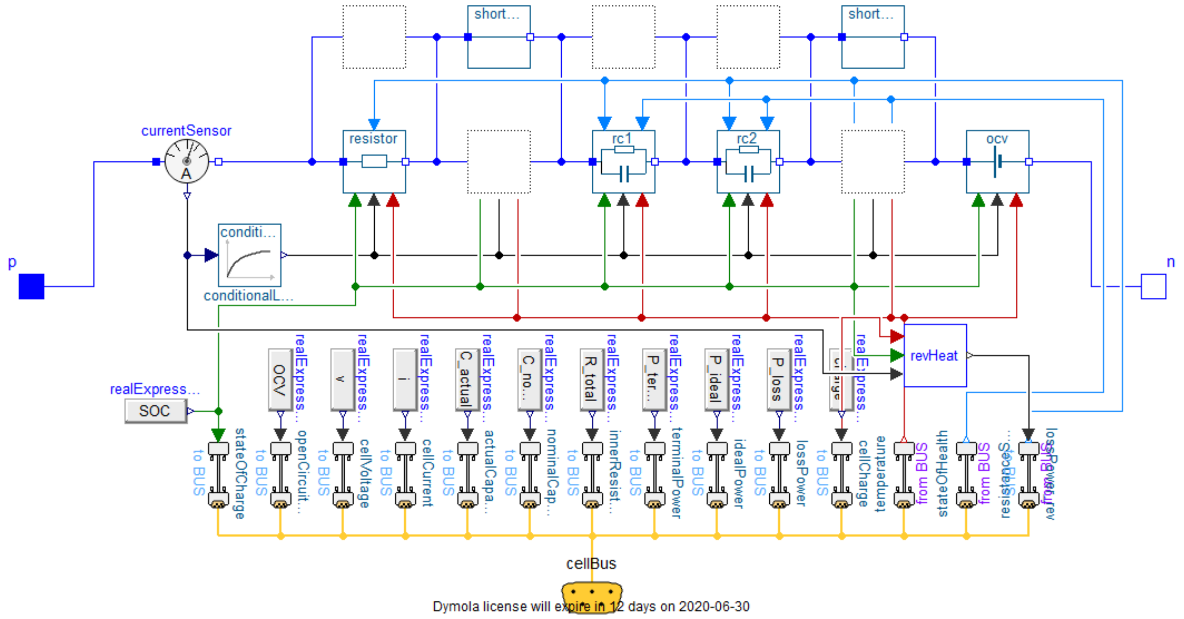

*Figure 73 Electric Model in Layer 4, ECM structure*

### *Layer 5: Electric model 3_RC network*

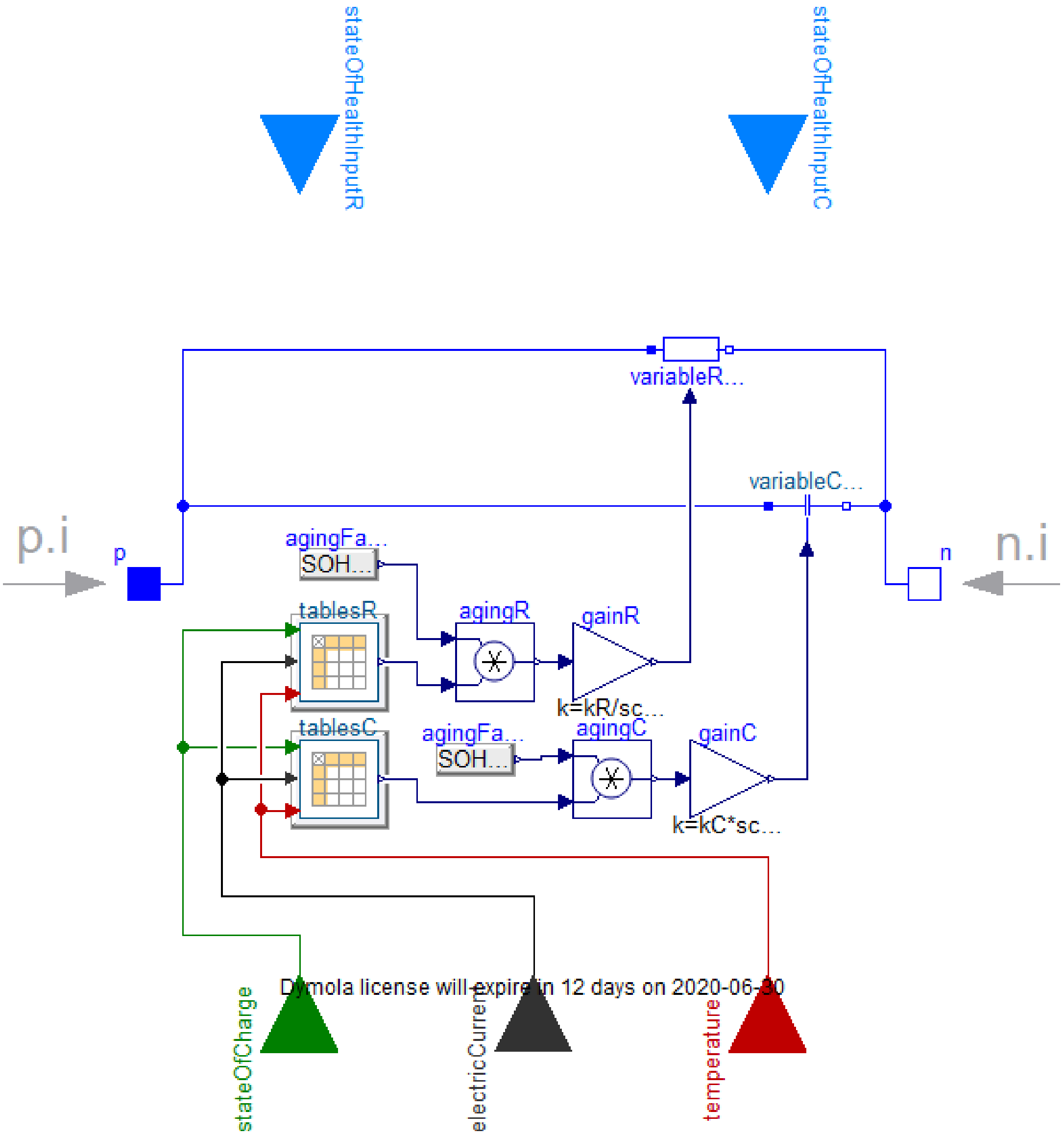

*Figure 74 Electric Model in Layer 5, RC network details & look-up tables.*

### *Layer 3: Thermal model 1 overall*

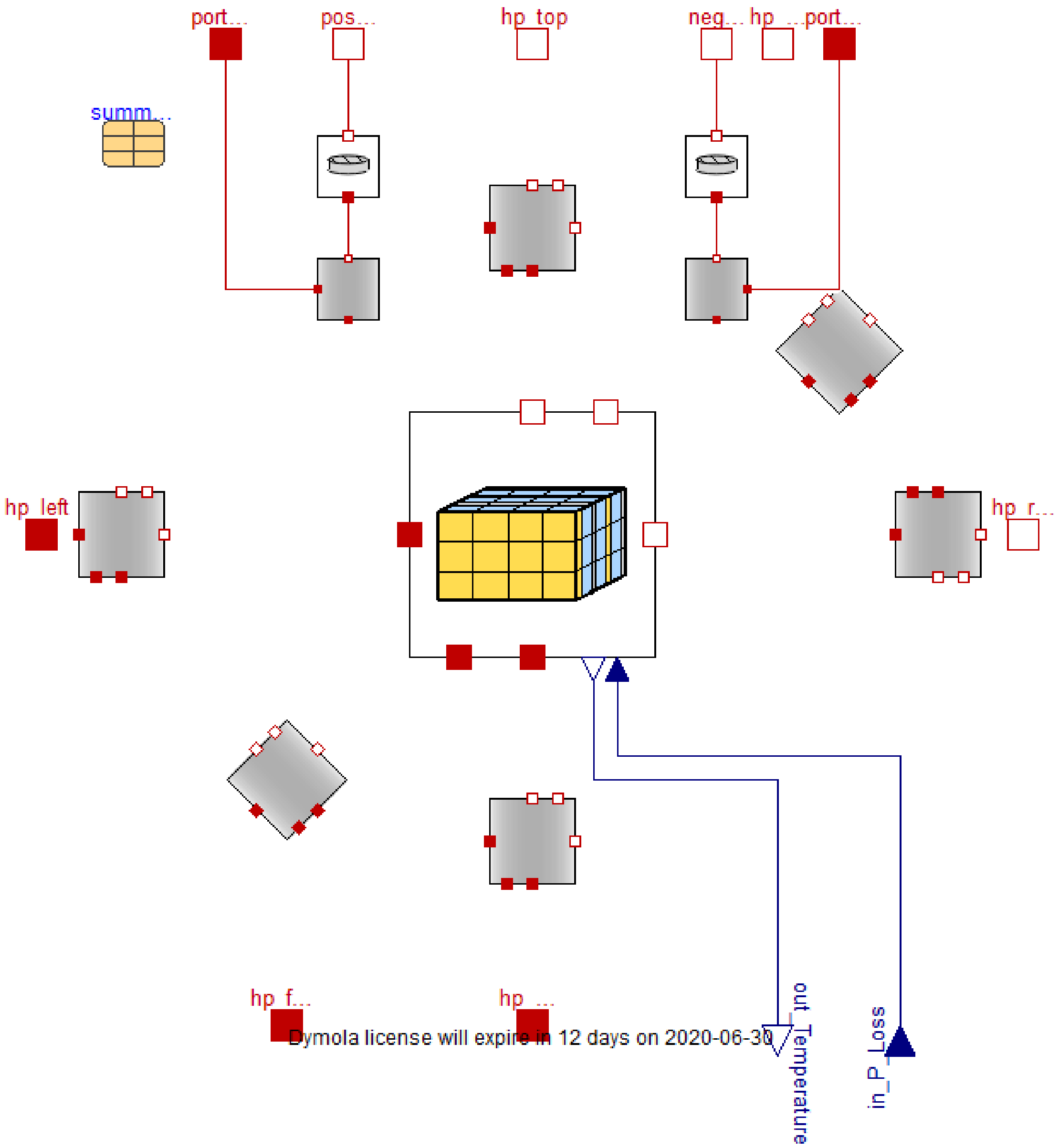

*Figure 75 Thermal Model in Layer 3, Overall structure.*

### *Layer 4: Thermal model 2 casing model*

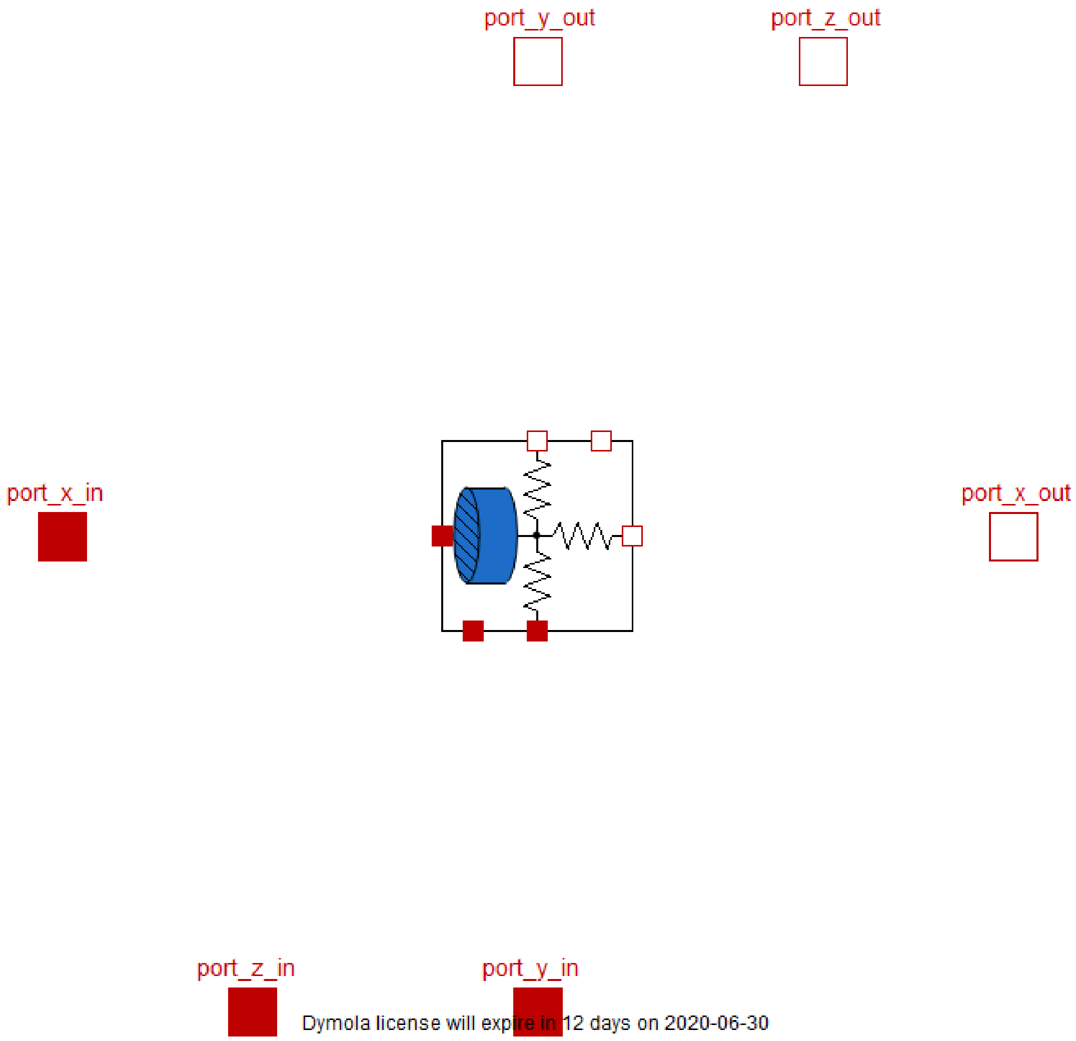

*Figure 76 Thermal Model in Layer 4, thermal resistance & thermal conductance*

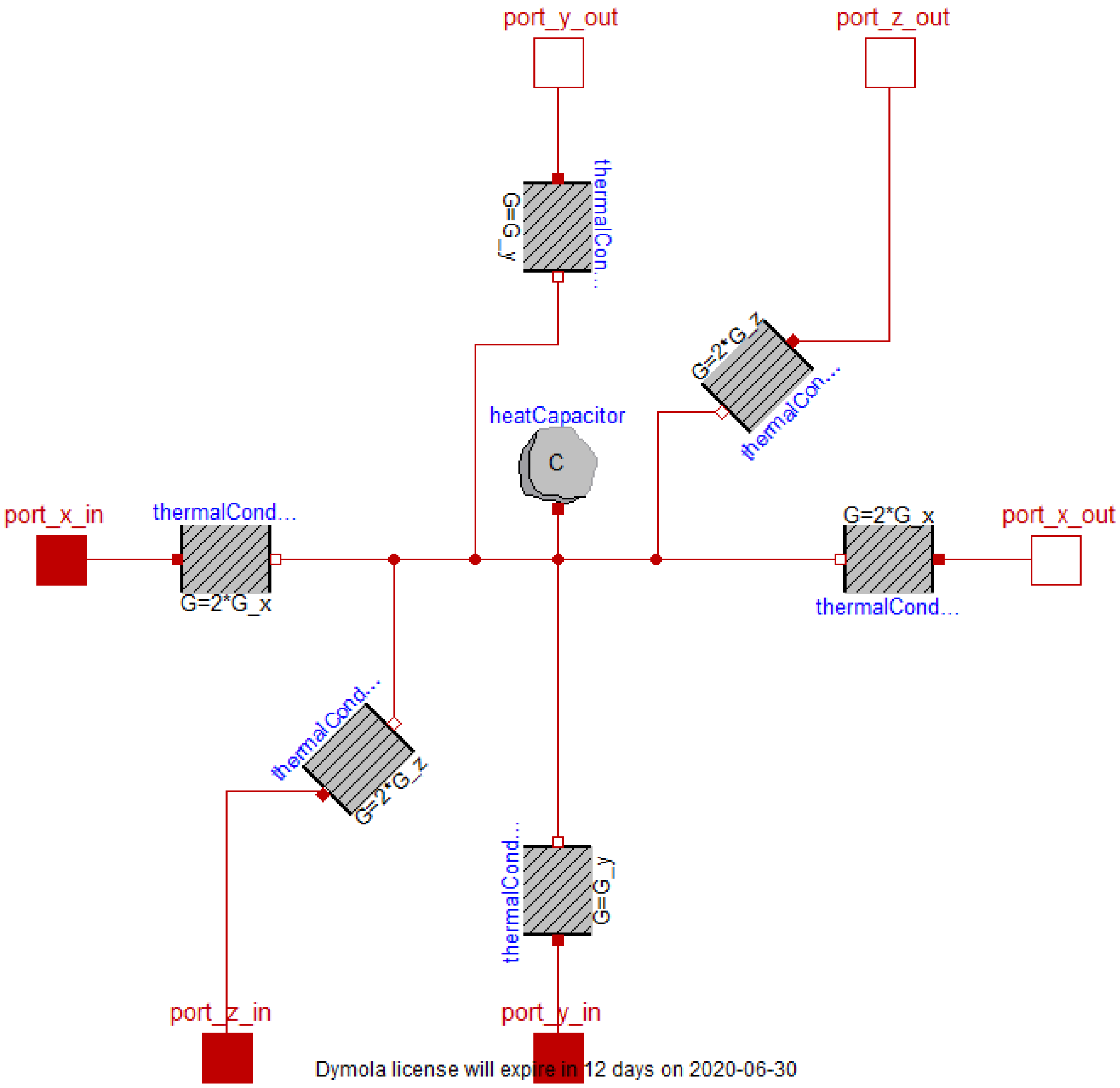

*Figure 77 Thermal Model in Layer 4, thermal resistance & thermal conductance*

### *Layer 4: Thermal model 3 battery core model: current collectors & electrode stack*

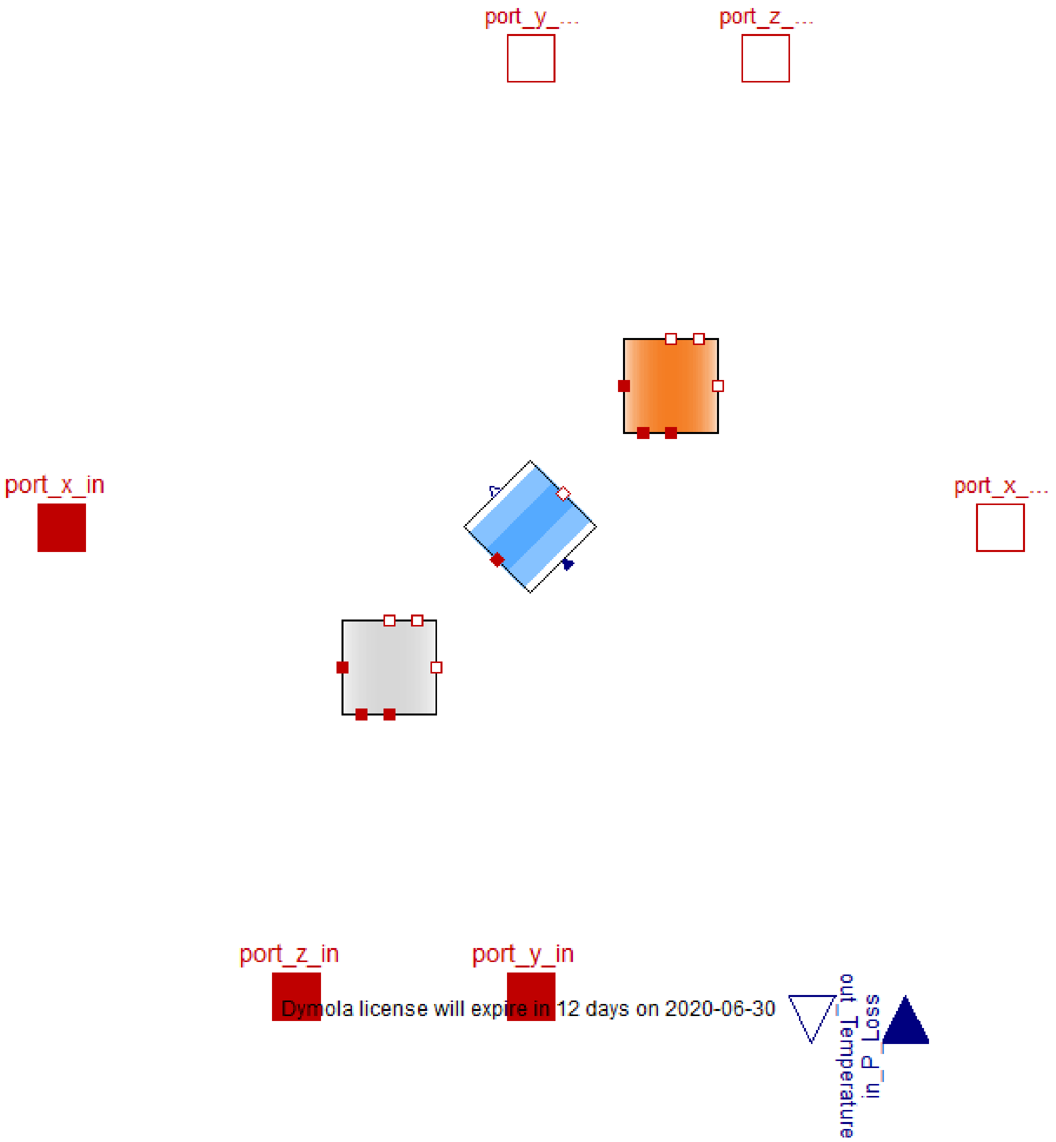

Dymola license will expire in 12 days on 2020-06-30

*Figure 78 Thermal Model in Layer 4, electrode stack and current collectors' structures.*

## *Layer 5: Thermal model 4 electrode stack model*

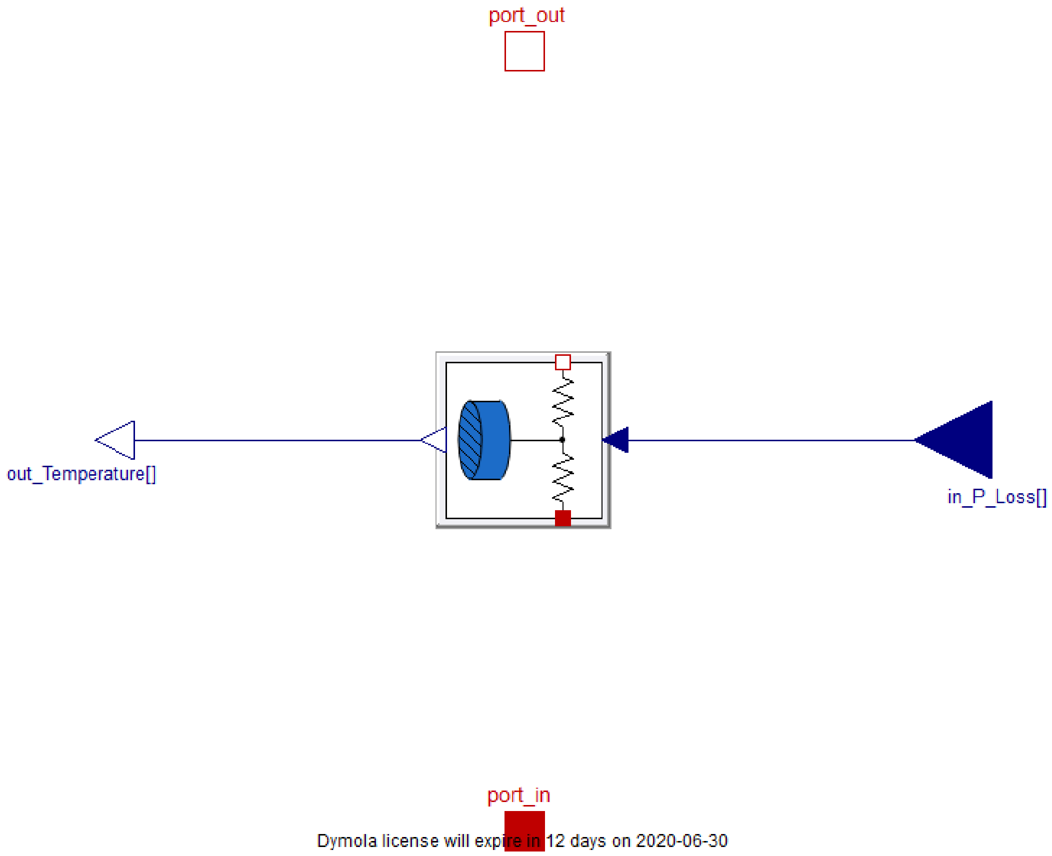

*Figure 79 Thermal Model in Layer 5, electrode stack structures.*

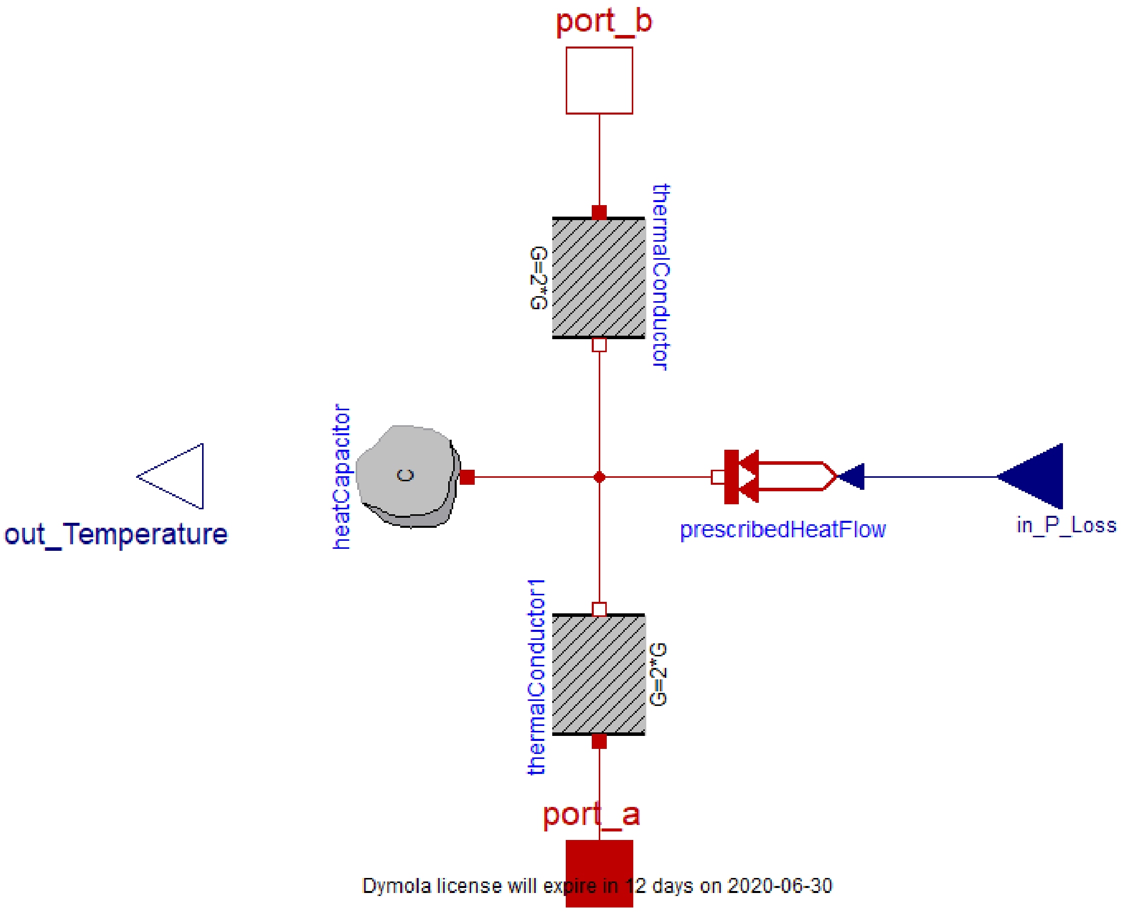

*Figure 80 Thermal Model in Layer 5, electrode stack structures.*

### *Layer 5: Thermal model 5 Current collector model*

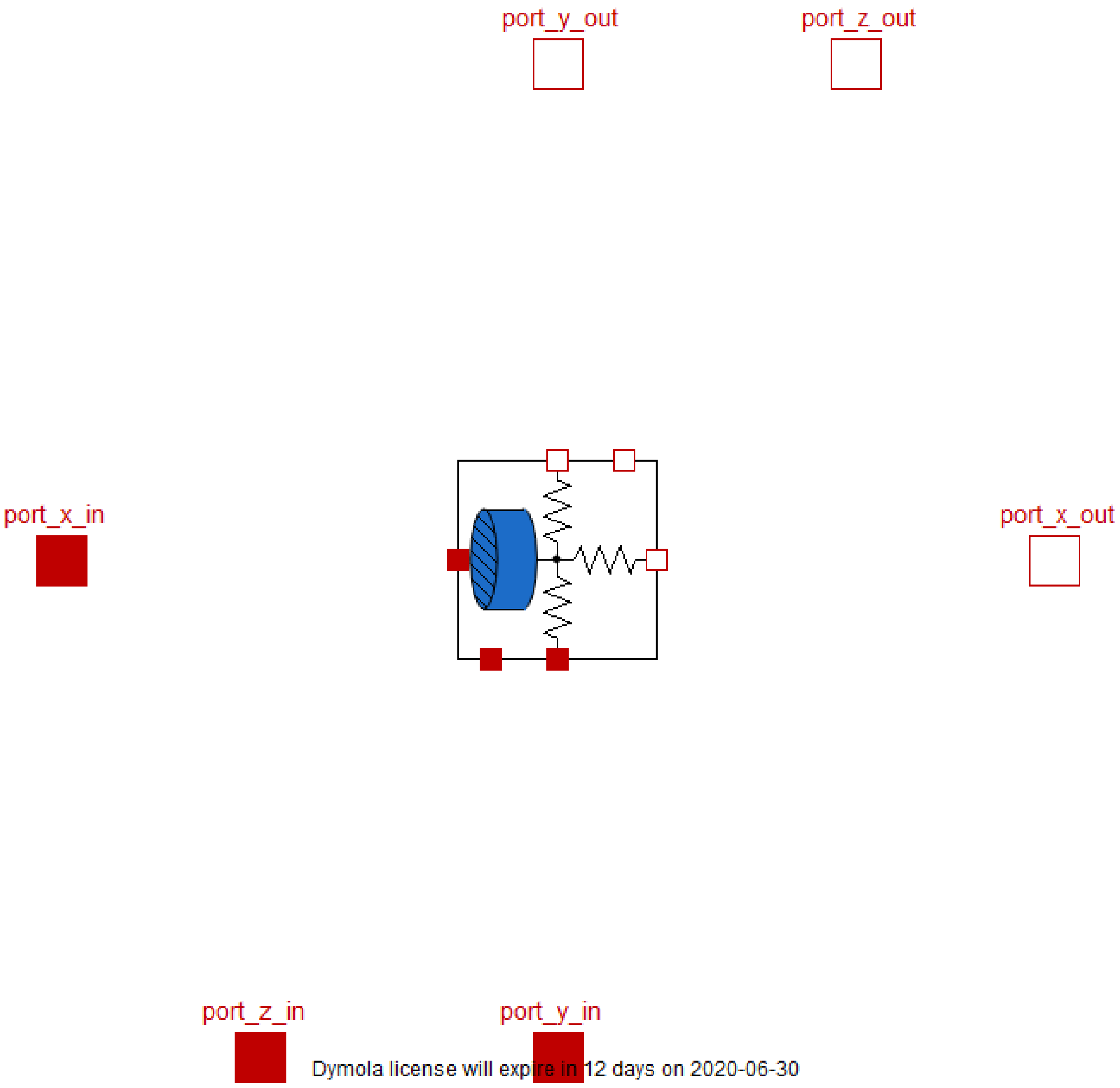

*Figure 81 Thermal Model in Layer 5, current collector structures*

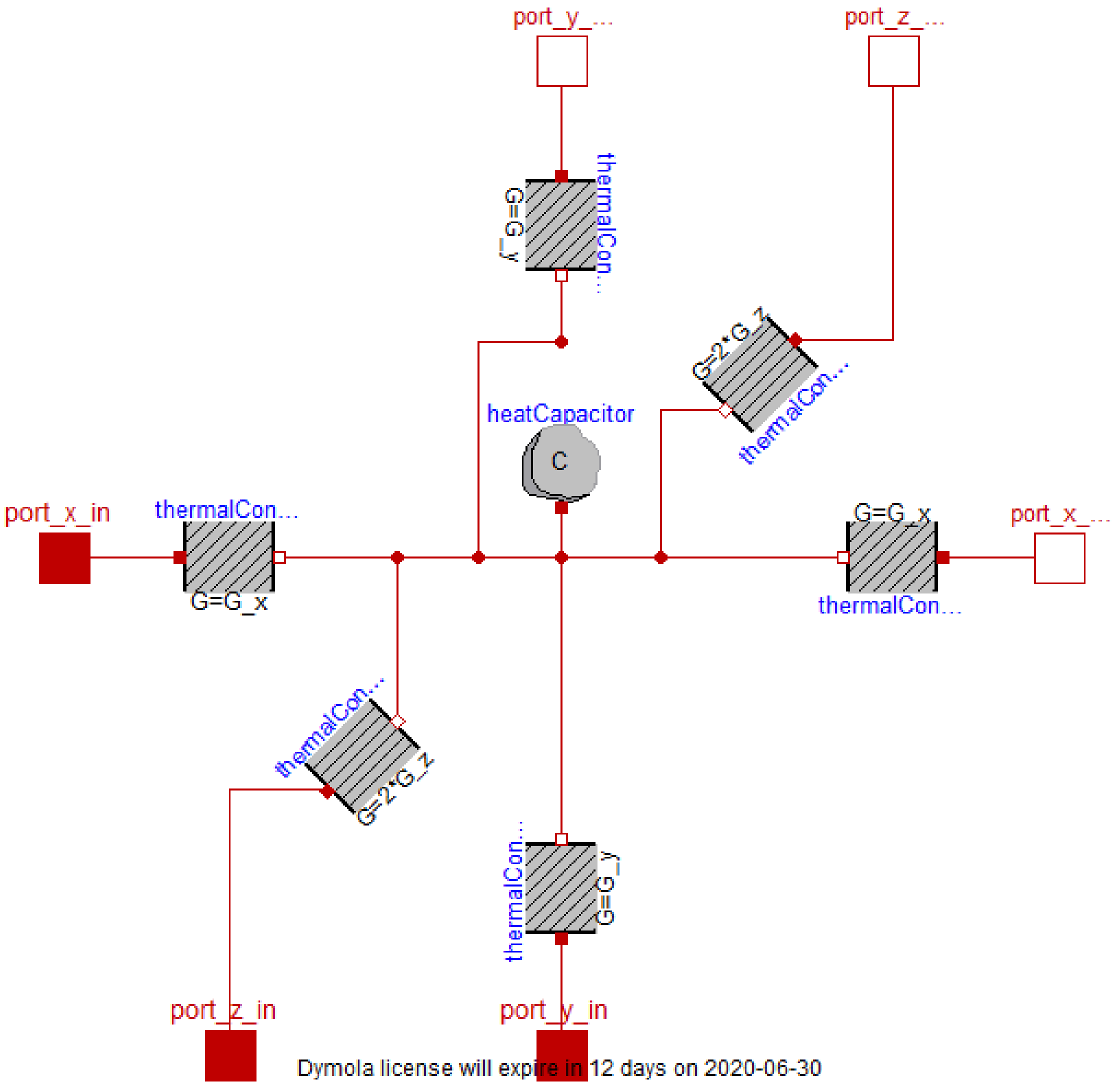

*Figure 82 Thermal Model in Layer 5, current collector structures*

## *Thermal boundary conditions 1: Cell Cooling Coefficient*

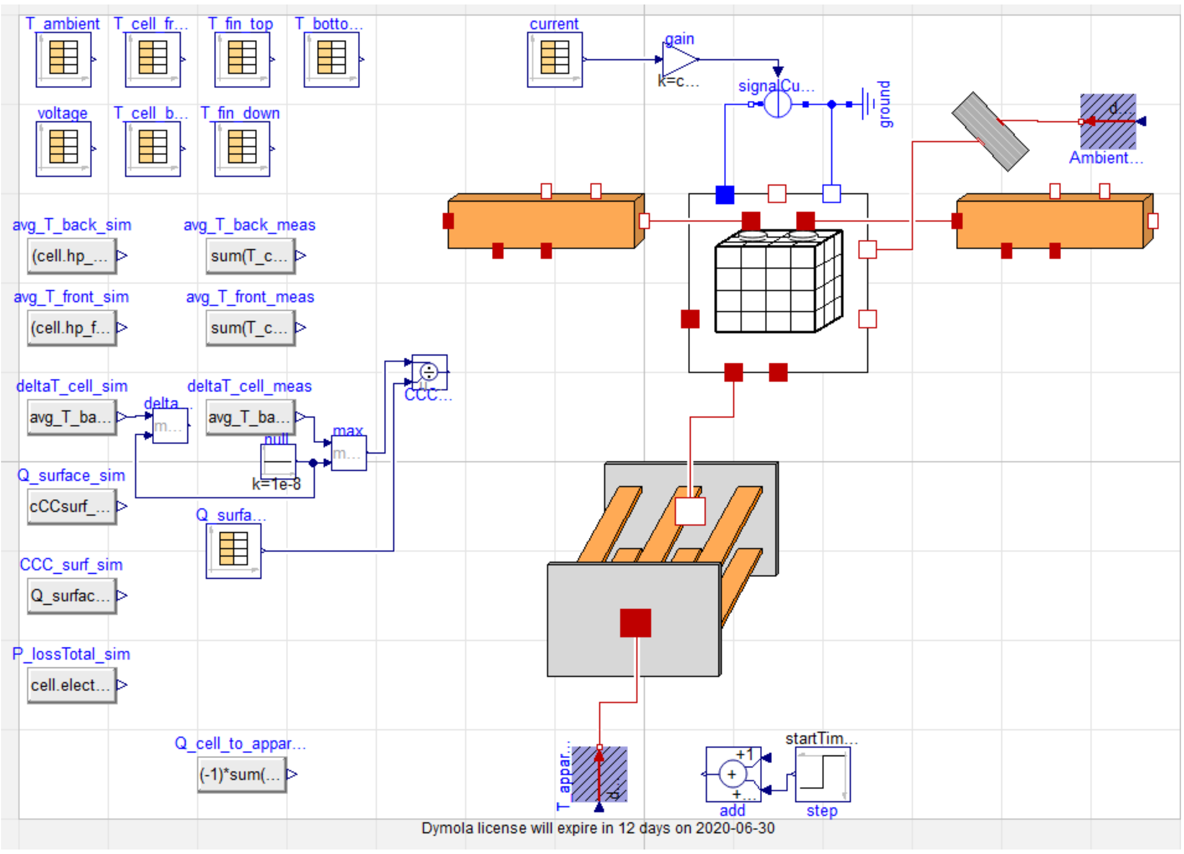

Dymola license will expire in 12 days on 2020-06-30

*Figure 83 CCC thermal boundary condition within Dymola*

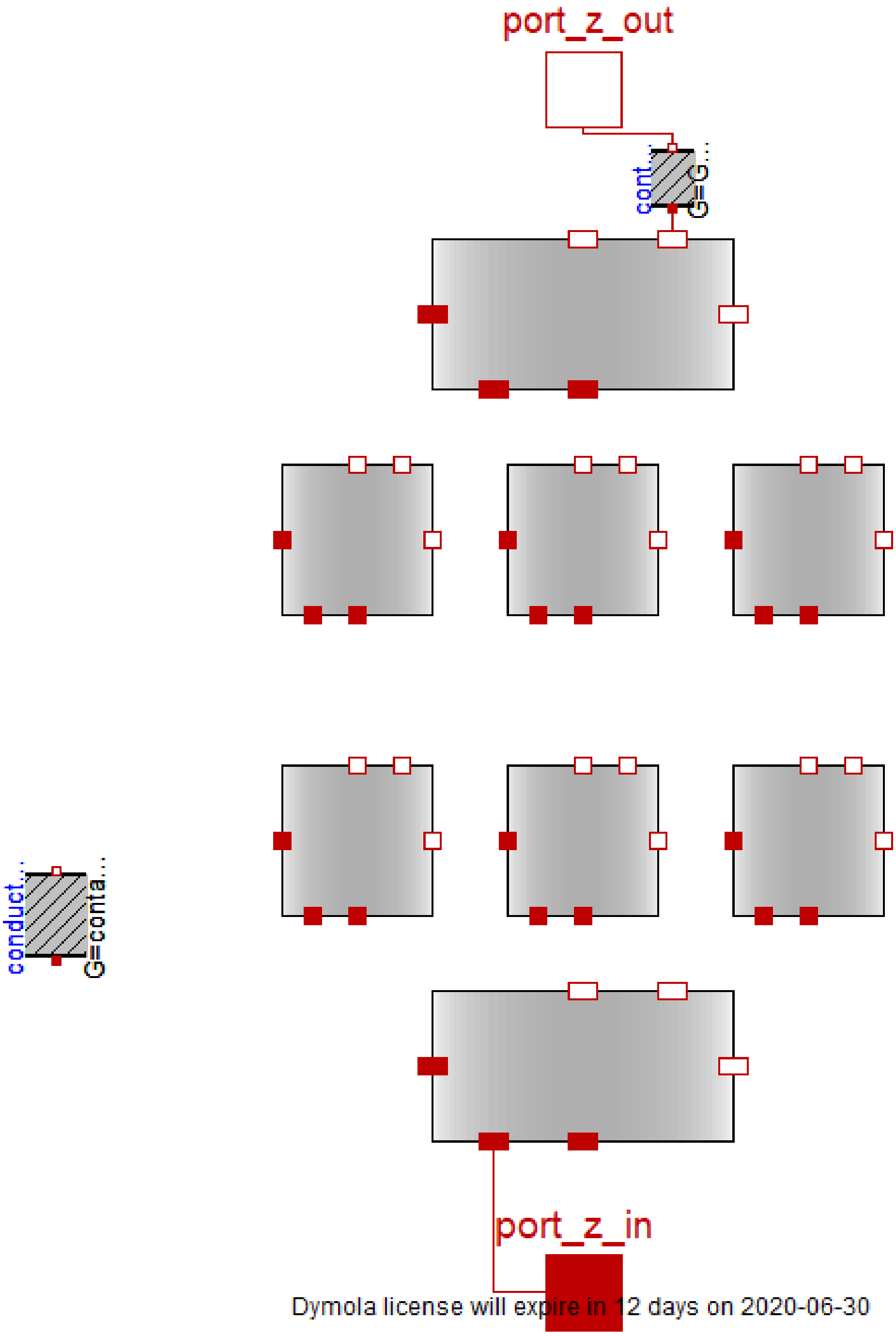

Dymola license will expire in 12 days on 2020-06-30

*Figure 84 CCC thermal boundary condition within Dymola: Aluminium testing apparatus & brass fins model*

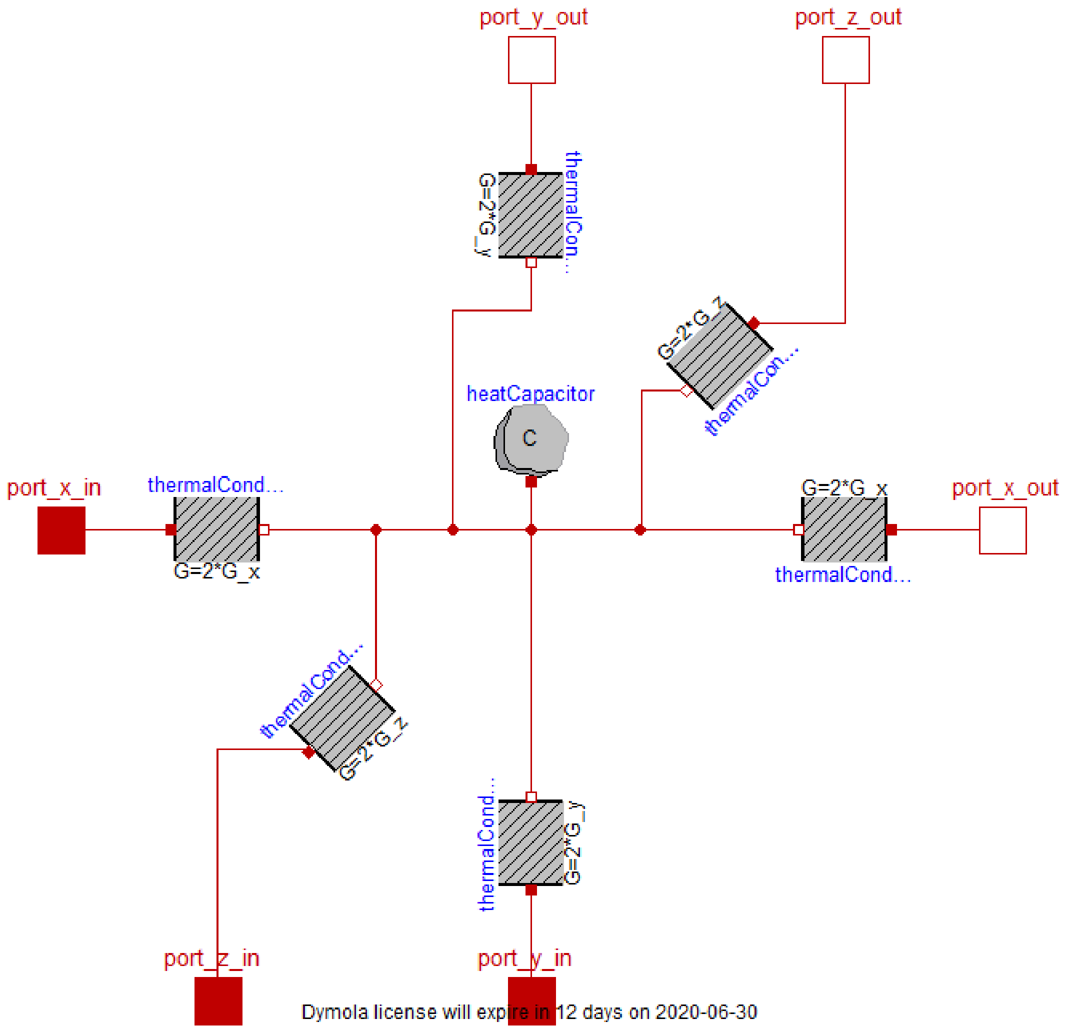

*Figure 85 CCC thermal boundary condition within Dymola: Aluminium testing apparatus & brass fins model, inner structure, thermal resistance & thermal conductance*

### *Thermal boundary conditions 2: Drive Cycle & Thermal parameter fitting*

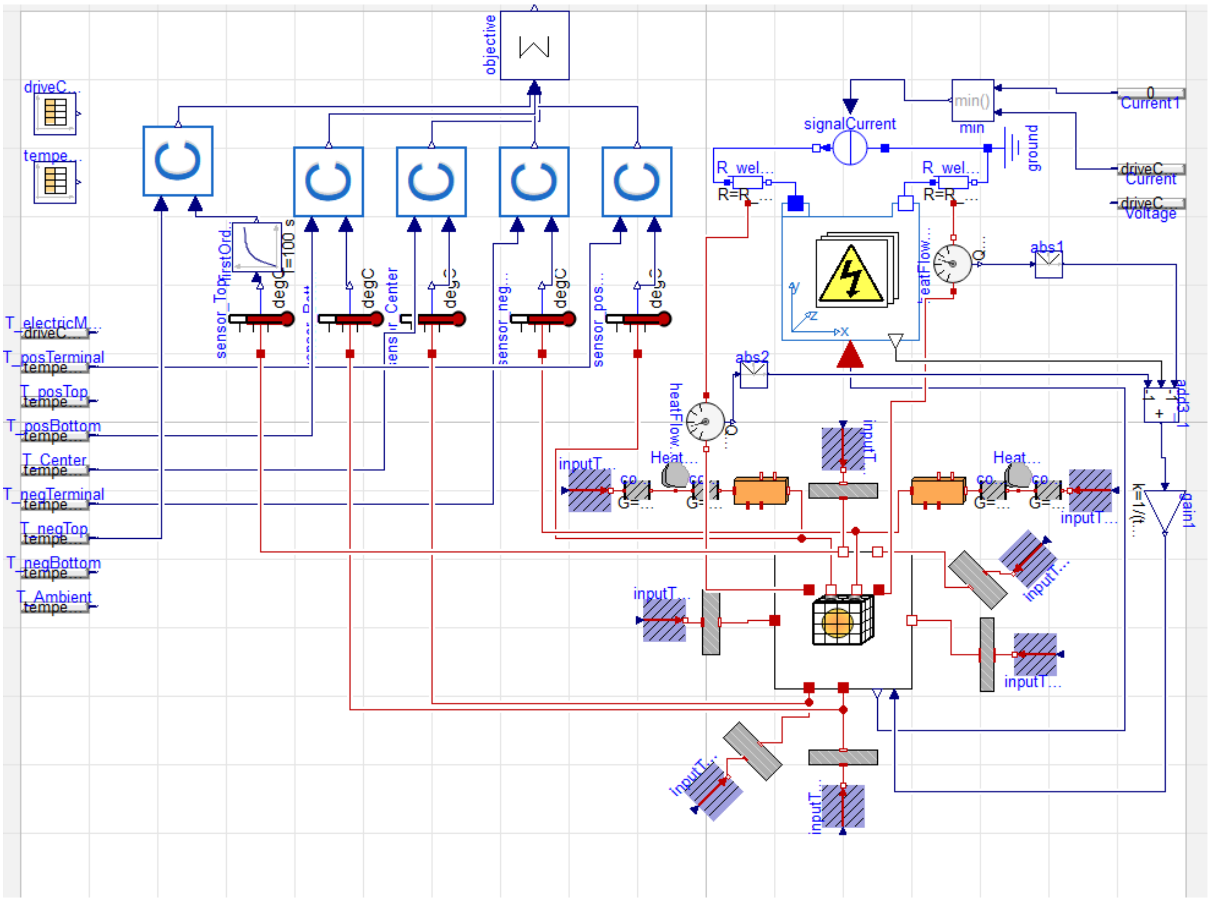

*Figure 86 Thermal boundary condition: Parameter fitting on the drive cycle validation.*

# Appendix 3: Certificate of Contribution/Participation

The letter issued by Dassault Systèmes® is attached here, where the detailed contribution and outputs have been clearly listed:

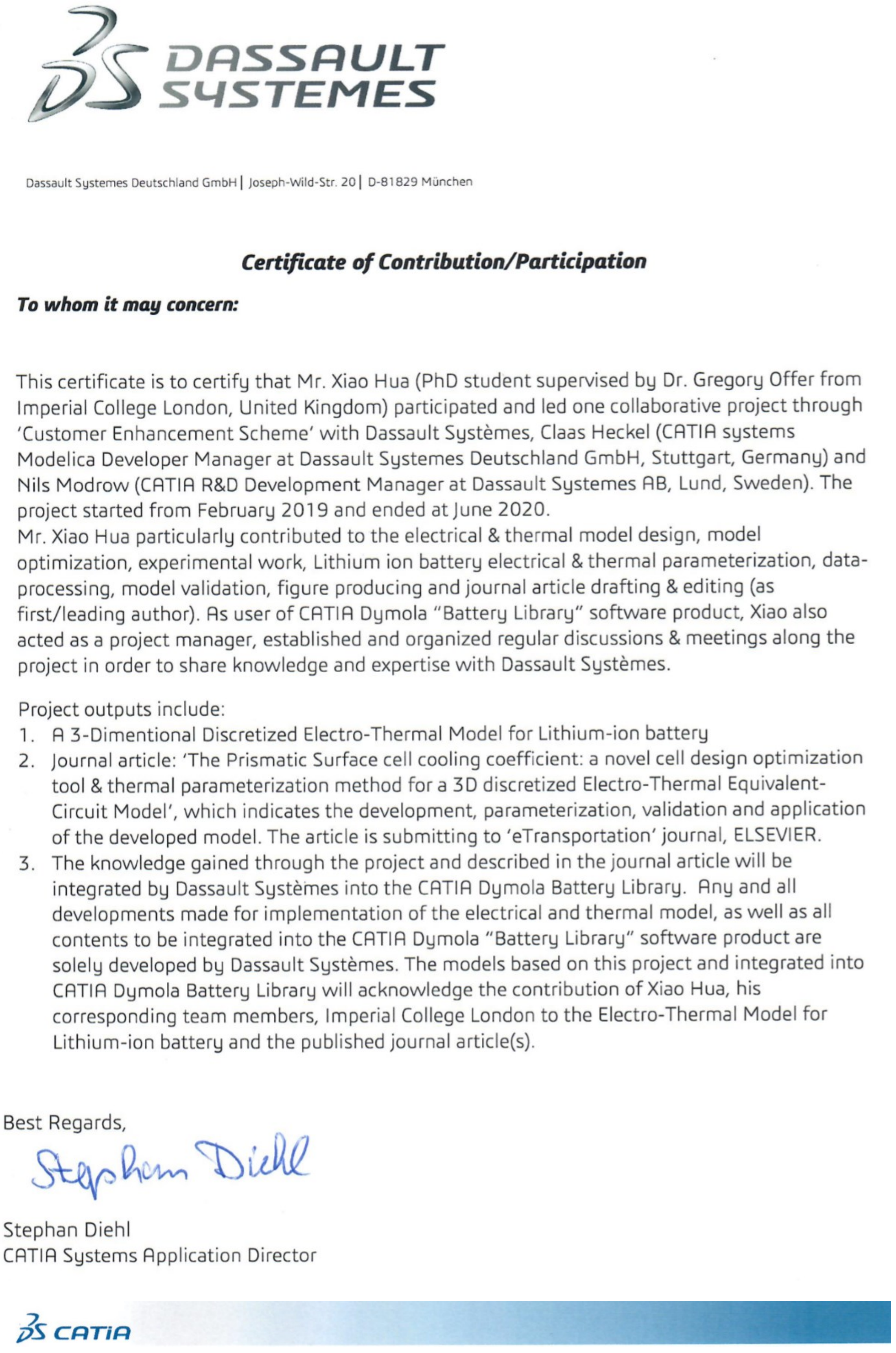

Dassault Systemes Deutschland GmbH | Joseph-Wild-Str. 20 | D-81829 München

## *Certificate of Contribution/Participation*

***To whom it may concern:***

This certificate is to certify that Mr. Xiao Hua (PhD student supervised by Dr. Gregory Offer from Imperial College London, United Kingdom) participated and led one collaborative project through 'Customer Enhancement Scheme' with Dassault Systèmes, Claas Heckel (CATIA systems Modelica Developer Manager at Dassault Systemes Deutschland GmbH, Stuttgart, Germany) and Nils Modrow (CATIA R&D Development Manager at Dassault Systemes AB, Lund, Sweden). The project started from February 2019 and ended at June 2020.
Mr. Xiao Hua particularly contributed to the electrical & thermal model design, model optimization, experimental work, Lithium ion battery electrical & thermal parameterization, data-processing, model validation, figure producing and journal article drafting & editing (as first/leading author). As user of CATIA Dymola "Battery Library" software product, Xiao also acted as a project manager, established and organized regular discussions & meetings along the project in order to share knowledge and expertise with Dassault Systèmes.

Project outputs include:

1. A 3-Dimentional Discretized Electro-Thermal Model for Lithium-ion battery
2. Journal article: 'The Prismatic Surface cell cooling coefficient: a novel cell design optimization tool & thermal parameterization method for a 3D discretized Electro-Thermal Equivalent-Circuit Model', which indicates the development, parameterization, validation and application of the developed model. The article is submitting to 'eTransportation' journal, ELSEVIER.
3. The knowledge gained through the project and described in the journal article will be integrated by Dassault Systèmes into the CATIA Dymola Battery Library. Any and all developments made for implementation of the electrical and thermal model, as well as all contents to be integrated into the CATIA Dymola "Battery Library" software product are solely developed by Dassault Systèmes. The models based on this project and integrated into CATIA Dymola Battery Library will acknowledge the contribution of Xiao Hua, his corresponding team members, Imperial College London to the Electro-Thermal Model for Lithium-ion battery and the published journal article(s).

Best Regards,

Stephan Diehl

Stephan Diehl
CATIA Systems Application Director

# Curriculum Vitae

*Xiao Hua was born in Jiangsu, People's Republic of China in 1994. He finished A-Levels at Abbey College Cambridge between 2010-2012 and graduated with A* in Mathematics, A* in Physics and A in Further Math. Between 2012-2016, he pursued a Master of Engineering (M.Eng.) in Electronic and Electrical Engineering at University College London (UCL), graduating with First Class Honours (Top 1%). Between 2016-2020 he pursued a PhD in the Department of Mechanical Engineering at Imperial College London under the supervision of Dr. Gregory J. Offer, with full PhD scholarship awarded. His research on lithium-ion/lithium-sulfur batteries thermal management, engineering, simulation, battery management system is presented in this thesis.*